METHOD DEVELOPMENT IN BIOLOGICAL SOLID-STATE NMR

Michael Matthew Jolly

THESIS SUBMITTED TO THE SCHOOL OF CHEMISTRY GRADUATE SCHOOL IN PARTIAL FULFILMENT OF THE REQUIREMENTS FOR AWARD OF THE DEGREE OF DOCTOR OF PHILOSOPHY BY THE UNIVERSITY OF SOUTHAMPTON

FACULTY OF NATURAL AND ENVIRONMENTAL SCIENCES

SCHOOL OF CHEMISTRY

UNIVERSITY OF SOUTHAMPTON

DECEMBER 2017

UNIVERSITY OF SOUTHAMPTON

ABSTRACT

FACULTY OF NATURAL AND ENVIRONMENTAL SCIENCES

School of Chemistry

Thesis for the degree of Doctor of Philosophy

METHOD DEVELOPMENT IN BIOLOGICAL SOLID-STATE NMR

Michael Matthew Jolly

Solid-state nuclear magnetic resonance (ssNMR) has proved to be a useful tool in the analysis of structural and dynamic properties of proteins. However, the inherent low sensitivity of NMR hinders further advancements of the field. This thesis focuses on improving the sensitivity of ssNMR, be this through an improvement in signal to noise or an effective improvement in sensitivity by enhancing the information content.

The mixed rotational and rotary resonance (MIRROR) sequence[1] was employed to facilitate protein backbone assignment under moderate spinning speeds. Through the band selective nature of MIRROR, bidirectional transfer of magnetisation from the C_{CO} site to the adjacent C_α and to the C_α of the next amino acid is possible. When applied to a 3D-NCOCA experiment this may be used to double the information content, providing correlations from $C_{CO}^{(i-1)}$ to both $C_\alpha^{(i-1)}$ and $C_\alpha^{(i)}$. The MIRROR recoupling of C_{CO} to C_α, is inherently low-power, allowing MIRROR to be utilised in a low-power experiment. Through this, greater enhancements in sensitivity per unit time can be realised.

The longitudinal relaxation time (T_1) limits the sensitivity per unit time at both room and cryogenic temperatures. To develop the use of relaxation agents for cryogenic NMR experiments, the room temperature relaxation properties and dynamics of the model protein, GB3, were explored. Site-specific relaxation measurements were used to understand the relaxation of residues in the protein and gain understanding into how this relates to the dynamics of the protein. In addition, low-temperature NMR measurements were used to investigate the effect temperature has on relaxation.

The ongoing development of polarisation enhancement methods and machinery have made great progress in recent years particularly on the application towards biomolecules. However, arguably the most promising polarisation enhancement technique, dynamic nuclear polarisation (DNP) suffers from a variety of problems. Namely, line broadening effects as a result of the low-temperatures required and through doping with paramagnetic agents. Furthermore, the current method of sample preparation for DNP via the use of doping with exogenous radicals is not viable for all samples. Endogenous radicals for the DNP of large biomolecules may offer several advantages to their exogenous counterparts, including but not limited to, a greater understanding of quenching effects and polarisation transfer. This thesis explores the possibility of creating pseudo-biradicals bound covalently to a protein surface to elicit enhancements through the cross effect DNP mechanism.

In summary, we have developed a range of methods that enhance the information content and sensitivity, which will provide new approaches for researchers investigating proteins using ssNMR.

Table of Contents

List of Tables

List of Figures

DECLARATION OF AUTHORSHIP

I, MICHAEL MATTHEW JOLLY

declare that this thesis and the work presented in it are my own and has been generated by me as the result of my own original research.

METHOD DEVELOPMENT IN BIOLOGICAL SOLID-STATE NMR

I confirm that:

1. This work was done wholly or mainly while in candidature for a research degree at this University;
2. Where any part of this thesis has previously been submitted for a degree or any other qualification at this University or any other institution, this has been clearly stated;
3. Where I have consulted the published work of others, this is always clearly attributed;
4. Where I have quoted from the work of others, the source is always given. With the exception of such quotations, this thesis is entirely my own work;
5. I have acknowledged all main sources of help;
6. Where the thesis is based on work done by myself jointly with others, I have made clear exactly what was done by others and what I have contributed myself;
7. Parts of this work have been published as:

Jolly, M. M.; Jarvis, J. A.; Carravetta, M.; Levitt, M. H.; Williamson, P. T. F., Bidirectional band-selective magnetisation transfer along the protein backbone doubles the information content of solid-state NMR correlation experiments. *J Biomol NMR* **2017,** *69*, 197.

Signed: .....

Date: .....

Acknowledgements

I would like to thank my supervisor Phil Williamson for all of his help and support over the past four years. Phil has continuously been encouraging me with my project and ensuring the work is heading in the right direction. I have learnt a lot from Phil, not just about NMR and academia, but he has influenced my view on many aspects of life. I would also like to thank my other supervisor Malcolm Levitt for bestowing much wisdom to direct the project. Malcolm was always welcoming with many helpful suggestions and advice.

Many people have played a part over the course of my PhD. A thank you is needed for all the members of the Williamson group and Levitt group. I thank James Jarvis for introducing me to the NMR spectrometer. I am grateful to Clemens Glaubitz for allowing me to spend time in his lab at Goethe-Universität. The members of Glaubitz lab were very welcoming during my stay. Johanna Baldus was very helpful in using their DNP setup. Assistance from Dinu Iuga during my time at Warwick University to use the 850 MHz facility is acknowledged.

Throughout the course of my PhD, I have had the fortune to interact with many interesting and kind people, with many friends made in the office area where I was located. I would especially like to extend my thanks to Luke Evans, who started his PhD at the same time as me in the Williamson lab. Luke has been of great help over the four years, with many insightful and often humorous discussions. Without Luke's friendship, the four years would undoubtedly have been much harder.

I would like to acknowledge the School of Chemistry and the School of Biological Sciences at the University of Southampton. Additionally, I acknowledge the iMR-CDT for funding my studentship.

Lastly, I thank all of my family for their support and encouragement. I especially want to thank my parents who have always pushed me to work hard.

Definitions and Abbreviations

1D	One dimensional
2D	Two dimensional
3D	Three dimensional
ASR	Anabaena sensory rhodopsin
BDPA	α,γ-bisdiphenylene-β-phenylallyl
BME	β-Mercaptoethanol
BMRB	Biological magnetic resonance bank
BSH-CP	Band selective homonuclear cross-polarisation
bTbk	bis-TEMPO-bis-ketal
CCPN	Collaborative computing project for NMR
CD	Circular dichroism
CE	Cross effect
CP	Cross-polarisation
CSA	Chemical shift anisotropy
CSI	Chemical shift index
cw	Continuous wave
DARR	Dipolar-assisted rotational resonance
DEER	Double electron-electron resonance
DNA	Deoxyribonucleic acid
DNP	Dynamic nuclear polarisation
dNTP	deoxyribose nucleoside triphosphates
DOTA	1,4,7,10-tetraazacyclododecane-1,4,7,10-tetraacetic acid

DQ	Double-quantum
DREAM	Dipolar recoupling enhanced by amplitude modulation
DSC	Differential scanning calorimetry
DSE	Differential solid effect
DSS	4,4-dimethyl-4-silapentane-1-sulfonic acid
DTA	Differential thermal analysis
DTPA	Diethylene triamine pentaacetic acid
DTPA	diethylenetriaminepentaacetic acid
DTT	Dithiothreitol
EDS	Electron dipolar system
EDTA	Ethylenediaminetetraacetic acid
EPR	Electron paramagnetic resonance
EZS	Electron Zeeman system
FID	Free induction decay
FMN	Flavin mononucleotide
FPLC	Fast protein liquid chromatography
FWHM	Full width half maximum
GB1	First immunoglobulin binding domain of protein G
GB3	Third immunoglobulin binding domain of protein G
GUI	Graphics user interface
HORROR	Homonuclear rotary resonance
IgG	Immunoglobulin G
IPTG	Isopropyl β-D-1-thiogalactopyranoside

LB	Lysogeny broth
MAS	Magic-angle spinning
MIRROR	Mixed rotational and rotary resonance
MTSSL	(1-Oxyl-2,2,5,5-tetramethylpyrroline-3-methyl) methanethiosulfonate
MW	Microwave
NCA	Nitrogen, α carbon
NCACX	Nitrogen, α carbon, unspecified carbon
NCO	Nitrogen, carbonyl carbon
NCOCX	Nitrogen, carbonyl carbon, unspecified carbon
NMR	Nuclear magnetic resonance
NZS	Nuclear Zeeman system
OD	Optical density
OE	Overhauser effect
PACC	Paramagnetic relaxation-assisted condensed data collection
PAGE	Polyacrylamide gel electrophoresis
PARIS	Phase-alternated recoupling irradiation scheme
PAS	Principal axis system
PBS	Phosphate buffered saline
PCR	Polymerase chain reaction
PCS	Pseudo contact shift
PDB	Protein data bank
PDSD	Proton-driven spin diffusion
R_1	Spin-lattice relaxation rate

$R_{1\rho}$	Spin-lattice relaxation rate in the rotating frame
R^2	Rotational resonance
R_2	Spin-spin relaxation rate
R^2TR	Rotational resonance in a tilted rotating frame
R^3	Rotary resonance recoupling experiment
*r*CW	Refocused continuous-wave
RDSD	$R2_n^v$-symmetry driven spin diffusion
REDOR	Rotational echo double resonance
rf	Radio frequency
RMSD	Root-mean-square deviation
RT	Room temperature
SDS	Sodium dodecyl sulphate
SE	Solid effect
SH3	SRC homology 3 domain
SNR	Signal to noise ratio
SPINAL-64	Small phase incremental alternation with 64 steps
ssNMR	Solid-state nuclear magnetic resonance
SW_f-TPPM	Swept-frequency two-pulse phase modulation
T_1	Spin-lattice relaxation time
$T_{1\rho}$	Spin-lattice relaxation time in the rotating frame
T_2	Spin-spin relaxation time
TEDOR	Transferred echo double resonance
TEMED	Tetramethylethylenediamine

TEMPO	(2,2,6,6-Tetramethylpiperidin-1-yl)oxyl
TM	Thermal mixing
ToSMTSL	Totapol series methane thiosulfonate spin-label
TOTAPOL	1-(TEMPO-4-oxy)-3-(TEMPO-4-amino)propan-2-ol
TPPI	Time proportional phase incrementation
TPPM	Two pulse phase-modulation
UV	Ultra violet
WT	Wild-type
XiX	X-inverse-X
ZFS	Zero-field-splitting
ZQ	Zero-quantum

Chapter 1: Introduction

Nuclear magnetic resonance (NMR) has continued to flourish as a prominent technique for the study of matter in the solid and liquid state ever since its discovery in the 1940s by Rabi, Bloch and Purcell.[2-3] Applications of NMR vary immensely among the scientific community for the analysis of dynamic, structural, and molecular interactions of a plethora of different materials, covering inorganic, organic and biological samples. Within the realm of structural biology, liquid-state NMR has found its place at the top, along with X-ray crystallography, as the foremost technique for the study of structural and dynamical properties of biomacromolecules. Liquid-state NMR owes its utility to an exploitation of the fast-rotational motion of molecules in solution, which leads to considerable simplifications in the spectra. As a result, high-resolution spectra, dominated by isotropic chemical shift effects are readily obtainable.

In contrast, rotational motions are restricted in the solid-state and as a result, anisotropic interactions are not averaged. As a consequence, for solid-state NMR (ssNMR), each orientation of the molecule will resonate at a slightly different frequency. Subsequently, a broadening of the lines and corresponding diminishment in resolution when compared to liquid-state spectra is observed. However, through retaining these orientation dependent interactions, the spectra are inherently rich in information relating to the structural properties of the system studied. Extraction of this information from complicated systems such as proteins, where information content is very dense and often overlapping has proven difficult and has likely been the main reason that solid-state NMR has not shown the universal exploitation of liquid-state NMR. Though intrinsically more difficult to utilise than liquid-state NMR, the last seven decades have shown remarkable technological and methodological improvements within the field of ssNMR. With many advancements providing a means of achieving high-resolution spectra and the extraction of both structural and dynamic properties. The technique has been firmly cemented in the field of structural studies for a range of solid matter, spanning utility for inorganic, organic, and biological solids. Within the field of structural biology, ssNMR has found its niche for the study of biopolymers that are solid in their natural state, including membrane proteins[4-6] and amyloid fibrils,[7-9] and such progress would otherwise likely not have been achievable without the study of model lyophilised[10] and microcrystalline systems.[11-12]

However, although ssNMR has come a long way, there are many pitfalls to the technique, particularly in terms of sensitivity, which often results in low signal to noise, requiring

several repeat scans to accumulate adequate signal enhancements. There are several approaches to polarisation enhancements in NMR. The simplest method, conceptually, is through a reduction in temperature, as at lower temperatures the average energy of spins is reduced, leading to a smaller percentage of the spins being able to populate the higher energy levels, and thus an enhanced polarisation is achieved. This is described by the properties of the Boltzmann distribution. In addition to this, enhanced levels of nuclear polarisation can also be achieved by exploitation of the fundamentally higher level of polarisation present in populations of unpaired electrons. This phenomenon is known as dynamic nuclear polarisation (DNP), and offers enhancements due to the higher gyromagnetic ratio of the electron in comparison to that of nuclei, with enhancements on the order of several hundred possible.

Within this body of work, we have focused on developing approaches for sensitivity enhancements in ssNMR. One of the major time-consuming steps in biomolecular ssNMR is resonance assignment. Through the utilisation of the second order dipolar recoupling scheme, the mixed rotational and rotary resonance (MIRROR) sequence,[1] we were able to both enhance the information content of ssNMR and optimise the signal per unit time of the experiment through use of a low-power regime.[13] We explored methods of sensitivity enhancements through low-temperature measurements and novel methods of DNP enhancements. Specifically, through analysis of particular relaxation agents suitable for spin-lattice relaxation (T_1) enhancement at low-temperature to help overcome the drastic increase in T_1 relaxation time. In addition, exploitation of the cross effect (CE) mechanism by design of endogenous pseudo-biradicals covalently tethered to the surface of a small protein has been explored as a means of DNP enhancement to try and overcome some of the disadvantages of conventional exogenous DNP agents.

1.1 Background to NMR

This section seeks to give an introduction to NMR and the concept of spin. The section is adapted from Spin Dynamics by Malcolm Levitt.[14]

Nuclei are composed of both neutrons and protons. Both of which belong to the family of hadrons known as baryons. As baryonic matter, neutrons and protons are made up of quarks, with protons being composed of two up quarks and one down quark and neutrons being composed of one up quark and two down quarks, where the colour force holds the quarks together. These baryons are in turn held together by the residual energy of this force, known as the nuclear force. Fundamental particles possess four intrinsic properties,

mass, charge, magnetism and spin, which leads to the composites of these particles also having these properties. Quarks possess a spin of value 1/2, which in turn by obeying the Pauli exclusion principle of fermions leads to neutrons and protons also having a spin of value 1/2. In the same manner, this leads to nuclei having a finite value of spin, dependent on its composition. Within the field of nuclear magnetic resonance (NMR) the properties of nuclear spin and nuclear magnetism are utilised to obtain very precise molecular structural information, unattainable by any other current exploitation of phenomena.

In the absence of a magnetic field, each orientation of the nuclei in space is of equivalent energy, and therefore degenerate. The application of a magnetic field leads to a splitting of this degeneracy into separate energy levels. Energy levels are dependent on the spin of the nuclei, according to $2I + 1$, where I is the spin quantum number and can take integers values of 0, 1, 2, 3, etc. and half-integer values of 1/2, 3/2, 5/2, 7/2, etc.

In the presence of a magnetic field, the nuclear magnetic moments will precess around the axis of the field from their current position, as they possess both a magnetic moment and angular momentum. Symmetry theory requires that the spin angular momentum ($\hat{S}$) is proportional to the magnetic moment ($\hat{\mu}$), $\hat{\mu} = \gamma\hat{S}$, where the proportionality constant is known as the gyromagnetic ratio (γ) and is given in rad $s^{-1}T^{-1}$. The rate of precession is proportional to the applied magnetic field, $\omega_0 = -\gamma B_0$, where ω_0 is the nuclear Larmor frequency in rad s^{-1} and B_0 is the magnetic field strength in T. The Larmor frequency of a particular nucleus under the presence of a specific field can be calculated from this relationship. Some commonly encountered gyromagnetic ratios are: $\gamma/2\pi$ for ^{1}H = 42.576 MHz T^{-1}, $\gamma/2\pi$ for ^{13}C = 10.705 MHz T^{-1}, $\gamma/2\pi$ for ^{15}N = -4.316 MHz T^{-1}.

As molecules are made up of magnetic particles, which are all rapidly moving due to thermal motion, a particular nucleus will observe a fluctuating magnetic field, which is the sum of the applied magnetic field and the time-dependent magnetic field due to the local environment.

These fluctuations in magnetic field observed by the nuclei allow a macroscopic nuclear magnetic moment to develop by the anisotropic wandering of the nuclei from their precessional cones, with a slight preference to align with the magnetic field due to the limited thermal energy available. Over time, the nuclei will relax to a new thermal equilibrium and a stable bulk magnetisation will be formed under the current conditions. The time taken for this to be achieved is known as the longitudinal relaxation time constant, T_1.

$$M_z(t) = M_{eq}\left(1 - \exp\left[-\frac{\tau}{T_1}\right]\right) \quad \textbf{(1.1)}$$

Where $M_z(t)$ is the z component of the magnetisation, M_{eq} is the equilibrium value of the magnetisation, τ is the time period, $\tau = t - t_{initial}$, where t is a time point and T_1 is the longitudinal relaxation time.

Due to the fact that the longitudinal nuclear spin magnetisation is four orders of magnitude smaller than the diamagnetism, caused by the orbital motion of electrons, detecting the longitudinal nuclear spin magnetisation is difficult. Current NMR spectroscopy takes advantage of transverse magnetization, conveniently created by the application of an electromagnetic pulse of radio frequency waves. The pulse is only active for the duration of time required for the magnetisation to be rotated into the transverse plane, and once removed the spins continue to precess around the external magnetic field with the magnetisation rotating in the x-y plane at the nuclear Larmor frequency. The x and y components of the magnetisation are given by:

$$M_y(t) = -M_{eq}\cos(\omega_0 t)\exp\left(-\frac{t}{T_2}\right) \quad \textbf{(1.2)}$$

$$M_x(t) = M_{eq}\sin(\omega_0 t)\exp\left(-\frac{t}{T_2}\right) \quad \textbf{(1.3)}$$

Where $M_y(t)$ and $M_x(t)$ are the respective magnetisation components of the x and y directions, t is the time and T_2 is the transverse relaxation time constant.

Due to the fluctuations in the magnetic field, each nucleus observes a slightly different magnetic field and therefore over time, the spins will become out of phase with each other, known as a loss of coherence, which is the origin of the decay of the transverse magnetisation. This happens on a timescale typically much shorter than the time taken for the longitudinal magnetisation to recover. For comparison, for biomolecules at 298 K ^{1}H T_1 is generally between $0.1\text{ s} \leq T_1 \leq 1\text{ s}$ at ambient temperature, while ^{1}H T_2 is generally between of $0.01\text{ s} \leq T_1 \leq 0.1\text{ s}$.

The precession of the bulk magnetic moment has an electric field affiliated with it and can be used to induce an oscillating current in a coil of wire, therefore enabling the detection of the signal. This signal is observed as a free induction decay (FID). Through the mathematical tool known as the Fourier transform one is able to convert the FID, which exists in the time domain, into the more easily interpretable frequency domain (Figure 1.1).

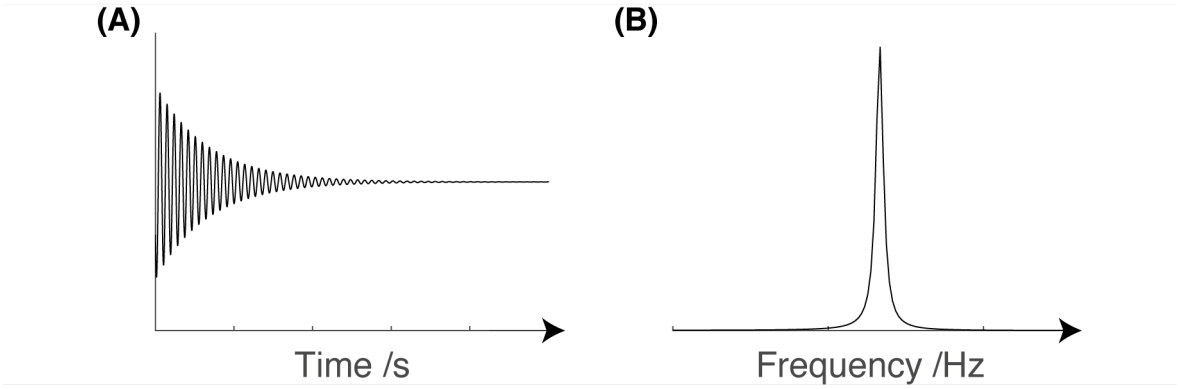

Figure 1.1 Illustration of the Fourier transform of an FID. Illustration of an FID (A) and the signal generated from this by Fourier transform (B). The frequency of the sinusoidal wave, ω = 70 Hz, phase angle of the sinusoid, φ = 0.

1.2 NMR Interactions

This section aims to form a foundation of knowledge on the basics of interactions in NMR, giving a superficial overview of the interaction terms of the Hamiltonian experienced by spins in a typical NMR experiment. The content summarises more thorough discussions of the theory of NMR previously published.[14-20]

1.1.1 Nuclear Spin Hamiltonian

A Hamiltonian, $\widehat{H}$, is an operator describing the total energy of the system. The nuclear spin Hamiltonian comprises all the information pertaining to the interactions of nuclei with non-zero spin in the presence of a magnetic field. It can be broken down into the internal and external components:

$$\widehat{H} = \widehat{H}_{Ext} + \widehat{H}_{Int} \quad \textbf{(1.4)}$$

Where $\hat{H}$ is the complete Hamiltonian for the energy of the system in units of J, $\widehat{H}_{Ext}$ constitutes the interaction energy of the spins within an external static magnetic field, B_0, in addition to radiofrequency (rf) fields, B_1, while $\widehat{H}_{Int}$ describes the internal interactions present. The external and internal components can be separated into their individual components as follows:

$$\widehat{H}_{Ext} = \widehat{H}_Z + \widehat{H}_{RF} \quad \textbf{(1.5)}$$

Where $\widehat{H}_Z$ is the Hamiltonian describing the Zeeman splitting by an external magnetic field and $\widehat{H}_{RF}$ describes the effect of an rf-pulse on the energy of the system. In a rotating frame,

the coordinate system is rotating at the Larmor frequency so the Zeeman interaction can be ignored in this frame.

$$\widehat{H}_{Int} = \widehat{H}_J + \widehat{H}_{CS} + \widehat{H}_D + \widehat{H}_Q \quad \textbf{(1.6)}$$

Where $\widehat{H}_J$ is the Hamiltonian describing the J-coupling between nuclei, $\widehat{H}_{CS}$ is the Hamiltonian describing the chemical shift anisotropy, $\widehat{H}_D$ is the Hamiltonian describing the dipolar interaction between nuclei and $\widehat{H}_Q$ is the Hamiltonian describing the quadrupolar interaction between nuclei and is only present for spins with $I > 1/2$.

1.1.2 External Interactions

1.1.2.1 The Zeeman Interaction

The Zeeman interaction describes the loss in degeneracy observed when an external magnetic field is exerted on a spin. In the presence of a magnetic field, the energy levels are split into $2I + 1$, known as the Zeeman splitting. This splitting is on the order of 10^8 Hz. Other lower energy splittings are also present which can be useful in determining structural and dynamic information of molecular systems.

The Hamiltonian describing the Zeeman splitting, in a Cartesian axis system is[21]:

$$\widehat{H}_Z = \overrightarrow{\hat{I}_1} \cdot (-\gamma) \overleftrightarrow{1} \cdot \vec{B}_0 \quad \textbf{(1.7)}$$

Where $\overrightarrow{\hat{I}_1}$ is the vector form of the nuclear spin operator, $\overrightarrow{\hat{I}_1} = \hat{I}_{1x}, \hat{I}_{1y}, \hat{I}_{1z}$ where "1" indicates which spin is referred to and $\overleftrightarrow{1}$ is the identity matrix. $\vec{B}_0$ is the vector to the external static magnetic field, in units of T, which is non-zero only in the z-axis, $\vec{B}_0 = (0,0,B_{0z})$, therefore equation (1.7) can be represented as:

$$\begin{aligned} \widehat{H}_Z &= -\gamma B_0 \hat{I}_{1z} \quad \textbf{(1.8)} \\ &= \omega_0 \hat{I}_{1z} \end{aligned}$$

Where $\hat{I}_{1z}$ is the z component of the spin operator, γ is known as the gyromagnetic ratio (or magnetogyric ratio), given in units of rad $s^{-1}T^{-1}$, and serves to quantify the magnitude of the interaction of the spin with the external magnetic field. The gyromagnetic ratio is the quotient of the particles magnetic moment to its angular momentum. B_0 represents the external static magnetic field, which is taken as along the z-axis in the laboratory frame.

$\omega_0 = -\gamma B_0$ and is the Larmor frequency in rad s^{-1}. The separation of energy levels is proportional to the Larmor frequency.

1.1.2.2 The Radio Frequency Interaction

An NMR experiment utilises pulses of rf-irradiation to manipulate spins. These pulses are directed orthogonal to the permanent static magnetic field $\overrightarrow{B_0}$. As a type of electromagnetic radiation, rf-irradiation takes the form of an oscillating magnetic field, denoted $\overrightarrow{B_1}$. The application of this field leads to a mixing of the Zeeman states when applied at a frequency, ω_{rf}, comparable to the Larmor frequency, ω_0, converting spins into detectable coherence states. This oscillating $\overrightarrow{B_1}$ field can be de-convoluted as follows:

$$\begin{aligned}\overrightarrow{B_1}(t) &= 2B_1\cos(\omega_{rf}t+\phi) \\ &= B_1(e^{i\omega_{rf}t+\phi}+e^{-i\omega_{rf}t+\phi})\end{aligned} \quad \textbf{(1.9)}$$

Where $\pm\omega_{rf}$ corresponds to the angular frequencies of the two components of B_1 rotating in opposite directions. ϕ defines the phase of the rf-pulse. When the rf-field is on the order of the nuclear Larmor frequency, i.e. $\omega_{rf} \cong \omega_0$, results in the positive component having a frequency suitably close to ω_0 to affect the angle of precession. The Hamiltonian describing the effect of an rf-pulse can be described as[21]:

$$\begin{aligned}\hat{H}_{RF} &= \overrightarrow{\hat{I}_1}\cdot(-\gamma)\overleftrightarrow{1}\cdot\vec{B}_1 \\ &= -\gamma B_1[\hat{I}_{1x}\cos(\omega_{rf}t+\phi)\pm\hat{I}_{1y}\sin(\omega_{rf}t+\phi)\end{aligned} \quad \textbf{(1.10)}$$

Moving to a reference frame rotating at ω_{rf}, the equation takes the form of:

$$\begin{aligned}\hat{H}_{RF}^{rot} &= -\gamma B_1[\hat{I}_{1x}\cos(\phi)+\hat{I}_{1y}\sin(\phi) \\ &= \omega_1[\hat{I}_{1x}\cos(\phi)+\hat{I}_{1y}\sin(\phi) \\ &= \omega_1\hat{I}_{1x} \text{ if } \phi = 0 \\ &= \omega_1\hat{I}_{1y} \text{ if } \phi = \pi/2\end{aligned} \quad \textbf{(1.11)}$$

In which $\omega_1 = -\gamma B_1$, is the nutation frequency, the angular frequency of the rf-pulse. The rf-pulse Hamiltonian serves to rotate the magnetisation vector from its principal position aligned with the z-axis to a position in the transverse plane where the magnetisation can be detected by the receiver coil as a free induction decay (FID).

1.1.3 Internal Interactions

The Hamiltonians for internal interactions are most conveniently expressed in irreducible spherical tensor notation, as this form is apt at dealing with the effects of rotations and following the orientation dependence of the interactions. In spherical tensor notation, the general form of the Hamiltonian is given by[21]:

$$\widehat{H} = C_{\mu} \sum_{l} \sum_{m=-l}^{+l} (-1)^{m} A_{l,m}^{(\mu)} \hat{T}_{l,-m}^{(\mu)} \tag{1.12}$$

Where C_{μ} is a constant for each particular interaction and μ indicates the type of interaction, l is the angular momentum quantum number (rank of the tensor), m is the magnetic quantum number and can take values of $m = -l, -l+1 \ldots l-1, +l$, $A_{l,m}^{(\mu)}$ represents the spatial tensor components, and $\hat{T}_{l,-m}^{(\mu)}$ is the irreducible spin tensor operator.

For a sufficiently high magnetic field, the secular approximation may be applied, as such the Hamiltonian is written in the rotating frame of reference. This holds for typical NMR spectrometers of field strength $4.7\ \text{T} \leq B_0 \leq 23.5\ T$ as the Zeeman interaction is at least a factor of 10^3 higher than that of the internal interactions. First-order perturbation theory dictates that the internal interactions can be considered to be perturbations of the Zeeman interaction, with only the commuting terms effecting the Hamiltonian[22], as such the Hamiltonian for internal interactions can be subdivided into commuting and non-commuting components:

$$\widehat{H}_{Int} = \widehat{H}^{1}_{Int} + \widehat{H}^{2}_{Int} \tag{1.13}$$

Where $\widehat{H}^{1}_{Int}$ commutes with the Zeeman Hamiltonian and $\widehat{H}^{2}_{Int}$ does not:

$$[\widehat{H}_Z, \widehat{H}^{1}_{Int}] = 0 \tag{1.14}$$
$$[\widehat{H}_Z, \widehat{H}^{2}_{Int}] \neq 0$$

Only terms that are diagonal in the Zeeman Eigen basis may commute with the Zeeman Hamiltonian. Terms that commute with the Zeeman Hamiltonian are known as secular terms, and such terms perturb the Zeeman Hamiltonian to first-order. Non-commuting terms do not affect the Zeeman Hamiltonian on a first-order level. Irreducible spherical tensor operators of $m = 0$ are the only terms to have on-diagonal elements within a Zeeman Eigen basis and thus commute with the Zeeman Hamiltonian as follows:

$$[\hat{H}_Z, \hat{T}^{(\mu)}_{l,-m}] = m\hat{T}^{(\mu)}_{l,-m} \tag{1.15}$$

Therefore, for tensors of rank 2, equation (1.12) may be reduced to:

$$\begin{aligned} \hat{H} &= C_\mu \sum_{m=0}^{2} A^{(\mu)}_{l,0} \hat{T}^{(\mu)}_{l,0} \\ &= C_\mu (A^{(\mu)}_{0,0}\hat{T}^{(\mu)}_{0,0} + A^{(\mu)}_{1,0}\hat{T}^{(\mu)}_{1,0} + A^{(\mu)}_{2,0}\hat{T}^{(\mu)}_{2,0}) \end{aligned} \tag{1.16}$$

Under the secular approximation, a general Cartesian tensor of rank 2 is described by:

$$\overleftrightarrow{A} = \begin{pmatrix} A_{xx} & A_{xy} & A_{xz} \\ A_{yx} & A_{yy} & A_{xz} \\ A_{zx} & A_{xy} & A_{zz} \end{pmatrix} \tag{1.17}$$

The above rank 2 Cartesian tensor can be expressed as the components of a rank 2 irreducible spherical tensor:

$$\begin{aligned} A_{0,0} &= \frac{-1}{\sqrt{3}}(A_{xx} + A_{yy} + A_{zz}) \\ A_{1,0} &= \frac{-i}{2}(A_{xy} - A_{yx}) \\ A_{1,\pm1} &= \frac{-1}{2}\Big((A_{zx} - A_{xz}) \pm i(A_{zy} - A_{yz})\Big) \\ A_{2,0} &= \frac{1}{\sqrt{6}}(3A_{zz} - (A_{xx} + A_{yy} + A_{zz}) \\ A_{2,\pm1} &= \pm\frac{1}{2}\big((A_{xz} - A_{zx}) \pm i(A_{yz} + A_{zy})\big) \\ A_{2,\pm2} &= \frac{1}{2}\big((A_{xx} - A_{yy}) \pm i(A_{xy} + A_{yx})\big) \end{aligned} \tag{1.18}$$

It is usually more helpful to represent a tensor in the principal axis system (PAS) of the interaction. In such a frame of reference the symmetric part of the Cartesian tensor (Equation (1.17) is diagonal. The orientation of the frame is dictated by the particular molecule and the interaction being observed. For the chemical shift, the z-axis is positioned according to the local electronic environment, aligning with the direction possessing the least shielding. In the case of the dipolar interaction, the z-axis of the PAS is aligned with the vector that connects the two interacting nuclei. Within the PAS, the terms of the irreducible spherical tensor components from Equation (1.18) may be represented as:

$$\rho_{0,0} = \frac{-1}{\sqrt{3}} A_{iso} \tag{1.19}$$

$$\rho_{1,0} = -i\sqrt{2} A_{xy}$$

$$\rho_{1,\pm 1} = -A_{xz} \pm A_{yz}$$

$$\rho_{2,0} = \sqrt{\frac{3}{2}} \delta_\alpha$$

$$\rho_{2,\pm 1} = 0$$

$$\rho_{2,\pm 2} = -\frac{1}{2} \delta_\alpha \eta_\alpha$$

In which the Cartesian tensor, $\overleftrightarrow{A}$, has been given as the isotropic value where:

$$A_{iso} = Tr[A] = A_{xx} + A_{yy} + A_{zz} \tag{1.20}$$

The reduced anisotropy is defined as:

$$\delta_\alpha = A_{zz} - \frac{A_{iso}}{3} \tag{1.21}$$

The asymmetry is given as:

$$\eta_\alpha = \frac{A_{yy} - A_{xx}}{\delta} \tag{1.22}$$

The principal components of the tensor in the PAS are ordered in terms of magnitude, following the Haeberlen convention[18] as:

$$\left| A_{zz} - \frac{A_{iso}}{3} \right| \geq \left| A_{xx} - \frac{A_{iso}}{3} \right| \geq \left| A_{yy} - \frac{A_{iso}}{3} \right| \tag{1.23}$$

The components of the irreducible spherical tensor in the PAS given in Equation (1.19), need to be rotated into the laboratory frame by the rotation term $A_{l,0}^{(\mu)}$, as given in Equation (1.16). This is performed through the use of the Wigner rotation matrix:

$$A_{l,m}^{(\mu)} = \sum_{m`=-l}^{+l} \rho_{l,m`} D_{m`,m}^{l}(\Omega_{PL}) \tag{1.24}$$

Where Ω_{PL} represents the Euler angles, $\Omega_{PL} = (\alpha_{PL}, \beta_{PL}, \gamma_{PL})$, which act as to coincide the PAS with the laboratory frame (hence subscript PL) through three sequential rotations[23]:

1. A rotation around the z-axis of α_{PL} where $(0 \leq \alpha_{PL} \leq 2\pi)$.
2. A rotation around the new y`-axis of β_{PL} where $(0 \leq \beta_{PL} \leq \pi)$.
3. A rotation around the new z``-axis of γ_{PL} where $(0 \leq \gamma_{PL} \leq 2\pi)$.

The Wigner rotation matrix is then given by:

$$D^{l}_{m`,m}(\Omega_{PL}) = e^{-i\gamma_{PL}m`} d^{l}_{m`,m}(\beta_{PL}) e^{-i\gamma_{PL}m} \quad \textbf{(1.25)}$$

With $d^{l}_{m`,m}$ corresponding to the matrix elements of the reduced Wigner matrix.[18, 20] Reduced Wigner matrix terms used for the rotation of observable secular terms into the laboratory frame are:

$$d^{0}_{0,0} = 1 \quad \textbf{(1.26)}$$

$$d^{2}_{0,0} = \frac{1}{2}(3cos^{2}\beta_{PL} - 1)$$

$$d^{2}_{\pm 2,0} = \sqrt{\frac{3}{8}} sin^{2}\beta_{PL}$$

The irreducible spherical tensor operators, $\hat{T}^{(\mu)}_{l,0}$, given in Equation (1.16) are different depending on the kind of interaction it describes, i.e. homonuclear spin-spin, heteronuclear spin-spin or spin-lattice interactions.

1.1.3.1 The Chemical Shift Anisotropy Interaction

The local environment of a nucleus such as surrounding nuclei, bond lengths and bond angles lead to a difference in local magnetic field experienced for nuclei in different environments. This can be attributed to the shielding/deshielding effects of orbiting electrons which lead to a deviation from the Larmor frequency observed from just the Zeeman splitting. This is known as the chemical shift anisotropy (CSA) and is of the order of 10^3 Hz. The Hamiltonian for describing the CSA in the rotating frame can be shown to be[21]:

$$\widehat{H}_{CS} = \left(\omega_0 \left(\sigma_{iso} + \frac{\delta_\alpha}{2} [(3\cos^2\beta_{PL} - 1) - \eta_\alpha \sin^2\beta_{PL} \cos(2\alpha_{PL})] \right) \right) \hat{I}_{1z} \quad \textbf{(1.27)}$$

Where δ_α is the reduced anisotropy, σ_{iso} is the isotropic shift and η_α is the asymmetry parameter and α_{PL} and β_{PL} are the Euler angles describing the transformation from the principal axis frame to the lab frame.

$$\delta_\alpha = \sigma_{zz} - \sigma_{iso} \quad \textbf{(1.28)}$$

$$\sigma_{iso} = \frac{\sigma_{xx+}\sigma_{yy} + \sigma_{zz}}{3} \quad \textbf{(1.29)}$$

$$\eta_\alpha = \frac{\sigma_{yy} - \sigma_{xx}}{\sigma_{zz} - \sigma_{iso}} \quad \textbf{(1.30)}$$

1.1.3.2 The J-Coupling Interaction

J-coupling is a result of the magnetic moment of nuclei, which have an effect on the local magnetic field of surrounding nuclei. This effect is mediated through bonds and is in general isotropic. Energy levels are split into $2nI + 1$, where n is the number of identical nuclei in an environment coupled with it, and I is the spin quantum number of the nucleus. The strength of this interaction is of the order of 10 Hz. The Hamiltonian describing the J-coupling for heteronuclear interactions in the rotating frame can be shown to be:[21]

$$\hat{H}_J^{(1,2)} = 2\pi J_{12} \hat{I}_{1z} \hat{I}_{2z} \tag{1.31}$$

Where J_{12} is the J-coupling constant between nuclei 1 and 2.

1.1.3.3 The Dipolar Coupling Interaction

Dipolar coupling represents the through space effect of the magnetic dipole moment of a nucleus on that of a neighbouring nucleus. This effect is intrinsically anisotropic and can, therefore, lead to broadening. This effect has proven very useful at assisting the assignment of nuclear resonances present in complex molecules in the solid state and measuring distances and dihedral angles. The dipolar coupling is typically of the order of 10^3 Hz. The dipolar coupling Hamiltonian in the rotating frame for a homonuclear spin pair and heteronuclear spin pair, respectively, can be shown to be as follows:[21]

Homonuclear spin pair:

$$\hat{H}_D^{(1,2)} = \frac{\delta_D^{(1,2)}}{2} \frac{(3\cos^2 {\beta_{PL}}^{(1,2)} - 1)}{2} [3\hat{I}_{1z}\hat{I}_{2z} - (\vec{\hat{I}_1}.\vec{\hat{I}_2})] \tag{1.32}$$

Heteronuclear spin pair:

$$\hat{H}_D^{(1,2)} = \frac{\delta_D^{(1,2)}}{2} \frac{(3\cos^2 {\beta_{PL}}^{(1,2)} - 1)}{2} [2\hat{I}_{1z}\hat{I}_{2z}] \tag{1.33}$$

Where $\delta_D^{(1,2)}$ is the dipolar coupling constant between the two nuclei and is μ_0 is the vacuum permeability, $\hbar$, is Planck's constant over 2π, and r is the distance between the nuclei.

$$\delta_D^{(1,2)} = -2\frac{\mu_0 \gamma_1 \gamma_2 \hbar}{4\pi r_{12}^3} \tag{1.34}$$

1.1.3.4 The Quadrupolar Coupling Interaction

Detailed discussion for the quadrupolar interaction is not required for this thesis as all the nuclei encountered during its course have a spin of $I = 1/2$, and thus possess no quadrupolar interaction. However, for the sake of completeness the interaction will be briefly discussed.

For spins where $I > 1/2$ there exists an electric quadruple moment which interacts with electric field gradients that are present due to the charge distribution of the nuclei. This leads to a quadrupolar coupling interaction of the order of 10^6 Hz. The Hamiltonian describing the first order quadrupolar coupling in the rotating frame can be shown to be:[21]

$$\widehat{H}_Q = \frac{\delta_Q}{2}\left[\frac{3\cos^2\beta_{PL} - 1}{2} - \frac{\eta_Q}{2}\sin^2\beta_{PL}\cos(2\alpha_{PL})\right](3(\hat{I}_{1z})^2 - I_1(I_1 + 1)) \quad \textbf{(1.35)}$$

Where δ_Q is the quadrupolar-coupling constant, C_{qcc} multiplied by a term taking into account the spin of the nuclei. And qQ is the quadrupolar moment multiplied by the electric field gradient tensor, V, e is the charge of the proton and η_Q is the asymmetry of the electric field.

$$\delta_Q = \frac{e^2qQ}{2\mathrm{I}(2\mathrm{I}-1)\hbar} = \frac{C_{qcc}}{2\mathrm{I}(2\mathrm{I}-1)} \quad \textbf{(1.36)}$$

$$\eta_Q = \frac{V_{yy} - V_{xx}}{V_{zz}} \quad \textbf{(1.37)}$$

1.2 Experimental Tools

1.2.1 Magic-Angle Spinning NMR

ssNMR spectra of powders are rich in information. Both the magnitude and the orientation of the chemical-shielding tensors and the dipolar-coupling tensors are encompassed within them, which can provide information on both structure and dynamics present. However, a difficulty arises with the extraction of this information from the spectrum as a result of the very broad lines, with often overlapping line shapes.

The most utilised method for enhancing the resolution and sensitivity of ssNMR spectra is magic-angle spinning (MAS).[24-25] MAS is the act of rotating the sample at high-speed around an angle of $\beta_{PL} = \arccos\frac{1}{\sqrt{3}} \approx 54.7356°$ with respect to the magnetic field, denoted the magic-angle (see Figure 1.2). Inhomogeneous anisotropic interactions (terms described by a spatial rank 2 irreducible spherical tensor, CSA, dipolar interactions, quadrupolar interactions[26]) are averaged at this angle due to the cancellation of terms containing a $(3\cos^2\theta - 1)$ dependence in the solid-state Hamiltonian. Where the spinning frequency (ω_R) surpasses the magnitude of the interaction, the result is the complete averaging of the anisotropic component, with the residual Hamiltonian pertaining to that of the isotropic contribution.[24]

However, for dipolar interactions, a spinning frequency of greater than the strength of the interaction is only successful at averaging the interaction for heteronuclear dipolar interactions. In the case of homonuclear interactions a spinning frequency much greater than the interaction is required to suppress the term. This is understood through the distinction of the two classes of Hamiltonians describing the interactions[24]: 1) a homogeneous Hamiltonian which is non-self-commutative through time (such as the homonuclear dipolar coupling), and 2) an inhomogeneous Hamiltonian which is self-commutative through time (such as the CSA and heteronuclear dipolar coupling). The effect of MAS on these two types of interactions is dissimilar. MAS frequencies less than the frequency of the anisotropic interactions may drastically improve resolution for spectra which are dominated by inhomogeneous interactions. While in contrast, one must greatly surpass the frequency of the interaction for improvements in resolution of spectra dominated by homogeneous anisotropic interactions.

Under situations where the anisotropic interaction is not fully removed the remaining anisotropic interaction manifests as a rotational echo within the free induction decay (FID),[24] visible as sidebands in the spectrum, spaced at intervals of the rotor period (ω_R), with an intensity dominated by homogeneous anisotropic interactions.[24] While the incomplete averaging of anisotropic interactions attenuates potential sensitivity enhancements, the presence of the sidebands allows one to extract information on the second-order tensor that describes the anisotropic interaction that is not readily attainable when the interaction is fully averaged. Such information can be instrumental in acquiring information indicative of the chemical nature of the nucleus, the molecular motions present and the relative orientation of the anisotropic interactions. However, relative orientation is

not necessarily informative on the orientation within the laboratory frame as a result of macroscopic disorder present.

We can understand the origins of this improvement in resolution under MAS by first looking at the rotating-frame Hamiltonian under rotation about a single axis:

$$\hat{H}(t) = \sum_{m=-l}^{+l} e^{im'\omega_R t} d^{l}_{m'0}(\beta_{PL})\, A^{(rot)}_{l,m'} \hat{T}_{l,0} \tag{1.38}$$

For the case of a second-rank tensor it can be shown that:

$$\begin{aligned}\hat{H}(t) = \Bigg[& e^{-2i\omega_R t}\sqrt{\frac{3}{8}} sin^2\beta_{PL} A^{(rot)}_{2,-2} + e^{-i\omega_R t}\sqrt{\frac{3}{8}}\sin(\beta_{PL})\, A^{(rot)}_{2,-1} \\ & + \frac{3cos^2\beta_{PL}-1}{2} A^{(rot)}_{2,0} - e^{i\omega_R t}\sqrt{\frac{3}{8}}\sin(2\beta_{PL})\, A^{(rot)}_{2,1} \\ & + e^{2i\omega_R t}\sqrt{\frac{3}{8}} sin^2\beta_{PL} A^{(rot)}_{2,2} \Bigg] \hat{T}_{2,0}\end{aligned} \tag{1.39}$$

We can apply average Hamiltonian theory to Equation (1.39), resulting in the zeroth-order average Hamiltonian term of:

$$\hat{H}^{(0)} = \frac{1}{\tau_R}\int_0^{\tau_R} \hat{H}(t)dt = \frac{3cos^2\beta_{PL}-1}{2} A^{(rot)}_{2,0} \hat{T}_{2,0} \tag{1.40}$$

Where τ_R is the cycle time of $\frac{2\pi}{\omega_R}$. With an angle, β_{PL} of the rotation axis at an angle where:

$$\beta_{PL} = \arccos\frac{1}{\sqrt{3}} \approx 54.7356° \tag{1.41}$$

This angle is known as the magic-angle, β_m. At β_m, $\hat{H}^{(0)}$ goes to zero and all spatial second-rank interactions are averaged out to the zeroth order. The magic angle is the

angle at which the reduced Wigner rotation matrix element $d^2_{00}(\beta)$ is zero. Isotropic interactions (zeroth-rank tensors) are not affected by MAS as:

$$d^0_{0,0}(\beta_m) = 1 \tag{1.42}$$

First-rank tensors are not removed, but scaled, dictated by:

$$d^1_{0,0}(\beta_m) = \frac{1}{\sqrt{3}} \tag{1.43}$$

The chemical shift Hamiltonian contains both an isotropic component and a spatial second-rank tensor component. The zeroth, first and second order of the chemical shift average Hamiltonian are given by:

$$\begin{aligned}\hat{H}^{(0)}_{CS} = &-\sum_k \frac{\omega_{0,k}}{\tau_R}\int_0^{\tau_R} \vec{\sigma}^{(k)}\hat{I}_{kz}\,dt - \sum_k \frac{\omega_{0,k}}{3\tau_R}\int_0^{\tau_R}\Big[e^{-2i\omega_R t}A^{(rot)}_{2,-2} + \\ &\sqrt{2}\Big(e^{-i\omega_R t}A^{(rot)}_{2,-1} - e^{i\omega_R t}A^{(rot)}_{2,1}\Big) + e^{2i\omega_R t}A^{(rot)}_{2,2}\Big]\hat{I}_{kz}dt = \\ &-\sum_k \omega_{0,k}\vec{\sigma}^{(k)}\hat{I}_{kz}\end{aligned} \tag{1.44}$$

$$\hat{H}^{(1)}_{CS} = \frac{-i}{2\tau_R}\int_0^{\tau_R} dt_2 \int_0^{t_2}\big[\hat{H}_{CS}(t_2), \hat{H}_{CS}(t_1)\big]dt_1 = 0 \tag{1.45}$$

$$\hat{H}^{(2)}_{CS} = 0 \tag{1.46}$$

In Equation (1.44) $\vec{\sigma}^{(k)}$ represents chemical shielding tensor. Under stroboscopic sampling, the zeroth order average Hamiltonian describes the time evolution of the system. When the average Hamiltonian is described fully by the zeroth-order Hamiltonian the interaction is known as a heterogeneous interaction with respect to sample rotation.

For the case of the dipolar coupling interaction Hamiltonian for a homonuclear dipolar-coupled spin pair, the time-dependent rotating-frame Hamiltonian is described by Equation (1.39), and results in the disappearance of the zeroth-order Hamiltonian under MAS:

$$\widehat{H}_D^{(0)} = \sum_{k \neq l} \frac{3cos^2\beta_m - 1}{2} A_{2,0}^{(rot)} T_{2,0}^{(k,l)} = 0 \quad \textbf{(1.47)}$$

For the first-order average Hamiltonian in can be shown that:

$$\widehat{H}_D^{(1)} = \frac{-i}{2\tau_R} \int_0^{\tau_R} dt_2 \int_0^{t_2} \left[\widehat{H}_D(t_2), \widehat{H}_D(t_1)\right] dt_1 = \quad \textbf{(1.48)}$$
$$\frac{-i2\pi}{24\omega_R} \sum_{k \neq l \neq m} \left(A_{2,-2}^{(rot)} A_{2,2}^{(rot)} - 2A_{2,-1}^{(rot)} A_{2,1}^{(rot)}\right) \left[T_{2,0}^{(k,l)}, T_{2,0}^{(k,m)}\right]$$

Equation (1.48) takes this form as the $T_{2,0}^{(k,l)}$ term of two spin pairs, with one of the spins being the same, leads to a non-commutative relationship. As a result, contributions to the higher-order average Hamiltonian are present and the interaction is known as a homogenous interaction with respect to sample rotation. The presence of the non-zero higher-order terms which are not averaged out under MAS will contribute to the broadening of the lines.

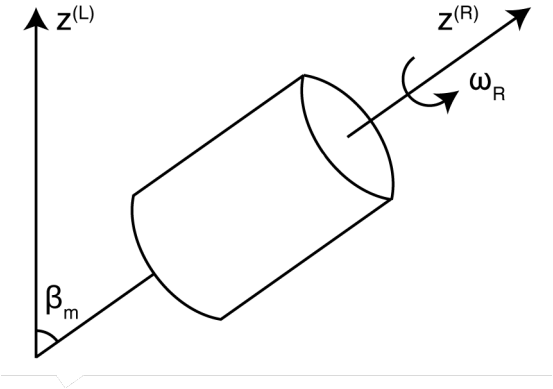

Figure 1.2 Rotor position under MAS. Where ω_R is the spinning frequency given in angular units, $z^{(L)}$ gives the z-direction of the laboratory frame, while $z^{(R)}$ represents the direction of the rotor-fixed frame. β_m is the magic-angle where $\beta_{PL} = \arccos\frac{1}{\sqrt{3}} \approx 54.7356°$.

1.2.2 Cross Polarisation

The design of the double-resonance experiment made way for many advancements to the field of ssNMR. This technique, which transfers magnetisation from ^{1}H to low-gamma nuclei involving the use of a doubly rotating frame experiment, is known as cross-polarisation (CP) and has become an essential component of any multi-dimensional pulsed ssNMR experiment.[27-28] Extending on the work of Hartmann and Hahn in 1962, Pines and co-workers first demonstrated the employment of CP in 1973 for the transfer of polarisation from ^{1}H to low-gamma nuclei. CP is composed of two simultaneous pulses, one on each channel, supplying on-resonance irradiation to the two spin systems to be exchanged between. This irradiation removes the magnetic field dependency present in the system.

In standard CP experiments, of the types consisting of spin-1/2 nuclei, the applied rf-fields, $\omega_{1,1}$ and $\omega_{1,2}$ (where $\omega_{1,i}$ is the applied rf-field of nucleus i) are strong enough to dominate all other interactions present. The Hamiltonian for the situation of CP, in the doubly rotating frame, is given as:

$$\hat{H}^{(1,2)}_{Hetero} = \Omega_1 \hat{I}_{1z} + \Omega_2 \hat{I}_{2z} + \frac{\delta_D^{(1,2)}}{2} \frac{(3\cos^2 \beta_{PL}{}^{(1,2)} - 1)}{2} \left[2\hat{I}_{1z}\hat{I}_{2z}\right] + \omega_{1,1}\hat{I}_{1x} + \omega_{1,2}\hat{I}_{2x} \quad \textbf{(1.49)}$$

In which Ω_i constitutes the offset and shift tensors of spins i. Under such a doubly rotating frame, it is possible to effectively excite, and spin lock, the entire NMR spectrum for each nucleus. By fulfilment of the Hartmann-Hahn matching condition, $\omega_{1,1} = \omega_{1,2}$, efficient ZQ magnetisation transfer is facilitated.

The importance of CP is three-fold. Firstly, the technique is crucially exploited for enhancement of magnetisation of low-gamma nuclei by transfer from abundant, high gamma protons. Through CP great enhancements in sensitivity are available, with the sensitivity of the enhanced nucleus enhanced by the ratio of the respective gyromagnetic ratios, with a 4-fold sensitivity enhancement possible for ^{13}C nuclei, and 10-fold sensitivity enhancement for ^{15}N possible.[27] Secondly, through CP experiments of protons to low-gamma nuclei, the magnetisation formed is reliant on the relaxation rate of the proton spin reservoir, which often has a significantly faster relaxation rate than low-gamma nuclei in the solid-state. Therefore, it is possible to increase the frequency of scans performed by a

reduction in the inter-scan delay. Thirdly, CP is instrumental in the acquisition of 2D-ssNMR datasets through multidimensional correlation experiments utilising double CP.[29-30]

The matching of the ω_1 fields initially caused some issues with the matching condition being very narrow and therefore requiring precise rf-pulses. Improvements to the technique were made that led to a reduction in the dependency of successful transfer to the exact setting of the matching condition.[31-34] This development was necessary during the advent of MAS and its inclusion to CP experiments as the Hartmann-Hahn matching profile is altered to include a further restraint to the conditions possible ($\pm(\omega_{1,1} \pm \omega_{1,2}) = n\omega_R$, where n is a positive integer, 0, 1, 2…). Therefore, the matching profile collapses to form a central transfer condition with sidebands separated at the spinning frequency also facilitating transfer when satisfied (see Figure 1.3 for example of Hartmann-Hahn matching profile).

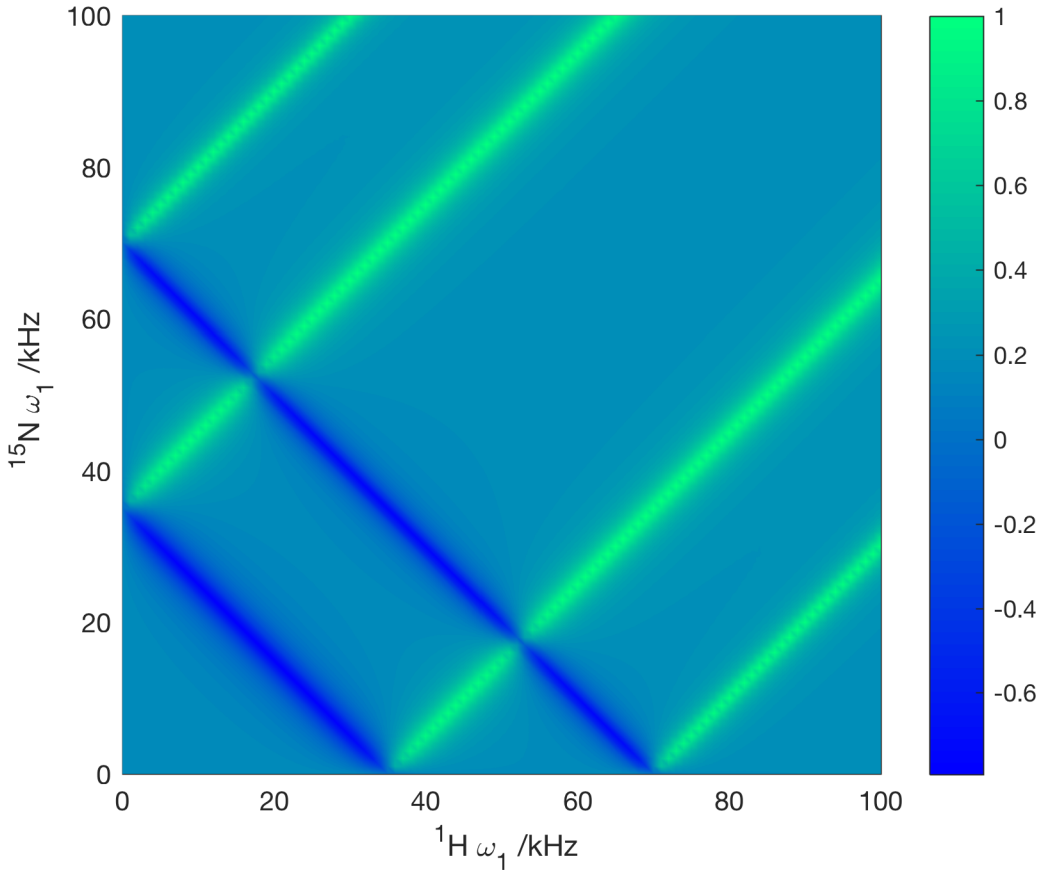

Figure 1.3 Simulated Hartmann-Hahn matching conditions at 35 kHz. Simulated in Spinach[35] for the CP transfer between ^{1}H and ^{15}N at 35 kHz MAS. Positive intensity DQ transitions ($\pm(\omega_{1,1} + \omega_{1,2}) = n\omega_R$, green) negative intensity ZQ transitions ($\pm(\omega_{1,1} - \omega_{1,2}) = n\omega_R$, blue).

1.2.3 Proton Decoupling

The lifetimes of transverse magnetisation (T_2) limits the utility of ssNMR of biomolecules,[36] with dipolar interactions being a dominant factor in their reduction.[37] It is worth noting that T_2 relaxation is the decay of transverse magnetisation and should be distinguished from T_2', which is the decay of the transverse magnetisation during a spin echo, which is used to refocus the inhomogeneous component of the broadening.[36] Dipolar interactions of low-gamma nuclei with adjacent protons result in detrimental line broadening effects, that are not readily averaged out by MAS. To counteract this spectral broadening, high power (>80 kHz) continuous wave proton decoupling sequences have been employed to saturate the proton reservoir.[38] Under typical conditions, proton decoupling sequences designed for use in solution-state NMR (GARP[39] or WALTZ[39]) are not sufficient to effectively remove line broadening present in ssNMR spectra.[40] In light of this, decoupling schemes utilising rapid phase alternation have been designed and shown success for proton decoupling in ssNMR.[40-41] In 1995 two pulse phase-modulation (TPPM)[41], a sequence comprised of a train of π-pulses with alternating phases, emerged as a powerful tool for proton decoupling. Several other schemes exploiting both phase and frequency modulation have been developed following on from TPPM.[42-45] The super cycle adaptation known as small phase incremental alternation with 64 steps (SPINAL-64),[46] has proven to be of great use in biological ssNMR, with the SPINAL-64 sequence being shown to perform favourably in comparison to TPPM.[47] The advantages of SPINAL-64 arise from its ability to handle inhomogeneities of the rf-fields and imperfections in pulse shapes, as well as more favourably dealing with resonance offsets, which can be attributed to the compensatory super cycles which form the backbone of the SPINAL sequence. A variant of TPPM has been developed, known as swept-frequency two-pulse phase modulation (SW_f-TPPM),[48] which as the name suggests employs incremented pulse durations, resulting in a sweep in modulation frequency. The sweep in modulation frequency not only improves the ease of optimisation but also results in enhanced decoupling capabilities when compared to standard TPPM decoupling and a slight improvement over SPINAL-64 decoupling.

In 2012 refocused continuous-wave (*r*CW)[49] decoupling was presented as a potential alternative to the previously developed techniques. *r*CW offers improved resolution enhancements, increased broadbandedness and high tolerances to rf inhomogeneity. In addition, the sequences are experimentally simple to set up and optimise. The technique functions by removing residual static high-order terms caused by interactions between

oscillating dipolar and anisotropic shielding tensors that are otherwise present in the effective Hamiltonian. *r*CW is composed of interleaved continuous wave (cw) decoupling with rotor-synchronised high-power π-refocusing pulses with alternating phases suitably placed throughout the cw decoupling. Other methods of proton decoupling by the biological ssNMR community include utilisation of homonuclear decoupling sequences, with noteworthy sequences being Lee-Goldburg[50], BLEW-24[51] and MREV-4[52]. Proton decoupling here is achieved through removal of homonuclear dipolar couplings present amongst protons, this results in a scaled heteronuclear dipolar coupling of the protons to the low-gamma nuclei present, which is susceptible to averaging through MAS or simultaneous irradiation of the low gamma nuclei.

For ssNMR experiments conducted at moderate MAS frequencies (above 25 kHz) phase-inversion decoupling has been shown to be an efficient means of decoupling. Notably, X-inverse-X decoupling (XiX)[44] has been particularly utilised. XiX is composed of two pulses of the same duration but with a phase shift of π rad. In general, decoupling schemes have been observed to offer the greatest enhancement in resolution when using the highest rf-field strength available, while avoiding rotatory resonance recoupling conditions.[53-54] The decoupling schemes are developed with the intention for use under a high-power decoupling regime, in which the nutation frequency of the rf-field is greater than both the homonuclear and heteronuclear couplings, as well as the MAS frequency employed. Experimentally, rf-field strengths of between 50-250 kHz are typically employed, subject to the MAS frequency and the size of the rotor. In addition, to avoid recoupling conditions, the rf-amplitude is chosen to be a factor of three or more greater than the MAS frequency. The need for high-power decoupling schemes restricts the utility of ssNMR for sensitive samples and limits the time for which decoupling can be employed. Furthermore, at high MAS frequencies optimum decoupling requires very high-power decoupling.[37]

As a consequence, focus has shifted to the development of low-power decoupling schemes, in which the rf-field strength is less than the MAS frequency, and usually between 10-20 kHz. While under low MAS frequencies, low-power decoupling schemes are often not feasible due to the recoupling conditions which lie in this region, and typically necessitate a decoupling strength of at least three times the MAS frequency.[55] However, it has been demonstrated that for biological solids spun at moderate MAS speeds low-power decoupling schemes become possible without causing unwanted resonance effects.[56] For ssNMR experiments where fast MAS is employed, new proton decoupling schemes have been developed that often utilise much lower rf-fields. Initially, the utility of low-power cw

proton decoupling was explored as an option for decoupling under high-speed MAS.[56] For situations where the MAS frequency is greater than the frequency of proton-proton interactions, low-power XiX proton decoupling has been developed.[57] For rigid solids this corresponds to MAS frequencies of above 40 kHz. In addition to low-power XiX decoupling, other research groups have attempted to modify existing pulse sequences for optimisation under a low-power regime. Of note is the development of low-power TPPM by Kotecha and co-workers in 2007. Kotecha proposed a variant of the sequence in which the proton rf-field strength of the decoupling sequence is set to $1/\omega_R$, with a pulse flip angle of π rad and phase alteration of approximately $20°$, enabling them to achieve efficient decoupling under significantly reduced field strengths.[58]

1.3 Dipolar Recoupling in MAS-ssNMR

1.3.1 Introduction to Dipolar Recoupling

Line broadening effects caused by anisotropic interactions that lead to a reduction in the sensitivity of ssNMR in solids are removed through the use of MAS. However, this simplification of the spectra leads to a loss of the information that the anisotropically broadened spectra are rich in. With fast enough spinning these solid-state spectra are essentially constructed entirely of isotropic chemical shifts. Though similar to the liquid state, the origins of line widths in the solid state are vastly different. Line widths in the solid-state are often larger than those seen in liquid-state NMR. The intrinsic line width is governed by the transverse relaxation, which originates from fluctuations in the local magnetic field from couplings to the lattice and motions, and as such is typically much greater in solids.[59-61] As MAS limits the size of nuclear dipolar interactions present in the spectra which are the major means of obtaining structural information from ssNMR spectra, methods have been developed to coherently and selectively reintroduce this information through clever design of rf-pulses. Such dipolar recoupling schemes have been present in the field for nearly 30 years now.[62] In contrast, in liquid-state NMR, structural information is not derived from dipolar recoupling techniques, rather from polarisation transfer mediated through relaxation assisted pathways.[17, 63]

1.3.2 Polarisation Transfer Experiments

Polarisation is usually transferred by two mechanisms: 1) via J-coupling as a through bond interaction or 2) via dipolar interactions through space. For the case of biological solids, the utilisation of dipolar recoupling is predominant in the field, though J-coupling based

methods are known.[64-65] Under the effect of an external magnetic field, spins are subjected to the Zeeman interaction, with the Hamiltonian for a two-spin system as follows:

$$\widehat{H}^{(1,2)} = \omega_{0,1}\hat{I}_{1z} + \omega_{0,2}\hat{I}_{2z} + \widehat{H}_D^{(1,2)} \quad \textbf{(1.50)}$$

The Zeeman term of the Hamiltonian is multiple orders of magnitude greater than the other spin interactions at fields on the order of 10 T (not counting the quadrupolar term). Therefore, the other spin interactions can be viewed as a modification to the Zeeman term. As a result, the energy levels can be calculated by just using first-order time-independent perturbation theory, known as the secular approximation. The form of the Hamiltonian varies for the case of a homonuclear spin pair or a heteronuclear spin pair, with corresponding Hamiltonians as follows:

$$\widehat{H}_{Homo}^{(1,2)} = \omega_{0,1}\hat{I}_{1z} + \omega_{0,2}\hat{I}_{2z} + \frac{\delta_D^{(1,2)}}{2}\frac{(3\cos^2\beta_{PL}{}^{(1,2)} - 1)}{2}[2\hat{I}_{1z}\hat{I}_{2z} - (\hat{I}_{1x}\hat{I}_{2x} + \hat{I}_{1y}\hat{I}_{2y})] \quad \textbf{(1.51)}$$

$$\widehat{H}_{Hetero}^{(1,2)} = \omega_{0,1}\hat{I}_{1z} + \omega_{0,2}\hat{I}_{2z} + \frac{\delta_D^{(1,2)}}{2}\frac{(3\cos^2\beta_{PL}{}^{(1,2)} - 1)}{2}[2\hat{I}_{1z}\hat{I}_{2z}] \quad \textbf{(1.52)}$$

Where $\omega_{0,i}$ is the Larmor frequency of $\hat{I}_i$, and $\delta_D^{(1,2)}$ the dipole moment between the two spins which is defined as:

$$\delta_D^{(1,2)} = -2\frac{\mu_0\gamma_1\gamma_2\hbar}{4\pi r_{12}^3} \quad \textbf{(1.53)}$$

In the case where $\omega_1 = \omega_2$, i.e. the energy when $|\alpha\beta\rangle = |\beta\alpha\rangle$, the transfer of polarisation is facilitated by the flip-flop term, $(\hat{I}_{1x}\hat{I}_{2x} + \hat{I}_{1y}\hat{I}_{2y})]$.[16] Consequently, a limit on the polarisation transfer is placed in that, the difference in chemical shift of the two spins must be significantly smaller than the dipolar term. In addition to this, the act of rotation of the sample at the magic angle leads to a time modulation of the rank 2 dipolar term that greatly reduces the coupling between the spins and therefore any potential polarisation transfer.

Dipolar recoupling experiments are referred to according to the order of the recoupling as described by the term in the Hamiltonian that is utilised to facilitate the recoupling. Here we reference to first-order and second-order dipolar recoupling sequences which are described by the following Hamiltonians respectively[38]:

$$\bar{\hat{H}}^{(1)} = \frac{1}{\tau_R}\int_0^{\tau_R} \hat{H}(t)dt \quad \textbf{(1.54)}$$

$$\bar{\hat{H}}^{(2)} = \frac{-i}{2\tau_R}\int_0^{\tau_R} dt_2 \int_0^{t_2} dt_1 \left[\hat{H}\,(t_2), \hat{H}\,(t_1)\right] \quad \textbf{(1.55)}$$

Where $\bar{\hat{H}}^{(1)}$ and $\bar{\hat{H}}^{(2)}$ refer to the first-order and second-order average Hamiltonian of $\hat{H}(t)$ over a rotor cycle time τ_R.

1.3.3 Spin Diffusion

Spin diffusion was first coined in 1948 by Bloembergen, as a means to describe the movement of spin order via a network of coupled nuclear spins with paramagnetic species present in the sample.[66-67] The mechanism of spin diffusion is understood to facilitate the transfer of spin polarisation amongst equivalent spins in close spatial proximity. Spin diffusion is used to explain the transfer of polarisation between any coupled spins with a difference in resonance frequency in frequency space. Though the term has seen some disagreement in its use, it is generally accepted that the term can be used to explain polarisation transfer processes that are characterised by a collection of rate equations. Theoretical analysis of the phenomena has been described, with the concept of double-quantum (DQ) flop-flop terms[68-69] and zero-quantum (ZQ) flip-flop terms[18, 70] widely accepted.

1.3.4 Proton-Driven Spin Diffusion and Rotational Resonance

Both proton-driven spin diffusion (PDSD) and rotational resonance (R^2) involve polarisation exchange amongst homonuclear spins. Through the development of 2D experiments, coupled with an improved understanding of the mechanisms surrounding spin diffusion in the solid-state and polarisation transfers[71-72] have led to the fruition of PDSD experiments.[73] Through PDSD experiments, effects as a result of differences in the chemical shift or via MAS are equalised through the strong coupling to abundant spins. The transfer mechanism in PDSD is not directly related to the distance between spins. Despite this, PDSD has proven itself to be a valuable tool in the structural biologist's toolbox, with the first 3D-structure of a protein in the solid-state determined via use of PDSD in 2002.[74] At high MAS, the effect of PDSD is significantly attenuated, with the efficiency of the transfer experiencing an inverse relationship to the frequency of MAS. In addition, the technique is also not suited for use at high magnetic field strengths due to a

lack of overlapping energy levels. With the efficiency drastically reduced above 15 T and distance restraints from the technique not possible under this regime.

The development of the dipolar-assisted rotational resonance (DARR)[75-76] technique attempts to rectify some of the drawbacks of PDSD. The technique functions by employing a DARR field upon the ^{1}H channel. DARR, which is characterised as a combined rotor and ^{1}H driven recoupling mechanism exploiting the ^{13}C/^{1}H dipolar coupling which is regained by continuous wave (cw) irradiation on ^{1}H with the ^{1}H rf-field intensity (ω_1^H) satisfying the rotary resonance condition $\omega_1^H = n\omega_R$ (where n = 1 or 2 and ω_R is the spinning frequency).[53] The DARR experiment is a ^{13}C/^{13}C recoupling method in which magnetisation coherences created on ^{1}H are transferred to ^{13}C nuclei, and then transferred, during a mixing time to other ^{13}C nuclei that are close in proximity that enables structural information from a molecular system to be understood due to the distance dependence of dipolar coupling.[77] The DARR experiment is commonly used in place of PDSD[78] as it actively recouples the ^{1}H's and ^{1}H/^{13}C coupling to enhance the rate of spin diffusion. This recoupling is particularly important at higher fields and spinning speeds where the ^{1}H/^{1}H dipolar couplings are attenuated. In a 2D-DARR experiment, all ^{13}C nuclei within a certain distance to each other are correlated by cross peaks in the spectrum. At short mixing times, all ^{13}C nuclei within one spin system are correlated by cross peaks in the spectrum. At very short mixing times, only adjacent ^{13}C nuclei are correlated by cross peaks in the spectrum, and at long mixing times, correlations between residues may also be present. Though a DARR experiment is capable of utility at spinning speeds greater than a standard PDSD experiment, the technique is still only designed for use at relatively low MAS spinning frequencies and moderate field strengths, indeed with spinning frequencies above 20 kHz, one observes a drastic reduction in the efficiency of polarisation transfer through DARR. A separate mechanism of magnetisation transfer is achieved at the so called rotational resonance (R^2) condition, $\Delta\omega_{iso} = n\omega_R$, in which the chemical shift difference, $\Delta\omega_{iso}$, is matched to a positive integer multiple of the spinning frequency, ω_R. R^2 is able to be matched for all molecular orientations, resulting in effective dipolar recoupling between homonuclear spin pairs. Research performed in the Griffin group enabled the technique to be utilised to extract distance measurements for protein systems.[79-80]

1.3.5 Rotating Frame Recoupling

The rotary resonance recoupling experiment (R^3),[53-54] in which the rf-irradiation amplitude is equalled to the spinning frequency, $\omega_1 = n\omega_R$, functions through the appearance of interference effects at a point in which the rate of precession $\omega_1/2\pi$, matches $\omega_R/2\pi$ or ω_R/π. For rotary resonance, $n = 1$ or $n = 2$. Spin-lock periods are incorporated into the sequence and are thus a form of rotating frame recoupling upon which the axis of recoupling is synchronised with the axis which the spin-lock field is created. The recoupling results in information corresponding to the heteronuclear dipolar interaction being reintroduced. In addition, in some situations information on the magnitude and orientation of the shielding anisotropy of the irradiated spin is also reintroduced.[53] The double-quantum homonuclear rotary resonance (2Q-HORROR)[55] experiment also exploits the R^3 matching condition of $n = 1/2$, i.e. $2\omega_1 = \omega_R$. In the case of 2Q-HORROR the sequence generates DQ coherences, with the sequence finding use in DQ filtering and for the measurement of homonuclear dipolar interactions. The magnetisation transfer utilised only has a small dependency on the orientation of the crystallite and has thus shown application for powder samples.

1.3.1 Difficulties with Recoupling Schemes Applied to Biopolymers

The aforementioned recoupling schemes are apt at the quantification of distances between homonuclear and heteronuclear singular spin pairs, though with application to biopolymers several challenges arise attributed to the complexity of the systems. Particularly, for first-order recoupling schemes difficulties are experienced in observing dipolar interactions from long-range spin pairs, primarily due to ^{13}C-^{13}C homonuclear dipolar truncation effects.[81] In addition, ^{13}C-^{13}C first-order recoupling schemes are attenuated through sub-optimal ^{1}H decoupling. In the case of heteronuclear recoupling schemes, such as rotational echo double resonance (REDOR)[82-83] and transferred echo double resonance (TEDOR)[84-85], the presence of multi-spin effects lead to difficulties in obtaining long-range distance measurements.

Dipolar truncation effects have persistently caused difficulties in the field of ssNMR with weak dipolar interactions typically being overshadowed by the strong dipolar interactions.[86-90] Dipolar truncation originates in ZQ and DQ first-order recoupling sequences in which the Hamiltonian describing the dipolar interaction consists of non-commuting terms that lead to strong couplings dominating the Hamiltonian.[81, 88-89]

1.4 Assignment Strategies in Biological ssNMR

1.4.1 $^{13}C/^{13}C$ Correlation Experiments

2D homonuclear dipolar recoupling experiments are exploited in MAS-ssNMR to facilitate the extraction of information from the spectra by the correlation of $^{13}C/^{13}C$ chemical shifts. This allows the separation of complex overlapping regions to be spread out over a 2D surface. From this, in favourable cases assignment of amino acid residues in a site-specific manner can be achieved.[29] The application of a particular homonuclear dipolar recoupling scheme results in the selective recoupling of specific spin systems within a close spatial proximity. In the context of a 2D spectrum, the recoupled spins manifest as cross peaks. Several homonuclear recoupling techniques exist that can be employed for the study of biopolymers, including the second-order recoupling schemes PDSD[73], DARR[77] and MIRROR.[1] In addition first-order DQ recoupling schemes DREAM[91-92], SPC5[87] and POST-C7[93] have been developed. Under a MAS regime of under 20 kHz, PDSD and DARR are often exploited for $^{13}C/^{13}C$ homonuclear recoupling correlation experiments (see Figure 1.5 for pulse sequence). This is due to their broadband nature, originating from an absence of chemical shift dependency of the resonance conditions. Furthermore, as second-order recoupling schemes, they are not overly affected by dipolar truncation effects.[81] Such effects often plague first order-recoupling schemes, which otherwise limit their ability to provide long-range structural restraints necessary for accurate 3D structure determination. Careful selection of the length of the mixing time can control the distance upon which nuclei are recoupled, with the longer the mixing time, the greater the number and distance of correlations. Appropriately short mixing times (~5 ms) typically will lead to recoupling between homonuclei separated by only one bond, such as correlations between C_α-C_β and C_α-C_{CO}. At longer mixing times further correlations between backbone residues and aliphatic side-chain nuclei, in addition to inter-residue correlations will likely be present (see Figure 1.4).

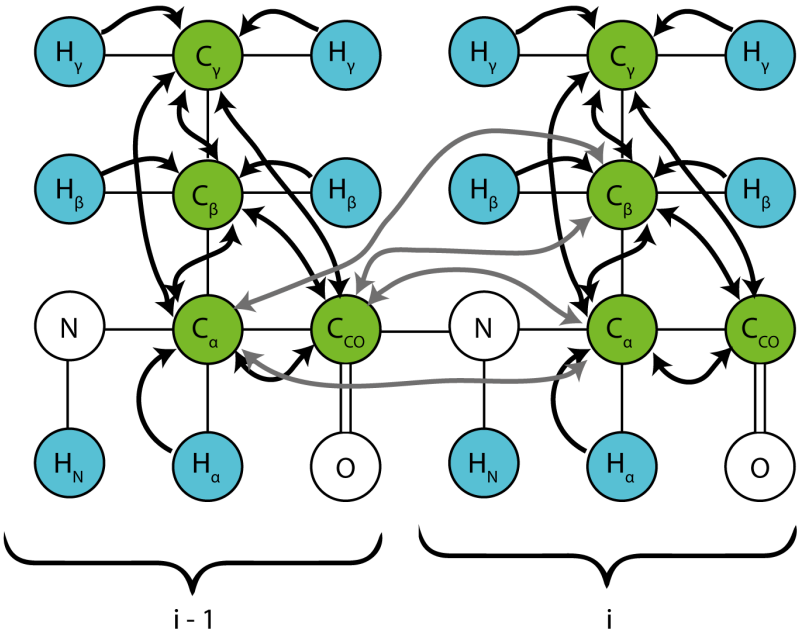

Figure 1.4 Illustration of the magnetisation transfer in homonuclear dipolar recoupling $^{13}C/^{13}C$ correlation experiments, such as the PDSD/DARR experiments. Magnetisation on the protons is transferred via CP to the adjacent carbon atoms (shown with black arrows). From here the magnetisation is allowed to transfer to other carbons during a set evolution period (shown with double headed black arrows). Inter-residue magnetisation transfer is also possible (shown with grey double-headed arrows).

A multitude of second-order recoupling conditions have been identified, including RDSD[94-95], PARIS[96], SHANGHAI[97], and notably, MIRROR[1]. Unlike the broadband schemes, PDSD/DARR, narrow-banded schemes are inherently band selective due to a dependency on chemical shift separation ($\Delta\omega_{iso}^{C}$) within the matching condition $\omega_1^H = n\omega_R \pm \Delta\omega_{iso}^{C}$.[1, 94] In contrast to the broadband experiments, correlations for C_α-C_β and C_α-C_{CO} must be performed in separate experiments due to the difference in $\Delta\omega_{iso}^{C}$ for the two sets of spin pairs (Figure 1.6).

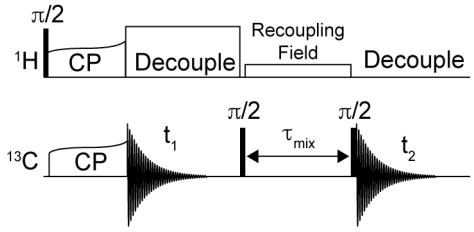

Figure 1.5 Pulse sequence for the $^{13}C/^{13}C$ homonuclear recoupling correlation. The experiment can be performed with no recoupling field employed (PDSD), or a recoupling condition can be achieved through the use of a recoupling field to satisfy a specific resonance condition.

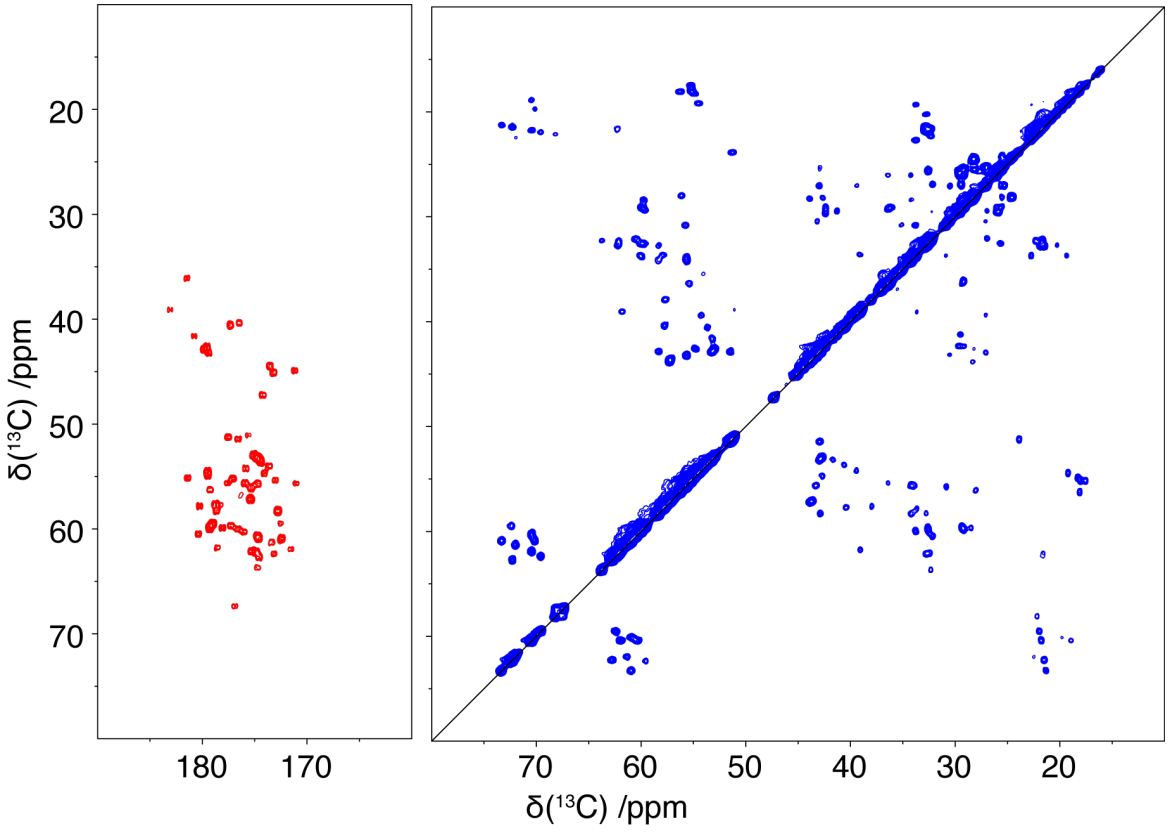

Figure 1.6 2D-Correlation spectra of microcrystalline [U-^{13}C,^{15}N]GB3 utilising MIRROR recoupling. MIRROR C_{CO}-C_α correlation and MIRROR C_α-C_β correlation to obtain inter-residue couplings. MIRROR C_{CO}-C_α correlation (A), MIRROR C_α-C_β correlation (B). Data acquired with 100 ms MIRROR mixing at 600 MHz, 35 kHz MAS, 298 K.

1.4.2 $^{13}C/^{15}N$ Correlation Experiments

For one to utilise $^{13}C/^{15}N$ correlation experiments, following the ^{1}H to ^{15}N CP, a second CP step is required to transfer coherences present on ^{15}N nuclei to the ^{13}C nuclei at which magnetisation is detected, known as double CP.[29-30] The selectivity of this polarisation transfer from ^{15}N to ^{13}C is a function of the rf-field strength, and under typical conditions the rf-field is sufficiently low to allow for band-selective excitement. The setting of the offset and Hartmann-Hahn condition dictates whether the magnetisation is directed towards the C_α or C_{CO} groups, with the corresponding experiments known as an NCA and NCO experiment respectively. An NCA correlates the $N^{(i)}$ with the $C_\alpha^{(i)}$. In the same manner, the NCO correlates the $N^{(i)}$ with the $C_\alpha^{(i-1)}$ (where i represents the number of the nitrogen peptide plane). Effective use of these experiments and homonuclear recoupling variants can be central in the establishment and sequential assignment of connectivities present along the protein backbone (see Figure 1.7 for NCO and NCA schematic).

Through the incorporation of homonuclear dipolar recoupling into the $^{13}C/^{15}N$ heteronuclear correlation experiment, the NCA/NCO can be extended upon to encode further useful information on connectivities. This results in so-called NCACX/NCOCX experiments (where CX refers to a transfer to an unspecified ^{13}C nuclei). The experiments can be acquired in 1D-ncaCX/ncoCX, 2D-NcaCX/NcoCX or 3D-NCACX/NCOCX variants (where the convention dictates a lower case refers to a dimension that is not evolved), where additional dimensions are added by allowing for an evolution in either the indirect ^{15}N dimension (t_1 evolution after first CP step) or the indirect ^{13}C dimension (t_2 evolution after second CP step). The experiments are often used in combination with homonuclear 2D-$^{13}C/^{13}C$ correlation experiments to further aid resonance assignment. Increasing the number of acquired dimensions greatly enhances the level at which resonances are resolved. This assists in resonance assignment, though at a cost of increasing the length of the experiment time. Therefore, an increase in dimensions is often used only when necessary due to overwhelming crowding in the spectrum. Typically, PDSD/DARR (at low MAS rates) or MIRROR (at moderate MAS rates) is employed to recouple the ^{13}C spins. The correlation observed will be entirely dependent on the homonuclear dipolar recoupling scheme selected.

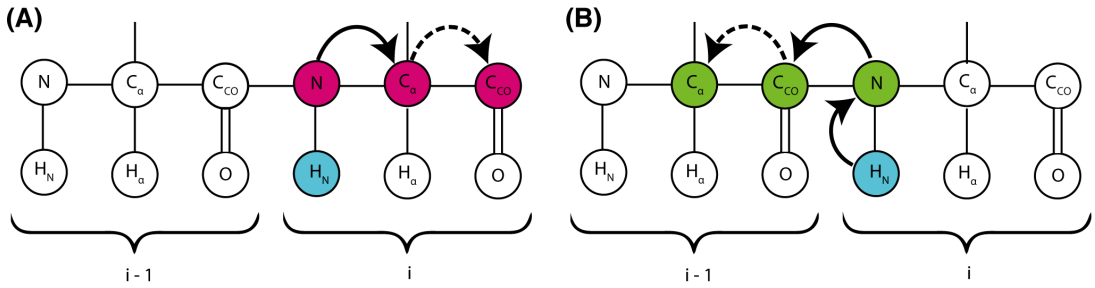

Figure 1.7 Transfers for NCA and NCO. NCA (A) CP steps for NCA shown as a solid black arrow. NCO (B) CP steps for NCO shown as a solid black arrow. Potential further transfers under a recoupling scheme to surrounding ^{13}C nuclei are represented by dashed arrows.

1.5 Electron Paramagnetic Resonance

1.5.1 Introduction

To characterise the spin-labels bound to the surface of the protein we utilised continuous wave (cw) electron paramagnetic resonance (EPR) spectroscopy. EPR is a technique which allows one to observe systems with unpaired electrons. The concept of EPR is based on the detection of the electron by excitation with electromagnetic radiation at the appropriate level for the transition, typically at the microwave region of the spectrum at a frequency of tens of GHz. In comparison to NMR, where the small energy gap between the ground and excited states leads to only a slight preference for the lower energy state, where only a small level of polarisation can be achieved without employing hyperpolarisation techniques. In the case of the electron, where the gyromagnetic ratio is approximately 660 larger than that of the proton,[98] this corresponds to a comparable increase in polarizability, and hence higher inherent sensitivity. EPR has shown utility in studying metal complexes.[99] A range of paramagnetic centres exists in the transition metals, such as V, Mn, Fe, Co, Ni, Cu, Mo, W, which are naturally present in certain biomolecules.[100] Furthermore, lanthanides can be incorporated into biological samples in solution or bound covalently. Through this, lanthanides have proven to be useful in probing information from biological systems.[101-103] In addition, organic radicals have been studied, particularly nitroxide radicals. Nitroxide radicals have proven to be paramount in studying various biological systems. Their applications include, but are not limited to, the spin-labelling of lipids for investigating binding interactions and orientation.[104] Paramagnetic centres have allowed for information on both naturally occurring metalloproteins and modified proteins

with a spin-label attached to be probed. They have shown particular use for distance measurements by exploiting double electron-electron resonance (DEER) in pulsed EPR.[105]

X-band EPR (approx~9 GHz frequency, static field of 0.33 T) is most typically used due to the commercial availability of the spectrometers. Only an electromagnet is required to generate the fields, but studies utilising higher frequency spectrometers are becoming more prominent due to the enhanced sensitivity and resolution that can be achieved at fields operating at the Q (35 GHz) and W (95 GHz) range. In this project, only X-band EPR will be used, though for our interest this microwave frequency range is suitable for ascertaining the information required.

1.5.2 Background and Theory

1.5.2.1 Zeeman Effect

EPR spectra are observable due to the phenomenon of the Zeeman effect, where the degeneracy of the electron spin state is split in the presence of a magnetic field. In a similar manner to the nuclear spin in NMR, for the case of a single S = ½ electron, there exist two energy levels $(2S + 1)$, in which the energy of the two are degenerate and therefore both equally likely to be occupied. The introduction of an external magnetic field leads to a splitting of the energy levels. With the spins either parallel or anti-parallel to the magnetic field, with the parallel state being the lower energy level and the anti-parallel the high-energy state. The energy of this interaction is obtained from the classical description for the energy of a magnetic dipole in a magnetic field and is represented by the spin Hamiltonian operator.

$$H = g_e \frac{\beta_e}{h} S B_0 \qquad \textbf{(1.56)}$$

Where g_e = 2.0023 and is the dimensionless isotropic g-value of a free electron. β_e is the Bohr magneton in J T^{-1}, h is the Planck constant in J s, B_0 is the external magnetic field strength in T. From Equation (1.56) the energies of the two states are obtained from the eigenvalues of H with spin quantum numbers m_s = ± ½

$$E = g_e \frac{\beta_e}{h} B_0 m_s \qquad \textbf{(1.57)}$$

Where E is the energy in Hz. The energy difference between the two levels is known as the electron Zeeman interaction and is linearly proportional to B_0, where irradiation with a

photon of microwave frequency can cause a transition to occur if the condition given in Equation (1.58) is fulfilled.

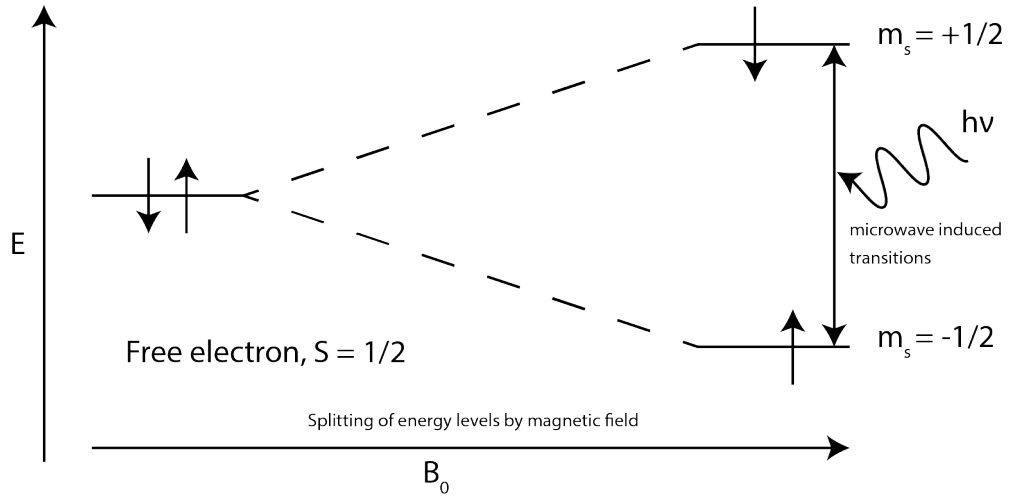

Figure 1.8 Diagram to illustrate the effect of a magnetic field, B_0, on the energy levels of an unpaired electron. Irradiation with photons of energy $h\nu$ can cause a change in energy level if the resonance condition given in Equation (1.58) is fulfilled.

$$\Delta E = \nu = g_e \frac{\beta_e}{h} B_0 \qquad \textbf{(1.58)}$$

An EPR spectrum is characterised by four parameters, the spectral intensity, the linewidth, g-tensor, and the multiplet structure (hyperfine coupling). The following sections will discuss these with simulations and demonstrate the parameters variation on the EPR spectra where relevant.

1.5.2.2 Spectral Intensity

Integration of the derivative spectrum to give the spectrum in an absorption form, more familiar to what is observed in NMR, leads to peak intensities generally proportional to the concentration of unpaired electron spins (See Figure 5.10 for example). The spectral intensity can be affected by quenching between electrons in close proximity under high concentration conditions. In addition, the saturation of resonances where the absorption of radiation by the sample reduces the population difference between the two energy levels will affect the spectral intensity.

1.5.2.3 The g-Tensor

The g-tensor is the quantification of the local magnetic field experienced by an electron. The g-tensor is described by a second rank tensor, (see Equation (1.59)).

$$g = \begin{bmatrix} g_x & 0 & 0 \\ 0 & g_y & 0 \\ 0 & 0 & g_z \end{bmatrix} \quad \textbf{(1.59)}$$

The g-tensor is intrinsically anisotropic in that the value is orientation dependent, where the anisotropy becomes apparent when viewed as a powder because each orientation gives rise to a different resonance. The g-tensor has a few names of similar meaning, often used interchangeably: the g-value/g-factor, both refer to a g-tensor that is isotropic. g-tensors where $g_x = g_y \neq g_z$ are known as axial, and g-tensors where $g_x \neq g_y \neq g_z$ are known as orthorhombic. In solution rapid tumbling of the molecule results in the averaging of the principal components of the g-tensor, resulting in an isotropic value, $g_{iso} = \frac{1}{3}(Tr(g))$, giving rise to a single resonance when molecular tumbling is fast enough that the anisotropy observed is averaged on an EPR timescale.

The magnetic field felt by the paramagnetic centre is influenced by not just the external magnetic field, B_0, but also the local magnetic fields of the surrounding atoms, this leads to an effective field that is experienced by the electron (Equation (1.60)).

$$B_{eff} = B_0(1 - \sigma) \quad \textbf{(1.60)}$$

Where σ represents the effects of local magnetic fields. Equation (1.58) for the energy of a free electron can be expanded on to include the effect of local fields.

$$\nu = g_e \frac{\beta_e}{h} B_{eff} = g_e \frac{\beta_e}{h} B_0(1 - \sigma) \quad \textbf{(1.61)}$$

The free electron g-value is typically combined with $(1 - \sigma)$ and denoted as g, and known as the g factor.

$$\nu = g \frac{\beta_e}{h} B_0 \quad \textbf{(1.62)}$$

From Equation (1.62), it is possible for one to determine the value of g in an EPR experiment in which one measures both the field and the frequency at which an electron is brought into resonance. The anisotropic nature of the g-factor can be utilised to ascertain information about the electronic structure of the paramagnetic species. Linewidths

observed are dependent on the rotational correlation time. The binding of a small paramagnetic species to a large biomolecule would lead to a larger rotational correlation time and therefore one would expect to observe an increase in the linewidth.

In many transition metals, which contain greatly varying electronic environments, a large range of g-tensors have been observed,[99] in comparison to free radicals, namely nitroxide radicals, where little deviation from a value of 2 is observed. Figure 1.9 illustrates the effect of the g-tensor on a simulated spectrum of MTSSL with varying values of the g-tensor. A shift in the spectra to a lower field is observed on increase in the g-tensor.

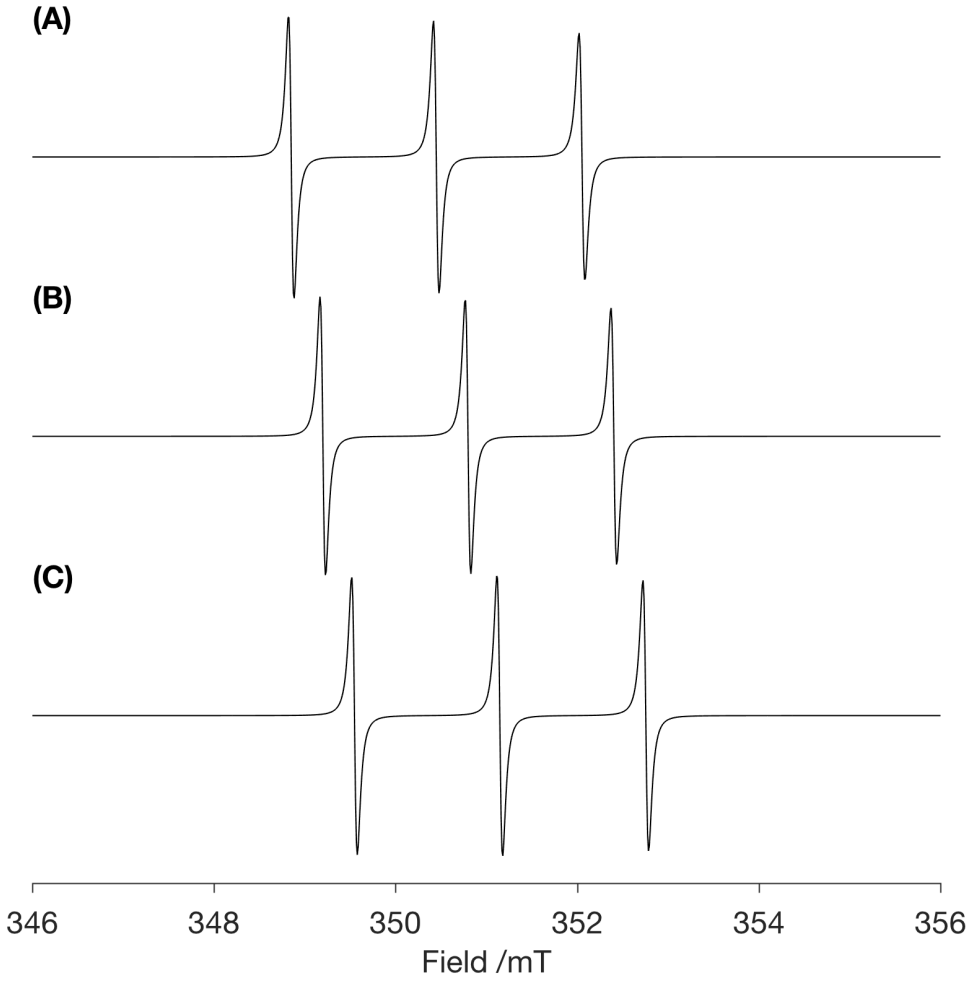

Figure 1.9 Simulation of the variation in $g_{(y)}$ to demonstrate effect on EPR spectra. g_x; 2.0086, g_z; 2.0032, $A_{(x,y,z);}$ 6.23, 6.23, 35.7 mT, linewidth; 0.1 mT, τ_c 0.01 ns. g_y varied from, 2.0126 (A) 2.0066 (B), 2.0006 (C).[106] Parameters from MTSSL bound peptide.[107]

1.5.2.4 Hyperfine Coupling

The hyperfine coupling, A, describes the coupling exhibited between electrons and nuclei, with an anisotropic component to the coupling arising due to a dependency on the molecular orientation. As with the g-tensor, the hyperfine coupling is a rank two tensor, typically given in units of MHz (see Equation (1.63)).

$$A = \begin{bmatrix} A_x & 0 & 0 \\ 0 & A_y & 0 \\ 0 & 0 & A_z \end{bmatrix} \quad \textbf{(1.63)}$$

Where (x,y,z) represents the PAS and A_x, A_y, A_z are the principal values of A.

Hyperfine splitting occurs due to an interaction of the electron spin (S) with the nuclear spins (I). This interaction is the result of two methods of communication between the spins. The first mechanism is a through space dipolar interaction present between electron and nuclei, with the interaction being directional and anisotropic in nature due to the use of the dipolar coupling which is itself anisotropic. The second mechanism in which a hyperfine coupling can occur is via a so-called "Fermi contact", in which a delocalisation of unpaired electrons on the nuclei results in a coupling between the spins. The Fermi contact mechanism is isotropic in nature. In solution samples, where dipolar interactions appear as relaxation effects through averaging due to molecular tumbling, the Fermi contact is the predominant effect observed in EPR spectra.

To visualise the effect of the EPR spectra when the hyperfine coupling is changed, a simulation in EasySpin[106] was conducted on a simulation of MTSSL in solution.[108] It can be observed that the effect of varying the isotropic hyperfine coupling is to decrease or increase the splitting of the resonance, in this case between a single electron and ^{14}N nucleus.

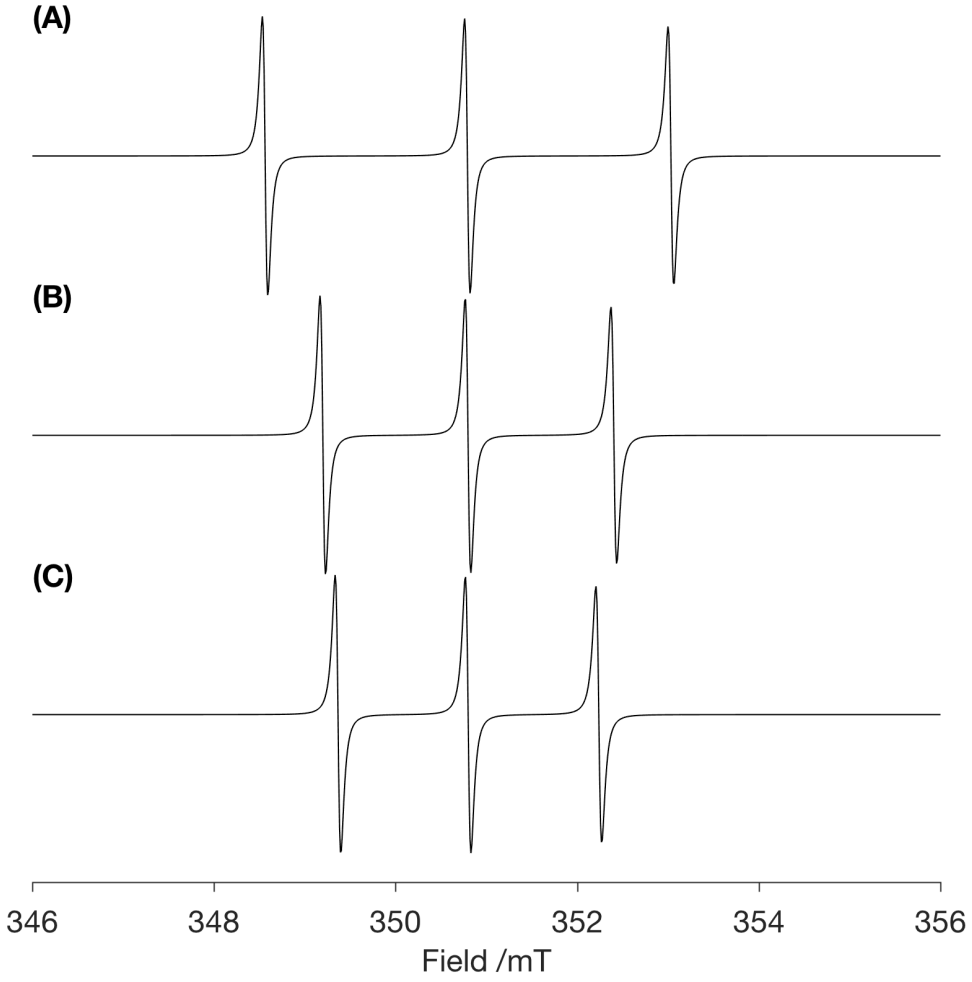

Figure 1.10 Simulation to show the effect of a variation in the hyperfine coupling (A) on the spectra of MTSSL.[106] Spectra simulated using parameters from the literature for MTSSL in water[108]. $g_{(x,y,z)}$ 2.00800, 2.00586, 2.00199, $A_{(iso)}$ 16.12 mT, Lw 0.1 mT, τ_c 0.01 ns.

1.5.2.5 Origins of Linewidths

The full width half maximum (FWHM) of the EPR lines has an inverse relationship with the relaxation time. As with NMR, there are two main fundamental relaxation mechanisms, The longitudinal relaxation time, T_1, and the transverse relaxation time, T_2. The T_1 relaxation, which describes the time for the spin to relax to its equilibrium position after a disturbance caused by the absorption of MW radiation, resulting in fluctuating magnetic fields experienced by the polarised spin, which act as the primary method of T_1 relaxation. T_2 relaxation is related to the loss in the coherence of the spins after a deviation from equilibrium. A faster relaxation leads to broader lines. For transition metal species, short T_1

relaxation is often the determining factor.[109] This necessitates that transition metal species be studied with EPR at low-temperature where effects of T_1 relaxation are reduced. Fortunately, nitroxide radicals do not exhibit such short T_1 relaxation rates so can lend themselves to probe systems at room temperature with little difficulty. Other than relaxation effects on line broadening, inhomogeneous broadening is the other major component. In addition, effects from electron-electron dipolar interactions can also exhibit a broadening effect on the EPR line shape. Inhomogeneous broadening occurs due to the presence of a continuum of local magnetic field strengths. This is an anisotropic effect, related to the rotational correlation time of the species, where the faster the rate of tumbling the greater the averaging of the local magnetic fields experienced on the EPR timescale. The linewidth is dependent upon the rotational correlation time of the molecule, with shorter rotational correlation times leading to sharper resonances, while slower tumbling leads to broadening. In the case of species where relatively long T_1 relaxation is present, the inhomogeneous line broadening can dominate the spectra in circumstances of incomplete averaging. Figure 1.11 demonstrates the effect of molecular tumbling on the EPR spectra. It can be observed that at a slower correlation time, on an EPR timescale an array of molecular orientations is observed, with the maximum broadening observed in the powder spectra.

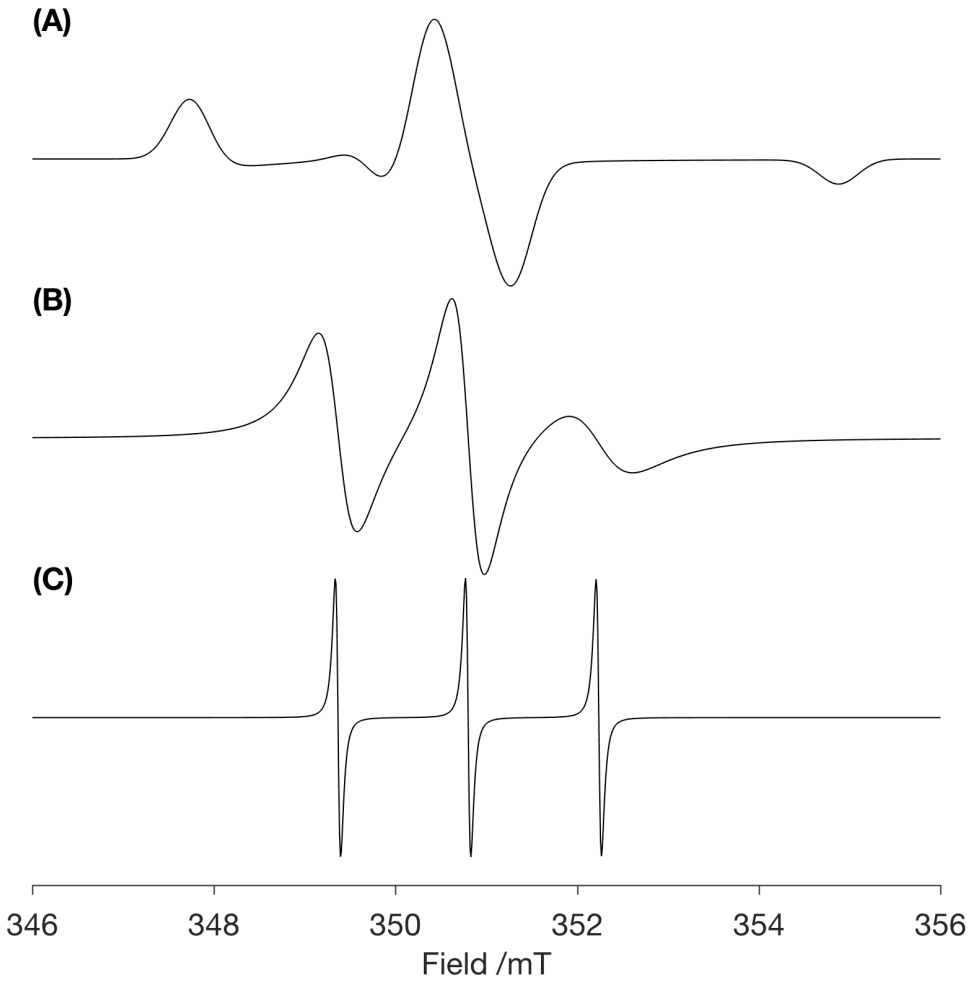

Figure 1.11 Simulation to show the effect on the EPR line shape on variation in the correlation time. From a powder spectrum with line broadening of 0.5 mT (A), 80 ns correlation time (B), 0.0012 ns correlation time (C).[106] Values of A and g from MTSSL spin-label bound to a short peptide sequence.[107]

Chapter 2: Sample Preparation

2.1 ssNMR Model Protein Systems

For method development in biological ssNMR, it is desirable to have a well-characterised model system. Such model systems are necessary to enable techniques designed on these relatively simple, well characterised biopolymers to be applied to more complex systems, systems lacking previous characterisation, or both. In the case of model protein systems for method development in ssNMR, the SH3 domain,[10, 12, 74, 110] ubiquitin[111] and immunoglobulin G (IgG) binding domains of streptococcal protein G[12, 112] have all shown extensive use.

The research conducted within this thesis has focused on the third immunoglobulin binding domain of protein G (GB3) as the model system. Protein G is present on the surface of bacteria belonging to the genus *Streptococcus*, a spherical Gram-positive bacterium. The protein functions to expedite high-affinity binding to IgG, facilitated through the action of three homologous domains, denoted B1, B2 and B3. Each domain constitutes 56 amino acids which are arranged to form a single α-helix and four β-sheet strands[112-113] (see Figure 2.1 for the solution-state NMR structure of GB3). The first crystal structure of GB3 was generated through X-ray crystallography.[114] Subsequently after, a liquid-state NMR structure of 1.1 Å resolution was determined by Ulmer and co-workers utilising measurements of $^{13}C/^{13}C$ and $^{13}C/^{15}N$ residual dipolar couplings.[115] Following on from this, Vögeli *et al.*, through an ensemble based structure determination procedure via ensemble-averaged distance restraints acquired from exact nuclear Overhauser effect (NOE) rates were able to acquire a liquid-state NMR structure, with a backbone RMSD of 0.47 Å.[116]

Such diversity in the approach to structure determination has enabled a thorough evaluation of the pioneering techniques used for the elucidation and refinement of protein structures.[117-118] In addition to structural studies, the binding domains of protein G have found use as model systems for analysis of protein dynamics and folding.[119-120] The protein G binding domains owe in part their utility to method development in ssNMR due to their great thermal stability, which exceeds 85 °C. This stability, in addition to the absence of disulphide bonds, allows for relatively simple and robust purification techniques without the need for purification tags to achieve high yields, of suitable purity for ssNMR studies.[112] In contrast to other model systems protein G binding domains possess the advantage of preparation in a microcrystalline form.[113, 121-122] Microcrystalline preparations

possess a higher degree of sample homogeneity, originating from the enhanced local order present in crystals. This results in high-resolution ssNMR being routinely available. In addition, the corresponding denser crystal packing attributed to the microcrystalline structure allows for more protein to be packed into a rotor, effectively enhancing the achievable sensitivity by increasing the number of observable spins.[123] The favourable distribution of peak positions in the correlation spectra of protein G binding domains enables the vast majority of resonances to be well resolved, allowing site-specific information on the residues to obtained. In addition, observation of all resonances in the protein are possible which is uncommon of protein spectra in general, the carboxyl and amino termini and loop regions are also visible.[113]

Due to these overwhelming advantages of the protein G binding domains for ssNMR studies, the third immunoglobulin binding domain of protein G (GB3) was used as the model system for the studies in this project.

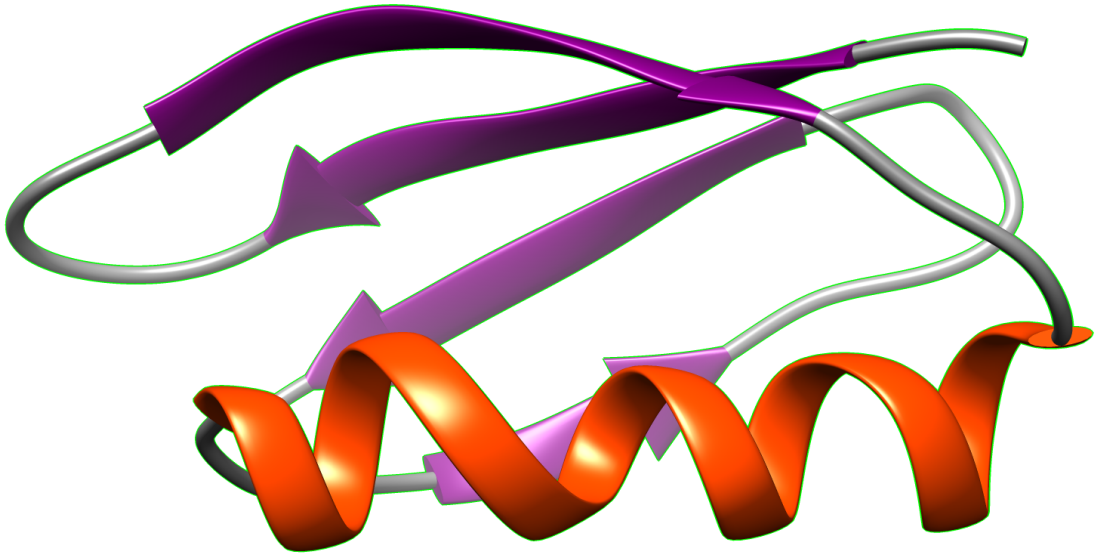

Figure 2.1 Liquid-state NMR backbone structure of GB3. Depicted structure obtained by Vögeli *et al.* through an ensemble based structure determination procedure via ensemble-averaged distance restraints acquired from exact NOE rates, with a backbone RMSD of 0.47 Å.[116] PDB ID: 2LUM.

2.2 Materials and Methods

Standard sterile techniques were used in all microbiological experiments. Sterilisation of growth media and heat stable solutions was achieved with a PriorClave autoclave (PriorClave Ltd) (121 °C, 25 min). Heat-labile solutions (antibiotics) were sterilised by filtration through 0.22 μm filters (Millipore). Growth media were supplemented with antibiotics (100 μg mL^{-1} Ampicillin, though dependant on specific cell strain antibiotic resistance). The GB3 plasmid used was provided by Dr Donghan Lee (The Max Planck Institute for Biophysical Chemistry, Gottingen) as a pET plasmid, with expression controlled by a T7 promoter and an ampicillin resistance gene to allow for selection.

2.2.1 Construction of GB3 Cysteine Mutants

From the wild-type (WT) GB3 plasmid, mutant plasmids were constructed with one or two cysteine point mutations (A48C, D46C-A48C, E24C-K28C). These were introduced through the polymerase chain reaction (PCR), with primers (Table 2.1) and the Phusion site-directed mutagenesis kit (ThermoFisher Scientific, Loughborough, UK) included in the reaction mixture (37.9 μL Water, 10 μL 5X Phusion HF Buffer, 1μL 10mM dNTP Mix, 0.25 μL forward primer, 0.25 μL reverse primer, 0.1 μL GB3 template DNA, 0.5 μL Phusion Hot Start II DNA Polymerase). Successful mutation was confirmed by DNA sequencing of the entire genes (Eurofins, Luxembourg).

Table 2.1 Table of primers used for site-directed mutagenesis of GB3.

Primer	Sequence
A48C Forward	5’-ACTGAATAGGATCCGGCTGCTAACAAAGCCC-3’
A48C Reverse	5’-AACTGTAAAGGTCTTAGTGCAATCGTCGTAAGTCC -3’
D46C-A48C-Forward	5’-TTGGACTTACTGCGATTGCACTA-3’
D46C-A48C Reverse	5’-ACACCGTCAACACCGTTGTC-3’
E24C-K28C Forward	5’-CTGTTGATGCTTGCACTGCAGAATGCGCTTTCAAAC-3’
E24C-K28C Reverse	5’-CTTTAAGTAGTTGTTTCGCCTTTCAATG-3’

2.2.2 DNA Gel Electrophoresis

DNA electrophoresis was performed on the PCR reaction (5 μL sample) and a 1 kb DNA molecular weight marker (Fisher BioReagents). Each sample had gel loading buffer (Sigma-Aldrich) (1 μL) added. Samples were resolved on a 1 % agarose gel (50 mL 1x TAE, 0.5 g agarose and 4 μL ethidium bromide) at 120 V for 30 min. The gel was imaged (SynGene imager) to verify whether the PCR amplification was successful.

2.2.3 DNA Ligation

A ligation reaction was performed on each linear PCR product by combining the reaction components (0.5 μL T4 DNA ligase, 10-20 ng PCR product, 2 μL 5X rapid ligation buffer, with 9.5 μL of nucleotide free water), followed by inverting the solution and brief centrifugation (25 °C, 13000 rpm, 10 s). The sample was then incubated at room temperature (5 min) followed by storage (-20 °C).

2.2.4 Transformation

For DNA multiplication DH5α competent cells were used. For protein expression studies BL21(DE3) competent cells were used. The competent cells (stored at -80 °C) were thawed on ice (<4 °C, 10 min). The plasmid solution (1 μL, <4 °C) was then added with gentle mixing to an aliquot (20 μL, 4 °C) of thawed competent cells and the cells were kept on ice (<4 °C, 30 min). Cells were then heat shocked (42 °C, 45 s) before being returned to the ice (<4 °C, 2 min). LB media (10 g/L bacto-tryptone, 5 g/L bacto-yeast extract, 10 g/L NaCl, deionised water to a final volume of 1 L) (900 μL, 37 °C) was added to the heat shocked cells which were then incubated with shaking (37 °C, 200 rpm, 1 h). Antibiotic (100 mg/L ampicillin) supplemented LB media plates were incubated at the same time (37 °C, 1 hr). The plates were then spread with transformed cell solution (120 μL) and incubated (37 °C, 16 h). Single colonies were picked and used to inoculate overnight cultures from which glycerol freezes were produced. Plates were then sealed and stored (4 °C).

2.2.5 DNA Miniprep

E. coli cells were harvested from overnight cultures by centrifugation (10 mL, 4 °C, 7500 rpm, 5 min). Plasmid DNA was isolated using the Wizard® *Plus* SV Minipreps Plasmid DNA Purification System. Cells resuspended in cell resuspension solution (250 μL), cell lysis solution was added (250 μL), followed by inversion, before neutralisation solution

was added (350 µL), solution was then centrifuged (4 °C, 13000 rpm, 10 min). The lysate was decanted into the spin column with attached collection tube and centrifuged (4 °C, 13000 rpm, 1 min). The flow-through was discarded, wash solution added to spin column (3 X 750 µL) before further centrifugation (4 °C, 13000 rpm, 1 min). The isolated plasmid DNA was then eluted with sterile water (100 µL).

2.2.6 SDS-PAGE

Gel Preparation

SDS-PAGE gels were prepared with a 10 % resolving gel and a 4 % stacking gel. Gels were prepared by combining their respective components, followed by applying the gels to moulds, with the resolving gel (3.33 mL 30% acrylamide mix, 3.33 mL deionised water, 3.33 mL gel buffer, 10 µL TEMED, 50 µL 10% ammonium persulfate, total volume 10 mL) being allowed to set before addition of the stacking gel (0.66 mL 30% acrylamide mix, 2.9 mL deionised water, 1.24 mL gel buffer, 10 µL TEMED, 25 µL 10% ammonium persulfate, total volume 5 mL) and comb.

Sample Analysis

Samples were prepared by mixing 1:1 with 2x SDS-PAGE loading buffer (2.5 mL Tris.HCl (pH 6.8, 0.2 M) (50 mM final), 154 mg DTT (0.1 mM final), 200 mg SDS (2 % (w/v) final), 10 mg Bromophenol Blue (0.1% (w/v) final), 1 mL Glycerol (10% (w/v) final), deionised water to a final volume of 10 mL) and denaturing (95 °C, 10 min). Samples (20 µl) were then loaded onto the gel and electrophoresis was carried out (200 V, 45 min, in 1x SDS-PAGE loading buffer). Gels were stained with InstantBlue (Sigma-Aldrich) for 1 h followed by rinsing in water before photographing.

2.2.7 Overexpression of Unlabelled GB3

Unlabelled GB3 was expressed using the following protocol. A plasmid encoding GB3 was transformed into *E. coli* BL21(DE3) cells, then grown at 37 °C in LB media (10 mL, 10 g/L bacto-tryptone, 5 g/L bacto-yeast extract, 10 g/L NaCl) supplemented with 100 mg/L ampicillin overnight. The overnight culture was then transferred to 500 mL of LB and grown at 37 °C. Protein expression was induced at an OD_{600} of ~0.7, with 1 mM isopropyl β-D-thiogalactoside (IPTG) at 37 °C for 4 h. Cells were pelleted and resuspended in phosphate buffered saline (PBS) (137 mM NaCl, 2.7 mM KCl, 10 mM Na_2HPO_4, pH 7.4).

2.2.8 Overexpression of Labelled GB3

Uniformly labelled (^{15}N or ^{13}C, ^{15}N) GB3 was expressed using the following protocol. A plasmid encoding GB3 was transformed into *E. coli* BL21(DE3) cells, then grown at 37 °C in LB media (10 mL) supplemented with 100 mg/L ampicillin for 16 h. The culture was then centrifuged (4000 rpm) and the cells resuspended in 500 mL of M9 minimal media (6 g/L Na_2HPO_4, 3 g/L K_2HPO_4, 0.5 g/L NaCl, 1 mM $MgSO_4$, 1 mM $CaCl_2$) supplemented with 1 g/L $^{15}NH_4Cl$, 2 g/L U-^{13}C-glucose and 100 mg/L ampicillin and grown at 37 °C. Protein expression was induced at an OD_{600} of ~0.7, with 1 mM isopropyl β-D-thiogalactoside (IPTG) at 18 °C for 16 h. Cells were pelleted and resuspended in phosphate buffered saline (PBS) (137 mM NaCl, 2.7 mM KCl, 10 mM Na_2HPO_4, pH 7.4).

2.2.9 Sample Preparation

The resuspended GB3 containing cells were sonicated and insoluble material removed by centrifugation. The supernatant was heated to 80 °C for 10 min and the insoluble material removed by centrifugation. Ammonium sulphate was added to the supernatant to 60 % w/v saturation and allowed to equilibrate for 2 h, and precipitant was again separated by centrifugation. The GB3 was subsequently precipitated in 90 % w/v ammonium sulphate. The pellet was dissolved in 25 mM tris, pH 8, and desalted with a PD-10 gel filtration column. Anion exchange chromatography was performed with 25 mM tris, pH 8 (5 ml HiTrap Q HP), with GB3 eluting at ~0.25 M NaCl. Monomeric GB3 was isolated by gel-filtration (Sephadex 75) with 100 mM NaCl, 25 mM bis-tris, pH 6.5. Peak fractions were pooled and concentrated to ~30 mg/ml with Generon Vivaspin 5 kDa MWCO filters. Crystallisation was achieved by the addition of 2-methyl-2,4-pentanediol to 60 % v/v of the total sample volume at 30 mg/mL protein concentration and allowed to incubate at 0 °C for ~48 h. The sample was centrifuged into a 1.6/1.3 mm zirconia rotor. A silicone-based glue was used to seal the rotor to maintain sample hydration.

2.3 Results and Discussion

2.3.1 Expression of Cysteine Mutants

The selected mutations were introduced through site-specific mutagenesis orchestrated through the polymerase chain reaction (PCR). The success of the PCR reactions was determined through the use of DNA gel electrophoresis. Each PCR product was run on a separate lane and in a linear form, along with a sample of the WT-GB3 in a linear and circular form for reference. A DNA base pair marker was also used to determine the length of the DNA species and compared to the known length of the plasmid (~6000 base pairs). Once the presence of a DNA band of the right length was observed to confirm successful polymerisation, the plasmid sample was ligated, and a sample sent off for Sanger sequencing to verify the DNA sequence. Once confirmed the now circular mutant plasmids were transformed into *E. coli* BL21(DE3) cells for expression of the protein.

2.3.2 Expression and Purification of GB3

For use in ssNMR studies both WT and cysteine mutant strains of GB3 (unlabelled and uniformly ^{15}N and $^{13}C/^{15}N$) were expressed and purified and subsequently crystallised. The expression and purification process was followed with SDS-PAGE (Figure 2.2). Through comparison of the SDS-PAGE of the pre/post induction cell lysates, one can see that induction with IPTG results in an increase in protein expression of several of the proteins present in the cells. Importantly, the expression of GB3 is enhanced, seen as a band at ~6 kDa (consistent with the molecular weight of GB3 of 6.21 kDa). After the expression, the steps of the purification were performed and followed by SDS-PAGE (Figure 2.2).

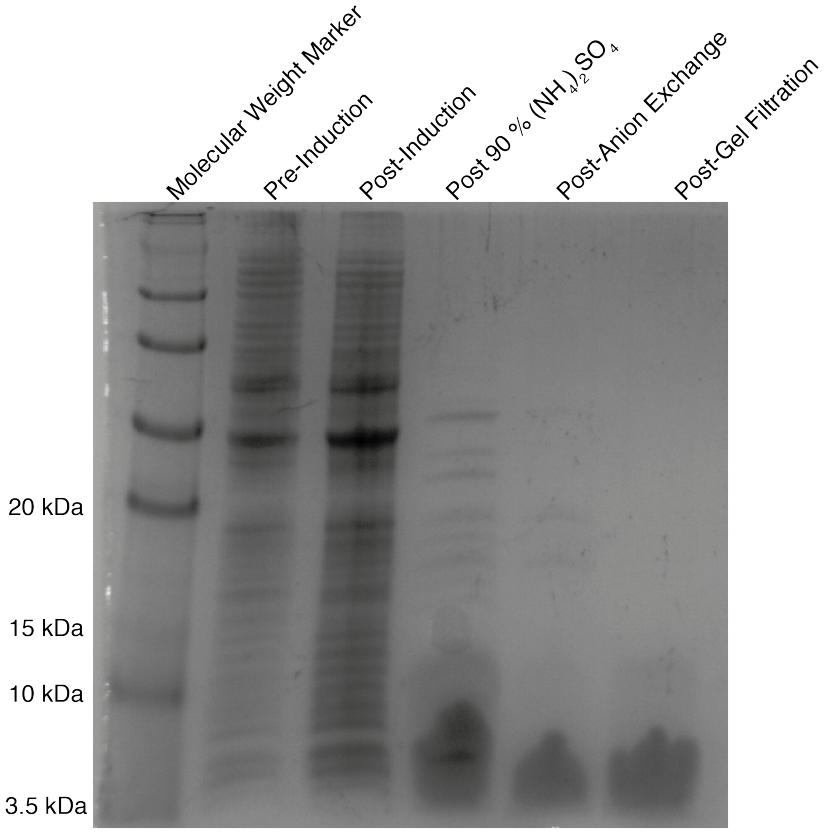

Figure 2.2 SDS-PAGE of the purification of GB3. Lanes show the progressive purification of GB3. The GB3 band is observed at ~6 kDa.

After precipitation with ammonium sulphate the protein, though high in purity as dictated by the SDS-PAGE, is contaminated with nucleic acids as evidenced through measurement of the absorbance at 260 nm/280 nm, which was greater than 1.5 at this step of the purification. In addition, one can see that after the ammonium sulphate precipitation there are still several high molecular weight protein impurities in the GB3 sample necessitating further purification. This was addressed through the use of anion exchange chromatography (chromatograph is shown in Figure 2.3), which further purified the protein, separating the GB3 sample from other proteins that have different binding affinities to the column with SDS-PAGE used to determine which fractions contained purified GB3 so that they could then be combined. The anion exchange chromatogram possesses two peaks. One of which is split into two and elutes at ~0.1 - 0.3 M NaCl and the second eluting at >0.6M NaCl. The peak eluted at low salt concentration had an absorbance at 260 nm/280 nm of ~0.5, which is indicative of protein with little DNA contamination. This peak was verified to contain GB3 as when a sample was analysed with SDS-PAGE a single intense band at ~6 kDa was observed (Figure 2.2). For the second peak eluting at >0.6M NaCl, the ratio of the absorbance measurements at 260 nm/280 nm

was ≥ 2.0, indicative of a sample almost entirely composed of nucleic acids and little to no protein, this was verified by SDS-PAGE as a blank lane with no protein bands.

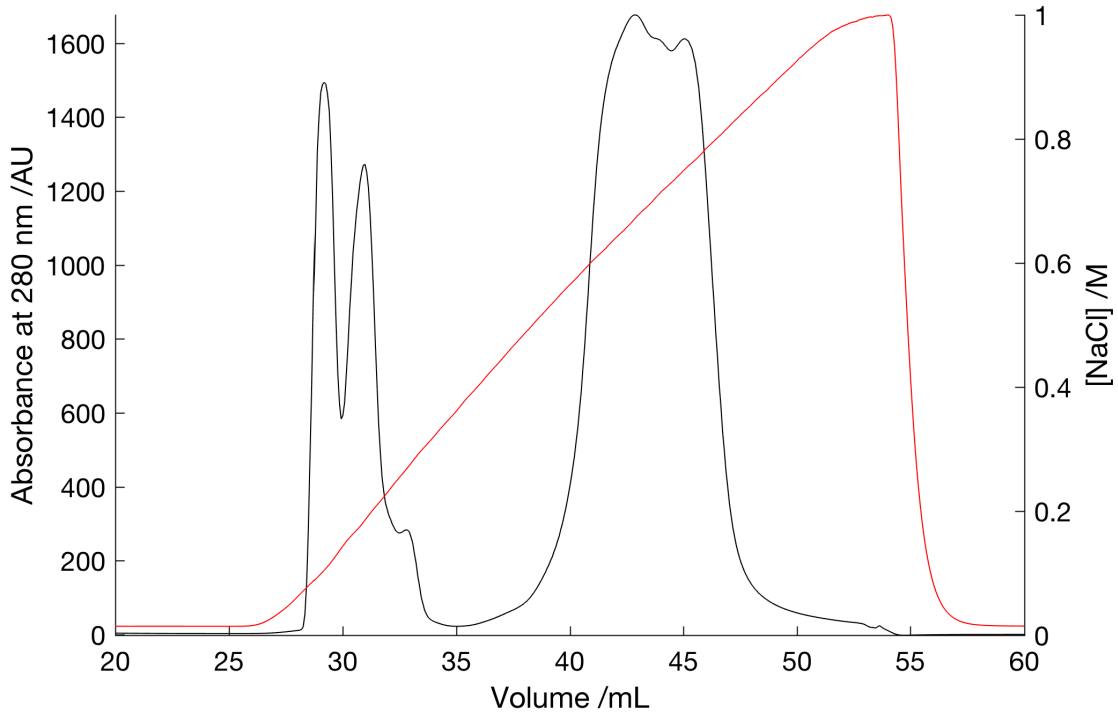

Figure 2.3 Anion exchange chromatogram of WT-GB3. Obtained to track which fractions contain protein via their absorbance of UV light at 280 nm. GB3 is eluted from the column at a salt concentration of approximately 0.25 M. The large peak at 0.6 M NaCl corresponds to that of DNA. Absorbance at 280 nm (black), NaCl concentration (red).

Though significantly higher in purity after the anion exchange chromatography, it was deemed necessary to further purify the protein, to ensure homogenous crystal formation. In addition, exchange into a low salt buffer was desirable. This was achieved through the use of gel filtration chromatography (chromatograph is shown in Figure 2.4). Fraction purity was determined with SDS-PAGE and GB3 containing fractions were pooled and concentrated. The gel filtration chromatogram showed only one peak, with a corresponding dip in conductivity. The subsequent peak in ion conductivity is indicative of the salts present in the sample coming off the column.

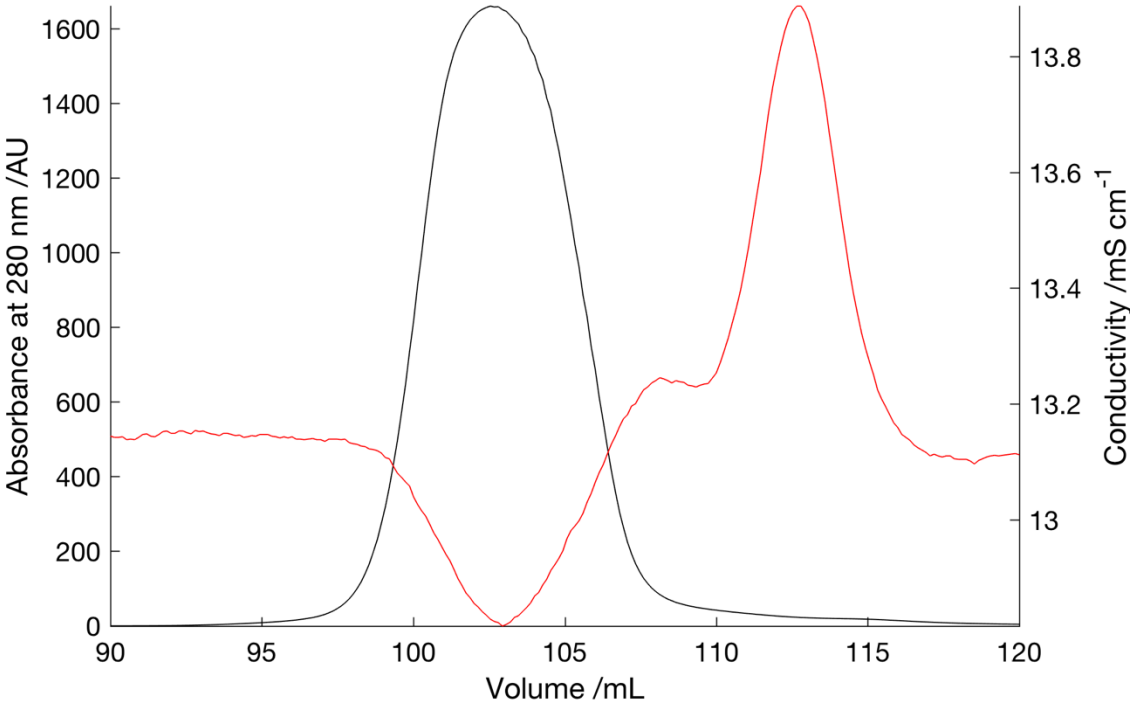

Figure 2.4 Gel filtration chromatogram of WT-GB3. Obtained to track which fractions contain protein via their absorbance of UV light at 280 nm. Absorbance at 280 nm (black), conductivity (red).

A mass spectrum was acquired for each of the samples to determine whether the alleged protein was that of the desired GB3 sample (Figure 2.5). This was also performed for the cysteine mutant samples (Figure 5.8). This was determined by calculating the expected molecular weight of the GB3 sample from the sequence and comparing it with the deconvoluted mass spectrum obtained via the maximum entropy algorithm. From Figure 2.5 it is clear that each of the GB3 samples has been successfully purified, with the most intense peak corresponding to the expected molecular weight of GB3. The yield of purified GB3 protein obtained from each preparation was approximately 90 mg/L for growth on unlabelled LB media, and approximately 60 mg/L for labelled growth on M9 media. The yield of the mutant GB3 protein obtained from each preparation was approximately 20 mg/L for growth on unlabelled LB media, and approximately 15 mg/L for labelled growth on M9 media.

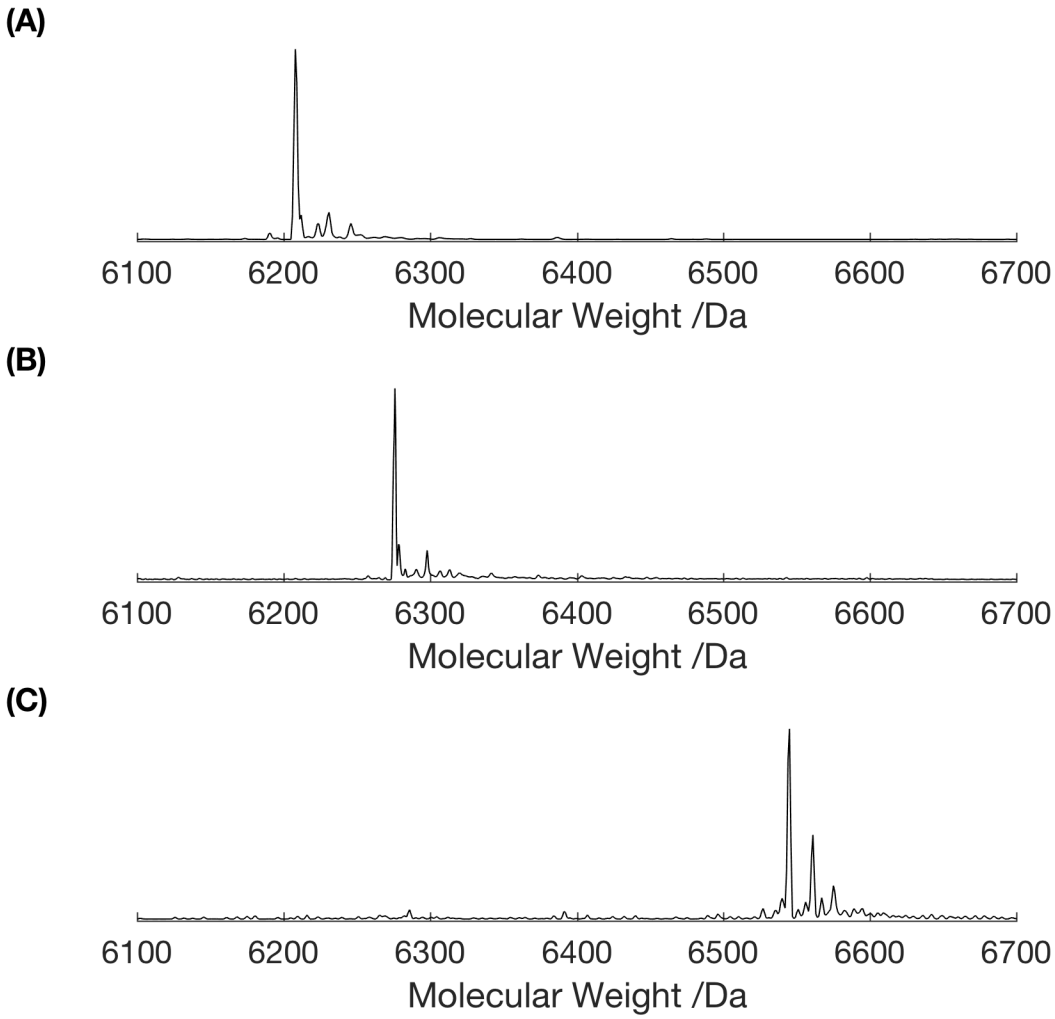

Figure 2.5 Deconvoluted time of flight mass spectra, via the maximum entropy algorithm to obtain the uncharged mass of the protein. Spectrum for unlabelled GB3, with a mass of 6208 kDa (A). Spectrum for [U-^{15}N]GB3, with a mass of 6276 kDa (B). Spectrum for [U-^{13}C/^{15}N]GB3, with a mass of 6548 kDa (C).

Chapter 3: A Novel Approach to Protein Assignment in ssNMR

3.1 Introduction

A prerequisite for site-specific structural and dynamic studies of proteins by ssNMR is a backbone resonance assignment. While proton-detected methods of resonance assignment and structure determination are becoming increasingly more popular and less time consuming with the advent of ultrafast MAS (>60 kHz) probes,[124-128] the assignment process is still commonly achieved using ^{13}C-detected experiments on uniformly ^{13}C/^{15}N labelled samples at rotation frequencies below 60 kHz.[129-133] Though other approaches are used, the most common method to assign the protein backbone with ^{13}C-detected experiments is to use separate two- and three-dimensional heteronuclear NCC correlation experiments of the type NCOCA/NCOCX to obtain inter-residue correlations, and NCACO/NCACX to obtain intra-residue correlations, usually in combination with other two- and three-dimensional hetero- and homonuclear experiments.[134-137] NCOCX and NCACX experiments are both typically performed with band selective polarisation transfer by cross-polarisation (CP) from $^{15}N^{(i)}$ spins to either adjacent $C_{Co}^{(i-1)}$ (NCOCX) or $C_{\alpha}^{(i)}$ (NCACX) spins, followed by a homonuclear dipolar recoupling sequence to transfer spin polarisation between local ^{13}C spins. Numerous homonuclear dipolar recoupling sequences exist, each with specific features that confer advantages for particular applications or experimental conditions, as reviewed by De Paëpe[62] and Mithu[138].

An apparent opportunity to condense the acquisition time required for sequential assignment of uniformly labelled solid proteins in this manner is to simultaneously record inter-residue (NCOCX type) and intra-residue (NCACX type) correlations in a single experiment, effectively doubling the information content of typical NCC experiments, and halving the required acquisition time. This type of bidirectional inter- and intra- residue polarisation transfer is exploited frequently in solution-state NMR experiments for protein assignment, such as HNCA[139] and HNCACB[140]. In these liquid-state experiments, polarisation on $N^{(i)}$ spins is simultaneously transferred via the J-couplings to both the adjacent $C_{\alpha}^{(i)}$, and the preceding $C_{\alpha}^{(i-1)}$, resulting in a spectrum with both inter- and intra-residue correlations. For this reason, in favourable cases, either of these experiments can be

sufficient to assign the backbone resonances of a protein in a single experiment.[140] This bidirectional approach is however rarely encountered in the assignment of solid proteins. This may be attributed to the fact that using the J-coupling to transfer polarisation in solid samples is often inefficient compared to dipolar recoupling, particularly at lower MAS rates, due to typically large inhomogeneous linewidths, and short coherence lifetimes. 3D heteronuclear correlation spectroscopy using J-based transfers for resonance assignment in solid proteins has been demonstrated previously, where extensive deuteration of samples can help to achieve the required linewidths and coherence lifetimes but is not essential.[64-65]

In terms of using the hetero- and homonuclear dipolar recoupling methods more commonly used in ssNMR assignment methods to simultaneously record inter- and intra- residue correlations, one possibility would be to recouple ^{15}N spins to ^{13}C spins in a non-selective manner, i.e. NCX rather than NCO or NCA. This method has been demonstrated previously, via a 3D-ZF-TEDOR-DARR experiment using broadband TEDOR rather than specific CP for ^{15}N-^{13}C polarisation transfer, simultaneously recoupling $N^{(i)}$-$C_{CO}^{(i-1)}$, and $N^{(i)}$-$C_{\alpha}^{(i)}$dipolar interactions, before a broadband ^{13}C mixing period using DARR.[141] This method has the disadvantage of requiring that the entire protein ^{13}C spectral width (≥175 ppm) be acquired in the indirect dimension of a 3D experiment, however, practically necessitating non-uniform sampling (NUS) or deliberate spectral aliasing in order to realise the acquisition timesaving over acquisition of separate NCOCX and NCACX spectra. Alternatively, one could exploit the ^{13}C/^{13}C homonuclear dipolar recoupling step to simultaneously recouple the $C_{\alpha}^{(i)}$-$C_{CO}^{(i-1)}$ and $C_{\alpha}^{(i-1)}$-$C_{CO}^{(i-1)}$ dipolar interactions after a specific ^{15}N-^{13}C CP transfer. However, many homonuclear dipolar recoupling sequences used for ^{13}C/^{13}C recoupling are not able to efficiently simultaneously recouple the smaller $C_{\alpha}^{(i)}$-$C_{CO}^{(i-1)}$dipolar interaction, as well as the $C_{\alpha}^{(i-1)}$-$C_{CO}^{(i-1)}$ interaction, due to dipolar truncation and/or relayed transfers reducing the intensity of the comparatively long-range $C_{\alpha}^{(i)}$-$C_{CO}^{(i-1)}$ correlation.[142]

In this body of work, we demonstrate that at moderate MAS frequencies (35 kHz), the mixed rotational and rotary resonance (MIRROR) homonuclear recoupling sequence may be incorporated into a 2D- or 3D-NCC correlation experiment to record simultaneously inter- and intra-residue MIRROR-NCOCA spectra by efficiently recoupling both the $C_{\alpha}^{(i-1)}$-$C_{CO}^{(i-1)}$ and $C_{\alpha}^{(i)}$-$C_{CO}^{(i-1)}$ dipolar interactions after a specific ^{15}N-^{13}C CP transfer step. The MIRROR sequence was chosen as it is a second-order, band-selective homonuclear recoupling sequence, that requires only low ^{1}H rf-amplitudes and has been shown to be

efficient at moderate MAS frequencies.[1] First-order sequences have been utilised to band selectively recouple the C_α-C_{CO} dipolar interaction including band selective homonuclear CP (BSH-CP)[143-145] and rotational resonance in a tilted rotating frame (R^2TR)[146-147]. Such sequences are however more susceptible to dipolar truncation than second order recoupling sequences suppressing transfer through the longer range $C_\alpha^{(i)}$-$C_{CO}^{(i-1)}$ interaction.[143-145] Broadband homonuclear recoupling sequences such as PDSD and DARR, which operate well at low magnetic fields and spinning frequencies were not chosen, as relayed transfers to sidechain ^{13}C spins would potentially dilute the required spin polarisation transferred from the C_{CO} to the C_α. The same is true of broadband second-order sequences that operate efficiently at higher magnetic fields and spinning rates, such as PARIS[148], SHANGHAI[149] and PAR[150].

The reintroduction of the second order terms under the MIRROR condition relies on setting the amplitude of the proton rf-irradiation (ω_1^H) to a multiple of the spinning speed (ω_R) plus or minus the isotropic chemical shift difference between the ^{13}C nuclei (C_{CO} to C_α) to be recoupled ($\Delta\omega_{iso}^C$) (Equation (3.1)).

$$\omega_1^H = n\omega_R \pm \Delta\omega_{iso}^C \qquad \textbf{(3.1)}$$

As the recoupling condition is dependent on the isotropic chemical shift separation, the transfers are inherently band-selective. Band selective transfers offer a number of advantages for backbone assignments, facilitating the directed transfer of magnetisation along the protein backbone, whilst restricting the transfer of magnetisation to the protein sidechains which would otherwise compromise signal intensity. These properties have previously been exploited in assignment schemes which exploit band-selective cross polarisation[144, 151] and rotational resonance in the tilted rotating frame[152]. At moderate MAS frequencies (40 kHz) the MIRROR condition has been shown to efficiently recouple the C_α-C_{CO} dipolar interaction to record $^{13}C/^{13}C$ correlation spectra in uniformly labelled proteins.[1] Several groups have utilised MIRROR to assist in characterisation in a variety of systems.[153-155] Here, we show that the efficiency of the MIRROR sequence is such that it may be used to recouple both the $C_\alpha^{(i-1)}$-$C_{CO}^{(i-1)}$ and $C_\alpha^{(i)}$-$C_{CO}^{(i-1)}$ dipolar interactions in one bidirectional transfer step. Furthermore, the polarisation transfer to $C_\alpha^{(i)}$ and $C_\alpha^{(i-1)}$spins is relatively uniform throughout the protein sequence, which we attribute to the fixed geometry of the peptide plane regardless of secondary structure. These transfer properties

facilitate the reliable, robust observation of both inter- and intra-residue correlations. It is shown that the MIRROR sequence can be incorporated into a 3D-NCOCA experiment, and that the 3D-MIRROR-NCOCA alone can be used to straightforwardly assign the backbone resonances of a microcrystalline sample of the 56-residue model protein GB3, representing a 50 % saving in terms of acquisition time over separate NCOCX and NCACX experiments. Moreover, since MIRROR uses relatively low-power rf-fields, it can be combined with low-power CP and decoupling schemes permitting the construction of a low-power MIRROR-NCOCA experiment where recycle delays are limited by the T_1 of the sample rather than the probe duty cycle. Together these properties allow for the efficient acquisition of a 3D dataset which allows a complete backbone assignment to be made in a single experiment acquired within 24 hours.

3.2 Materials and Methods

3.2.1 Solid-State NMR Spectroscopy

Unless otherwise stated all measurements were conducted at 14.1 T on an Agilent DD2 600 MHz NMR spectrometer (Yarnton, UK) equipped with a 1.6 mm triple resonance magic-angle spinning probe. Samples were spun at 35 kHz, and the temperature regulated to 273 K. For all triple resonance experiments the pulse sequence shown in Figure 3.1 was employed. For 'high-power' ^{1}H-^{15}N CP the carrier frequencies were set to the centre of the ^{1}H (~5 ppm) and ^{15}N (~120 ppm) spectrum. Optimal ^{1}H-^{15}N CP was obtained with a 1.5 ms contact pulse with a ^{1}H field of ~105 kHz and a ^{15}N field of ~70 kHz. For 'high-power' ^{15}N-^{13}C CP the ^{15}N carrier frequency was set to the middle of the amide region (120 ppm) and the ^{13}C to the centre of the C_{CO} region (~172 ppm). The spin-lock fields were set to 5/2 times the spinning speed, 87.5 kHz, for ^{15}N and 3/2 times the spinning speed, 52.5 kHz, for ^{13}C. Maximal transfer was observed after 7 ms CP. During ^{15}N-^{13}C CP, 135 kHz continuous wave proton decoupling was applied. Under such conditions, magnetisation transfer occurred exclusively from the ^{15}N to the carbonyl carbons. Following transfer from the amide nitrogens to the carbonyls in the protein backbone, magnetisation was transferred between carbon sites using a weak rf-field on the protons that satisfied either the dipolar assisted rotary resonance condition ($\omega_1^H = n\omega_R$) or the MIRROR condition ($\omega_1^H = n\omega_R \pm \Delta\omega_{iso}^C$), where ω_1^H is the proton rf-field amplitude, ω_R is the rotation frequency and $\Delta\omega_{iso}^C$ is the isotropic chemical shift difference of a chosen ^{13}C spin-pair. During all evolution periods 120 kHz SPINAL proton decoupling was applied with phase flip angles of 10° and 5°. All π/2 pulses on ^{1}H, ^{13}C and ^{15}N were set to at 2.4, 3.2, and 3.1 μs respectively.

For 'low-power' measurements, high power decoupling was replaced with low-power TPPM decoupling[156] with a phase alternation of 20° and a pulse length of 55 μs. For ^{1}H-^{15}N and ^{15}N-^{13}C transfers low-power recoupling conditions were established with spin-lock fields of 62 kHz on ^{1}H and 8 kHz on ^{15}N for ^{1}H-^{15}N, and 25 kHz on ^{15}N and 10 kHz on ^{13}C for ^{15}N-^{13}C CP transfers. All 'hard' pulses on ^{1}H, ^{13}C and ^{15}N were kept at 2.4, 3.2, and 3.1 μs respectively.

All 2D and 3D experiments were acquired with States-TPPI phase sensitive detection, employing a ^{15}N spectral width of 5 kHz and 64 complex points and a C_{CO} spectral width of 2.5 kHz and 32 complex points. All spectra were externally referenced to the downfield resonance of adamantane at 40.48 ppm compared to DSS[157]. Multidimensional data sets were processed in NMRPipe[158], prior to analysis and assignment in CCPN Analysis 2.4[159-160]. For both the direct and indirect ^{13}C dimensions the data was processed with a Lorentz-to-Gauss window function, with an inverse exponential width of 10 Hz and a Gaussian broadened width of 40 Hz. In the indirect ^{13}C dimension the data was linear predicted to 128 complex data points. For the indirect ^{15}N dimension the data was processed with a Lorentz-to-Gauss window function, with inverse exponential width of 20 Hz and a Gaussian broadened width of 40 Hz.

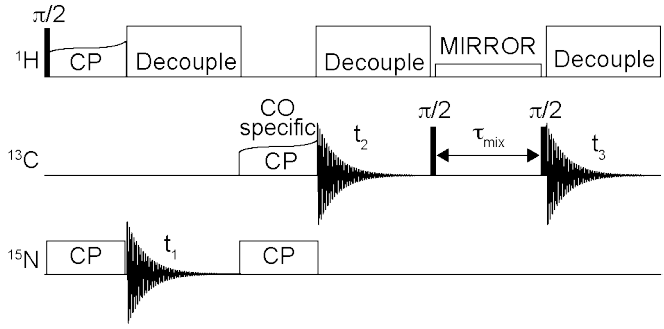

Figure 3.1 The 3D-MIRROR-NCOCA pulse sequence employed. 2D-NcoCA data were acquired with no C_{CO} evolution in the indirect dimension, t_2. 1D-ncoCA spectra used for determining MIRROR conditions and C_{CO}/C_{α} transfer was acquired with no evolution in either the ^{15}N (t_1) or C_{CO} (t_2) indirect dimensions. All other experimental details are reported in the materials and methods.

3.2.2 Numerical Simulations of Magnetisation Transfer Under the MIRROR Condition

Simulations were conducted using Spinach[35] for a 6-spin system to both confirm the position of resonance conditions and investigate magnetisation transfers (see Figure 3.2). Simulated magnetisation transfers were first created on the $C_{CO}^{(i-1)}$ (spin 2) spin and observed transferring to either the $C_{\alpha}^{(i-1)}$ (spin 1) or the $C_{\alpha}^{(i)}$ (spin 3). A Floquet space of rank 4 was used. A repulsion ab 400 octahedral powder was used. Mixing time of 10 ms, MAS frequency of 35 kHz, B_0 field strength of 14.1 T, temperature of 298 K.

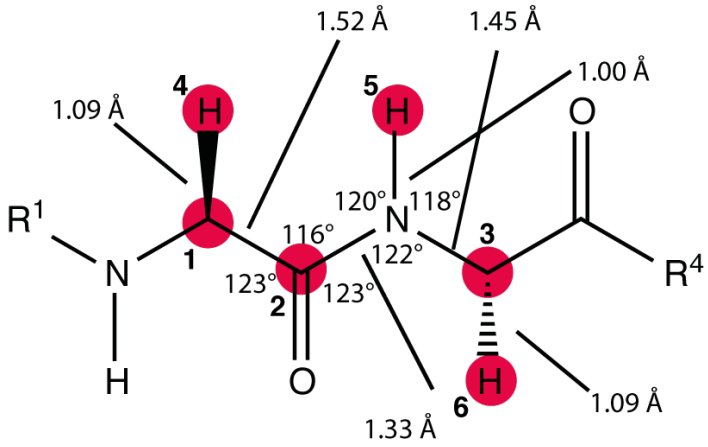

Figure 3.2 Protein backbone highlighting in red atoms simulated. Bond lengths and angles taken into account for the magnetisation transfer are also shown. Simulation used 6 spins where magnetisation transfers from the $C_{CO}^{(i-1)}$ (spin 2) to both $C_{\alpha}^{(i-1)}$ (spin 1) and $C_{\alpha}^{(i)}$ (spin 3) were observed.

Table 3.1 Atom coordinates used in the simulation.

N	Spin	X coordinate /Å	Y coordinate /Å	Z coordinate /Å
1	^{13}C	+0.000	+0.000	+0.000
2	^{13}C	+1.320	+0.750	+0.000
3	^{13}C	+3.750	+0.570	+0.000
4	^{1}H	+0.000	-1.000	+0.000
5	^{1}H	+2.420	-1.000	+0.000
6	^{1}H	+3.750	+1.570	+0.000

Table 3.2 Isotropic chemical shifts of atoms used in the simulation.

N	Spin	Chemical shift /ppm	Offset isotropic Zeeman interaction /Hz
1	^{13}C	50.0	-7549.4196

2	^{13}C	170.0	-25668.0266
3	^{13}C	45.0	-6794.4776
4	^{1}H	0.3413	-204.8969
5	^{1}H	0.3413	-204.8969
6	^{1}H	0.3413	-204.8969

Table 3.3 Dipolar couplings of atoms used in the simulation.

Interacting spins	Dipolar interaction /Hz
1,2	1.04E+04
2,3	6.07E+03
1,4	3.70E+04
2,4	2.06E+03
1,5	3.51E+03
2,5	4.19E+03
3,5	2.19E+03
4,5	2.66E+03
2,6	4.25E+03
3,6	3.70E+04
4,6	1.71E+02
5,6	6.43E+02

3.3 Results and Discussion

3.3.1 MIRROR Resonance Conditions at 35 KHz

Optimal recoupling under the MIRROR condition occurs when the proton rf-amplitude, ω_1^H, fulfils the condition $n\omega_R \pm \Delta\omega_{iso}^C$ (see Figure 3.3). Based on the isotropic chemical shifts obtained from the BMRB,[161] the average frequency separation, $\Delta\bar{\omega}_{iso}^C$, between the C_{CO} and C_α at 14.1 T, the field employed here, is 18.75 kHz. This gives rise to theoretical MIRROR conditions at 16.25, 18.75, 51.25 and 53.75 kHz. To identify conditions under which optimal transfer occurs experimentally, the C_α signal intensity obtained after 100 ms MIRROR mixing was plotted as a function of the MIRROR recoupling field (Figure 3.4A). Transfer occurs at two conditions approximately 5 kHz wide that are centred at 18.75 and 50.5 kHz in good agreement with the predicted values ($n\omega_R \pm \Delta\omega_{iso}^C$). The absence of any transfer at the n = 1 DARR condition (35 kHz) should be noted, highlighting the poor efficiency of this technique at moderate spinning frequencies. The presence of the MIRROR conditions and absence of DARR condition was also investigated using numerical spin dynamical simulations. Comparison of the build-up of magnetisation at these two matching conditions (Figure 3.4) shows that maximal transfer occurs with a ^{1}H rf-amplitude of 18.75 kHz, where transfer occurs under the n = 0, $+\Delta\omega_{iso}^C$ and n = 1, $-\Delta\omega_{iso}^C$ resonance conditions. Although the superimposition of the two matching conditions leads to efficient transfer of magnetisation, through the judicious choice of spinning speed the width of the matching condition can be tailored by varying the separation between the n = 0, $+\Delta\omega_{iso}^C$ and n = 1, $-\Delta\omega_{iso}^C$ conditions. Transfer under the 50.5 kHz matching condition results in a 25% reduction in the total amount of magnetisation transferred from the C_{CO} to the C_α, mirroring earlier reports that showed maximal transfer efficiencies at the lower power matching conditions.[1] When normalised against the total intensity of the carbonyl region approximately 40 % of the magnetisation is transferred from the C_{CO} region to the C_α region of the spectrum, with the bulk of the magnetisation transferred within the first 50 ms of recoupling. The extent of transfer is comparable to other band-selective transfers including band selective CP albeit with significantly reduced rf-ampliitudes.[162]

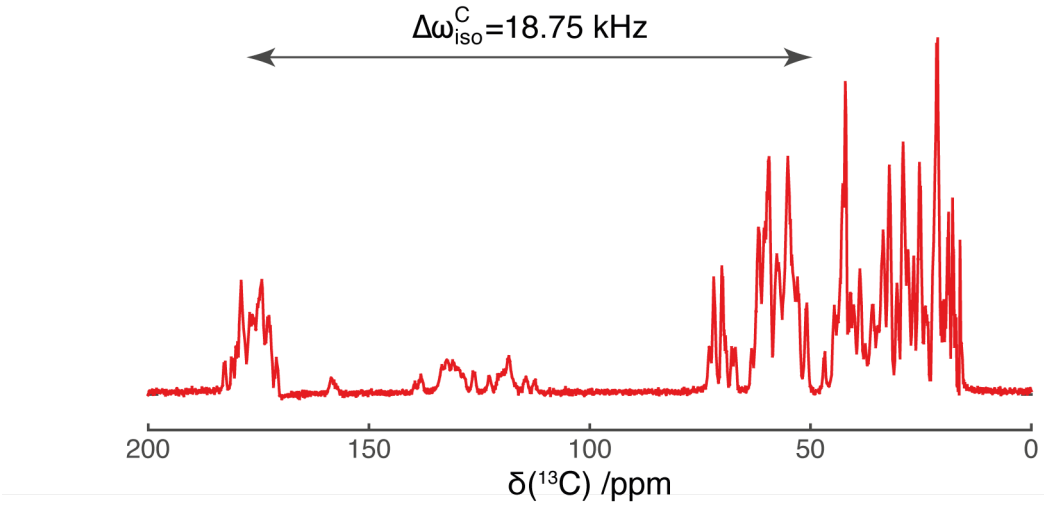

Figure 3.3 1D-^{1}H-^{13}C CP to demonstrate the width between recoupled nuclei, $\Delta\omega_{iso}^{C}$. $\Delta\omega_{iso}^{C}$represents the difference in isotropic chemical shifts between C_{CO} and C_{α} regions.

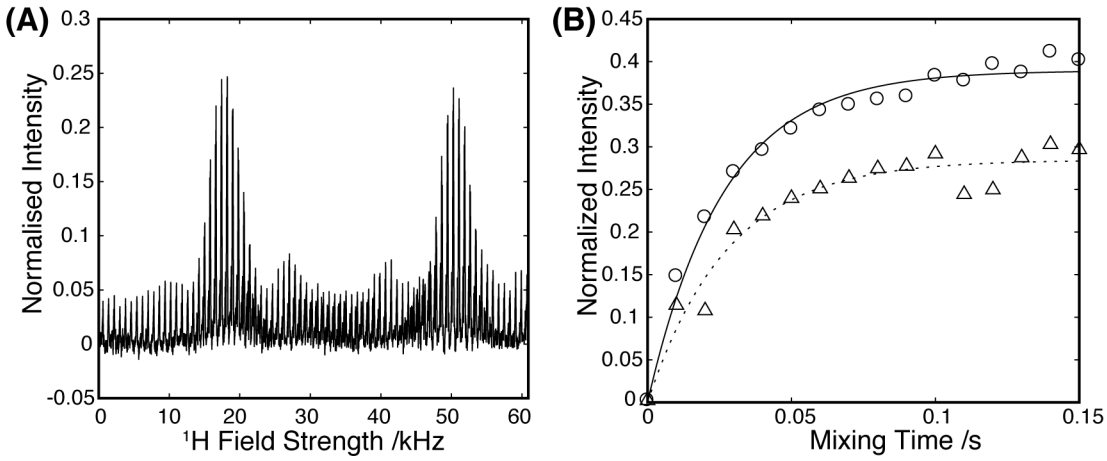

Figure 3.4 Signal from C_{α} region of a 1D-ncoCA spectrum of microcrystalline GB3 following a 100 ms period of MIRROR recoupling as a function of the MIRROR recoupling rf-field (A). Build-up of C_{α} magnetisation in a 1D-ncoCA spectrum of microcrystalline GB3 as a function of MIRROR recoupling period for the recoupling condition at 18.5 kHz (◯, —) and 50 kHz (△,---) (B). The amplitudes in A and B are normalised to the integrated intensity of the carbonyl region in the absence of any MIRROR recoupling. Data acquired at 14.1 T with 35 kHz MAS.

2D-NcoCA data (Figure 3.5A) demonstrate that efficient transfer is observed across the C_{α} region with resonances from 40 to 70 ppm exhibiting similar recoupling efficiencies.

This suggests that at 14.1 T B_0 field strength and 35 kHz spinning speed, the MIRROR recoupling bandwidth is sufficient to actively recouple the entire C_{CO}/C_α envelopes, even in the absence of any modulation of the MIRROR recoupling field. As expected, and in contrast to DARR experiments conducted at lower spinning speeds, little of the magnetisation is relayed out to the sidechains following transfer of magnetisation from the C_{CO} to C_α. Indeed, the resonances not attributable to C_α arise from correlations with ^{13}C sites on amide sidechains. These exhibit a similar chemical shift dispersion and strong dipolar couplings to C_{CO} groups. The selective nature of the transfer limits the diffusion of magnetisation throughout the protein leading to enhanced intensity in the C_α region of the spectrum.

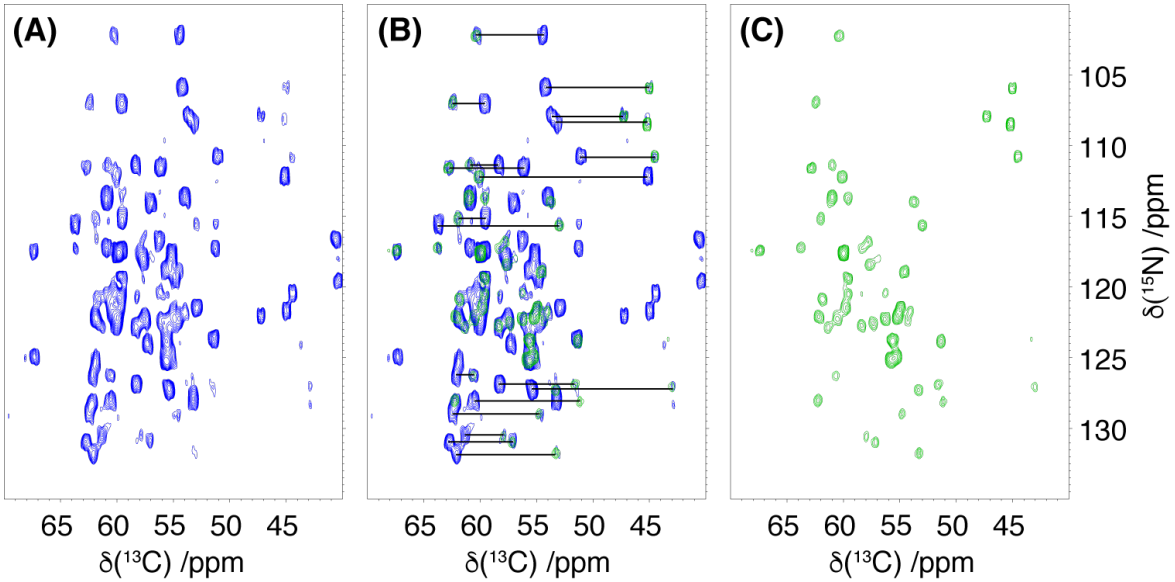

Figure 3.5 2D-NcoCA/NCA spectra of microcrystalline GB3. 2D-NcoCA spectrum of microcrystalline GB3 using 100 ms MIRROR transfer from transfer of magnetisation from the C_{CO} to C_α (A, blue), superimposition of the NcoCA (blue) with the NCA spectrum (green) (B), and the NCA spectrum (C, green). Tie lines in (B) highlight the presence of connectivities between intense peaks arising from the $NCOCA_{(i-1)}$ and the weaker peaks arising from the $NCOCA_{(i)}$ transfer.

To assess the bandwidth of the MIRROR condition, 2D-NcoCA experiments were recorded (Figure 3.6) with a 16.65, 18.75 and 20.35 kHz MIRROR rf-amplitude (A, B and C respectively) corresponding to a ±10 % offset from the optimal transfer at the $n = 0$, $+\Delta\omega_{iso}^{C}$ and $n = 1$, $-\Delta\omega_{iso}^{C}$ MIRROR condition. As apparent in the data across 3.7 kHz range in MIRROR rf-amplitude the recoupling profile is similar for all resonances in the spectra with coupling observed not only between the C_{CO} and C_α's of the individual amino

acids. Also apparent in the spectra are resonances from C_β resonances (~65-70 ppm) of threonines within the sample which are adjacent spectrally to the C_α envelope and C_{CO} resonances present in the sidechains of amino acids containing carboxylic and amide functional groups (35-45 ppm).

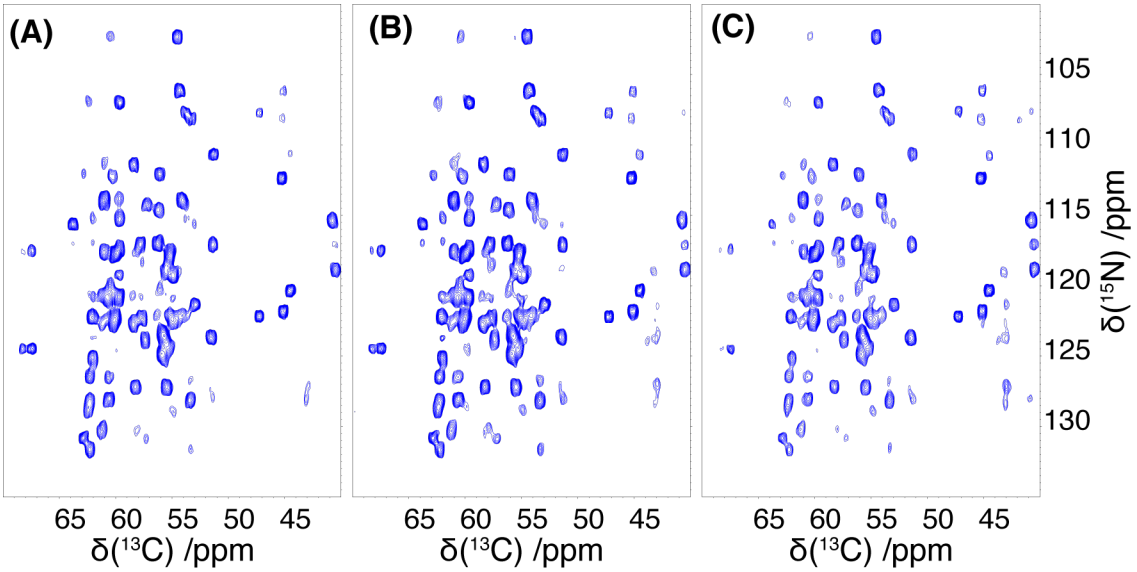

Figure 3.6 Analysis of MIRROR condition bandwidth. To assess the bandwidth of the MIRROR condition, 2D-NcoCA experiments were recorded with a 16.65, 18.75 and 20.35 kHz MIRROR rf-amplitude (A, B and C respectively) corresponding to a ±10% offset from the optimal transfer at the $n = 0$, $+\Delta\omega_{iso}^{C}$ and $n = 1$, $-\Delta\omega_{iso}^{C}$ MIRROR condition.

To assess the utility of the technique at higher field where the variation in $\Delta\omega_{iso}^{C}$ will increase with field and the recoupling bandwidth may become comparable to the chemical shift distribution, NcoCA data were acquired at 20 T (Figure 3.7). At the higher field with 50 kHz MAS, transfer is still observed at the $n = 0$, $+\Delta\omega_{iso}^{C}$ and $n = 1$, $-\Delta\omega_{iso}^{C}$ condition, although the overall signal sensitivity is lower due to the smaller sample volumes available in the smaller diameter rotors. Intensity is observed from 70 to 40 pm, indicating that transfer occurs quite uniformly across the C_α region, even at the high magnetic field, and without the need to resort to amplitude or phase modulation of the MIRROR recoupling rf-field.[1, 163]

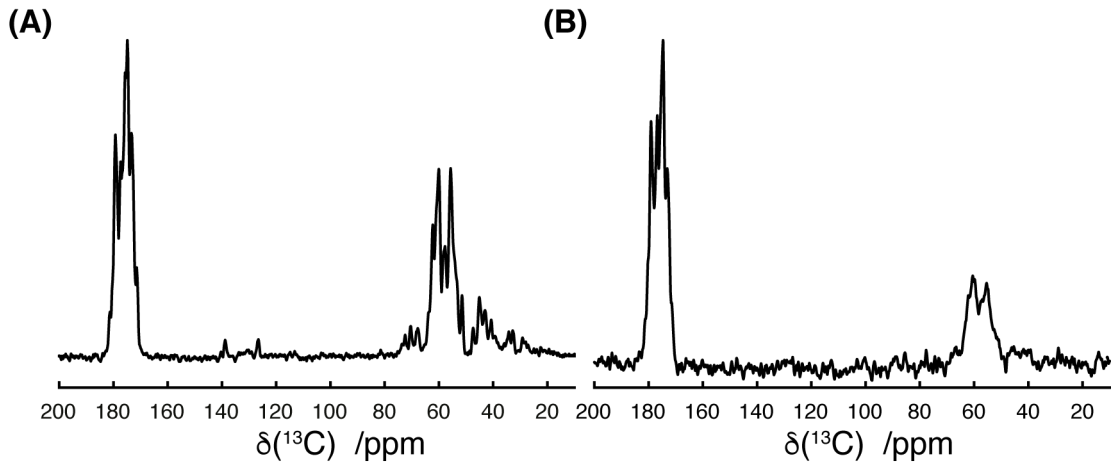

Figure 3.7 Comparison of bandwidths at high magnetic fields. Comparison of recoupling bandwidth at 14.1 T and 20 T, 600 and 850 MHz proton Larmor frequency respectively. 1D-ncoCA spectrum of GB3 acquired at 35 kHz with 18.75 kHz MIRROR recoupling field, the $n = 0$, $+\Delta\omega_{iso}^{C}$ recoupling condition at 14.1T (A). 1D-ncoCA spectrum of GB3 acquired at 50 kHz with 26.5 kHz MIRROR recoupling field, the $n = 0$, $+\Delta\omega_{iso}^{C}$ recoupling condition at 20 T (B).

3.3.2 Investigating Magnetisation Build-Up on C_α Sites

Closer inspection of the 2D-NcoCA spectrum in Figure 3.5A reveals that in addition to the intense resonances arising from the transfer of magnetisation from $N^{(i)}$ to $C_{CO}^{(i-1)}$ to $C_\alpha^{(i-1)}$ weaker correlations whose intensity is approximately 50 % of the intensity of the $NCOCA^{(i-1)}$ peaks are also present for each of the nitrogen sites. Magnetisation on $C_\alpha^{(i-1)}$ and $C_\alpha^{(i)}$ was ensured to be the result of transfer from $C_{CO}^{(i-1)}$ during the MIRROR mixing time through the set-up of ^{15}N to ^{13}C CP exclusively from the ^{15}N to the carbonyl carbons prior to the recoupling. Comparison of this data with the corresponding NCA spectrum (Figure 3.5B/C) reveals that these weaker resonances correspond to the transfer of magnetisation of $N^{(i)}$ to $C_{CO}^{(i-1)}$ to $C_\alpha^{(i)}$. Typically, at lower spinning speeds using broadbanded transfers we have not systematically observed these long-range correlations, presumably due to dipolar truncation effects and loss of intensity as magnetisation is transferred out to the amino acid side-chains. In this instance though it is apparent that by band selectively recoupling the C_{CO} to the C_α region of the spectra correlations are observed to both the adjacent and more proximal C_α. Given the fixed geometry surrounding the peptide bond, the distances between the $C_{CO}^{(i-1)}$ and the $C_\alpha^{(i-1)}$ and $C_\alpha^{(i)}$ remain constant at 1.52 Å and 2.43 Å respectively, irrespective of the backbone conformation of the protein. Given this fixed geometry, it is expected that the transfer of magnetisation

from the $C_{CO}^{(i-1)}$ to the $C_{\alpha}^{(i-1)}$ and $C_{\alpha}^{(i)}$ would be similar for all sites within the proteins, something that is qualitatively apparent in the 2D-NcoCA spectrum of GB3 (Figure 3.5A/B) where in well resolved regions each nitrogen resonance possesses pairs of C_{α} resonances irrespective of its location within the protein. A quantitative analysis of the magnetisation transfer (Figure 3.8, Table 7.1) from the C_{CO} to the two C_{α} sites reveals that the rate of transfer to the two sites is similar. Time constants of between 20 and 40 ms are observed when exchange is modelled as an exponential process. This suggests that the observed difference in resonance intensities is not due to differences in transfer rates, but rather to differences in the extent to which magnetisation is transferred. The more distant $C_{\alpha}^{(i)}$ site typically exhibits an intensity of 40 to 60 % of that observed for the direct transfer to the $C_{\alpha}^{(i-1)}$ site (Figure 3.5, Table 7.1).

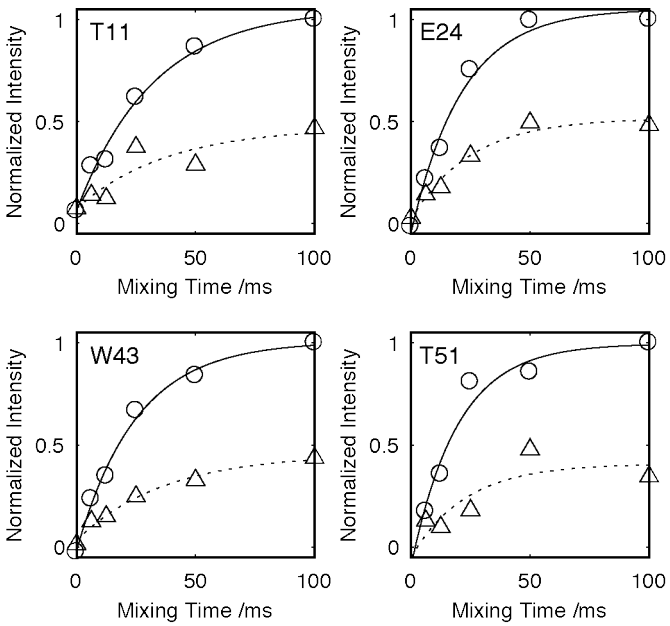

Figure 3.8 Residue site-specific magnetisation build-up on C_α sites. Plots showing the build-up of magnetisation following transfer from $C_{CO}^{(i-1)}$ to $C_\alpha^{(i-1)}$ (◯,-) and $C_{CO}^{(i-1)}$ to $C_\alpha^{(i)}$ (△,--) for selected resonances. Data integrated from the corresponding 2D-NcoCA spectra of a microcrystalline preparation of GB3. All data normalised to the maximum intensity of the $C_\alpha^{(i-1)}$, and fitted to an exponential build-up. Data acquired at 14.1 T with 35 kHz MAS.

Through simulations investigating the protons responsible for the magnetisation transfer (Figure 3.9), as expected the $C_\alpha^{(i-1)}$ magnetisation builds up faster than the $C_\alpha^{(i)}$ magnetisation but it seems the $C_\alpha^{(i)}$ magnetisation is continuing to increase which is not what we see experimentally. Experimentally we see the $C_\alpha^{(i-1)}$ peak is about three times as large as that of the $C_\alpha^{(i)}$ peak. Removing the proton attached to the nitrogen (spin 5), as expected the $C_\alpha^{(i-1)}$ magnetisation builds up faster than the $C_\alpha^{(i)}$ magnetisation but it seems the $C_\alpha^{(i)}$ magnetisation is continuing to increase which is not what we see experimentally. The $C_\alpha^{(i)}$ build up seems to have been affected more initially yet seems to continue to build up whereas the $C_\alpha^{(i-1)}$ seems to plateau. Removing the proton near $C_\alpha^{(i-1)}$ (spin 4) greatly reduced magnetisation transfer to the $C_\alpha^{(i-1)}$ without reducing magnetisation transferred to $C_\alpha^{(i)}$. Removing the proton near $C_\alpha^{(i)}$ (spin 6) greatly reduced magnetisation transfer to the $C_\alpha^{(i)}$ without reducing magnetisation transferred to $C_\alpha^{(i-1)}$.

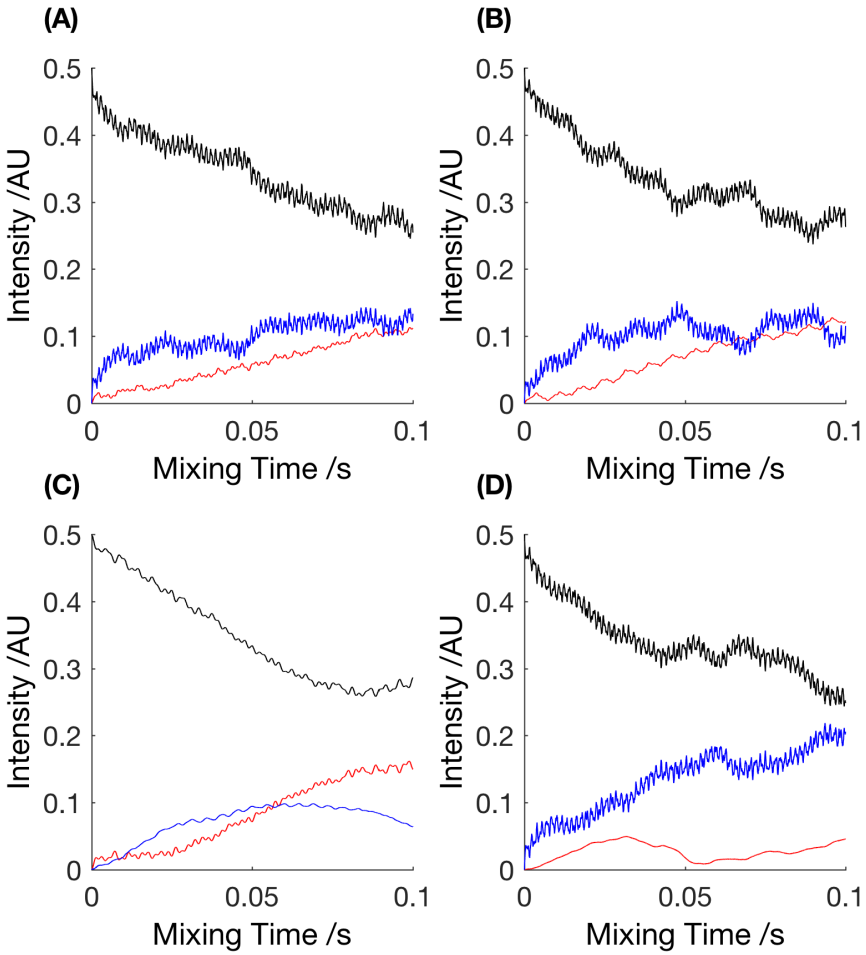

Figure 3.9 Simulation of magnetisation on backbone ^{13}C atoms for different configurations of neighbouring protons. Magnetisation is first created on spin 2 ($C_{CO}^{(i-1)}$) and observed under a ^{1}H rf-field during an evolution time transferring to spins 1 and 3 ($C_{\alpha}^{(i-1)}$and $C_{\alpha}^{(i)}$). All 6 spins (A) spin 5, the nitrogen ^{1}H removed (B), spin 4, the $C_{\alpha}^{(i-1)}$ ^{1}H removed (C) spin 6, the $C_{\alpha}^{(i)}$ ^{1}H removed (D). Magnetisation build up on $C_{\alpha}^{(i)}$ (red), magnetisation decay on $C_{CO}^{(i-1)}$ (black), magnetisation build up on $C_{\alpha}^{(i-1)}$ (blue).

3.3.3 Application of Bidirectional Transfer to Protein Backbone Assignment

In the context of a 2D-NcoCA experiment, the presence of the coupling from the $C_{CO}^{(i-1)}$ to the $C_{\alpha}^{(i)}$ and $C_{\alpha}^{(i-1)}$ sites allow nitrogens in the peptide backbone to be simultaneously correlated to the (i) and (i-1) residues in a single experiment. The presence of additional peaks in the NCOCA spectrum has previously been observed when employing broadbanded homonuclear recoupling sequence such as PDSD and in such instances

viewed unfavourably as it can lead to increased spectral crowding.[162] This spectral crowding can in part be overcome through the acquisition of 3D-NCOCA spectra (Figure 7.2). Importantly though, the MIRROR transfer results in systematic and efficient transfer from the $C_{CO}^{(i-1)}$ to $C_{\alpha}^{(i)}$ and $C_{\alpha}^{(i-1)}$ sites with little/no coupling to other sites. This simplifies the analysis of the data as the resulting C_{α} strip plots contain only two resonances, the stronger showing the correlation between $N^{(i)}$ and $C_{\alpha}^{(i-1)}$ and the weaker that between $N^{(i)}$ and $C_{\alpha}^{(i)}$ (Figure 7.2). This facilitates the assignment process as all the connectivities necessary for a backbone assignment are present in a single data set. For those familiar with solution NMR protein backbone assignments, the resulting spectrum can be thought of as analogous to the liquid state HNCA,[164-166] albeit with an inversion of the relative intensities of the C_{α} resonances of the current and preceding amino acid. The spectra can therefore be interpreted in a similar manner to solution-state HNCA data, 'walking' through the C_{α} slices to sequentially assign the protein backbone.

When incorporated into a low-power scheme, the low rf-amplitudes employed for MIRROR recoupling offer significant advantages for the analysis of protein samples, since rf-induced sample heating is greatly limited. The use of weak rf-fields permits a reduction in recycle delay, whose minimum value is normally limited by the duty cycle of the probe/spectrometer under high-power conditions. Furthermore, MIRROR recoupling and the assignment scheme highlighted above is compatible with the low-power decoupling and CP schemes[57, 156, 167] and paramagnetic assisted condensed data collection schemes (PACC)[168-169].

To demonstrate the potential savings in acquisition time we have incorporated the MIRROR recoupling into an NCOCA experiment where all polarisation transfer and decoupling steps have been replaced by low-power equivalents (Figure 3.12), allowing the recycle time to be reduced from 2.5 s to that which is optimal for the T_1 of the sample (700 ms). During all evolution times, SPINAL decoupling[46] was replaced by low-power TPPM[156], allowing a reduction of ^{1}H rf-amplitudes from 135 kHz to 8.75 kHz. Low-power CP conditions can also be identified by arraying both ^{1}H and ^{15}N field strengths during the CP period to locate a suitable low-power condition, with efficient transfer from ^{1}H to ^{15}N achieved using double quantum CP at the $n = 2$ condition,[170-172] with a ^{1}H spin-lock field of 62 kHz and a ^{15}N of 8 kHz, whilst optimal transfer from ^{15}N to ^{13}C obtained at the $n = 1$ double quantum CP condition with a ^{13}C spin-lock field of 10 kHz and a ^{15}N field of 25 kHz (see Figure 3.10). A comparison of the peak intensities of these conditions with the high-power variants is given in Figure 3.11. As is apparent, the replacement of polarisation transfer steps with low-power equivalents has little effect on the overall resolution and sensitivity of the overall experiment, even at these moderate spinning frequencies. The only noticeable difference between the low-power and high-power variants is the absence of intensity between 38 and 42 ppm which we attribute to the sidechains of the acidic amino acids.

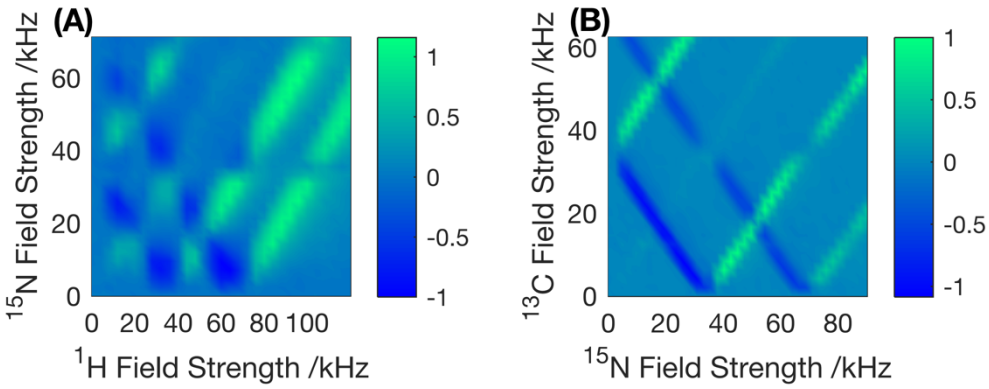

Figure 3.10 Experimental Hartmann-Hahn CP matching profiles. For the CP transfer from ^{1}H to ^{15}N at 35 kHz MAS (A), and the CP transfer from ^{15}N to $^{13}C_{CO}$ at 35 kHz MAS (B).

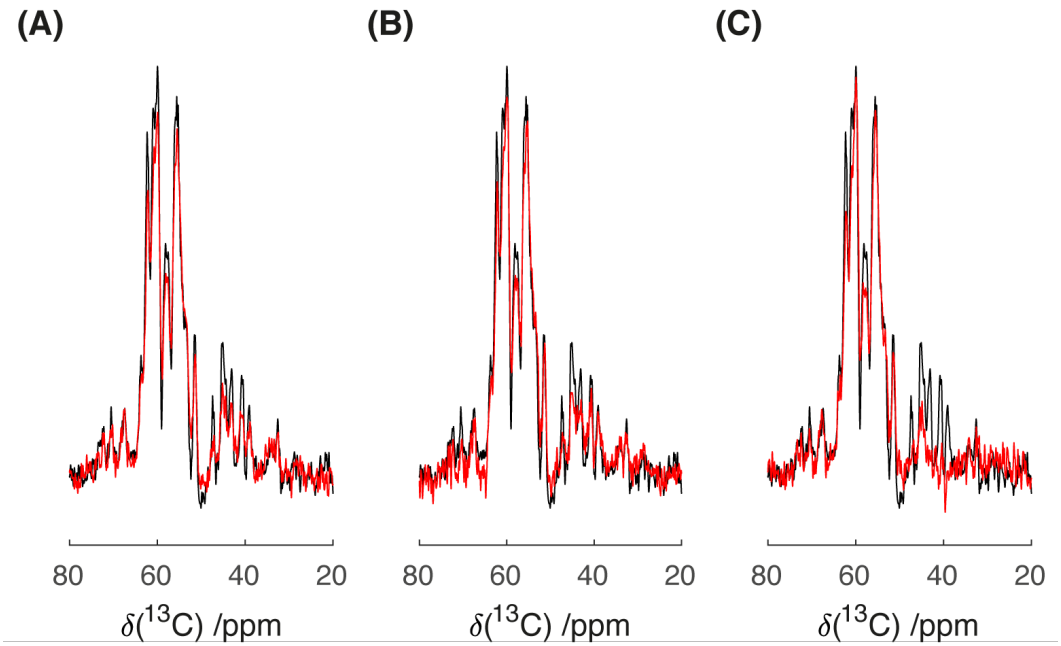

Figure 3.11 Efficiency of 'low-power' sequences. Comparison of transfer efficiency upon incorporating low-power decoupling and CP conditions. High-power NcoCA (black, A/B/C), acquired with ^{1}H and ^{15}N spin lock fields of 122 and 87.5 kHz respectively during ^{1}H-^{15}N and ^{15}N and ^{13}C spin lock fields of 87.5 and 52.5 kHz respectively for ^{15}N-^{13}C CP. During acquisition 135 kHz SPINAL decoupling was applied. Effect of sequentially replacing high-power SPINAL decoupling with low-power TPPM (8.75 kHz rf-field) (red, A), high-power ^{1}H-^{15}N CP with a low-power DQ-CP condition (red, B), and a low-power ^{13}C/^{15}N DQ-CP transfer (red, C). Data normalised to maximum intensity observed under high-power conditions.

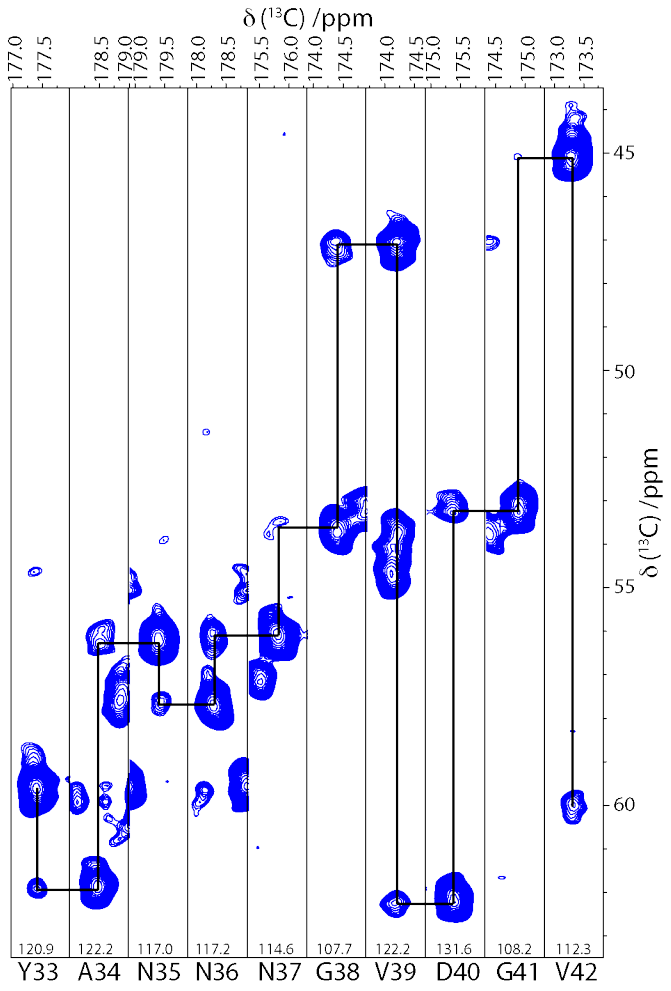

Figure 3.12 Strip plot of low-power 3D-NCOCA experiment for connectivities between residues Y33 to V42 with tracing through backbone. Chemical shift for each ^{15}N plane is given at the bottom of each slice. Large peaks in each nitrogen dimension are the $C_{CO}^{(i-1)}$ to $C_{\alpha}^{(i-1)}$, while the smaller peak is the $C_{CO}^{(i-1)}$ to $C_{\alpha}^{(i)}$ correlation.

The reduction in recycle time allowed a single 3D-NCOCA experiment, providing the complete backbone assignment of the 56-residue protein, GB3, to be performed in as little as 12.5 hours. This may be compared with 45 hours for the equivalent high-power experiment. A comparison of the data quality is shown in (Figure 7.2). Further time saving may be made through the use of paramagnetic dopants to accelerate T_1 relaxation, allowing a further reduction in recycle time.

3.4 Conclusion

In summary, we demonstrate that MIRROR recoupling enables the bidirectional transfer of magnetisation from the C_{CO} site to the adjacent C_{α}, and to the C_{α} of the next amino acid. In the context of a 3D-NCOCA experiment this doubles the information content providing correlations from $C_{CO}^{(i-1)}$ to both $C_{\alpha}^{(i-1)}$ and $C_{\alpha}^{(i)}$. The presence of these two correlations permits the sequential assignment of the protein backbone without the need for conducting multiple 3D experiments. Furthermore, the low rf-amplitudes required for the most efficient MIRROR recoupling conditions enable the construction of 'low-power' experiments facilitating further reductions in the data acquisition time.

Chapter 4: Paramagnetic Relaxation Agents for Room-Temperature and Cryogenic NMR

4.1 Introduction

Measurement at cryogenic temperatures is important in NMR. At cryogenic temperature, as a result of the Boltzmann distribution, sensitivity enhancements are achieved.[173] In addition, sensitivity enhancements due to a reduction in thermal noise at cryogenic temperatures are also observed. Furthermore, at cryogenic temperatures, dynamic nuclear polarisation (DNP) mechanisms become more favourable. One of the significant drawbacks of cryogenic temperatures for NMR is the long spin-lattice relaxation time, T_1, necessitating an increased inter-scan delay for thermal equilibrium to be re-established.[174] In addition, the freezing of molecular motions results in inhomogeneous line broadening of the spectra. The increased T_1 times can be reduced through the employment of suitable relaxation agents.

The focus of this chapter was to investigate how paramagnetic relaxation agents can be used to facilitate cryogenic NMR measurements. Initially, experiments focus on studying the relaxation of GB3, at room temperature, as dynamics at room temperature are indicative of broadening effects at cryogenic temperatures. Following this, a suitable relaxation agent for biological applications, for use at room and cryogenic temperatures will be investigated. Finally, the effect of cryogenic temperatures on the T_1 and spectral resolution will be explored.

4.1.1 Low-Temperature NMR

The sensitivity of any spectroscopic technique is determined by the difference in energy level population. This relationship is described by the Boltzmann equation:

$$\frac{N_{-1/2}}{N_{+1/2}} = \frac{g_{-1/2}}{g_{+1/2}} e^{(-\frac{\Delta E}{k_B T})} \quad \textbf{(4.1)}$$

Where N_{m_s} is the population of the energy level with spin quantum number m_s, g_{m_s} is the degeneracy of the energy level with spin quantum number m_s, ΔE is the difference in the energy levels with spin quantum numbers $m_s = +1/2$ and $m_s = -1/2$, k_B is the Boltzmann constant and T is the temperature in K. As ΔE is proportional to the magnetic

field strength, B_0, increasing B_0 will lead to an increase in the sensitivity. Decreasing the temperature can be used to the same effect (Figure 4.1). Unfortunately, at cryogenic temperatures, due to the lack of motion in the system, inhomogeneous line broadening is observed. This inherent broadening at cryogenic temperatures limits the spectral resolution that can be achieved as inhomogeneous broadening cannot be averaged with MAS.

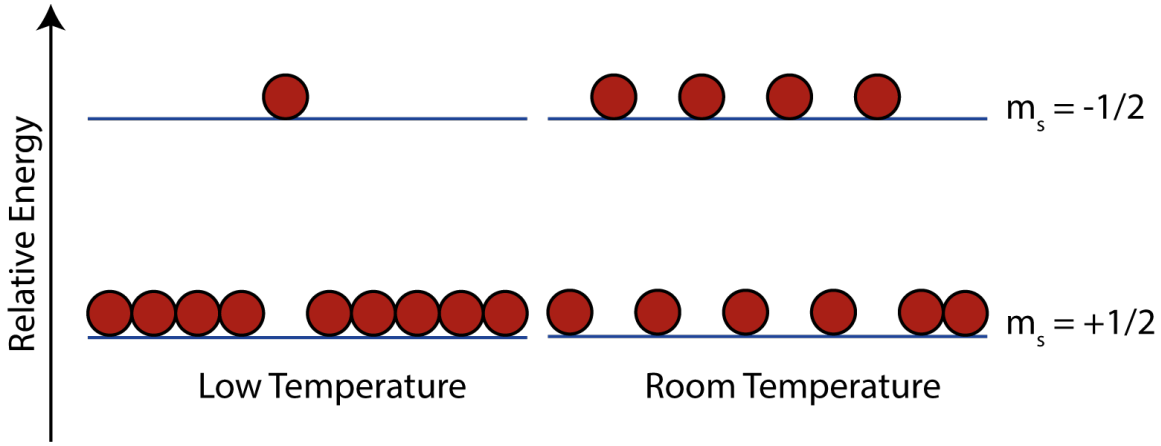

Figure 4.1 Illustration of the effect of temperature on energy level population between the $m_s = +1/2$ and $m_s = -1/2$ states present in spin $1/2$ nuclei, observed at low-temperature and room temperature. This increase in population difference is responsible for the observed sensitivity enhancements at cryogenic temperature.

Several methods have been developed to enhance the level of nuclear spin polarisation, such as DNP, and the utilization of the properties of the para spin isomer of hydrogen.[175-177] Polarisation enhancements through low-temperature were coined the 'brute force' approach in a review on nuclear orientation by Roberts and Dabbs.[178] Recent developments in the field have been made by Tycko *et al.* In which they use a custom-made probe that allows magic angle spinning at 25 K achieving sensitivity enhancements that follow a $1/T$ dependence between 25 and 79 K.[179] It has been hypothesised that, by doping a sample with a suitable paramagnetic relaxation agent, the T_1 at low-temperature can be reduced, enabling massive sensitivity enhancements within a reasonable time frame to be realised.[174] Chelates of specific lanthanide ions have shown promise at functioning as relaxation agents at low-temperature. For a paramagnetic species to be an effective paramagnetic relaxation agent the electron spin relaxation time must be approximately equal to the inverse of the nuclear Larmor frequency, which is generally of the order of 10^{-9} s, with the maximum relaxivity occurring when this condition is fulfilled.[180] The electron spin relaxation time varies for different species and is dependent on temperature, where a reduction in temperature causes an increase in electron spin relaxation time. Therefore, a

particular relaxation agent may function well at a certain temperature while another relaxation agent does not and vice versa. At room temperature complexes of gadolinium have proven effective relaxation agents. Due both to the condition in which the electron relaxation rate is close to the nuclear Larmor frequency and to the large magnitude of the isotropic tensor component of the electron g-factor owed to its seven unpaired electrons. An isotropic g-factor is important so not to cause pseudo-contact shifts (PCS).[181] Unlike gadolinium, holmium and dysprosium, don't function well at room temperature due to their comparatively fast electronic relaxation rate, with electron spin relaxation times on the order of 10^{-12} s at room temperature.[182] At cryogenic temperatures these electron relaxation times are on the order of 10^{-9} s, upon which they should work effectively as paramagnetic relaxation agents.[174, 183]

4.1.2 Correlation Times

Time-scales of random molecular motion are quantified with a correlation function $g(\tau)$. This function corresponds to the probability of there being a correlation between the molecular orientation with a defined external axis as a function of time. At an infinitesimally small interval (∂t) the molecular position will be comparable to the point defined by $t = 0$, but after an extended period this correlation will decrease, generally exponentially with time leading to the equation $g(\tau) = \exp\left(-\frac{t}{\tau_c}\right)$, with t the time in s and τ_c the correlation time in s. The correlation time for overall tumbling is found to be proportional to molecular weight and to have an inverse relationship with temperature. The correlation time of a macromolecule in solution, with a hydrodynamic radius given by R_h in m, with viscosity η, in Pa s. is given by $\tau_c \approx 4\pi R_h^3 \eta / 3kT$, with k representing the Boltzmann constant in J K^{-1}, and T the temperature in K. The correlation time can be thought of as the average time taken for rotation by 1 rad from the starting position to occur. For biomacromolecules in solution, the total rotational diffusion of the molecules results in all available orientations being sampled within a short space of time. Correlation times for the overall rotational diffusion is dependent on the size of the molecule though will lie between the picosecond to nanosecond range.[184] To get a feeling for timescales, solution-state NMR studies on GB1 determined correlation times for molecular motions present ranging from 0.8 to 5 ns.[185]

4.1.3 Dynamic Processes in Proteins

At room temperature, motion provides an efficient mechanism for relaxation. At low-temperature dynamics in the system is reduced. Though dynamics at cryogenic temperatures are limited, dynamics present at room temperatures are indicative of the broadening effects at low-temperature.[186] A high degree of dynamics results in broadening at low-temperature due to the greater number of confirmations possible. When motions are restricted at low-temperature, each conformation will be present, leading to inhomogeneous broadening. A vast array of methods have been developed that span a wide range of timescales to extract information on dynamical processes present in molecules (see Figure 4.2 on NMR time-scales and methods). Very slow processes, such as hydrogen exchange and protein denaturation which typically happen on a timescale where the correlation time, $\tau_c > 1$ s, can be followed through analysing the changes in a sequence of time-resolved spectra. Time-resolved 2D-spectra on the sub-second timescale have recently been developed to monitor dynamic processes on this timescale.[187-189] Slow dynamic processes on a timescale of $\tau_c < 1$ s, such as protein folding and hydrogen exchange can be observed through line-shape effects present in both liquids and solids in addition to 2D-exchange spectroscopy. Dynamic processes on a timescale between $1\ \mu s \leq \tau_c \leq 1$ ms, such as side-chain motions, cis-trans isomerisation and hydrogen-bond dynamics, can be revealed through rotating-frame relaxation measurements. Fast dynamic processes on a timescale between $10\ ps \leq \tau_c \leq 1$ µs, such as overall rotational tumbling, conformational transitions, and side-chain motions can be tracked through the employment of laboratory-frame relaxation measurements.[190] Very fast dynamic processes on a timescale of $\tau_c < 10$ ps, are known to scale relaxation parameters but NMR techniques cannot be used to measure motions on this timescale.[191] Dynamic processes which result in a change in the local chemical shift of the nuclei lead to line broadening effects, i.e. side chain motions, cis-trans isomerisation, hydrogen-bond dynamics.

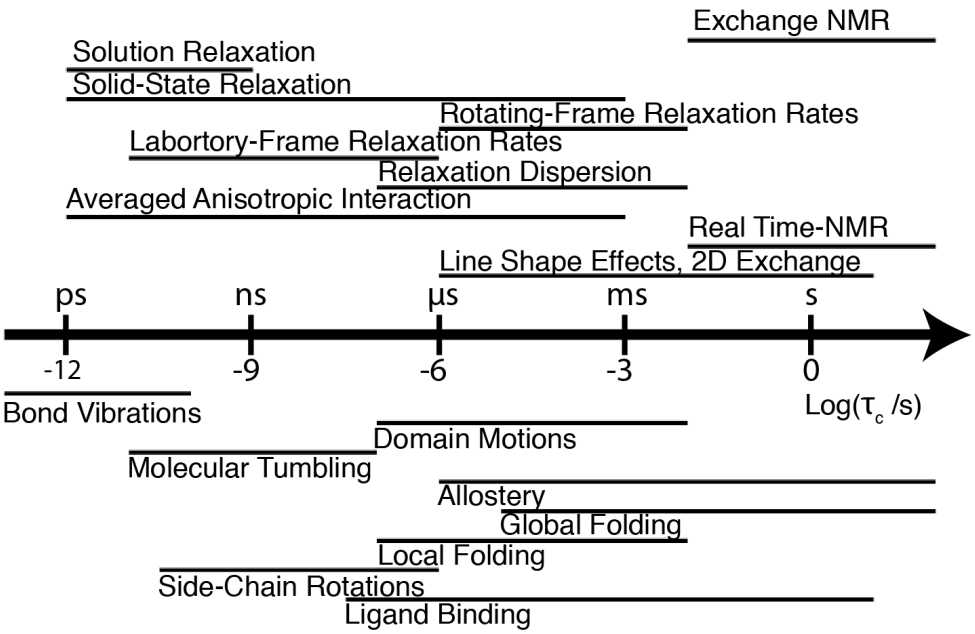

Figure 4.2 NMR time-scales of molecular motions and the NMR techniques available to observe each regime. Adapted from Lewandowski 2013.[190]

The factors effecting the dynamics of hydrated proteins under a reduction in temperature were outlined by Siemer *et al.* to be: 1) the formation of an ice or glass matrix by the bulk solvent. 2) The interaction of the solvent-accessible side-chains with the solvent molecules of the hydration shell. 3) Thermal motions of the protein independent of the solvent, such as librations, side-chain rotations and low-frequency breathing modes.[192] Proteins at low-temperatures have been described as caged by the immobilised solvent molecules. This is stated to occur under the protein glass transition temperature, T_g.[193] At temperatures below T_g the effect of the solvent is attenuated, with the solvent independent thermal motions dominating. At temperatures below T_g and above 100 K methyl group rotations are present,[194-195] with further reductions in temperature to as low as 90 K resulting in the dynamics of aromatic side-chains undergoing slow ring-flips.[194]

4.1.4 Origins of Line Broadening in ssNMR

In contrast to liquid-state NMR, in ssNMR the independency of coherent (reversible time evolution and sharp lines) and incoherent (irreversible time evolution and broad lines) processes is less well defined. There are two forms of spectral broadening: 1) Inhomogeneous broadening, which originates from the occupation of several conformers on measurement timescale. This form of broadening is characterised by a narrow diagonal in a correlation experiment, a T_2 relaxation time shorter than what would be expected based on the linewidth of the spectra and the ability to burn holes in the spectra (here we refer to T_2 relaxation as the decay of transverse magnetisation and should be distinguished from T_2', which is the decay of the transverse magnetisation during a spin echo). The effect of inhomogeneous broadening can be lessened through advancements in sample preparation techniques. 2) Homogenous broadening, which originates from an increase in the natural linewidth. This form of broadening is characterised by a broad diagonal in a correlation experiment, a T_2 in alignment with what would be expected based on the linewidth of the spectra and the inability to burn holes in the spectra. Homogenous line broadening represents a fundamental restriction[24] (See Figure 4.3 for illustration of the two types of broadening). Homogeneously broadened lines, which result from a coherent Hamiltonian (such as a homonuclear dipolar coupling), an appropriate manipulation of the spin through a sequence of rf-pulses can be effectively refocused, known as a magic echo. However, if the line broadening is the result of relaxation processes caused by stochastic motional averaging, then it is not feasible to refocus the spins through a manipulation of the Hamiltonian. It is, therefore, necessary to distinguish between line broadening originating from incoherent relaxation processes and line broadening originating from coherent evolution. In contrast to homogeneously broadened lines, inhomogeneously broadened lines are built up of a large number of separate narrow lines, significantly narrower than the resulting line shape. It is possible to use rf-pulses to manipulate the broadening resulting from inhomogeneous effects, and the evolution of inhomogeneous effects can be refocused by particular refocusing pulse sequences. Inhomogeneous lines are caused by a dispersion of isotropic interactions, such as the chemical shift or J-couplings or by residual powder patterns caused by anisotropic interactions.[196]

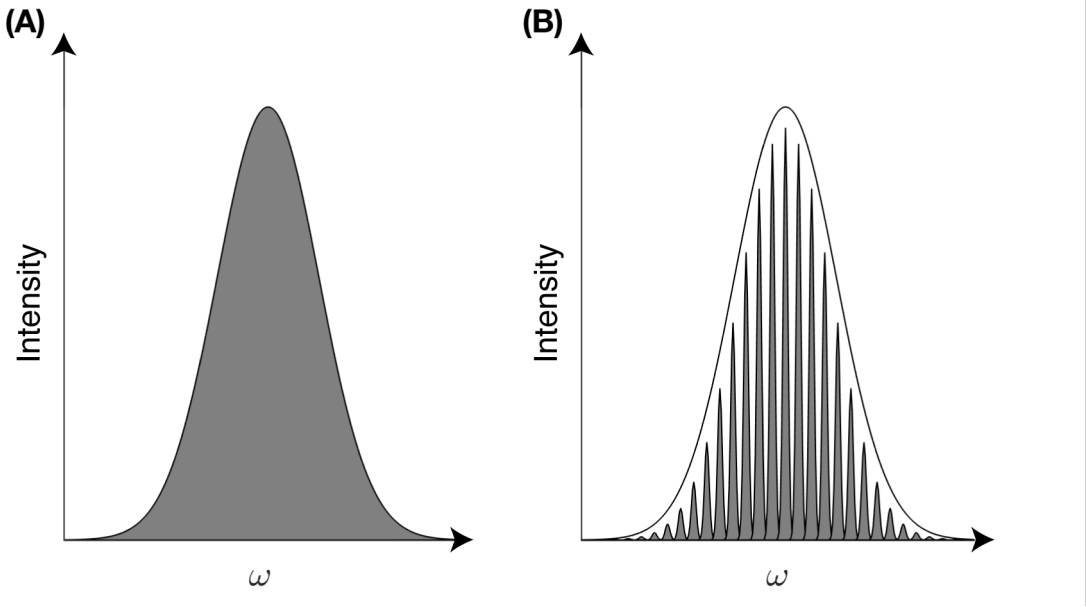

Figure 4.3 Illustration of homogeneous broadening (A) Vs inhomogeneous broadening (B). Where ω is the frequency of the NMR resonance.

4.1.5 Measuring Relaxation

In ssNMR, one may measure: 1) the spin–lattice relaxation time/rate constant (T_1/R_1), also known as longitudinal relaxation. 2) The spin–spin relaxation time constant (T_2/R_2), also known as transverse relaxation. 3) The spin–lattice relaxation time constant in the rotating frame ($T_{1\rho}/R_{1\rho}$). The theory of these relaxation processes is well documented in the literature.[197-204] Considerable care must be taken when interpreting the experimental relaxation constants determined. Typically, the measurement of T_1 constants is the most common and arguably the most useful. Within a complex system, the T_1 constants for specific sites are not necessarily unique. For a homonuclear spin system, with strong homonuclear coupling and minimal chemical shift variation between sites, the system can be approximated to contain degenerate transitions, exhibiting mono-exponential decay under the presumption that the homonuclear dipolar coupling is the dominant means of relaxation. In such a case, one will observe a uniform relaxation time for each spin regardless of the varying environments. For the case of a heteronuclear system, the scenario is complicated accordingly. Under static or low spinning speed conditions, decoupling of the protons is not possible and a multi-exponential decay is to be expected if the relaxation is to proceed mainly through heteronuclear dipolar coupling. In such a situation, separate resonances will decay at a different rate, and in addition to the direct

relaxation via stochastic modulation, spin diffusion will also be present, enabling an effective means to shuttle polarisation between spin sites under the condition the system is not in equilibrium. The process participating in the rate-limiting step will dictate which process will dominate relaxation.

The process of spin diffusion may be reduced to a degree by disruption of the system, through a reduction in the couplings between proton spins.[67, 205-206] Firstly, one means of reduction is the employment of high-speed MAS, due to the zeroth-order average Hamiltonian being minimised, in addition to the first-order average Hamiltonian exhibiting inverse proportionality with the spinning speed.[207] Any relaxation rate determined below the spin diffusion limit is a function of the spinning speed. The point at which a sample of the spectral-density is acquired will also be dependent on spinning speed, in the same way that rotating-frame relaxation measurements are also modulated by the spinning speed.[208] Secondly, an additional means of spin diffusion suppression is by the employment of a spin-lock field to restrict the average magnetisation along an effective field at the magic angle. Homonuclear dipolar coupling of zeroth order can be minimised through this means, though higher-order terms will be unaffected and a reduced rate of spin diffusion will still be present.[198-199] The application of a spin-lock field will also result in a modulation of the relaxation behaviour observed, leading to a superposition of spin-lattice and spin-spin relaxation rates in addition to altering the frequencies at which samples of the spectral-density function are taken. Thirdly, a combination of rotating-frame and laboratory-frame spin diffusion can result in an echo upon which the effective spin diffusion is averaged out. This method results in the extracted relaxation rate being a time average of the spin-lattice and spin-spin relaxation rates.[209]

Of the three methods of spin diffusion suppression, high-speed MAS is in general considered to be the best choice when measuring the spin-lattice relaxation rate, due to its greater reduction in spin diffusion, up to first-order terms, and the minimal impact on observed relaxation behaviour. When comparing relaxation at different spinning speed regimes, the influence on the modified sampling frequencies of the spectral density function must be disentangled from that of spin diffusion.[209] This is important in consideration that the overwhelming majority of cryogenic NMR and DNP experiments are performed in the low spinning speed regime.

The measurement of spin-spin relaxation rates is greatly complicated due to the presence of large coherent line broadening caused by heteronuclear and homonuclear dipolar couplings. In a similar manner to R_1 measurements, high-speed MAS will reduce the effect

of homonuclear and heteronuclear dipolar couplings on R_2 measurements but the couplings cannot be entirely removed. According to first-order average Hamiltonian theory, a scaled dipolar coupling persists, which results in a line broadening effect in addition to the relaxation. Echo sequences have been designed to refocus this coherent broadening though one must be meticulous to ensure that the residual decay is solely due to incoherent relaxation. For dilute heteronuclear spins, strong coupling to an abundant nucleus also results in this coherent broadening, though in contrast, the application of high-power heteronuclear decoupling can suppress the remaining coherent line broadening components significantly. Any remaining linewidth can then be attributed to remaining coupling to protons or chemical shift inhomogeneities present in the sample. The employment of a succession of π-pulses for echo formation can be used to refocus these contributions due to their linear nature. Complications from strong ^{1}H-^{1}H interactions, which result in an increased decay of the detected magnetisation which cannot be refocused, can be restricted by a reduction in the time between π-pulses. When considering the practicality of such R_2 measurements, for such decoupling, high-power is required which may not be possible for extended periods of time on current ssNMR probes.

The measurement of the spin–lattice relaxation time constant in the rotating frame, $R_{1\rho}$, pose similar difficulties as those experienced with the measurement of R_1 and R_2. The decay resulting from residual dipolar coupling must be suppressed and care should be taken to ensure that the effect of spin-diffusion is minimal.[210]

Due to the blurred line between coherent and incoherent effects in the solid-state, the analysis of ssNMR relaxation data is considerably more difficult than the liquid-state counterpart. One must ensure that the relaxation being observed originates from incoherent relaxation processes and are not the result of the coherent evolution of the density operator under dipolar terms of the Hamiltonian, or a superposition of the two. Once one has acquired reliable data that can be attributed to incoherent relaxation processes the next step is the interpretation of the data using an appropriate physical model to extract and decipher information on the dynamics of the system.[211-212]

4.1.6 Relaxation Enhancement in the Solid-State

An understanding of how relaxation enhancement through paramagnetic doping occurs in the solid-state is necessary for selecting a suitable relaxation agent that selectively reduces

T_1 without reducing T_2. The T_1 and T_2 relaxation times of a nucleus are reduced by a paramagnetic species due to the paramagnetic relaxation enhancements (PRE) that the paramagnetic species confers. This PRE is due to the fluctuating magnetic field that the nucleus experiences, as a result of the paramagnetic species.[213] In the specific case of biomolecules in the solid-state where molecular tumbling and chemical exchange can be considered negligible Solomon dipolar relaxation is the predominant mechanism for causing PRE. Solomon dipolar relaxation encompasses relaxation due to a modulation of the electron spin-lattice relaxation.[213]

From the Solomon–Bloembergen equations longitudinal and transverse relaxation enhancements are given to be:[180, 214-215]

$$\Gamma_1 \approx \frac{2}{15}\left(\frac{\mu_0}{4\pi}\right)^2 \frac{\gamma_I^2 g_e^2 \beta_e^2 S(S+1)}{r^6}\left(\frac{3\tau_c}{1+\omega_I^2\tau_c^2}+\frac{7\tau_c}{1+\omega_e^2\tau_c^2}\right) \quad \textbf{(4.2)}$$

$$\Gamma_2 \approx \Gamma_{1\rho} \approx \frac{1}{15}\left(\frac{\mu_0}{4\pi}\right)^2 \frac{\gamma_I^2 g_e^2 \beta_e^2 S(S+1)}{r^6}\left(4\tau_c+\frac{3\tau_c}{1+\omega_I^2\tau_c^2}+\frac{13\tau_c}{1+\omega_e^2\tau_c^2}\right) \quad \textbf{(4.3)}$$

Where Γ_1 and Γ_2 are the corresponding longitudinal and transverse relaxation enhancements respectively. Defined as the relaxation rate of a species with PRE present minus the relaxation rate of a species without PRE present. γ_I and γ_e are the nuclear and electron gyromagnetic ratios respectively. ω_I and ω_e are the nuclear and electron Larmor frequencies, respectively. β_e is the Bohr magneton, g_e is the free electron g-value, τ_c is the correlation time for the electron spin-lattice relaxation, S is the spin angular momentum operator representing the electron spin and r is the electron-nuclear distance respectively. One may plot the enhancement as a function of distance (Figure 4.4) for both T_1 and T_2 PRE effects. It is observed that a species with a slow electron relaxation rate (TEMPO) causes T_2 relaxation from a longer electron nuclear distance, whereas a species with a fast electron relaxation rate (gadolinium) causes T_1 relaxation from a longer distance. Therefore, such species can be considered to act as T_2 and T_1 relaxation agents respectively. A species with a significantly faster electron relaxation rate, several orders of magnitude faster, e.g. holmium, under Solomon dipolar relaxation is predicted to cause negligible relaxation except only when the paramagnetic species and the nuclei in question are very close in proximity.

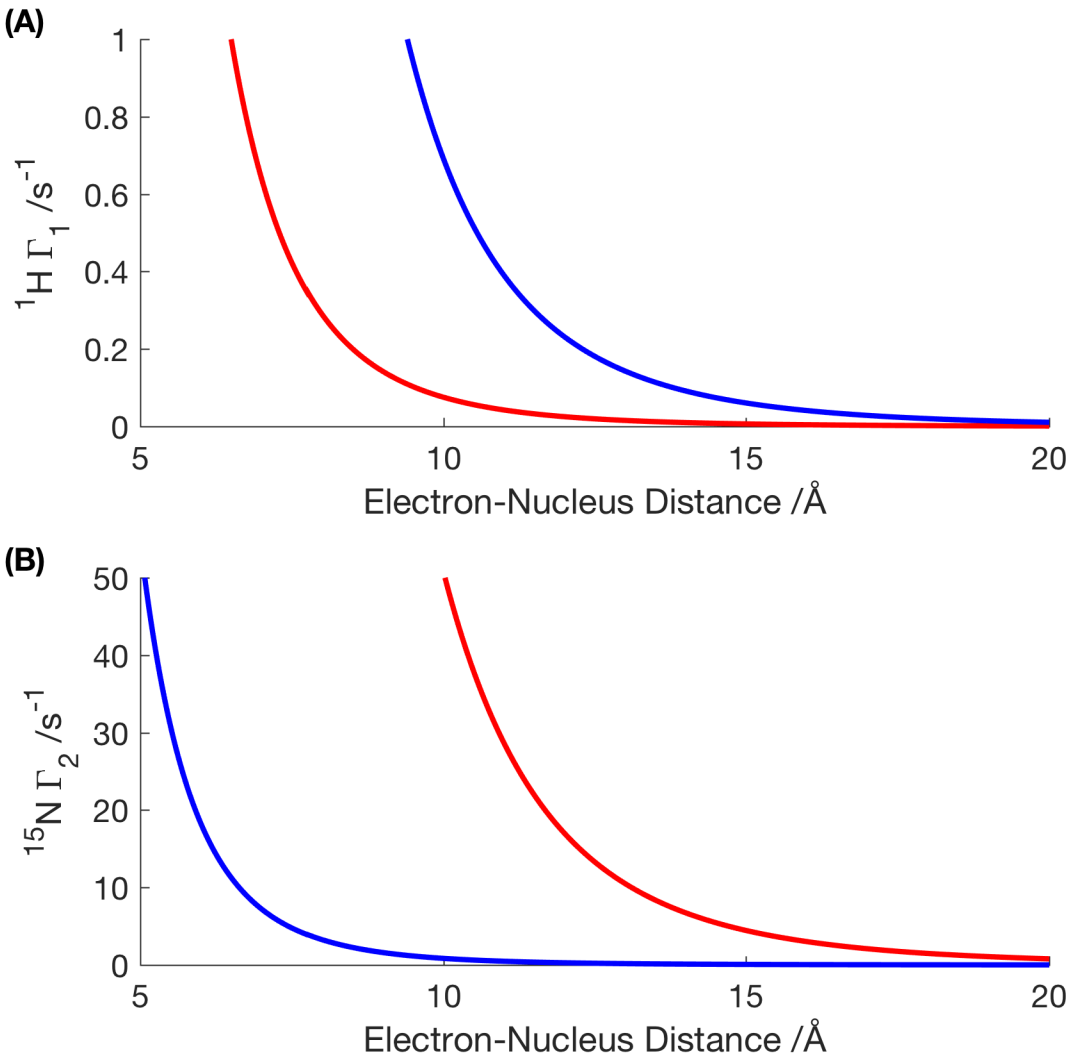

Figure 4.4 Dipolar contributions to the relaxation rate. ^{1}H longitudinal nuclear spin relaxation rate (A) and dipolar contributions to the ^{15}N transverse nuclear spin relaxation rate (B), due to the presence of TEMPO (red line) and Gd^{3+} (blue line) paramagnetic centers, with correlation time, τ_c for the electron spin-lattice relaxation of 100 x 10^{-9} s and 1 x 10^{-9} s respectively ($S = 1/2$ for both species).[213, 216-217] Calculated as a function of the electron–nucleus distance using the Solomon–Bloembergen equations.[180, 214-215]

4.2 Materials and Methods

4.2.1 Room-Temperature NMR Measurements

1D saturation recovery (Figure 4.5B) and spin echo experiments (Figure 4.5D) were performed with ^{15}N enriched GB3 to determine T_1 and T_2. Experiments were performed at 14.1 T on a Bruker Avance-2 600 MHz spectrometer equipped with a 2.5 mm TR-MAS probe at 10 kHz spinning. Microcrystalline GB3 (~10 mg) was prepared by adding hexylene glycol to ~30 mg/mL GB3 in pH 6.5 25 mM bis-tris and left for 1-2 days to form crystals. Crystals were transferred into a 2.5 mm rotor (Bruker) with the aid of centrifugation. For ^{1}H-^{15}N CP the carrier frequencies were set to the centre of the ^{1}H (~5 ppm) and ^{15}N (~120 ppm) spectra. Saturation recovery and spin echo experiments were recorded with 256 scans. Saturation recovery experiments were recorded with τ_1 delays of increments 0.001, 0.01, 0.025, 0.05, 0.1, 0.2, 0.4, 0.8, 1.2, 1.6, 2, 3, 4, 5, 10, 15 s. Spin echo experiments were recorded with τ_1 delays of increments 0.2, 2, 4, 6, 8, 10, 12, 14, 16, 18, 20, 22, 24, 26, 28, 30, 32, 34, 36, 38, 40 ms. Saturation recovery and spin echo experiments were analysed and integrated using matNMR[218]. All spectra were externally referenced to the downfield ^{13}C resonance of adamantane at 40.48 ppm compared to DSS.[157] During all evolution periods 135 kHz SPINAL-64 decoupling[46] was applied with phase flip angles of 10° and 5°. All $\pi/2$ pulses on ^{1}H and ^{15}N were set to at 2.5, and 3.0 µs respectively.

Unless otherwise stated all other measurements were conducted at 14.1 T on an Agilent DD2 600 MHz NMR spectrometer (Yarnton, UK) equipped with a 1.6 mm triple resonance magic-angle spinning probe. Microcrystalline ^{13}C/^{15}N enriched GB3 (~5 mg) was transferred into a 1.6 mm rotor (Agilent) with the aid of centrifugation. Samples were spun at 35 kHz, and the temperature regulated at 283 K. For ^{1}H-^{15}N CP the carrier frequencies were set to the centre of the ^{1}H (~5 ppm) and ^{15}N (~120 ppm) spectra. Optimal ^{1}H-^{15}N CP was obtained with a 1.5 ms contact pulse with a ^{1}H field of ~105 kHz and a ^{15}N field of ~70 kHz. For ^{15}N-^{13}C CP the ^{15}N carrier frequency was set to the middle of the amide region (120 ppm) and the ^{13}C to the centre of the C_α region (~55 ppm). The spin-lock fields were set to 5/2 times the spinning speed, 87.5 kHz, for ^{15}N and 3/2 times the spinning speed, 52.5 kHz, for ^{13}C. Maximal transfer was observed after 7 ms CP. During ^{15}N-^{13}C CP, 135 kHz continuous wave proton decoupling was applied. During all evolution periods 135 kHz SPINAL proton decoupling was applied with phase flip angles of 10° and 5°. All $\pi/2$ pulses on ^{1}H, ^{13}C and ^{15}N were set to at 2.4, 3.2, and 3.1 µs respectively.

All 2D experiments were acquired with States-TPPI phase sensitive detection, employing a ^{15}N spectral width of 5 kHz and 64 complex points. All spectra were externally referenced to the downfield resonance of adamantane at 40.48 ppm compared to DSS.[157] Multidimensional data sets were processed in NMRPipe[158], prior to analysis and assignment in CCPN Analysis 2.4[159-160]. For the ^{13}C dimension the data was processed with a Lorentz-to-Gauss window function, with an inverse exponential width of 10 Hz and a Gaussian broadened width of 40 Hz. For the indirect ^{15}N dimension the data was processed with a Lorentz-to-Gauss window function, with inverse exponential width of 20 Hz and a Gaussian broadened width of 40 Hz.

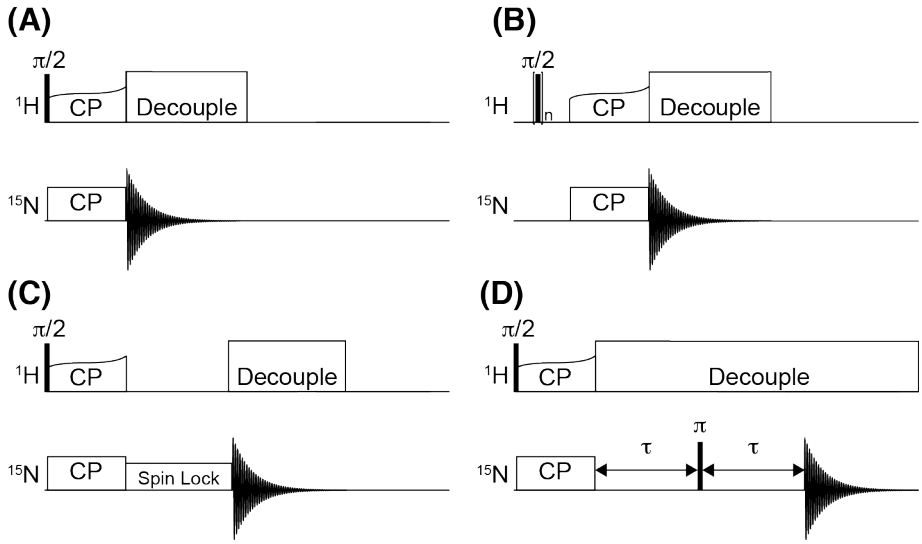

Figure 4.5 1D-pulse sequences used for relaxation studies. ^{1}H to ^{15}N CP (A), saturation recovery for the determination of ^{1}H T_1 (B), spin-lock for the determination of ^{15}N $T_{1\rho}$ (C), spin echo for the determination of ^{15}N T_2 (D).

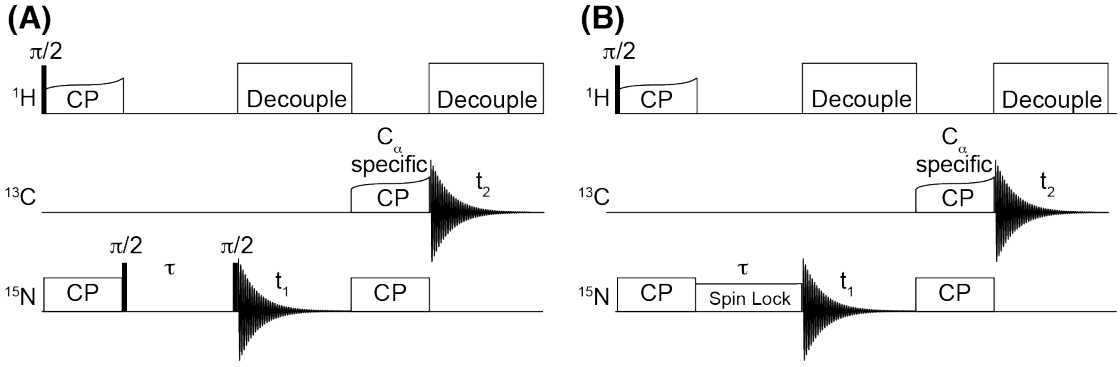

Figure 4.6 2D-pulse sequences for determination of site-specific ^{15}N T_1 (A), and ^{15}N $T_{1\rho}$ (B).

4.2.2 Low-Temperature NMR Measurements

Low-temperature NMR measurements were conducted at Goethe University Frankfurt, in the laboratory of Professor Clemens Glaubitz. ^{13}C detected experiments were performed on uniformly labelled [U-^{13}C,^{15}N]GB3 microcrystalline samples (~15 mg), prepared by adding hexylene glycol to ~30 mg/mL GB3 in pH 6.5 25 mM bis-tris and left for 1-2 days to form crystals. Samples were spun down and the supernatant removed and 100 μL of 7:3 gylcerol-d_8/D_2O added and allowed to soak overnight.

All MAS experiments were performed on a Bruker 400 DNP system consisting of a 400 MHz WB Avance II NMR spectrometer and a 3.2 mm HCN Cryo MAS probe. All experiments were performed with 8 kHz MAS. ^{13}C CP experiments were recorded using ramped CP from ^{1}H to ^{13}C during 0.6 ms. Saturation recovery experiments were recorded with 8 scans. Saturation recovery experiments were recorded with τ_1 delays of increments 0.01, 0.1, 0.2, 0.5, 0.7, 1, 1.5, 2, 3, 4, 5, 7, 10, 15, 20, 50 s. Saturation recovery experiments were analysed and integrated using TOPSPIN 3.5 (Bruker) and matNMR[218]. All spectra were externally referenced to the downfield ^{13}C resonance of adamantane at 40.48 ppm compared to DSS.[157] SPINAL-64 decoupling[46] at 100 kHz was employed for all experiments during acquisition.

4.3 Results and Discussion

4.3.1 Site-Specific Relaxation Studies

4.3.1.1 Site-Specific ^{15}N R_1 Relaxation Studies

R_1 measurements probe motions on the order of 1 ps to 1 ns, with such motions including bond vibrations and side-chain rotations. For WT-GB3, the average of the site-specific ^{15}N R_1 is 0.05 s^{-1} (T_1 of 20 s). Through analysis of the ^{15}N R_1 rate constants for the [U-^{13}C,^{15}N]GB3 nitrogen backbone (and Figure 4.8) it is observed that some regions relax faster than others. Comparison with the structure indicates that rates arising from regions corresponding to residues with a high degree of secondary structure, i.e. in the α-helix and β-sheets, are significantly lower than more mobile regions. On approaching the ends of these regions and into the connecting loops, where the structure is less well defined, we observe an increase in R_1 suggesting that on the timescales at which R_1 measurements can probe, there is an increase in the amplitude of motions present. Worth noting is the fastest and slowing relaxation rate, which help to understand the range of motions present. Residue G41 shows the fastest relaxation, with a rate of 0.25 s^{-1} (T_1 of 4 s). The fast relaxation of G41 can be attributed to its location in the connecting loop where the structure is less well defined and a larger range of conformations are possible. In contrast, residue T55 shows the slowest relaxation with a rate of 0.011 s^{-1}(T_1 of 100 s). This is likely due to the residues location embedded in the interior of the protein where motions are restricted. Also noteworthy is W43, which is the sole tryptophan residue in GB3, and due to the indole ring, possess unique chemical shifts separated from that of other residues. This peak separation is useful when investigating linewidths at low-temperature. The R_1 relaxation of this residue is 0.025 s^{-1} (T_1 of 40 s). This relaxation rate is relatively slow and is explained by the location of the residue embedded in the core of the protein structure.

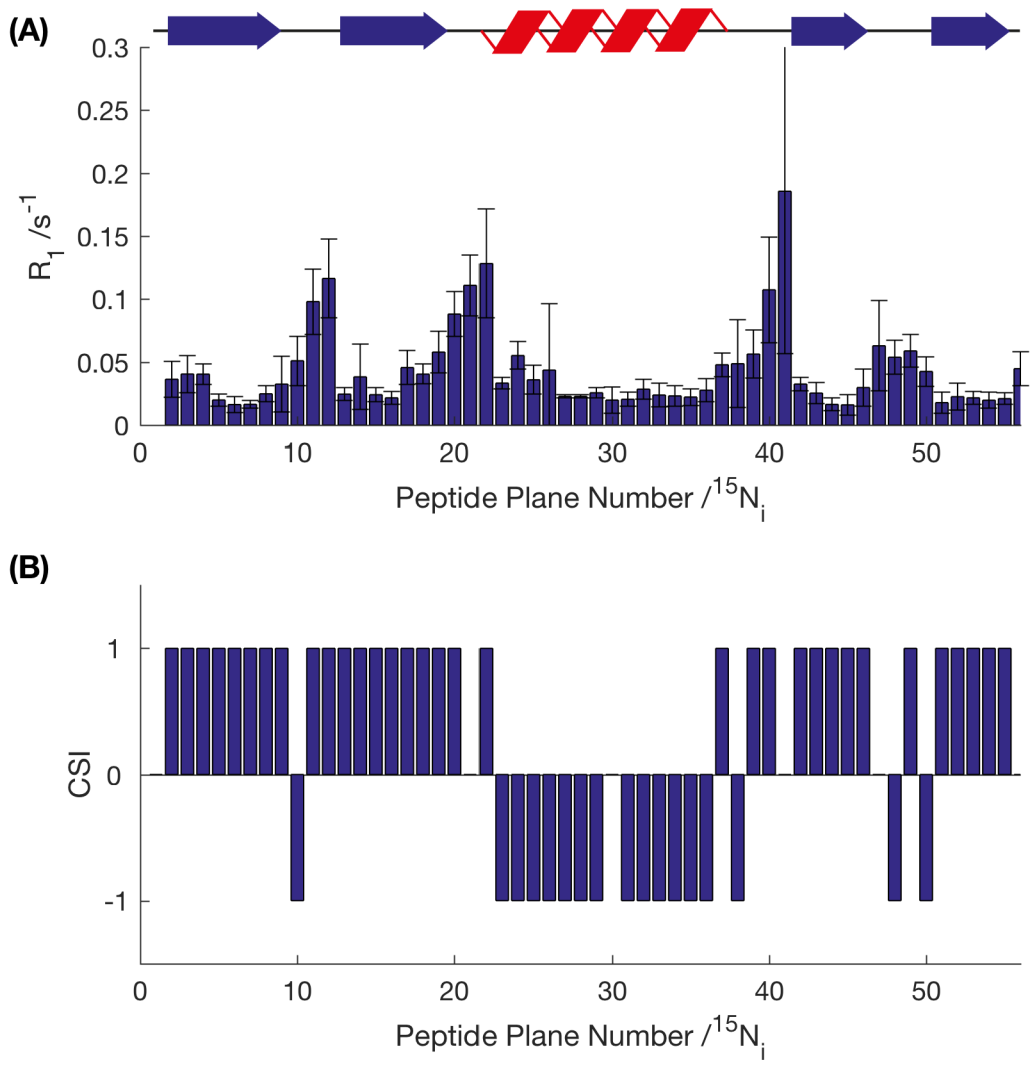

Figure 4.7 Site-specific ^{15}N R_1 of the [U-^{13}C,^{15}N] GB3 nitrogen backbone at 35 kHz MAS, 283 K. Figure displays the 15N R1 rate constants as a function of the peptide plane number of the backbone 15N atom (A). The chemical shift index (CSI) of GB3 from the ssNMR assignment of GB3 (B), for comparison of secondary structure to the relaxation rate. With a positive CSI representing a β-sheet secondary structure, and a negative CSI representing an α-helix secondary structure.

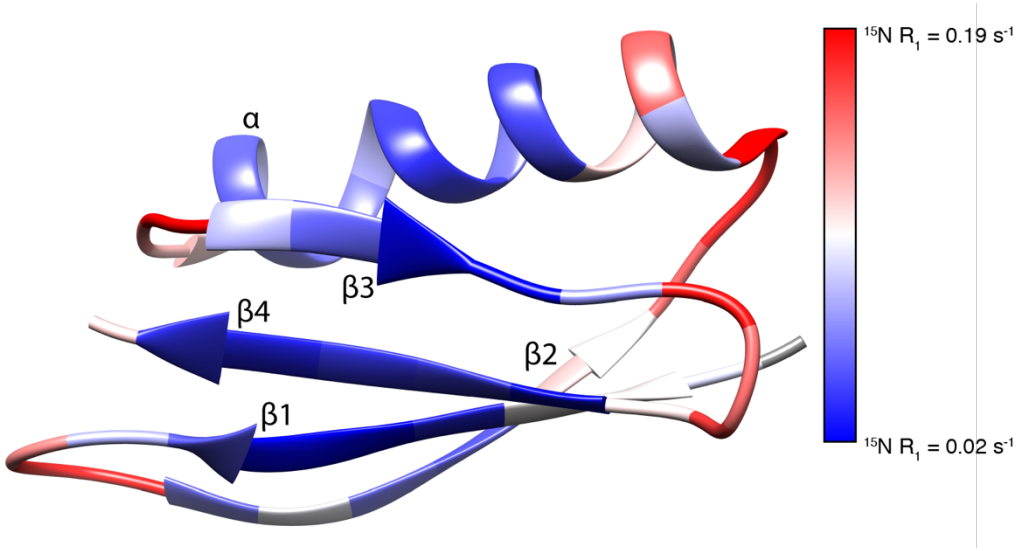

Figure 4.8 Site-specific ^{15}N R_1 for the [U-^{13}C,^{15}N]WT-GB3 nitrogen backbone, mapped to the structure of WT-GB3, where shades of red represent a fast relaxation rate, up to 0.19 s^{-1} and shades of blue represent a fast relaxation rate, down to 0.02 s^{-1}. Crystal structure PDB ID: 2LUM.

For the [U-^{13}C,^{15}N]A48C-GB3 nitrogen backbone, the average of the site-specific ^{15}N R_1 is 0.05 s^{-1} (T_1 of 20 s). The general relaxation profile is similar to that of WT-GB3, indicating the protein has not been greatly perturbed by the mutation (Figure 4.9 and Figure 4.10). However, there are some differences. Direct comparison of the relaxation rate indicates that a local perturbation close to the site of mutagenesis is present (Figure 4.11). Namely residues 48, 49, 40 and 41 have experienced a significant increase in relaxation, potentially as a result of a reduction in local stability. Interestingly, at the opposite end of the secondary structure (residues 20 and 21) to the site where the mutation is present a perturbation is also experienced. This suggests that the mobility of proteins is not only determined locally but mutations can affect dynamics at remote sites (Figure 4.11).

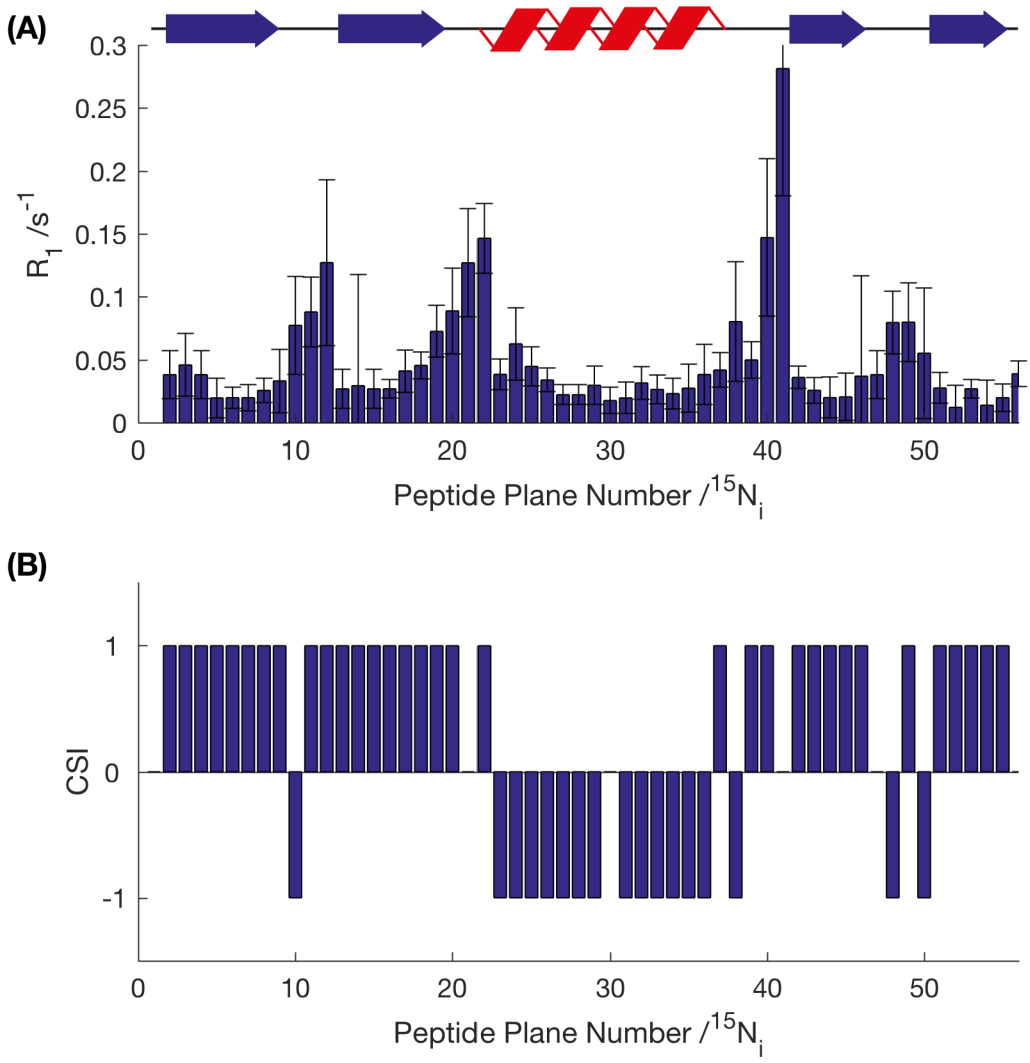

Figure 4.9 Site-specific ^{15}N R_1 of the [U-^{13}C,^{15}N]A48C-GB3 nitrogen backbone at 35 kHz MAS, 283 K. Figure displays the ^{15}N R_1 rate constants as a function of the peptide plane number of the backbone ^{15}N atom (A). The chemical shift index (CSI) of GB3 from the ssNMR assignment of GB3 (B), for comparison of secondary structure to the relaxation rate. With a positive CSI representing a β-sheet secondary structure, and a negative CSI representing an α-helix secondary structure.

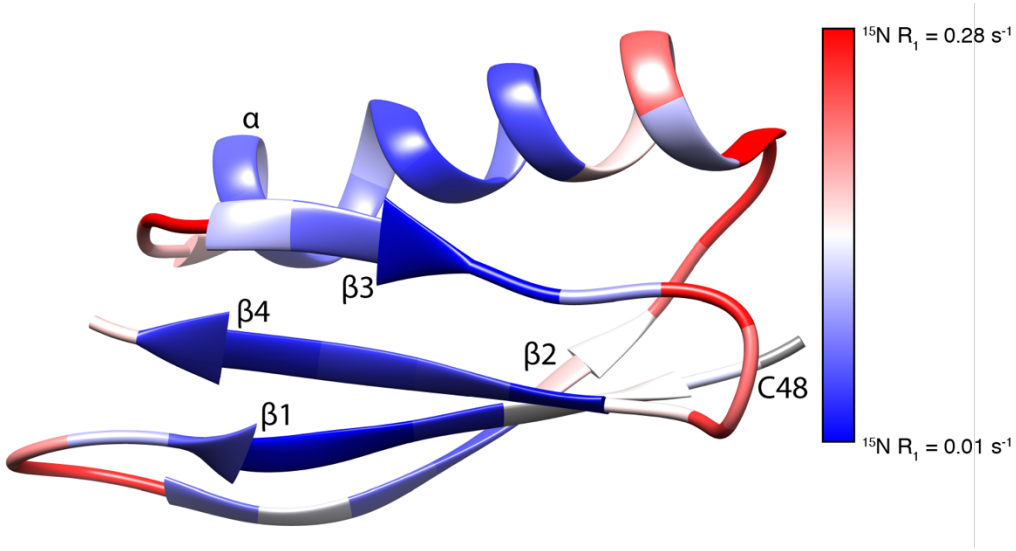

Figure 4.10 Site-specific ^{15}N R_1 rate constants for the [U-^{13}C,^{15}N]A48C-GB3 nitrogen backbone, mapped to the structure of A48C-GB3, where shades of red represent a fast relaxation rate, up to 0.28 s^{-1} and shades of blue represent a fast relaxation rate, down to 0.01 s^{-1}. Crystal structure PDB ID: 2LUM.

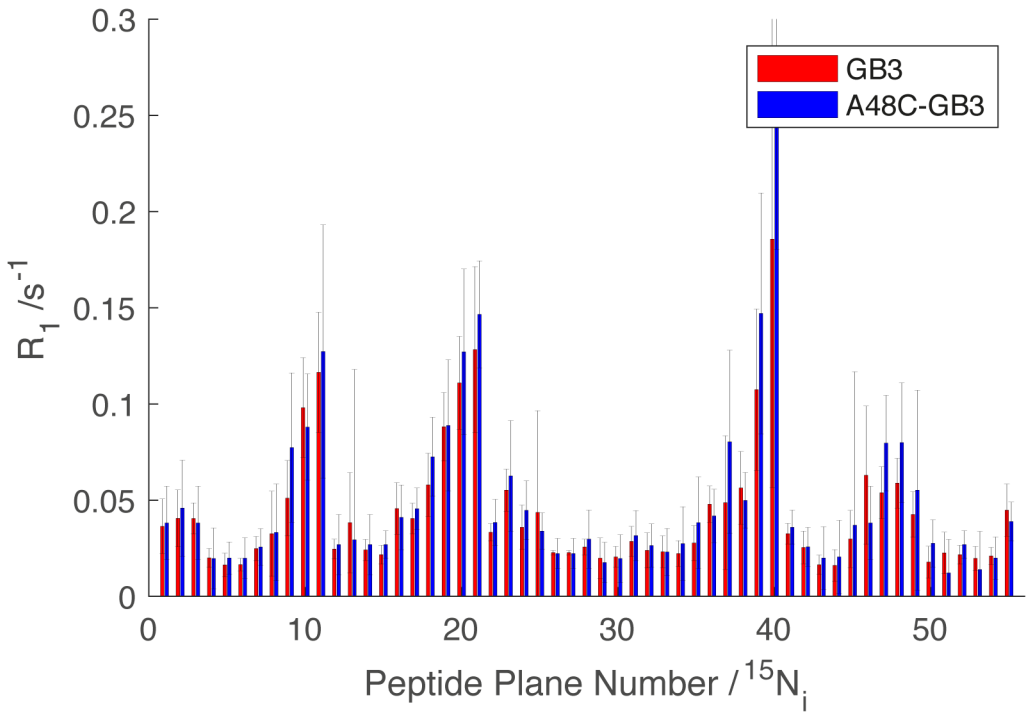

Figure 4.11 Comparison of ^{15}N R_1 rate constants for the [U-^{13}C,^{15}N]GB3 nitrogen backbone against the [U-^{13}C,^{15}N]A48C-GB3 nitrogen backbone.

4.3.1.2 Site-Specific ^{15}N $R_{1\rho}$ Relaxation Studies

$R_{1\rho}$ measurements can probe motions on the order of 1 ns to 1 ms, with such motions including local folding and global folding, in addition to domain motions. The average of the site-specific ^{15}N $R_{1\rho}$ is 2.5 s^{-1} ($T_{1\rho}$ of 0.4 s). Analysing the ^{15}N $R_{1\rho}$ rate constants for the [U-^{13}C,^{15}N]GB3 nitrogen backbone (Figure 4.12 and Figure 4.13) it is observed that there is some diversity in rates observed in certain regions. Through comparison to the structure, it is indicated that certain connecting loops possess enhanced relaxation rates in comparison to the bulk of the residues. This suggests that on the timescales at which $R_{1\rho}$ measurements can probe, there is an increase in the amplitude of motions present. Interestingly, in contrast to the R_1 measurements, $R_{1\rho}$ measurements seem to indicate less variation of motion on the timescale probed, with only a few loop regions exhibiting significantly greater relaxation rates than the α-helix and β-sheet regions. This is interesting as it highlights the differences in motions present in each region. With bond vibration, molecular tumbling and side-chain rotations high for all connecting loop regions but local folding restricted in some. However, due to the relatively low spinning speed regime at which the measurements were performed, the coherent contribution to the relaxation rates is still relatively high and ineffectively averaged. Therefore, the site-specific relaxation rates acquired are not indicative of the true relaxation rates of the amino acid residue but are an average.

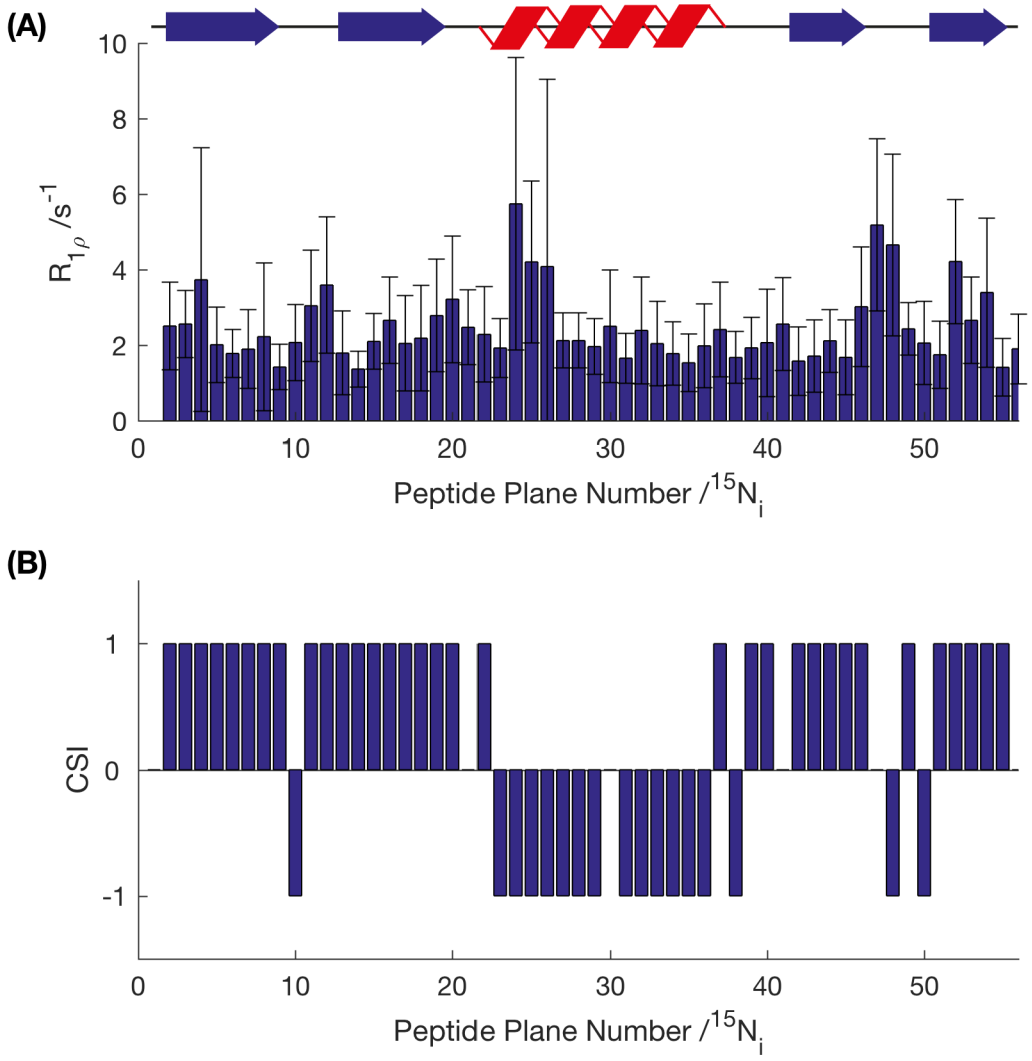

Figure 4.12 Site-specific ^{15}N $R_{1\rho}$ of undoped WT-GB3 with 20 kHz spin-lock field at 35 kHz MAS, 283 K. Figure displays the ^{15}N $R_{1\rho}$ rate constants as a function of the peptide plane number of the backbone ^{15}N atom (A). The below plot shows the CSI of GB3 (B) from the ssNMR assignment of GB3 for comparison of secondary structure to the relaxation rate, with a positive CSI representing a β-sheet secondary structure, and a negative CSI representing an α-helix secondary structure.

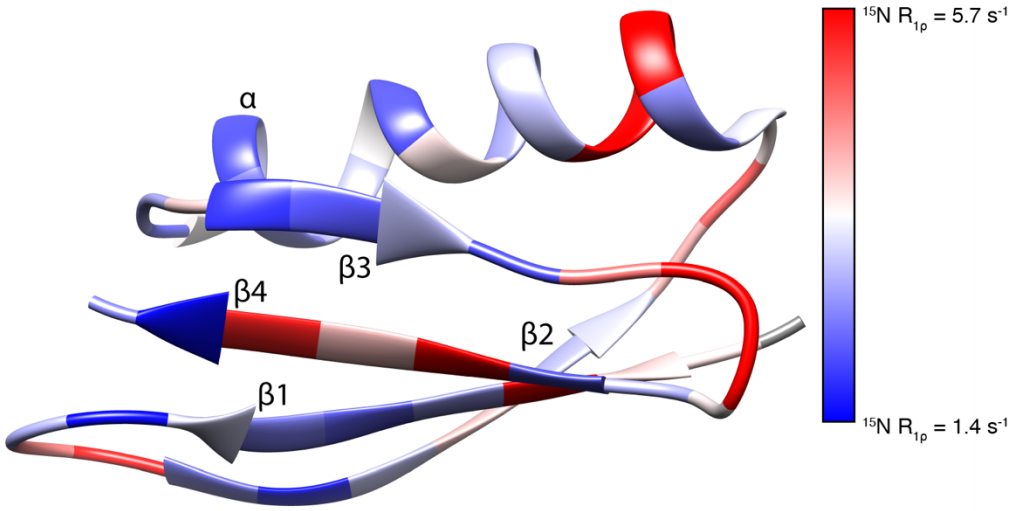

Figure 4.13 Site-specific ^{15}N $R_{1\rho}$ rate constants for the [U-^{13}C,^{15}N]WT-GB3 nitrogen backbone, mapped to the structure of WT-GB3, where shades of red represent a fast relaxation rate, up to 5.7 s^{-1} and shades of blue represent a fast relaxation rate, down to 1.4 s^{-1}. Crystal structure PDB ID: 2LUM.

4.3.1.3 Comparison to the Homologous Protein, GB1

Comparing the ^{15}N R_1 and the ^{15}N $R_{1\rho}$ rate constants for the [U-^{13}C,^{15}N]GB3 nitrogen backbone with that of the [U-^{13}C,^{15}N]GB1 nitrogen backbone collected by the Lewandowski group[219] it can be seen that the relaxation rate constants are of the same order and the general trend as for GB3. With higher relaxation rates observed for loop regions over β-sheets and α-helices (Figure 4.16 and Figure 4.17). The very rapid relaxation of G41, located in the loop region just before the fourth β-sheet present in GB3 is also observed for GB1. The average of the site-specific ^{15}N R_1 of GB3 is 0.05 s^{-1}, with the average of the site-specific ^{15}N R_1 of 0.04 s^{-1} determined for GB1 by the Lewandowski group.[219] The average of the site-specific ^{15}N $R_{1\rho}$ of GB3 is 2.5 s^{-1} with the average of the site-specific ^{15}N R_1 of 1.6 s^{-1} determined for GB1 by the Lewandowski group. Comparing the sequences of the two proteins (see Figure 4.14) it is observed that GB3 and GB1 are 89 % identical, varying only at residues 6, 7, 19, 24, 29, 42. For GB3: V6, I7, K19, E24, A29, V42 and for GB1: I6, L7, E19, A24, V29, E42. This small variation between the two would suggest that there is very little structural variation between the two and indeed, comparison of the crystal structures (Figure 4.15) results in an RMSD of 0.956 Å. However, specific variations between the two proteins where aliphatic residues are replaced with charged residues would likely lead to a difference in interactions and as a result variations in the mobility experienced in these regions.

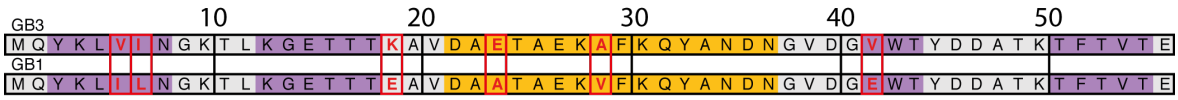

Figure 4.14 Sequence comparison for GB3 and GB1, with the number above referring to the residue number, with orange indicating an α-helix region, purple a β-sheet region, and grey a connecting loop or terminal region. Sequence variation between GB3 and GB1 is highlighted in red. GB3 and GB1 are 89 % identical, varying only at residues 6, 7, 19, 24, 29, 42. For GB3: V6, I7, K19, E24, A29, V42 and for GB1: I6, L7, E19, A24, V29, E42.

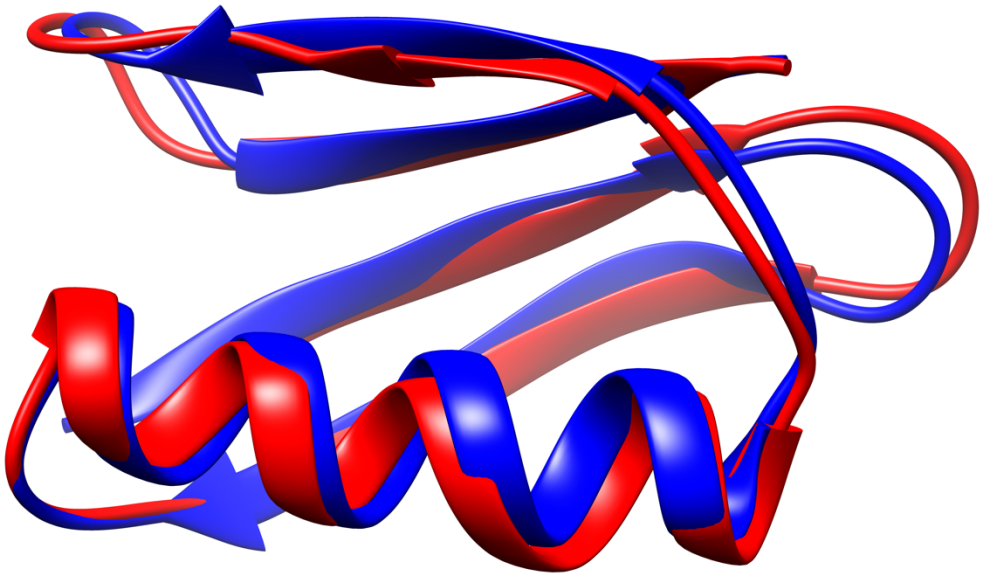

Figure 4.15 Crystal structure comparison for GB3 and GB1. GB3 (red, PDB ID: 2LUM), GB1 (blue, PDB ID: 2QMT). RMSD of 0.956 Å.

Detailed analysis of the ^{15}N $R_{1\rho}$ site-specific rate constants of [U-^{13}C,^{15}N]GB3 and [U-^{13}C,^{15}N]GB1 (Figure 4.17) show significant differences at residues 19, 24, 47 and 48. At sites 19 and 24 we find these residues are different (for GB3: K19, E24, for GB1: E19, A24). At sites 47 and 48 we find these residues are the same (E47, A48). This indicates that the dynamics changes are remote from the site of mutation. From this, it would seem that variation in the third β-sheet of the protein considerably influences the dynamics in the subsequent connecting loop.

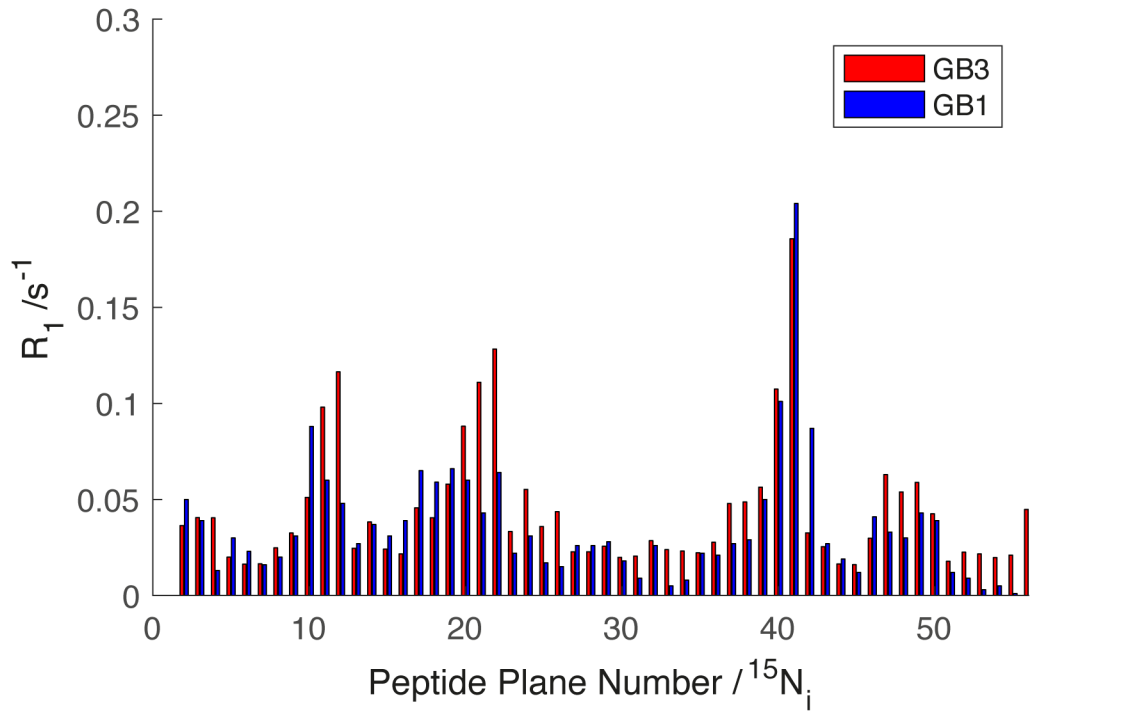

Figure 4.16 Comparison of the ^{15}N R_1 site-specific rate constants of [U-^{13}C,^{15}N]GB3 and [U-^{13}C,^{15}N]GB1. ^{15}N R_1 rate constants plotted as a function of the peptide plane number of the backbone ^{15}N atom. Measurements performed on GB3 were carried out at $\omega_{0H}/2\pi$ = 600 MHz, $\omega_R/2\pi$ = 35 kHz, and with a sample temperature of 283 K. Measurements performed on GB1 in the Lewandowski group were carried out at $\omega_{0H}/2\pi$ = 600 MHz, $\omega_R/2\pi$ = 60 kHz, and with a sample temperature of 300 K. GB1 data reproduced from Lamley 2015 with permission from the publisher.[219] Copyright (2015) Royal Society of Chemistry.

.

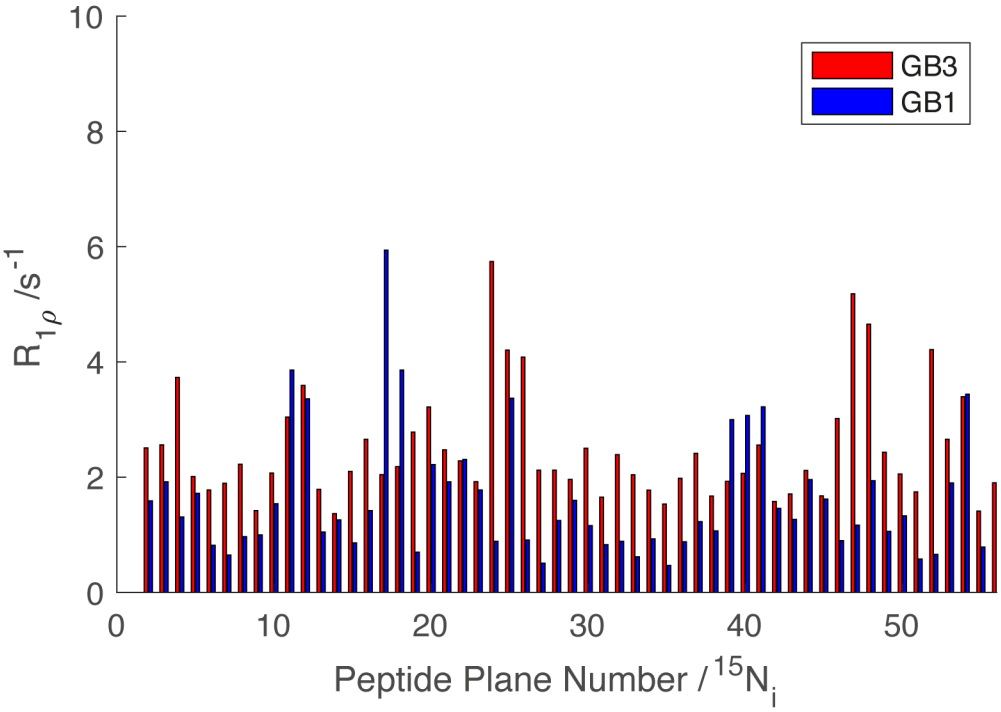

Figure 4.17 Comparison of the ^{15}N $R_{1\rho}$ site-specific rate constants of [U-^{13}C,^{15}N]GB3 and [U-^{13}C,^{15}N]GB1. ^{15}N $R_{1\rho}$ rate constants plotted as a function of the peptide plane number of the backbone ^{15}N atom. Measurements performed on GB3 were carried out at $\omega_{0H}/2\pi$ = 600 MHz, $\omega_R/2\pi$ = 35 kHz, with a spin-lock nutation frequency of $\omega_1/2\pi$ = 20 kHz and with a sample temperature of 283 K. Measurements performed on GB1 in the Lewandowski group were carried out at $\omega_{0H}/2\pi$ = 600 MHz, $\omega_R/2\pi$ = 60 kHz, with a spin-lock nutation frequency of $\omega_1/2\pi$ = 17 kHz and with a sample temperature of 300 K. GB1 data reproduced from Lamley 2015 with permission from the publisher.[219] Copyright (2015) Royal Society of Chemistry.

4.3.2 Low-Temperature Studies on WT-GB3

Ultimately, the goal of this chapter was to investigate the T_1 effects at cryogenic temperatures. 1D-^{1}H to ^{13}C CP experiments were used to observe the effect of slow cooling on GB3 (Figure 4.18). The spectrum at 280 K is typical of what would be expected for microcrystalline GB3 at 9.4 T and 8 kHz MAS, with several resolved resonances identifiable. As the temperature at which the spectrum is recorded is lowered, an increased broadening is observed, with maximum linewidths observed at 107 K. It would appear that there are no step-like changes in the spectra, with the linewidths gradually increasing on each further temperature reduction. One may expect a sudden change in resolution at around 200 K, which is known to be where the protein glass transition temperature (T_g) occurs.[220] The protein T_g represents the temperature at which a significant change in the dynamical properties of the protein occurs. Temperatures above the T_g exhibit dynamics predominated by large-scale motions of entire domains, whereas below the T_g harmonic vibrations are the dominate dynamic process present.[220] This lack of a step-like change at the protein T_g has been reported before by Linden and co-workers studying the effects of cryogenic temperatures on resolution and relaxation rates upon slow cooling of a precipitated preparation of SH3.[221] Siemer *et al.* explained how that the formation of a glass matrix influences the dynamics of hydrated proteins[221] and indeed this can be observed in the relaxation data of GB3 acquired, where upon passing the T_g of the cryoprotectant (glycerol (60% w/v) aqueous solution) used (159 K by differential thermal analysis (DTA)[222] and 163.60 K by differential scanning calorimetry (DSC)[223] the ^{1}H T_1 begins to increase drastically. The definition of the T_g of the cryoprotectant varies from that of a protein, in that for the cryoprotectant it essentially represents the point in which the liquid can no longer flow or more formally, the temperature at the onset of the increase in heat capacity.[224] The ^{1}H T_1 was observed to increase from 1.6 s at 170 K to 3.4 s at 150 K, where before this temperature increases in the ^{1}H T_1 had been minimal. An analysis of linewidths from 2D-spectra at cryogenic temperature for WT-GB3 and doped GB3 samples is given in in §5.3.9.

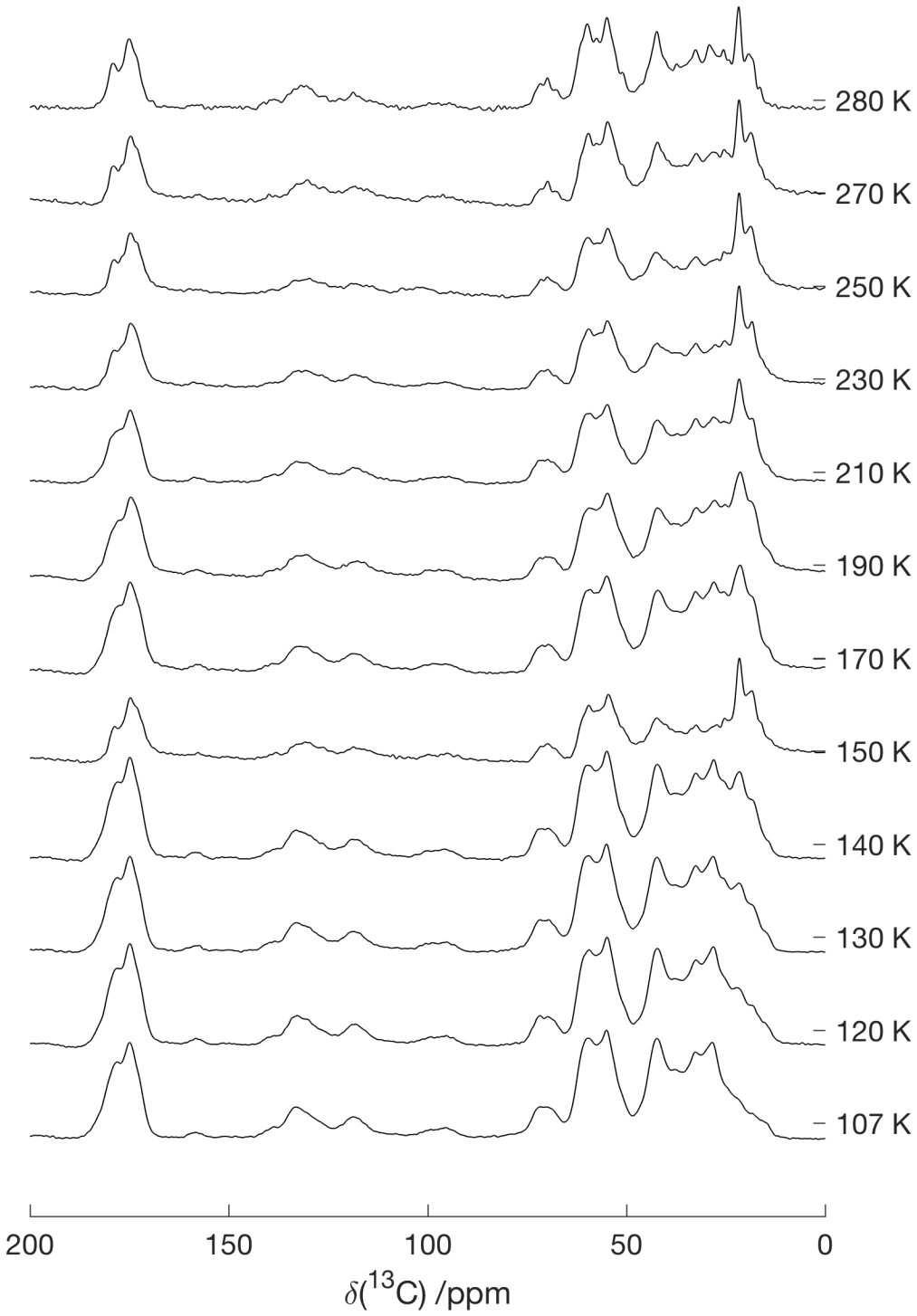

Figure 4.18 Resolution of GB3 ^{1}H-^{13}C CP spectra as a function of temperature. $\omega_R/2\pi$ = 8 kHz, $\omega_{0H}/2\pi$ = 400 MHz.

The ^{1}H T_1 of WT-GB3 was investigated as a function of temperature (Figure 4.19). The global ^{1}H T_1 relaxation ranged from 0.7 s (280 K) to 13.4 s (107 K) as measured by proton saturation-recovery experiments. The ^{1}H T_1, which is 0.7 s at room temperature, increased gradually as the temperature is reduced up until the T_g of the cryoprotectant was reached, upon which the ^{1}H T_1 began to drastically increase. This is evident by noting the data points at 170 K and 150 K, with the ^{1}H T_1 jumping from 1.8 s to 3.4 s. The immobilisation of the solvent results in the removal of several forms of dynamics previously accessible through protein-solvent interactions. This likely leads to a loss in available relaxation pathways, explaining the extended T_1 relaxation times observed.

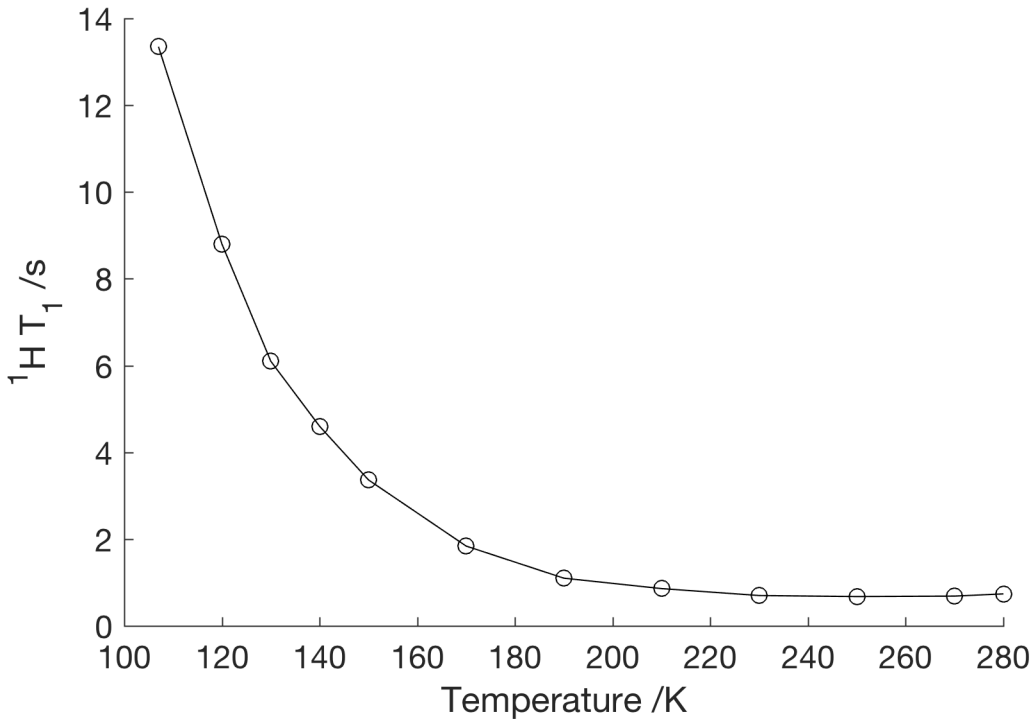

Figure 4.19 ^{1}H T_1 as a function of temperature, for undoped WT-GB3. $\omega_R/2\pi$ = 8 kHz, $\omega_{0H}/2\pi$ = 400 MHz.

4.3.3 Relaxation Studies on Doped Microcrystalline GB3

4.3.3.1 T_1 and T_2 Relaxation Experiments

Relaxation experiments were performed on undoped WT-GB3 and in the presence of various levels of doping with a particular relaxation agent. The purpose of these experiments was to identify relaxation agents which gave greatest enhancement in T_1 relaxation without unduly affecting the line shape. Gadolinium was selected to investigate as it has previously been shown to function well as a T_1 relaxation agent.[216] Holmium has been previously investigated as a low-temperature relaxation agent so doping with holmium was also explored.[174] The nitroxide radical TEMPO is analogous to the MTTSL radical, which will be used for spin-labelling of proteins for DNP experiments in Chapter 5. It is therefore useful to also investigate the relaxation of a nitroxide radical.

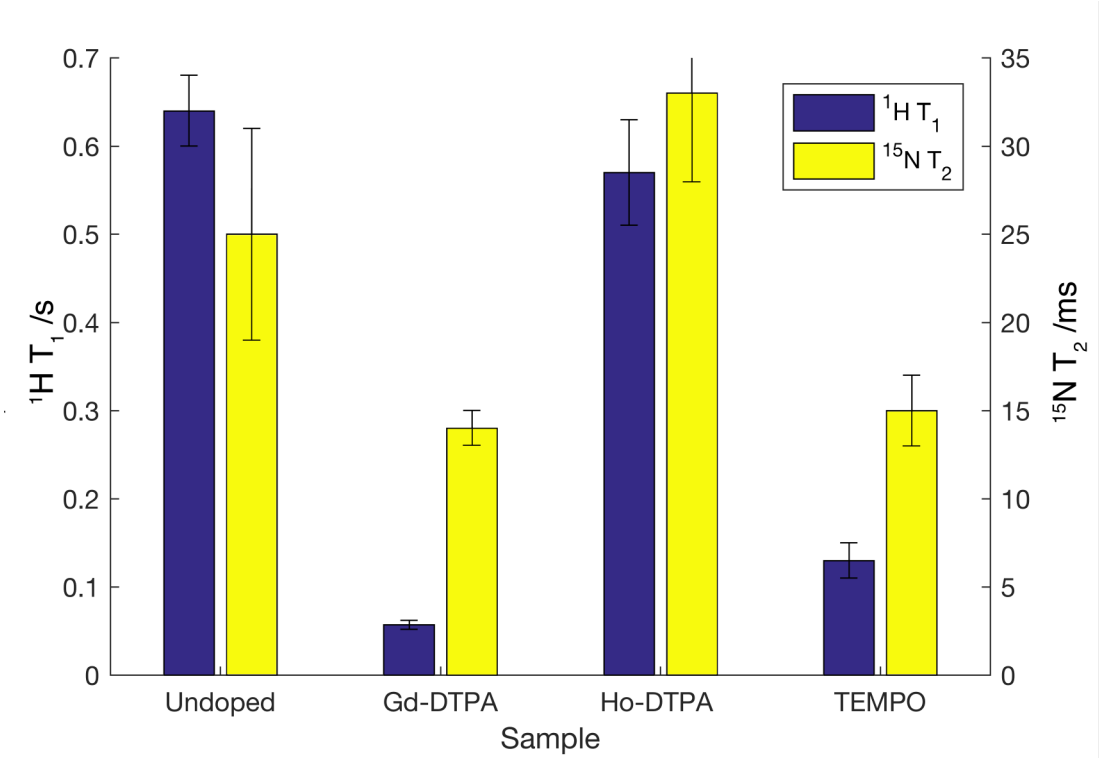

Figure 4.20 Bar chart of the ^{1}H T_1 and ^{15}N T_2 relaxation time constants determined from the ^{15}N backbone envelope of [U-^{15}N]GB3. For doped samples a concentration of 1 mM of dopant was used. $\omega_R/2\pi$ = 10 kHz, 295 K. Error bars show 95 % confidence limits.

From the ^{1}H T_1 data obtained for the backbone resonances it is observed that all three dopants reduced ^{1}H T_1 with Gd-DTPA having the greatest effect of around a ten-fold decrease in ^{1}H T_1 in comparison to the control at 295 K, with TEMPO having a 6-fold

decrease, though with a reduction in the T_2 as can be predicted from its electronic relaxation rate.[213] Ho-DTPA doping led to a small decrease in the ^{1}H T_1 (see Figure 4.20 and Table 4.1).

Table 4.1 ^{1}H T_1 and ^{15}N T_2 relaxation time constants determined from the ^{15}N backbone envelope of [U-^{15}N]GB3. 95% confidence limits given in brackets. $\omega_R/2\pi$ = 10 kHz, 295 K.

Sample	T_1 /s	T_2 /ms
GB3	0.64 (0.6, 0.67)	26 (20, 31)
GB3 + 1mM Gd DTPA	0.057 (0.053, 0.062)	14 (13, 15)
GB3 + 1mM Ho DTPA	0.57 (0.51, 0.63)	32 (28, 36)
GB3 + 1mM TEMPO	0.13 (0.11, 0.15)	15 (13, 16)

From the T_2 relaxation data obtained for the backbone resonances the TEMPO and Gd-DTPA dopant agents seemed to reduce the T_2 relaxation time, whereas the Ho-DTPA seemingly increased T_2 relaxation time with respect to the undoped sample (Table 4.1).

4.3.3.2 Site-Specific Relaxation Data

To determine if there was any site-specific relaxation taking place the ^{1}H T_1 of individual residues was measured by integrating the area of each peak individually (Figure 4.21).

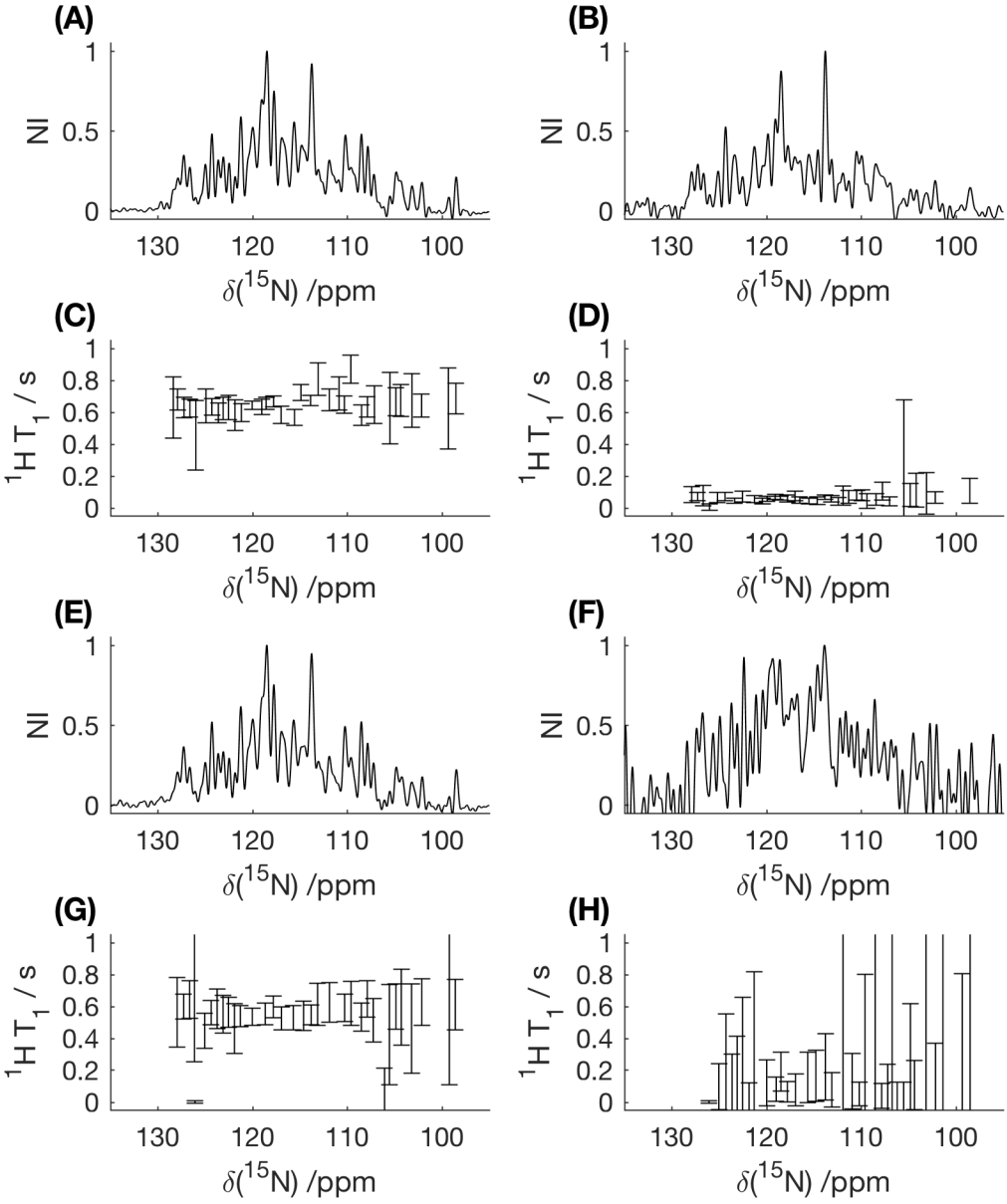

Figure 4.21 Site-specific ^{1}H T_1 relaxation time constants for GB3 as a function of chemical shift determined from the ^{15}N backbone resonances of [U-^{15}N]GB3. ^{1}H-^{15}N CP spectra at 295 K of undoped GB3 (A), 1 mM Gd doped GB3 (B), 1 mM Ho doped GB3 (E), 1 mM TEMPO doped GB3 (F). Relaxation rate for each peak at 295 of undoped GB3 (C), 1 mM Gd doped GB3 (D), 1 mM Ho doped GB3 (G), 1 mM TEMPO doped GB3 (H). $\omega_R/2\pi$ = 10 kHz.

The site-specific relaxation constants determined were similar to that of the total resonances indicating that under the experimental conditions employed no site-specific relaxation was observed (Figure 4.21). This was potentially due to the low spinning speed at which the experiments were carried out so that the ^{1}H dipolar couplings were not efficiently removed, causing the nuclei to relax at similar rates due to spin diffusion.

4.3.3.3 Effect of Dopant Concentration on Relaxation

A series of relaxation experiments were performed with varying concentrations of dopants added in order to ascertain the effect on concentration on the T_1 (Figure 4.22). As expected the longitudinal relaxation rate is enhanced as the concentration is increased. From a plot of R_1 as a function of concentration the proton longitudinal relaxivity of the relaxation agent can be determined (where relaxivity describes the relaxation effect as a function of concentration). The proton longitudinal relaxivity, ^{1}H r_1, at 283 K was determined to be 16.1±1.3 $s^{-1}mM^{-1}$ for Gd-DTPA and 0.93±0.01 $s^{-1}mM^{-1}$ for Ho-DTPA.

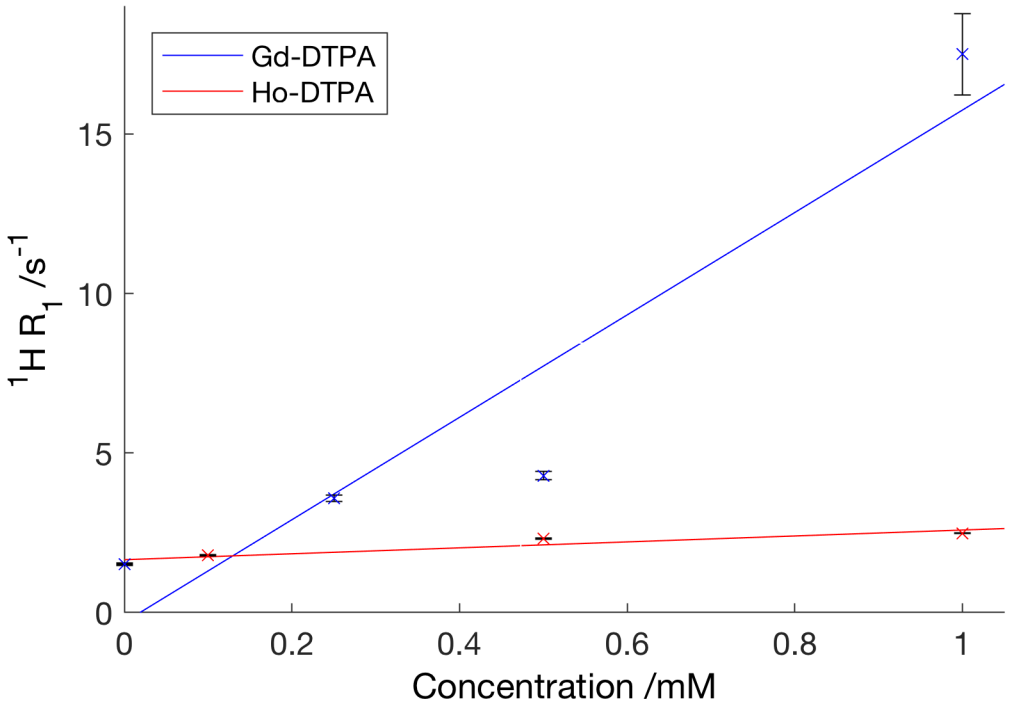

Figure 4.22 Plot of ^{1}H R_1 for Gd-DTPA and Ho-DTPA doped GB3 as a function of concentration to determine the proton longitudinal relaxivity, ^{1}H r_1. ^{1}H r_1 of Gd-DTPA dopant: 16.1±1.3 $s^{-1}mM^{-1}$. ^{1}H r_1 of Ho-DTPA dopant: 0.93±0.01 $s^{-1}mM^{-1}$. Microcrystalline [U-^{15}N]GB3 backbone integrated. Measured at 298 K, $\omega_R/2\pi$ = 10 kHz.

4.4 Conclusions

Site-specific R_1 and $R_{1\rho}$ measurements of microcrystalline [U-^{13}C,^{15}N]GB3 were used to understand the relaxation of residues in the protein and gain understanding into how this relates to the dynamics of the protein. A comparison was made to compare WT-GB3 to a cysteine mutant of the protein, A48C-GB3. In addition, the relaxation of GB3 was compared to GB1.

Low-temperature NMR measurements of microcrystalline [U-^{13}C,^{15}N]GB3 were used to investigate the effect temperature has on the T_1 relaxation. In addition, the effect on the resolution as a function of temperature was explored.

MAS-ssNMR saturation recovery and spin echo experiments were performed on microcrystalline [U-^{15}N]GB3 to obtain the ^{1}H longitudinal relaxation constants and ^{15}N transverse relaxation constants (see Table 4.1). The ^{1}H longitudinal relaxation constants were determined site-specifically to determine whether the relaxation agent was located in a particular region in the crystals. At 10 kHz spinning speed and with a dopant concentration of 1 mM there was no significant difference between the values for proton longitudinal relaxation constants for individual nitrogen backbone resonances in each sample. Repeating the experiments at higher spinning speeds to reduce spin diffusion may provide information on if and where the relaxation agents locate themselves in the sample. An investigation into the relaxivity of dopant agents was carried out through varying the concentration of dopant in microcrystalline [U-^{15}N]GB3 samples. The proton longitudinal relaxivity, ^{1}H r_1, at 283 K was determined to be 16.1±1.3 $s^{-1}mM^{-1}$ for Gd-DTPA and 0.93±0.01 $s^{-1}mM^{-1}$ for Ho-DTPA.

Chapter 5: Dynamic Nuclear Polarisation of Spin-Labelled Proteins

5.1 Introduction

Dynamic nuclear polarisation (DNP) refers to a technique in which large nuclear polarisations can be achieved by transferring polarisation from paramagnetic centres present in the sample. Typically, a nitroxide radical is used as the paramagnetic species. The electron spin polarises thermally with respect to the field. This polarisation can be transferred to specific nuclei in the sample, enabling the nuclear polarisation to be enhanced by an amount determined from the quotient of the electron and nuclear gyromagnetic ratios, γ_e/γ_I. This gives potential enhancement values of 660 for ^{1}H and 2640 for ^{13}C.[98] Such enhancements lead to a much higher signal to noise ratio (SNR) being obtained from the same number of scans in comparison to acquisition without nuclear polarisation enhancement[225] (see Figure 5.1) and with sensitivity being proportional to the square root of time, can lead to drastic reductions in required acquisition times. These massive enhancements in sensitivity make DNP an attractive technique for structural and mechanistic investigations into biological macromolecules.

DNP has been used extensively in nuclear magnetic resonance (NMR) and has been exploited to a greater extent than other methods of nuclear polarisation enhancement currently being explored such as the use of parahydrogen and low-temperature NMR.[173, 226] Enhancements in nuclear polarisation are desired as under normal experimental conditions the population difference between the relevant energy levels is of the order of $1\text{x}10^{-5}$, resulting in the low sensitivity of the technique, hence the need for repeat scans to obtain a suitable SNR.

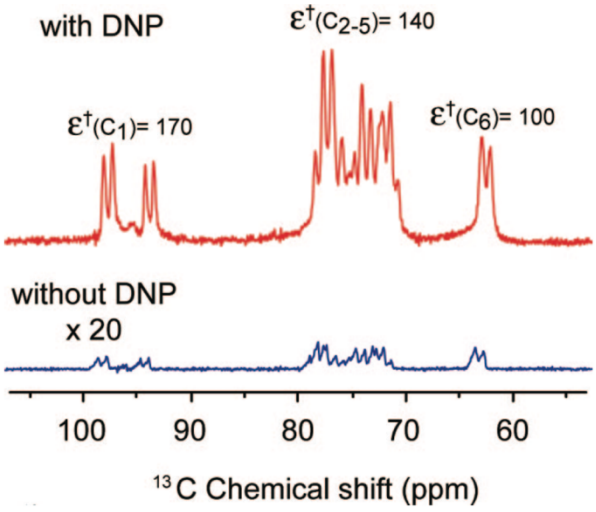

Figure 5.1 NMR spectrum of ^{13}C labelled glucose in deuterated solvent doped with the radical TOTAPOL to illustrate the sensitivity enhancements achieved by using DNP, where ε† is the DNP enhancement. Figure reproduced from Joo. C 2009 with permission from the publisher.[227] Copyright (2009) American Chemical Society.

5.1.1 Types of DNP Setup

DNP can be exploited in both the solid and liquid states. There are two methods of solid-state DNP that are most commonly utilised. 1) Dissolution DNP whereby high levels of nuclear polarisation are first achieved in a spectrometer at low-temperature and relatively low magnetic field. Once the sample has been polarised it is quickly dissolved and shuttled to another spectrometer at room temperature and at a higher magnetic field. From here NMR experiments can be performed.[228-229] 2) MAS DNP, unlike static DNP, the condition for polarisation to be transferred becomes a function of sample rotation, with DNP enhancements arising at energy level anti-crossings which are fulfilled periodically with each rotor cycle.[229-233]

5.1.2 Mechanisms of DNP

The mechanisms of DNP have been elucidated in both the liquid and solid state. In the liquid-state DNP is believed to occur through the Overhauser effect (OE)[98, 234]. In the solid-state, there are four mechanisms through which DNP can proceed. The mechanisms can be characterised according to the number of paramagnetic centres participating in the polarisation transfer step. 1) The OE in solids occurs through a modulation of the hyperfine coupling.[235] 2) The solid effect (SE) occurs when a single electron is involved in the polarisation transfer to the nuclei.[236] 3) In the cross effect (CE) a pair of coupled electrons

interact with the nuclei to facilitate the transfer of magnetisation when the corresponding radiation is supplied.[237-238] 4) Thermal mixing (TM) polarisation transfer is achieved according to spin thermodynamics by polarisation transfer from multi-electron coupled spin systems to the nuclei.[226, 239]

In DNP experiments several variables can be selected to effect which mechanism is the dominant pathway of nuclear polarisation taking place. Parameters that can affect which mechanism is present include the strength of the nuclear-nuclear, electron-electron and hyperfine dipolar interactions, the inhomogeneous line width of the EPR spectra of the paramagnetic species used, the relaxation rates of both the nuclei and the electrons and the Larmor frequency of the nuclei.[229, 231-232, 240-242]

5.1.2.1 The Overhauser Effect

The OE was the first DNP mechanism discovered and involves the disturbance of nuclear spin populations while microwave irradiation saturates electron spin transitions. The OE relies on relaxation processes to simultaneously flip the nuclear and electron spins. Time-dependent scalar and dipolar interactions are the foundation of these relaxation processes with translational and rotational movement dictating the dipolar interaction and chemical exchange along with fast relaxation dictating the process under scalar coupling.[243] For the OE to take place in solids, mobile electrons must be available. For the OE the product of the electron Larmor frequency, ω_{0e}, with the correlation time, τ_c, must be less than one. For large values of ω_{0e}, this condition is hard to fulfil, leading to the OE being inefficient at high magnetic field strength, though not necessarily zero.[244]

5.1.2.2 The Solid Effect

Nuclear polarisation enhancement via the SE occurs by irradiating the electron-nucleus spin system with MW radiation at the correct frequency to cause a forbidden zero-quantum (ZQ) or double-quantum (DQ) transition. The frequency required to excite this transition is obtained from the addition or subtraction of the nuclear Larmor frequency (ω_n) from the electron Larmor frequency (ω_e). A positive enhancement in polarisation is achieved by irradiating the DQ transition and a negative enhancement is achieved by irradiating the ZQ transition.[225]

The condition that must be fulfilled for the SE is $\omega_{mw} = \omega_{0S} \pm \omega_{0I}$, where ω_{mw} is the frequency of MW irradiation, ω_{0S} the electron Larmor frequency, and ω_{0I} the nuclear Larmor frequency.[226] The two-spin mechanism proceeds through the excitation of forbidden electron-nuclei transitions, which through the mixing of states are allowed to some extent. For efficient enhancements through the SE, both the inhomogeneous and homogeneous EPR linewidths of the radical must be less than the nuclear Larmor frequency to be hyperpolarised. Without fulfilment of this condition, the DQ and ZQ transitions are too broad and overlap, and with their enhancements being positive and negative, respectively, the enhancements are effectively cancelled out. Any enhancement in such a system is due to the residual net enhancement, known as the differential solid effect (DSE).[245] A point worth noting is that the SE is not often used at high field due to the ω_0^{-2} field dependency as a result of the mixing of adjacent nuclear spin states.[246] However, at high MW amplitudes, the SE mechanism is more effective.[246]

5.1.2.3 Thermal Mixing

The mechanism of TM can be explained using the concept of spin temperature.[247] The electron-nuclear spin system can be represented as three baths, the electron dipolar system (EDS), the electron Zeeman system (EZS), and the nuclear Zeeman system (NZS). Each bath is affected by the presence of the other baths. Under the condition that the nuclear Larmor frequency is less than the homogeneous width of the electron paramagnetic resonance (EPR) line, irradiation with MW frequencies off resonance to the EPR transition can be used to produce a large polarisation of the paramagnetic species. In terms of spin temperature, this is equivalent to a reduction in temperature of the EDS. The interaction of the EDS and NZS leads to a cooling of the NZS, occurring through a three-body exchange process, without the loss of energy from the system. This is equivalent to an increase in the polarisation of the nuclei.[248]

5.1.2.4 The Cross Effect

The CE occurs by exciting a spin system comprised of two coupled electrons and a nucleus with irradiation equal to the Larmor frequency of either one of the electrons. Spin systems participating in the CE must satisfy the condition that the difference of the electron Larmor frequencies is equal to the nuclear Larmor frequency. This condition results in degenerate energy levels and effective mixing of the nuclear and electron states.[231] Achieving this matching condition causes the energy levels to become degenerate, leading to the lower

nuclear energy level becoming more populated and therefore the nuclear magnetisation is enhanced.[232]

The Hamiltonian of the CE (Equation (4.3)), where $\widehat{H}$ represents the Hamiltonian, ω_{0i} is the frequency of radiation of species i, $\hat{S}_i$ is the electron spin operator $\hat{I}_i$ is the nuclear spin operator. A_i is a value representing the secular hyperfine coupling of species i, B_i is a value representing the pseudosecular hyperfine coupling of species i, d is a constant required for the dipolar coupling term component of the Hamiltonian, and J is a constant required for the exchange term component of the Hamiltonian. Equation from Ni. Q 2013.[232]

$$\widehat{H} = \omega_{0S1}\hat{S}_{1z} + \omega_{0S2}\hat{S}_{2z} - \omega_{0I}\hat{I}_z + \left(A_1\hat{S}_{1z} + \mathrm{A}_2\hat{S}_{2z}\right)\hat{I}_z + \left(B_1\hat{S}_{1z} + \mathrm{B}_2\hat{S}_{2z}\right)\hat{I}_x + d\left(3\hat{S}_{1z}\hat{S}_{2z} + \overrightarrow{S_1}.\overrightarrow{S_2}\right)\hat{I}_z - 2J\overrightarrow{S_1}.\overrightarrow{S_2} \qquad \textbf{(5.1)}$$

The first and second terms in the Hamiltonian comprise the electron Zeeman components of the Hamiltonian, the third term comprises the nuclear Zeeman component. The next two terms encompass the electron-nuclear hyperfine coupling, followed by a term for the electron-electron dipolar coupling and a final term representing the exchange coupling.[232] From the Hamiltonian, an energy level diagram can be constructed (see Figure 5.2). The energy level diagram illustrates how irradiation at the previously discussed matching condition leads to the described enhancements.

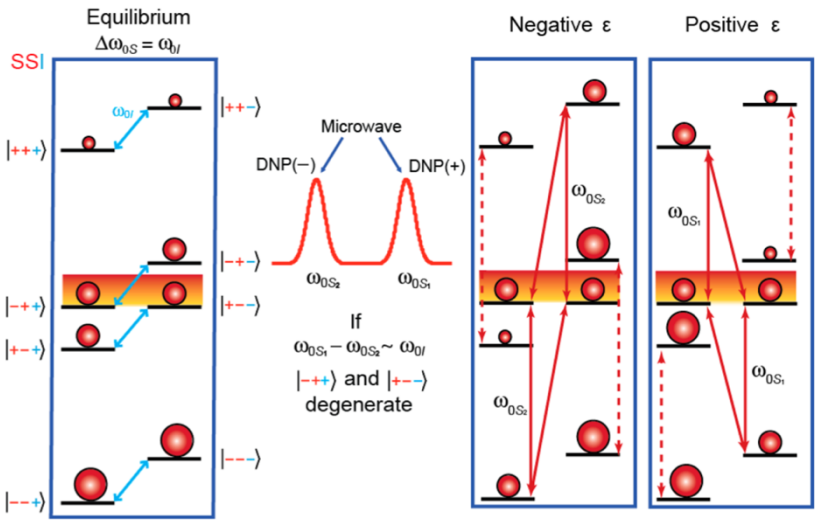

Figure 5.2 Energy level diagram to illustrate the CE DNP mechanism. Figure reproduced from Ni. Q 2013 with permission from the publisher.[232] Copyright (2013) American Chemical Society.

The CE is now a universally accepted and understood mechanism of DNP with a secure background of theoretical work on how precisely the magnetisation is transferred from electrons to nuclei by this effect, enabling the mechanism to be fully exploited. Many groups are now researching to utilise the technique to its full potential, and applications of the technique have been used to study different nuclei in varying materials such as surface functionalised mesoporous silica nanoparticles[249-252] as well as being applied to the study of biological samples.[253]

5.1.3 Sensitivity Enhancements

Recent method development studies on the employment of paramagnetic agents for DNP enhancements of biomolecules has partially focused on the attachments of the radical to the surface of the biomolecule. These studies have not necessarily been undertaken with the intention of achieving an improved DNP enhancement but rather interested in improving other aspects of the technique when applied to biomolecules. Rossini *et al.* highlighted other factors for gains in overall spectral enhancements that are important.[252] The actual enhancement factor from DNP, which is given as the quotient of the MW on spectrum to that of the MW off spectrum is itself is subject to many variables. Including but not limited to, the concentration and structure of the polarising agent employed, the field strength, temperature and spinning rate experiments are conducted under. In addition, the frequency and intensity of microwave irradiation, the composition of the solid sample,

i.e. frozen solution, crystalline structure or other, as well as the level of sample deuteration,[254-259] all play a major roll on the DNP enhancement achieved. However, the DNP enhancement is just part of the overall signal enhancement that one can achieve from the exploitation of paramagnetic species in NMR. The radical not only enables polarisation to be transferred from the electrons, but it also exerts an effect on the longitudinal relaxation time of the sample, $T_{1,}$ known as the DNP enhanced relaxation time, T_{DNP}. The polarising agent also impacts on the number of spins in the sample which fit into the area known as the diffusion barrier, these spins don't add to the NMR signal. These factors influence the overall sensitivity enhancement factor that is achieved by the DNP experiment as a whole (with the sensitivity defined as described by Ernst and Bodenhausen as the ratio of signal to noise per the square root of unit of time per unit of mass[17]). Rossini and Emsley, in their report on the DNP enhancement of a silica surface, explained how other effects on signal enhancement can be included in determining the absolute enhancement. Namely, paramagnetic effects on enhancements due to reductions in longitudinal relaxation times. In addition, the Boltzmann contribution from acquisition at the low temperatures.

The work concluded with the result that the overall greatest enhancement did not, in general, occur from conditions in which the DNP enhancement itself was greatest due to reductions in sensitivity at very high concentrations of polarising agents, but rather when there is a compromise between DNP enhancement, quenching and relaxation effects.

When looking at the overall DNP sensitivity enhancement factor it is required to take into account that, in NMR experiments, one will not simply acquire a single scan of their system, but several scans, separated by a recycle delay, which can at low-temperature be rather large without an enhanced rate through paramagnetic doping. With the presence of paramagnetic species, the unpaired electrons facilitate an enhancement in the longitudinal relaxation rate. Consequently, the recycle delay is often set by what it is limited by in terms of T_1. When further reductions due to hardware or sample heating problems are not an issue, one can also benefit from sensitivity enhancement in the effective sensitivity enhancement per unit time that the paramagnetic agent provides through this effect.[260]

The overall DNP sensitivity enhancement factor is quantified by multiplying the enhancement, ε, (which is obtained from dividing the integrated intensity of the MW on DNP spectrum by the MW off spectrum) by a quenching factor, θ, (which is obtained by

taking the integrated intensity of the MW on DNP spectrum divided by both ε and the integrated intensity of an analogous sample but without the paramagnetic doping). This value can then be further multiplied by a factor that takes into account the rate at which the scans can be obtained, which is the T_1 of the sample at this value divided by the DNP enhanced longitudinal relaxation time.

$$\Sigma = (\varepsilon)(\theta)\sqrt{\frac{T_1}{T_{DNP}}} = (\varepsilon)(\theta)\sqrt{\kappa} \quad \textbf{(5.2)}$$

Where ε is the DNP enhancement from the ratio of integrated intensities of MW on vs MW off, θ is the quenching factor, T_1 is the longitudinal relaxation time of the sample, T_{DNP} is the DNP enhanced longitudinal relaxation time, and κ is the ratio of T_1 to T_{DNP}. Equation (5.2), that quantifies the overall DNP sensitivity enhancement factor can be modified to account for the added enhancement owing to the Boltzmann contribution achieved by the low-temperature by multiplying by the ratio of the temperature used to record the DNP experiment divided by the standard room temperature in which one would typically perform experiments at.

$$\Sigma^{\dagger} = (\frac{298\ K}{100\ K})(\varepsilon)(\theta)\sqrt{\kappa} \quad \textbf{(5.3)}$$

A further expansion on the idea of quantifying the sensitivity enhancements of DNP is given by Takahashi and De Paëpe[261], where they include factors to account for differences in probes, varying magnetic field strengths, sensitivity enhancement due to a reduction in thermal noise at low-temperature, line width differences and different samples volumes.[261] In addition to this, the enhancement achieved has been observed to vary between experiments dependent on how the paramagnetic species causes a particular coherence to relax.[252, 262-263]

5.1.4 Polarising Agents

In "conventional" DNP methods MW's are applied in a continuous fashion to saturate the electron transitions of the radical species.[226] A theoretical maximum enhancement of $\varepsilon = 660$ in the case of protons hyperpolarised in this way is possible.[98] Unless the species naturally contains a paramagnetic centre, paramagnetic doping is required for DNP. The following sections discuss the choice of polarising agent to encourage a certain DNP mechanism to take place. The main factors affecting the mechanism undertaken include but are not limited to the line width of the EPR spectrum, the relaxation rate at the

temperature employed, and the solubility of the radical. The radical can act either exogenously, as an organic radical or paramagnetic metal ion added to the sample, or endogenously as a radical attached to the nuclear system to be enhanced, such as in the case of tethering nitroxide radicals to biomacromolecules. The employment of exogenous polarising agents, with the radical suspended in a glass-like matrix, for DNP have become ubiquitous in the field. Moreover, many groups use them as standard procedure for DNP enhancement experiments. Typically, due to the greater ease of set up in comparison to endogenous polarising agents and in general due to the superior enhancements that have been achieved. Considering this, although widely used, there is quite a lot of variability in the enhancement and thus a greater understanding of the practical elements of transfer may be of use.

Figure 5.3 illustrates some typical organic radicals utilised in various DNP schemes. For the SE a polarising agent with three-fold symmetry is desired to give narrow EPR linewidths, trityl OX063[264] and α,γ-bisdiphenylene-β-phenylallyl (BDPA[265]). The monoradical (2,2,6,6-tetramethylpiperidin-1-yl)oxyl (TEMPO[266]) exhibits broad line widths in comparison to the nuclear Larmor frequency so is suitable for use in TM when employed at a high enough concentration. For the CE, which relies on the interaction between two electrons and one nuclei, a close distance between the two electrons is preferable to achieve a suitably large dipolar coupling on the order of 20 MHz, this is most achievable with a biradical such as 1-(TEMPO-4-oxy)-3-(TEMPO-4-amino)propan-2-ol (TOATAPOL[267]), bis-TEMPO-bis-ketal (bTbk[268]) and 15-([(7-oxyl-3,11-dioxa-7-azadispiro[5.1.5.3]hexadec-15-yl)carbamoyl][2-(2,5,8,11-tetraoxatridecan-13-ylamino)]-[3,11-dioxa-7-azadispiro[5.1.5.3]hexadec-7-yl])oxidanyl (AMUPol[269]). S-(1-oxyl-2,2,5,5-tetramethyl-2,5-dihydro-1H-pyrrol-3-yl)methyl methanesulfonothioate (MTSSL[270-271]), a nitroxide radical containing a disulphide functional group enabling it to be tethered to cysteine residues in proteins has typically found use in EPR measurements of proteins but due to the radicals nature has also found use in various DNP techniques. The utility of the above radicals extends beyond the obvious necessity of their paramagnetic characteristics. They have found themselves applicable in both solid and liquid state DNP experiments owing to their other beneficial attributes, namely the long-lifetime of the radicals and the steric bulk surrounding the site of the unpaired electron leads to the species being remarkably unreactive. The surrounding functional groups in the molecules enable them to be soluble in a range of solvents typically used in the preparation of biological samples,

with the classic case of 'DNP juice' which constitutes 60/30/10 gylcerol-d_8/D_2O/H_2O ratio with polarising agent dissolved in solution, with a glassy matrix formed on cooling to DNP temperatures.

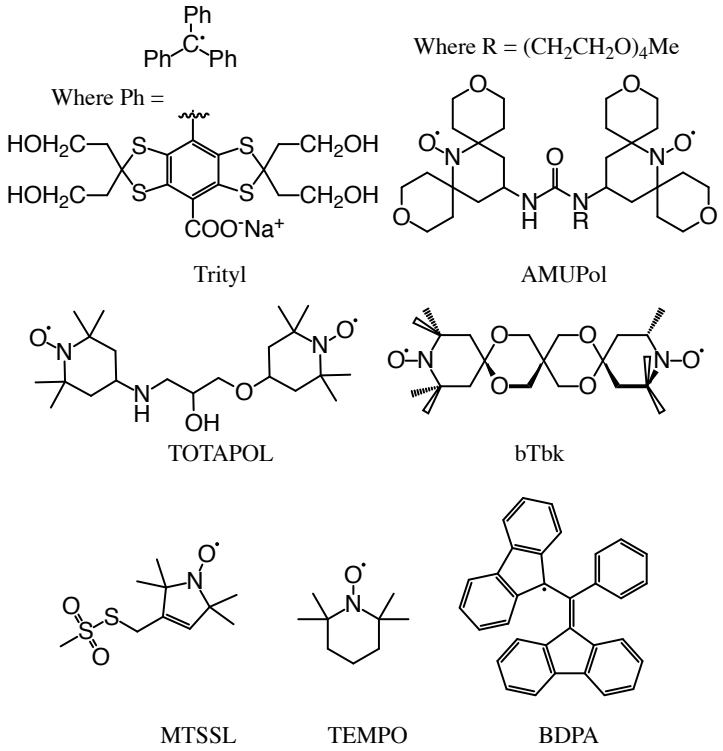

Figure 5.3 DNP radical examples. Example of the radicals that are employed to facilitate polarisation transfer in DNP experiments. The monoradicals, trityl OX063[264], BDPA[265] are used to exploit the SE. While the biradicals TOATAPOL[267], bTbk[268] and AMUPol[269] are used to exploit the CE. TEMPO[266] was used as a precursor in the design of biradical systems for the CE, though may also be exploited for TM. MTSSL[270-271], which contains a disulphide group for attachment to a thiol may be utilised in DNP experiments as will be explored later in the chapter, for CE DNP.

While the majority of DNP experiments focus on the use of organic radicals with a g-value close to that of the free election g value g_e, of 2.0023 (4.d.p), recent research has expanded to the employment of the more exotic paramagnetic centres of transition metals and lanthanides. Paramagnetic metal ions have the advantage of being naturally present in several systems of interest, in a biological context, metalloproteins which contain a paramagnetic centre or can have a diamagnetic centre replaced with a paramagnetic analogue. On a broader scope, many materials science fields perform studies involving paramagnetic nuclei, the ability to enhance the NMR signal of such systems with DNP would undoubtedly be greatly beneficial to these fields of research. In a review of

polarisation methods, Crabb described the use of Cr(V) and Nd compounds to achieve polarisation.[272]

5.1.4.1 Polarising Agents for the Overhauser Effect

The OE is known to depend on time-dependent spin-spin interactions, and so in the context of biological solids at liquid nitrogen temperatures and below, there are insufficient conducting electrons for the mechanism to be utilised in the same way as in liquid-state DNP.[273] While liquid-state DNP is reliant almost entirely on the OE, in solid-state DNP, the field is dominated by the CE and SE as the go-to mechanisms used for enhancing nuclear polarisation, specifically in biological systems as the OE has only been observed at any meaningful level in low viscosity liquids. The CE and SE are known to become less effective at higher magnetic field strengths and temperatures, presumably as a result of a reduction in the electronic relaxation rate.[274] In contrast, the OE is enhanced at higher magnetic fields, and also not adversely affected by elevated temperatures. As a result, recent interest has resurged into the technique, with Can and co-workers demonstrating the presence of a strong enhancement attributed to the OE in an insulating solid doped with the narrow line radicals BDPA and sulfonated-BDPA (SA-BDPA).[235, 275] For the OE, the rates of the double-quantum (DQ) and zero-quantum (ZQ) relaxation pathways must be inequivalent.[274] These cross-relaxation pathways are directed through the presence of a fluctuating hyperfine interaction, though in solution these pathways are the result of the highly dynamic solvent, for insulating solids this cannot be the case. Lelli and Emsley explored the potential for DNP at fields as high as 18.8 T in a temperature range from 100 K to room temperature, demonstrating that while other mechanisms are greatly attenuated under these conditions, the OE was able to give reasonable enhancements.[276]

It was recently described by Pylaeva and co-workers that the cause of such fluctuations leading to a significant OE in solids was the superposition of internal low frequency fields within the radical complex along with the broadening and coupling imposed on the radical by the surrounding medium. The spin density within the protons of the radical also fluctuate as a result of these local field fluctuations.[274] In the context of radical design these effects are caused by specific features of the radical and also explain why Pylaeva did not observe an OE using trityl OX063, also a narrow line radical, that naively one would expect to elicit the OE as with BDPA. The delocalised electronic system present in BDPA across the diphenylene rings linked by the allylic bridge dictates a corresponding

delocalisation in the spin density of the radical along with structural protons within the radical are attributed with enabling BDPA to mediate the OE in an insulating solid. Such characteristics are not present in trityl radicals. These criteria can be used as a guideline in the design of a polarising agent for OE-DNP that will lead to greater polarisation transfer. As detailed by Pylaeva and co-workers a greater mass around the fluorene sub-units of BDPA via substitutions with large groups, without removing proteins that have a strong hyperfine coupling to the paramagnetic centre, would attenuate the maximum frequency of the structural perturbations. Replacement with electron-donating groups would increase the level of spin density in the delocalised system, further strengthening the radicals polarising capabilities.[274]

5.1.4.2 Polarising Agents for the Solid Effect

With the stipulation that the homogeneous linewidth of the EPR transition is less than the nuclear linewidth, to separate out the double quantum and zero quantum forbidden transitions, trityl radicals[264] and BDPA[277] are the predominant polarisation agents that have been used to incite the SE. The use of BDPA for biological work is limited due to its lack of solubility in aqueous solvents typically used with biological samples.[230, 275] In comparison the trityl radical,[264, 278] which was originally intended for use in the OE,[279] is highly soluble in aqueous solutions so lends itself well for use in SE enhancements of biological systems.[280]

Gd^{3+} complexes have been utilised in conjunction with a trityl radical to enhance the efficiency on which polarisation is transferred from the trityl radical to the nuclei via the SE, hypothesised to occur through the presence of Gd^{3+} leading to a reduction in the electronic relaxation parameter, η, leading to a lowering of temperature of the spin bath of the nuclear Zeeman system.[281] Studies have been performed for dissolution DNP with Gd^{3+} complexes and Ho^{3+} complexes, with Gd^{3+} being shown to facilitate enhancements in polarisation more effectively, though this is counteracted by the increased rate in relaxation resulting in Ho^{3+} resulting in an overall more beneficial effect on polarisation.[282] In another study, Gd^{3+} and Mn^{2+} were explored for use as polarising agents, not just as mediators to facilitate the polarisation transfer as previously discussed. Though at low-temperature, the outer EPR resonances of Gd^{3+} and Mn^{2+} are greatly broadened, making them unsuitable for use in the SE, the central transition is still relatively narrow in comparison to the nuclear Larmor frequency, making the SE a feasible mechanism for these paramagnetic centres.[245] Of note was that the chelating agent used for Gd^{3+}, DTPA or DOTA lead to greatly

different electric field gradients at the paramagnetic centre,[283] with corresponding variances in their zero-field-splitting (ZFS) as a result. With the DOTA complex of Gd^{3+}, the enhancement profile achieved was characteristic of the SE, with separate negative and positive enhancement peaks for the ZQ and DQ transitions respectively.[245] Though for the DTPA Gd^{3+} complex the central EPR linewidth is considerably broader and the field dependent enhancement profile obtained more characteristic of the DSE, an inefficient means of polarisation enhancement. For the use of paramagnetic metal ions the choice of chelating agent should therefore be considered for optimum DNP enhancements.[245]

5.1.4.3 Polarising Agents for the Cross Effect

In experiments exploiting the CE, nitroxide radicals, generally those based on the compound TEMPO, are used (see Figure 5.3). As the CE is a three-body process requiring two electrons, derivatives of TEMPO in which the paramagnetic species contains two paramagnetic centres can be designed to achieve more efficient polarisation transfer via the CE. As CE requires the two paramagnetic centres to be at a particular orientation and proximity from each other, fixing the position of the radicals in a biradical can be used to increase the proportion of spin systems, which satisfy the condition required for the CE to take place.[232]

With original DNP studies being performed utilising TEMPO as the paramagnetic agent to transfer the polarisation to nuclei, further studies into DNP came across the CE, which worked effectively at polarisation transfers at a temperature range between 80-120 K. Initial work into the design or biradicals for DNP was performed by Hu, working in the group of Griffin to design a species of two TEMPO molecules attached together with polyethylene glycol linkers of varying chain length to determine the enhancement of ^{13}C nuclei in urea as a function of radical separation.[266] This work concluded that the closer the radicals were the greater the enhancement achieved, with a linear dependency of enhancement on the separation of the radicals. Results predicted the closest TEMPO separation of 1.43 nm would give an enhancement of 250 though it was stated that this was subject to a small electron-electron dipole coupling being conserved in comparison to the nuclear Larmor frequency and that the CE is the dominant mechanism. If electron-electron dipole coupling becomes comparable to the nuclear Larmor frequency the coupled electron pair will form a triplet ground state and the TM mechanism will become the predominant mechanism of polarisation transfer. Following this work several groups have looked into

the design and synthesis of varying poly-radical systems with a range of geometries and solubility properties. The biradical bTbK and variants based on its structure which at its base, contain two TEMPO species rigidly bound together in an orthogonal arrangement of the electron g-tensors. The biradicals AMUPol from the Tordo group and TOTAPOL from the Griffin group have been shown to offer the best all-around properties in terms of DNP enhancement and solubility and have been adopted by the biological NMR community for the MAS DNP NMR of proteins. Recent research in the field of biological NMR has focused on the attachment of spin-labels to the surface of biomacromolecules to achieve DNP enhancements in an attempt to alleviate certain disadvantages of the polarising agent being free in matrix (see §5.1.4.5 on covalently bound spin-labels.)

5.1.4.4 Polarising Agents for Thermal Mixing

For the TM mechanism, it is necessary for the paramagnetic centre to possess a homogeneously broadened EPR line, greater than the nuclear Larmor frequency. Organic monoradicals such as TEMPO which display homogenously broadened EPR lines are known to act via the TM mechanism.[284] Typical conditions involve the use of TEMPO at the relatively high concentration of 40 mM with enhancements up to $\varepsilon = 50$ observed at 5 T[285] though greatly attenuated to an enhancement of $\varepsilon = 20$ at the higher field of 9 T.[286]

In the context of biological samples, the exploitation of the TM mechanism has seen some success in the study of membrane proteins with Hall and Griffin achieving enhancements on ^{15}N of 50 for the protein T4 lysozyme.[287] Further to this Rosay and Griffin went on to study Y21M fd bacteriophage, a large biomolecule formed of both DNA and protein with a size of 8000 by 60 Å.[288] From their DNP experiments on the bacteriophage capsid, they were able to ascertain that polarisation is able to transfer, via ^{1}H spin diffusion to the centre of the capsid, proving that ^{1}H spin diffusion can be used to efficiently transfer polarisation enhancements in large biomolecules.[289] The TM mechanism has not been overly exploited in the high field DNP range, largely due to the necessity for homogenously broadened EPR spectra, while most are observed to be inhomogeneously broadened, leading to a preference for the CE.[290]

5.1.4.5 Covalently Bound Spin-Labels

Previously in the literature a few groups have explored the prospect of spin-labelling proteins with bi-radicals to achieve CE-DNP enhancements as opposed to radicals in solution. Initial experiments came from the work of Vitzthum and Bodenhausen,[291] in

which they attached a biradical to the carboxy terminus of a decapeptide to facilitate the CE-DNP mechanism, with enhancements of 4-fold achieved. Following this work, Mally and Miller[292] experimented with the prospect of endogenous radicals for DNP, by studying the naturally occurring radical system present in the flavin mononucleotide (FMN) semiquinone form of flavodoxin, with the attached monoradical co-factor for exploitation of SE DNP, leading to them achieving enhancements of 15-fold. From Wylie working in the McDermott group, a study into the potential use of monoradical nitroxides covalently bound on the surface of the membrane protein, gramicidin, attached to cysteines specifically chosen so that upon dimerisation and incorporation into the lipid membrane the protein dimer lines up so that a pseudo biradical is formed in which the CE may be achieved. The results achieved DNP enhancements up to 6-fold.[293] Their work was aimed at the prospect of avoiding issues with DNP polarisation agents with suitable solubility for the samples of often complex fluids used in measuring the NMR spectra of membrane proteins in their native states. They were also the first to observe the effect of a single monoradical placed in close enough proximity to facilitate the CE, whose applications are yet to be further explored in the field by other groups. Smith and Long performed DNP enhancement experiments on peptides inside a lipid bilayer by using spin-labelled lipids (a lipid with a monoradical attached to the phosphate head group), to achieve enhancements to a similar degree than that could be achieved with conventional methods, enabling them to reach enhancements up to 8.9.[294] In a similar manner, Fernández-de-Alba and DePaepe used a biradical labelled lipid to facilitate CE DNP, with enhancements up to 8.1 achieved.[295] Taking inspiration from the De Paëpe group where DNP polarising agents had been utilised in novel ways to achieve matrix-free samples such as TOTAPOL bound to the cell wall polymers (peptidoglycan) of *Bacillus subtilis* through electrostatic / van der Waals forces,[296] and TOTAPOL doped microcrystalline cellulose samples[261] where they aimed to increase the concentration of NMR active spins in their samples by reducing dilution from conventional methods of preparation in DNP juice, Voinov and Smirnov designed a variant of the biradical TOTAPOL which could be covalently attached to the cysteine residues of a protein, which they dubbed ToSMTSL (totapol series methane thiosulfonate spin-label).[297] They used this to spin-label lipid reconstituted heptahelical transmembrane protein Anabaena sensory rhodopsin (ASR) and perform CE DNP enhancement experiments to determine the effectiveness as a means of sensitivity improvement. This was in an attempt to overcome problems with sample preparation for DNP, relating to the need for a large portion of the sample to be occupied by a cryo-

protectant matrix, typically glycerol.[298] Consequently, a reduction in the protein concentration that can be achieved once the protein sample is pelleted ready to be packed into a rotor is observed.[261] As with the other implementations of radicals attached covalently to the protein,[293] the polarising agent is now located in a specific location on the surface of the protein, unlike with the use of conventional DNP methods where the polarising agent is dispersed within the matrix, it is difficult to pinpoint exactly where the polarising agent comes closest to the protein. Attachments of the spin-label to the protein itself can alleviate problems with spin-label solubility as well as allow for a larger range in the choice of cryoprotectant that can be used, whereas in general the standard is to use a solution containing 60 % glycerol. DNP enhancements ranging from 4 to 15-fold were achieved depending on sample preparation and was shown to be comparable to an enhancement of just over 15 that was achieved for a typical set up in DNP juice, though they explain how without the use of DNP juice for their sample they can achieve an increase in the amount of protein they can pack into the rotor, improving their overall sensitivity enhancement 4-fold.[297]

5.2 Materials and Methods

5.2.1 Molecular Dynamics

For this project to simulate the movement of two monoradicals covalently bound to the surface of a protein, the CHARMM-GUI double electron-electron resonance (DEER) simulation package was used. The CHARMM36 force field (C36 FF) was used, which was designed for use with lipid bilayers but is applicable for simulation studies of heterogeneous biomolecular systems.[299-300] The crystal structure of GB3, 2LUM was loaded into the software and coordinates of the monoradicals selected by choosing an amino acid residue upon which to transform to the model amino acid with monoradical attached. A time step of 0.001 fs was used, with 20000 frames for each simulation used, for a total of 20 ns of evolution time simulated.

5.2.2 Mutagenesis

As described in Chapter 2.

5.2.3 Protein Expression and Purification

As described in Chapter 2.

5.2.4 Spin-Labelling

The nitroxide spin-label (see Figure 5.7) was attached to [U-^{13}C,^{15}N]A48C-GB3, [U-^{13}C,^{15}N]D46C-A48C-GB3 and [U-^{13}C,^{15}N]E24C-K28C-GB3 via the following method. The DTT present in the purification buffer was removed using a succession of two PD10 desalting columns (GE Healthcare), equilibrated with 25 mM bis-tris, pH 6.5. Directly after the protein was incubated for approximately 16 h at 4 ˚C with a 5-fold molar excess (10 mM) of the nitroxide spin-label (1-Oxyl-2,2,5,5-tetramethylpyrroline-3-methyl) methanethiosulfonate (MTSSL), obtained from enzolifesciences (Exeter, UK). The unreacted reagent was removed with a desalting column in the same manner as before and the proteins were then concentrated using a Viva-Spin 5,000 MWCO appliance.

5.2.5 Mass Spectrometry

The success of the purification of GB3 and its mutants, both with and without nitroxide spin-labels was confirmed by the use of mass spectrometry. Samples were analysed using a

MaXis (Bruker Daltonics, Bremen, Germany) mass spectrometer equipped with a Time of Flight (TOF) analyser. Samples were introduced to the mass spectrometer via a Dionex Ultimate 3000 autosampler and uHPLC pump. Gradient 20% acetonitrile (0.2% formic acid) to 100% acetonitrile (0.2% formic acid) in five minutes at 0.6 mL min. Column, Acquity UPLC BEH C18 (Waters) 1.7 micron 50 x 2.1 mm. High-resolution mass spectra were recorded using positive/negative ion electrospray ionisation.

5.2.6 Circular Dichroism

To confirm that the GB3 mutants, both with and without MTSSL labelling adopted the same secondary structure as in the wild-type, conventional circular dichroism (CD) spectroscopy was performed using a nitrogen purged J-720 spectropolarimeter (Jasco, Tokyo, Japan). GB3 and its mutants were prepared at concentrations between 0.04 to 0.4 mg/mL in 1 mM bis-tris. Spectra were acquired at room temperature using a 1 mm path length fused silica cuvette (Hellma Analytics, Essex, UK) from 260 to 190 nm with 1 nm step resolution, 2 nm bandwidth, 50 nm/min scanning speed, and 1 s response time. The displayed spectra represent an average of 8 scans which were baseline corrected against the sample buffer. Data was clipped when the high tension (HT) voltage exceeded 600 V.

5.2.7 Electron Paramagnetic Resonance

EPR measurements were performed at the University of Southampton Interdisciplinary NMR Centre. cw-EPR spectra were acquired at X-band on a Bruker EMX cw-EPR spectrometer. Each cw-EPR spectrum was acquired with 5 s field sweeps with a central field of 3517 G and sweep width of 200 G, modulation frequency of 100 kHz, modulation amplitude of 1 G, and microwave power of 10 mW, microwave frequency of 9.85 GHz, at 295 K. The sample was pipetted into a 1.1 mm inner diameter quartz capillary (Wilmad LabGlass, Buena, NJ) and inserted into the resonator. EPR simulations were used to determine values for the hyperfine coupling tensor, A, the g-tensor and the correlation time τ_c by the fitting of the X-band spectra using the EasySpin toolbox for Matlab. Initial values were taken from the literature of MTSSL bound to a peptide[107] and a reasonable variation in the values was allowed to fit A, g and τ_c, employing the Nelder-Mead simplex minimization algorithm.

5.2.8 Solid-State NMR

Unless otherwise stated all measurements were conducted at 14.1T on an Agilent DD2 600 MHz NMR spectrometer (Yarnton, UK) equipped with a 1.6 mm triple resonance magic-

angle spinning probe. Samples were spun at 35 kHz, and the temperature regulated to 273 K. For ^{1}H-^{15}N CP the carrier frequencies were set to the centre of the ^{1}H (~5 ppm) and ^{15}N (~120 ppm) spectra. Optimal ^{1}H-^{15}N CP was obtained with a 1.5 ms contact pulse with a ^{1}H field of ~105 kHz and a ^{15}N field of ~70 kHz. For ^{15}N-^{13}C CP the ^{15}N carrier frequency was set to the middle of the amide region (120 ppm) and the ^{13}C to the centre of the C_{α} region (~55 ppm). The spin-lock fields were set to 5/2 times the spinning speed, 87.5 kHz, for ^{15}N and 3/2 times the spinning speed, 52.5 kHz, for ^{13}C. Maximal transfer was observed after 7 ms CP. During ^{15}N-^{13}C CP, 135 kHz continuous wave proton decoupling was applied. Under such conditions, magnetisation transfer occurred exclusively from the ^{15}N to the C_{α}. During all evolution periods 120 kHz SPINAL proton decoupling was applied with phase flip angles of 10° and 5°. All $\pi/2$ pulses on ^{1}H, ^{13}C and ^{15}N were set to at 2.4, 3.2, and 3.1 μs respectively.

All 2D experiments were acquired with States-TPPI phase sensitive detection, employing a ^{15}N spectral width of 5 kHz and 64 complex points. All spectra were externally referenced to the downfield resonance of adamantane at 40.48 ppm compared to DSS.[157] Multidimensional data sets were processed in NMRPipe,[158] prior to analysis and assignment in CCPN Analysis 2.4.[159-160] For the ^{13}C dimension, the data was processed with a Lorentz-to-Gauss window function, with an inverse exponential width of 10 Hz and a Gaussian broadened width of 40 Hz. For the indirect ^{15}N dimension the data was processed with a Lorentz-to-Gauss window function, with an inverse exponential width of 20 Hz and a Gaussian broadened width of 40 Hz. All other processing parameters are given in the corresponding figure legends.

5.2.9 DNP Experiments

DNP experiments were conducted at Goethe University Frankfurt, in the laboratory of Professor Clemens Glaubitz. ^{13}C detected DNP experiments were performed on uniformly labelled ^{13}C-^{15}N GB3 and its spin-labelled mutants; MTSSL-A48C-GB3, MTSSL-D46C-A48C-GB3, MTSSL-E24C-K28C-GB3. Microcrystalline samples (~15 mg) were prepared by adding hexylene glycol to ~30 mg/mL GB3 in pH 6.5 25 mM bis-tris and left for 1-2 days to form crystals. Samples were spun down and supernatant removed and 100 μL of 7:3 gylcerol-d_8/D_2O added and allowed to soak overnight. MTSSL labelling of samples was prepared with both complete labelling and 1 in 5 labelling. For the wild-type (WT) GB3 sample 12.5 mM AMUPol was added to soak solution for WT sample. Solution

samples were prepared by concentrating the sample to ~30 mg/mL in pH 6.5 25 mM bis-tris and adding gylcerol-d_8/D_2O to achieve 60/30/10 gylcerol-d_8/D_2O/H_2O ratio. The samples were centrifuged into Bruker 3.2 mm ZrO_2LT-MAS NMR rotors by removing the supernatant from the pellet and then centrifuging the entire pellet into the rotor. The sample was then spun in an NMR probe at a few kHz at room temperature to ensure an even distribution of the sample on the inner surface of the rotor to maximise the homogeneity of the sample going to cryogenic temperatures.

All MAS-DNP experiments were performed on a Bruker 400 DNP system consisting of a 400 MHz WB Avance II NMR spectrometer, a 263 GHz Gyrotron as the microwave source and a 3.2 mm HCN Cryo MAS probe. All experiments were performed with 8 kHz MAS with a microwave power at the probe of 10.5 W. During DNP experiments the temperature was kept at around 107 K. ^{13}C and ^{15}N CP experiments were recorded using ramped CP from ^{1}H to ^{13}C /^{1}H to ^{15}N during 0.6 ms. The ^{13}C detected double CP experiment (NCA) was performed using ramped CP ^{1}H to ^{15}N of 0.6 ms and a 3 ms specific CP[29] step for the ^{15}N to ^{13}C transfer. The ^{13}C/^{13}C-correlation experiments (PDSD) were recorded using ramped CP from ^{1}H to ^{13}C during 1.4 ms. 10 ms of PDSD mixing time was used. The recycle delays for each spectrum were determined by the determined ^{1}H T_1 relaxation time of the specific sample, due to the varying relaxation properties of each sample. Saturation recovery experiments were recorded with 8 scans. ^{1}H to ^{13}C /^{1}H to ^{15}N CP spectra were recorded with 8 and 32 scans respectively. 2D-NCA spectra were recorded with 8 scans. 2D-PDSD spectra were recorded with 2 scans. Saturation recovery experiments were recorded with τ_1 delays of increments 0.01, 0.1, 0.2, 0.5, 0.7, 1, 1.5, 2, 3, 4, 5, 7, 10, 15, 20, 50 s. DNP enhancement spectra and saturation recovery experiments were analysed and integrated using TOPSPIN 3.5 (Bruker) and matNMR[218]. All 2D-NCA spectra were acquired with States-TPPI phase sensitive detection, employing a ^{15}N spectral width of 2666.67 kHz and 32 complex points. All 2D-PDSD spectra were acquired with States-TPPI phase sensitive detection, employing a direct ^{13}C spectral width of 29761.904 kHz and 592 complex points and an indirect ^{13}C spectral width of 25000 kHz and 450 complex points. All spectra were externally referenced to the downfield ^{13}C resonance of adamantane at 40.48 ppm compared to DSS.[157] SPINAL-64 decoupling[46] at 100 kHz was employed for all experiments during acquisition.

5.3 Results and Discussion

5.3.1 Design of Double Cysteine Mutants for Optimal DNP Enhancement

To identify potential candidates for double cysteine mutants where MTSSL can be introduced such that an optimal geometry[257] to facilitate the CE-DNP mechanism can be found molecular dynamics simulations were performed. To perform molecular dynamic simulations CHARMM-GUI was utilised. CHARMM-GUI is a web-based graphical user interface which can be exploited in order for one to compute a variety of molecular simulation systems and input files to assist the usage of common and advanced simulation techniques. CHARMM-GUI uses CHARMM software,[301] which was designed as an academic research program for worldwide macromolecular dynamics and mechanics. The project was instigated at Harvard University from the research group of the Nobel Laureate Professor Martin Karplus.[302] CHARMM is designed to calculate energy minimisation and standard molecular dynamics. Potential energy functions are available for several biologically relevant systems such as proteins, nucleic acids, lipids and carbohydrates. CHARMM also possess functionality for varying chemical and conformational free energy calculations.

Using CHARMM[301], the movement of the protein, with the attached pseudo atoms, which represents the geometry and forcefield for the MTSSL, was able to be modelled, and from this a distribution of distances and angles between the two unpaired electrons could be determined (see Table 5.1). The simulations were conducted as a single protein molecule free in solution. However, as both MTSSL units are to be tethered in the same protein molecule it is a suitable model to determine an average of distances between MTSSL units attached to side-chains. It is clear that crystal packing may influence the conformation space available to MTSSL, therefore, this is addressed in part by inspection of the crystal lattice structure. From these distributions two suitable candidates (see Figure 5.4) were selected, the double cysteine mutants, E24C-K28C-GB3 and D46C-A48C-GB3, as they seemed to possess the greatest potential for facilitating the cross-effect, in that they had a good probability of having their electron orientation orthogonal, as well as being in close enough proximity to effectively elicit the CE (see Figure 5.5). The distance between the unpaired electrons being short enough was given preference over the condition of

orthogonality when selecting spin pairs as the simulation was limited in that the MTSSL monoradical was modelled as a single pseudo atom with the electron facing in a particular direction and changing as the molecule moves through space. Confidence that the placement of the spin-labels would be in a solvent accessible region and unlikely to hinder crystal formation was gained through examination of the protein structure using the crystal structure visualisation software, Chimera.[303] The crystal structure of protein G IgG-binging domain III, 2IGD, which is analogous to GB3 with the addition of a small amino acid tail of MTPAVTT at the carboxyl terminus of the protein (with the MQ amino acids in GB3 replaced by TT in the 2IGD structure) was loaded into Chimera. The analysis suggested that the MTSSL attachments would have room within the aqueous region of the crystal structure so as not to adversely affect crystal formation.

To determine the shell of sites where the signal may be quenched, a 20 Å shell was visualised around each MTSSL attachment point for the spin-labelled proteins. In addition to the double cysteine mutants for study of the CE, it was decided it would be a fruitful investigation to also prepare a single mutant for attachment of the nitroxide radical so that electron-electron interactions through spin-labels on separate protein molecules coming in close proximity could be observed. The single A48C-GB3 mutant was selected and to determine whether there would be potential for the spin-labels on neighbouring A48C-GB3 bound MTSSL molecules to be close enough in proximity for a CE to be achieved the attachment of the spin-label at this site was examined as with the double cysteine mutants and with a 20 Å shell created to visualise potential points where a condition would be possible.[266] Within this 20 Å shell it was shown that it would be possible for the MTSSL molecules to come in close enough proximity for some level of interaction to be achieved (Figure 5.6), though nothing could be said if a suitable orientation of the unpaired electrons could be achieved.

Table 5.1 Electron-electron distances and orientation angles determined for selected spin pairs simulated with CHARMM. Distributions quoted from the minimum and maximum probability at half the maximum value. Values quoted as mean and standard deviation.

Mutant pair examined	Unpaired electron- electron distance /Å	Unpaired electron- electron orientation /°
M1 E56	35.5±5.0	118±43
G9 T11	13.8±3.6	77±32
K10 T11	14.0±4.5	80±40
T11 L12	14.5±5.0	85±45
T11 K13	16.2±3.9	105±33
E24 K28	11±5.0	60±39
A26 K28	16.1±2.6	105±36
E27 K28	14.3±3.8	87±39
K28 A29	15.3±4.3	93±43
D46 A48	11.8±5.3	62±41
D46 T49	15.9±3.9	101±41
D47 A48	15.5±4.0	98±43
A48 T49	14.0±4.5	83±43
A48 K50	16.2±3.6	98±43

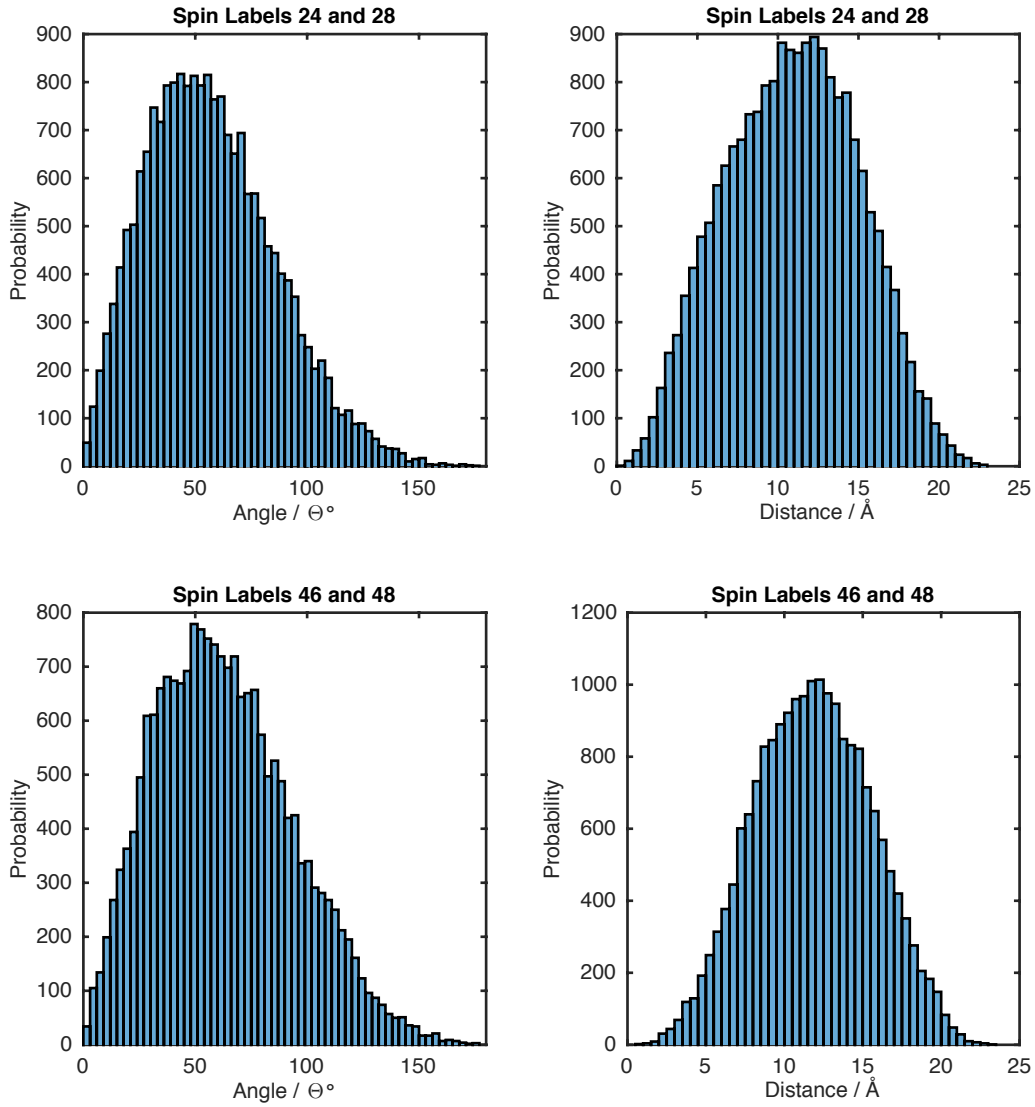

Figure 5.4 Histograms for the distribution of angles of orientation and distances between unpaired electrons simulated on pseudo atoms placed on specific GB3 mutants. Calculated angles and distance measurements for MTSSL radicals attached to the surface of GB3 at specific mutation points. Simulation carried out using CHARMM.[301]

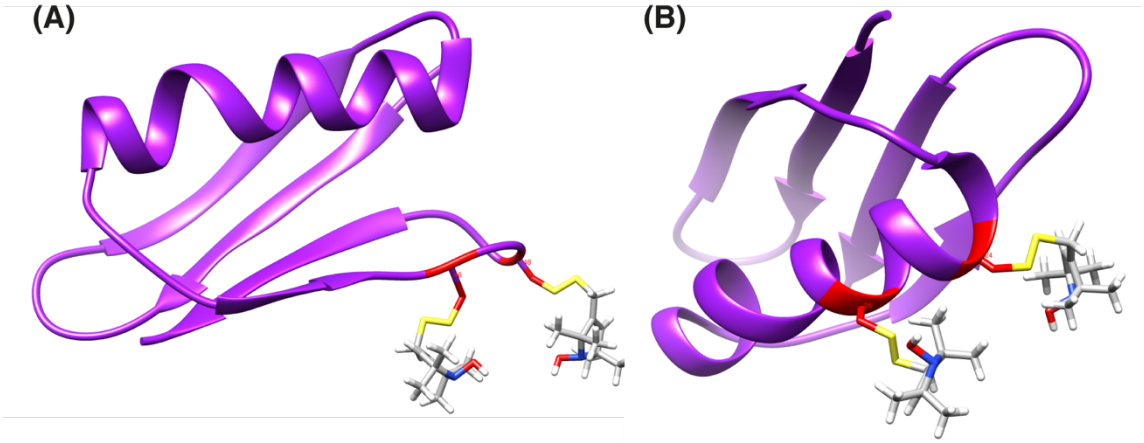

Figure 5.5 Crystal structures showing attachment of MTSSL to the double mutants shown for the D46C-A48C-GB3 mutant (A) and E24C-K28C-GB3 mutant (B).

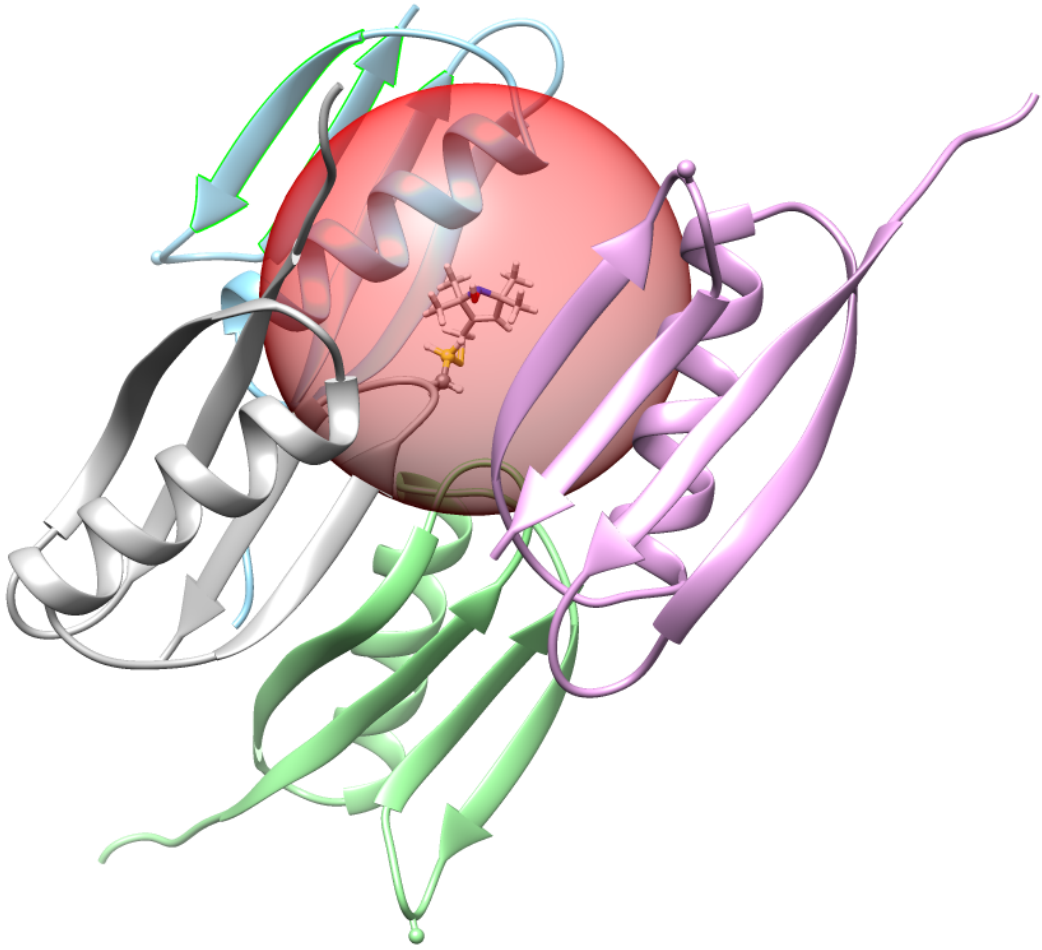

Figure 5.6 Crystal structure of MTSSL-A48C-GB3 showing crystal packing to show the inter-protein interactions for the MTSSL monomers with an interaction sphere at 20 Å.

5.3.2 Spin-Labelling

Spin-labelling was carried out as detailed in § 5.2.4, where GB3 cysteine mutants that had been designed, expressed and purified were reacted with the MTSSL molecule in a sulfonyl reaction to lead to the attachment of the spin-label to the sulphur atom of the cysteine residue of the protein (See Figure 5.7).[304] This procedure is often utilised in EPR for use in double electron-electron resonance (DEER) experiments.[105]

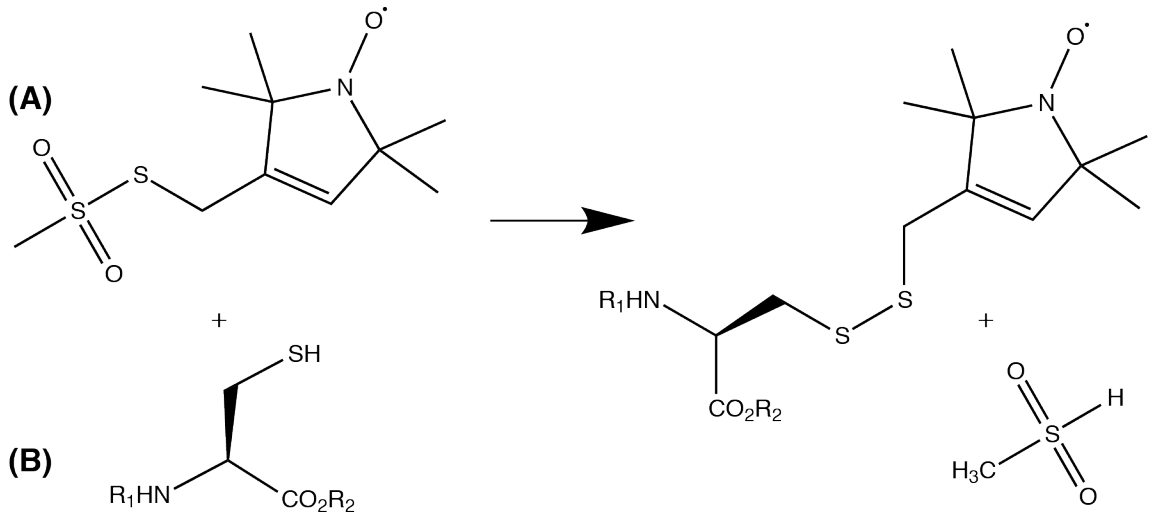

Figure 5.7 Reaction scheme for the spin-labelling of a cysteine residue within a protein. MTSSL reacts in a sulfonyl reaction with the cysteine residue of a protein (B). R_1 denotes the amino acid residues in the direction of the N-terminus and R_2 the amino acid residues in the direction of the C-terminus.

The labelling was then confirmed with mass spectroscopy (MS) to show that for the A48C-GB3 single mutant, the molecular weight of the protein had increased by that of 186 Da. In addition, for the double mutants, D46C-A48C-GB3 and E24C-K28C-GB3, the mass was increased by 372 Da. The increases in mass corresponds to the attachment of one and two MTSSL units respectively (Table 5.2 and Figure 5.8).

Table 5.2 Calculated molecular weights for GB3 samples.

Protein sample	Chemical formula	MW /Da	MTSSL labelled MW /Da
WT-GB3	$C_{274}H_{427}N_{69}O_{93}S_1$	6208	N/A
[U-^{15}N]WT-GB3		6276	N/A
[U-^{13}C,^{15}N]WT-GB3		6548	N/A
A48C-GB3	$C_{274}H_{427}N_{69}O_{93}S_2$	6240	6426
[U-^{15}N]A48C-GB3		6308	6494
[U-^{13}C,^{15}N]A48C-GB3		6580	6766
D46C-A48C-GB3	$C_{273}H_{427}N_{69}O_{91}S_3$	6228	6600
[U-^{15}N]D46C-A48C-GB3		6296	6668
[U-^{13}C,^{15}N]D46C-A48C-GB3		6567	6939
E24C-K28C-GB3	$C_{269}H_{418}N_{68}O_{91}S_3$	6157	6529
[U-^{15}N]E24C-K28C-GB3		6224	6596
[U-^{13}C,^{15}N]E24C-K28C-GB3		6491	6863

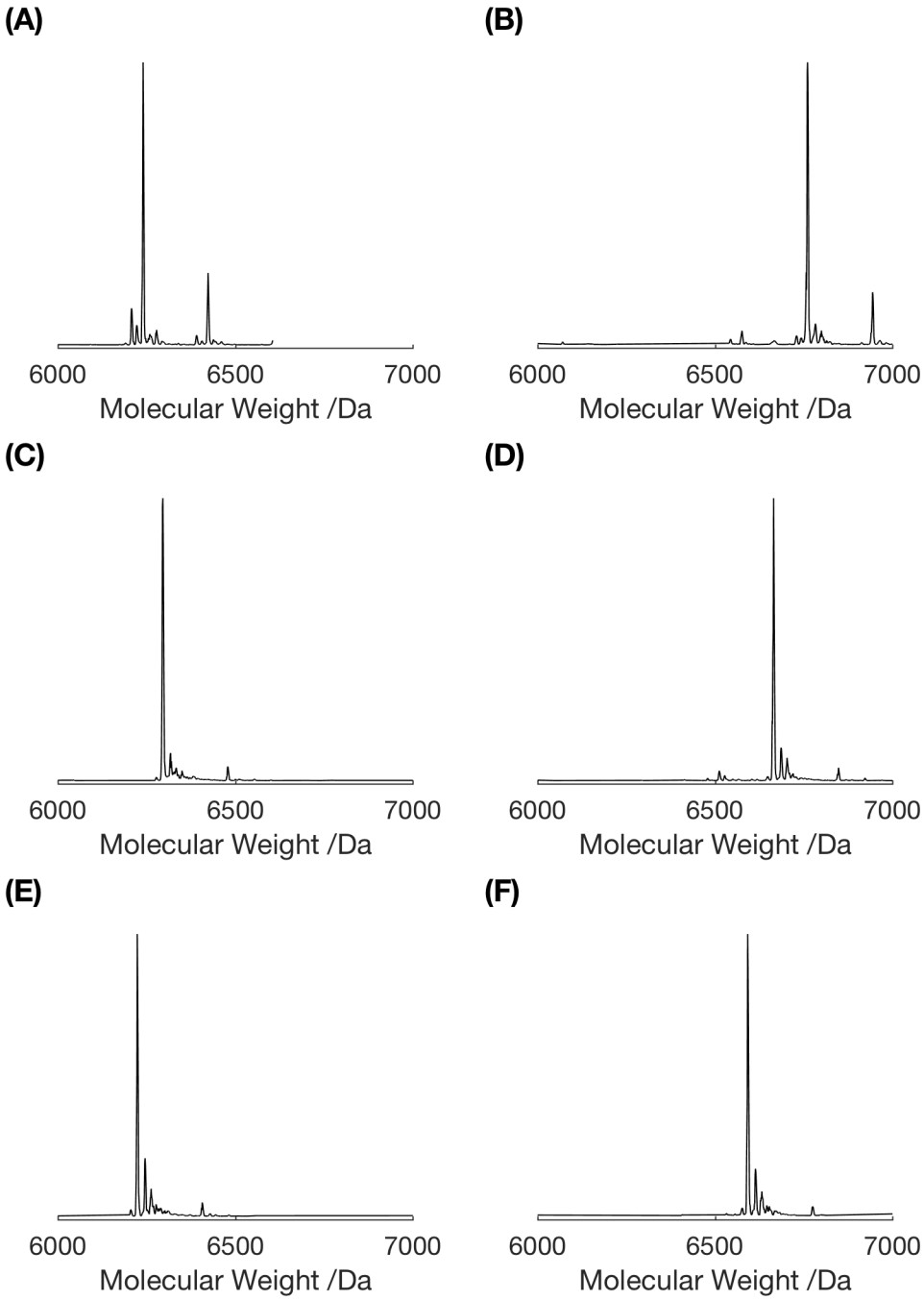

Figure 5.8 Entropy deconvolution mass spectra of GB3 cysteine mutants to confirm spin-labelling with the large peak corresponding to the molecular weight of the particular sample. Unlabelled A48C-GB3 spectrum (A), [U-^{13}C,^{15}N]MTSSL-A48C-GB3 spectrum (B), [U-^{15}N]D46C-A48C-GB3 spectrum (C), [U-^{15}N]MTSSL-D46C-A48C-GB3 spectrum (D), [U-^{15}N]E24C-K28C-GB3 spectrum (E), [U-^{15}N]MTSSL-E24C-K28C-GB3 spectrum (F).

To confirm that the GB3 mutants, both with and without MTSSL labelling adopted the same secondary structure as in the WT, conventional circular dichroism (CD) spectroscopy was performed, this technique enables one to determine the percentage of β-sheet and α-helix components present in a protein. In our case, we wanted to be able to compare this to WT-GB3, a protein of known β-sheet and α-helix components. The spectra gave supporting evidence that in solution the mutants and their corresponding spin-labelled counterparts adopted the same structure as the wild-type species (Figure 5.9). It is worth noting that for the spin labelled double mutants an extended region of intensity can be observed at approximately 210 nm. This region is indicative of an undefined structure and may suggest a slight reduction in structural stability. This seems to be particularly prominent for the MTSSL-D46C-A48C-GB3 mutant (Figure 5.9C).

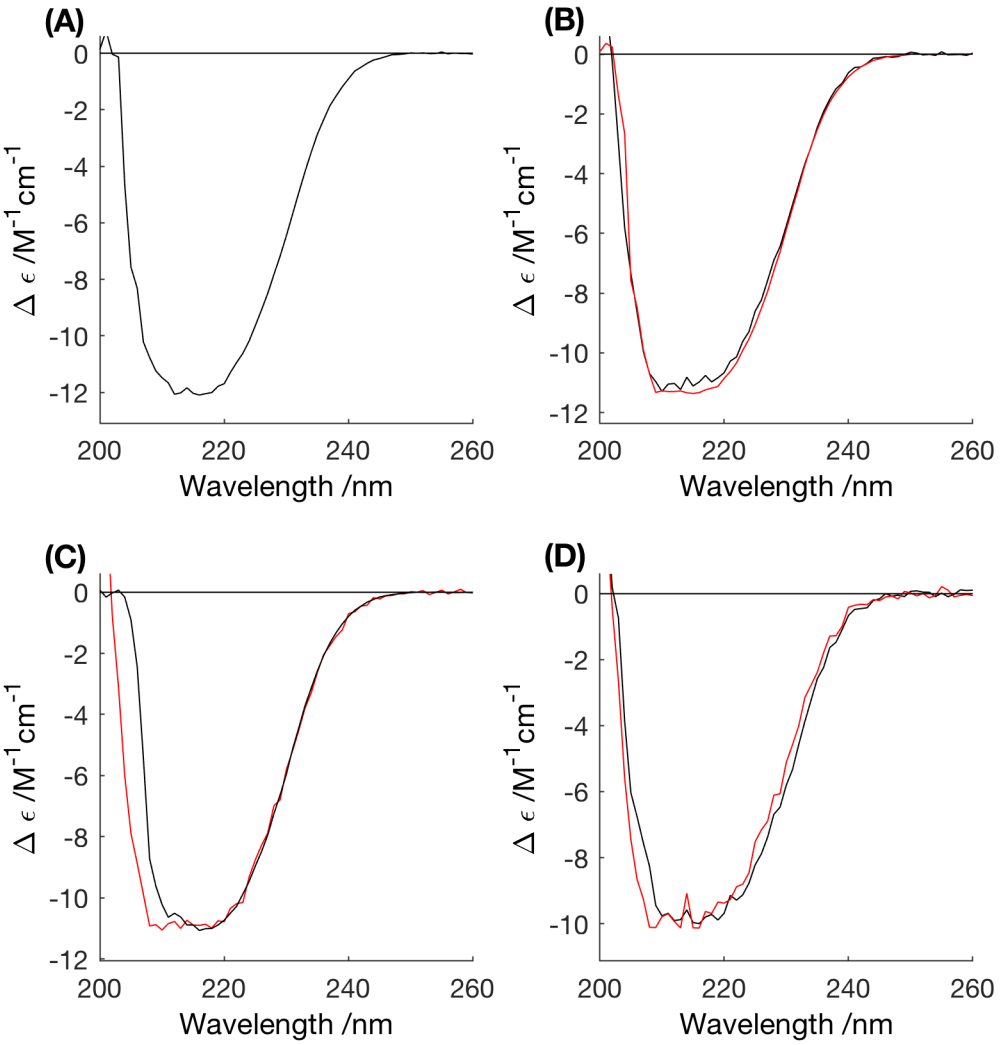

Figure 5.9 Circular dichroism spectra for GB3 samples, WT-GB3 (A), A48C-GB3 (B, black), MTSSL-A48C-GB3 (B, red), D46C-A48C-GB3 (C, black), MTSSL-D46C-A48C-GB3 (C, red), E24C-K28C-GB3 (D, black), MTSSL-E24C-K28C-GB3 (D, red). To investigate whether the protein structure of the mutants with and without spin-labelling is analogous to that of the wild-type protein. Where $\Delta\epsilon$ is delta epsilon, the molar circular dichroism which is the per residue molar absorption units of CD obtained from the machine units by taking into account protein concentration, residue number and path length.[305]

5.3.3 EPR Characterisation

To characterise the MTSSL labelled mutants cw-EPR was employed. This technique allows one to observe the electron spin of a paramagnetic species by inciting a resonance. To determine that the MTSSL spin-label present in the sample was covalently bound to protein, a control experiment where WT-GB3 was reacted with a 5X excess of MTSSL and desalted as described in the materials section was conducted. As expected no EPR signal was observed from such sample, indicating that the unbound MTSSL had been completely removed and that any signal observed in the following mutant samples must be that of protein-bound MTSSL. EPR spectra were recorded at varying concentrations. The spectra were integrated and the intensity of the peaks determined (see Figure 5.10). From this, it can be determined that concentration effects of the linewidth can be neglected as intensity is linear with concentration so broadening from increased viscosity is limited.

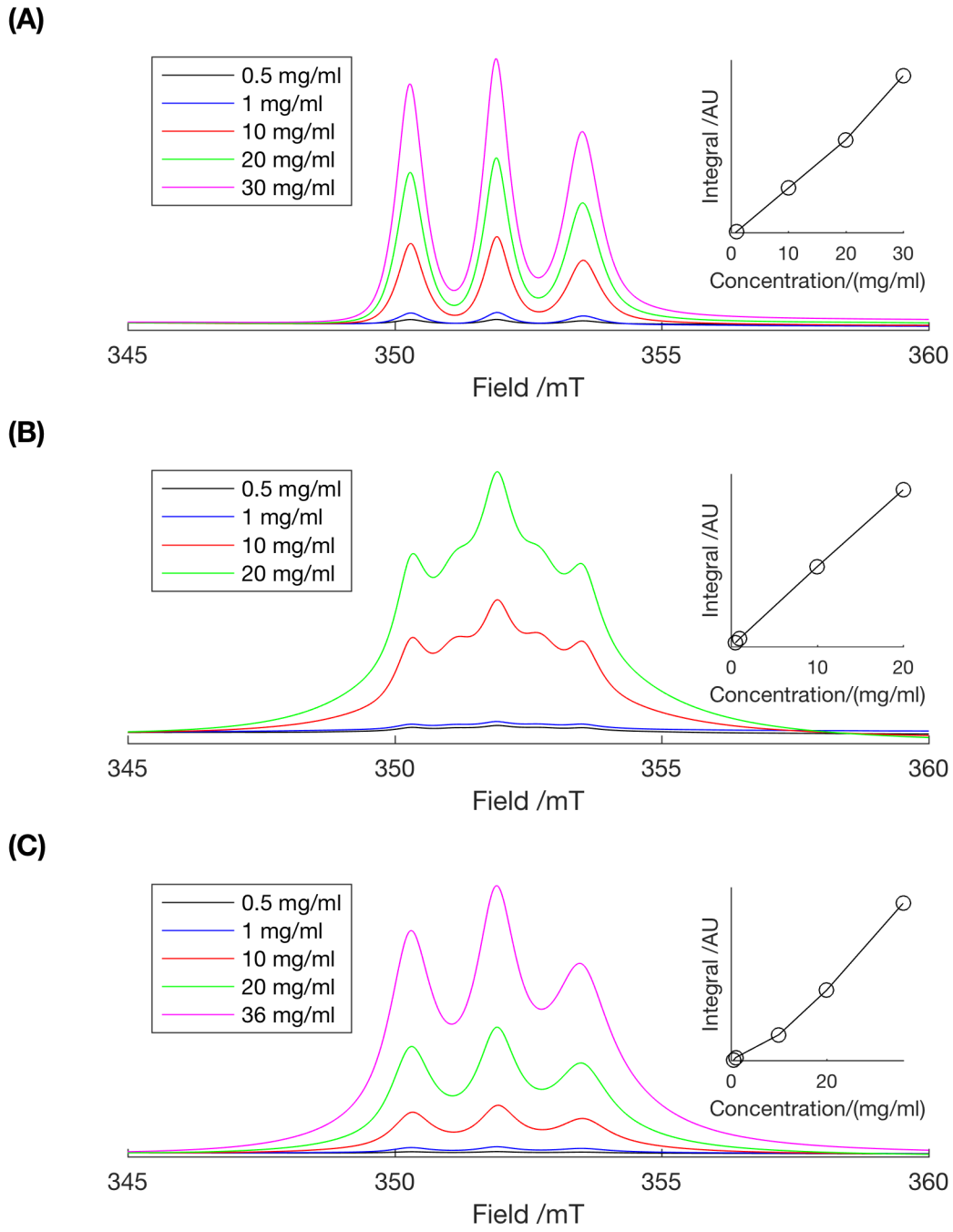

Figure 5.10 Integrated EPR spectra of MTSSL labelled mutants. Inset figure shows the intensity of the peak region. Spectra for MTSSL-A48C-GB3 (A), MTSSL-D46C-A48C-GB3 (B), MTSSL-E24C-K28C-GB3 (C).

Following this, EPR spectra for each of the mutants at 20 mg/mL protein concentration were recorded, along with an aqueous sample of 1 mM MTSSL for reference of the spin-label unattached to a protein (see Figure 5.11). For each of the spectra, as characteristic of

a nitroxide radical, we see three transitions (except for the MTSSL-D46C-A48C sample where additional splittings are observed resulting in 5 transitions present) present due to the hyperfine interaction between the unpaired electron with the ^{14}N nuclei. In comparison to MTSSL in solution, where the linewidth of the positive peak is 0.1 mT, for MTSSL-A48C-GB3 linewidths are of 0.5 mT. Similarly, for MTSSL-D46C-A48C-GB3 linewidths of 0.4 mT are observed for each of the five transitions. For MTSSL-E24C-K28C-GB3 linewidths of 0.7 mT for each of the three transitions were observed. The linewidths of each transition vary slightly in linewidth. A48C-GB3 exhibited linewidths of 0.4, 0.5, 0.6 mT in order of increasing magnetic field for each of the three transitions observed. Similarly, for MTSSL-D46C-A48C-GB3 linewidths of 0.5, 0.4, 0.4, 0.4, 0.4 mT for each of the five transitions were observed. For MTSSL-E24C-K28C-GB3 linewidths of 0.6, 0.6, 0.8 mT for each of the three transitions were observed.

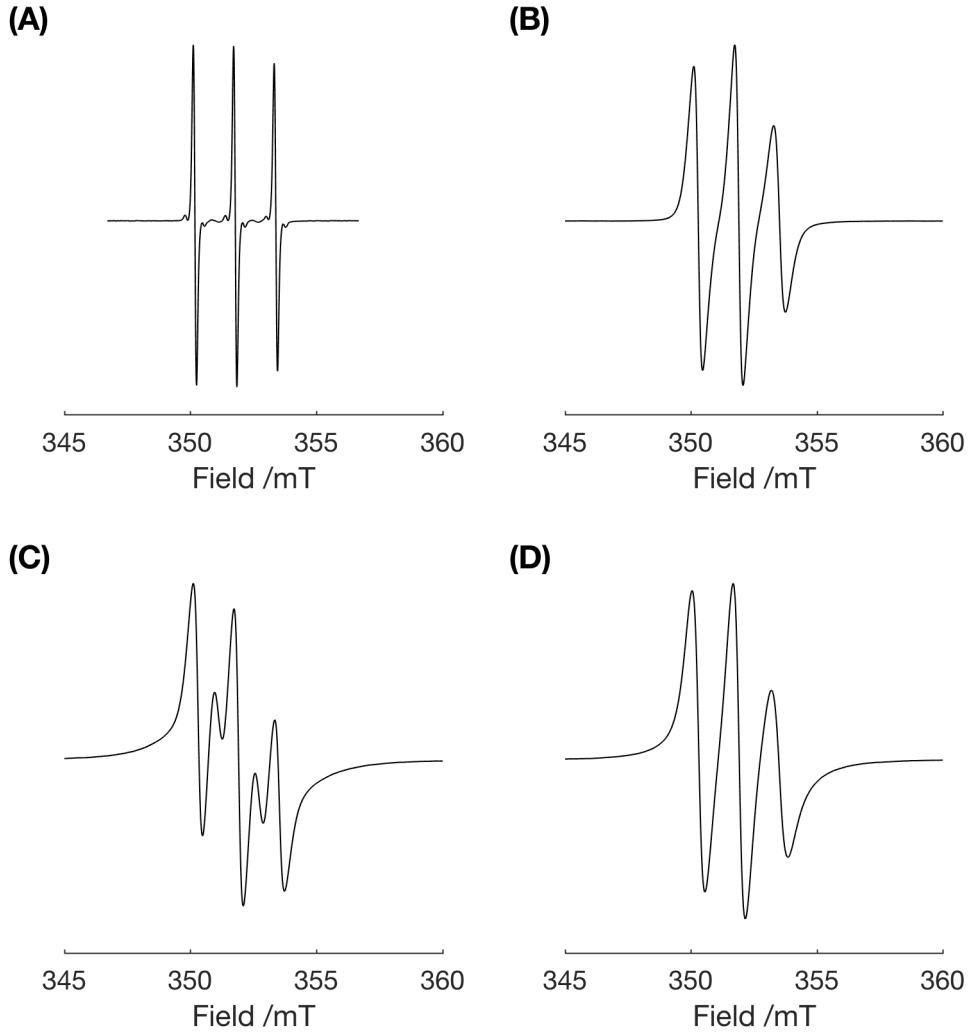

Figure 5.11 EPR spectra of MTSSL containing samples, for 1 mM MTSSL (A), 20 mg/ml MTSSL-A48C-GB3 (B), 20 mg/ml MTSSL-D46C-A48C-GB3 (C), 20 mg/ml MTSSL-E24C-K28C-GB3 (D).

The broadening effect on the spectra, owing to the attachment of the spin-label to a large biomolecule, arises due to a reduction in the rate of tumbling of the spin-label, quantified by the correlation time, τ_c (see Figure 1.11 for example of effect of increased τ_c on the EPR spectra). It was observed that the EPR spectra of the single mutant, A48C-GB3 with one MTSSL molecule, when compared to the double mutant, MTSSL-E24C-K28C-GB3, had a slightly less broad resonance. This was also true for the MTSSL-D46C-A48C-GB3. However, the appearance of an additional splitting could be seen in the MTSSL-D46C-A48C-GB3 spectra but this was not present in the other double mutant, MTSSL-E24C-K28C-GB3. These additional line broadening effects seen in the double mutants are likely due to electron-electron dipolar interaction which can lead to broadening in addition to a

change in the observed line shape (see Figure 5.12). Indeed, these electron-electron interactions experienced in the double mutant samples lead to complicated effects on the EPR line shape, effects in which the scope of this work was not sufficient to cover.[306]

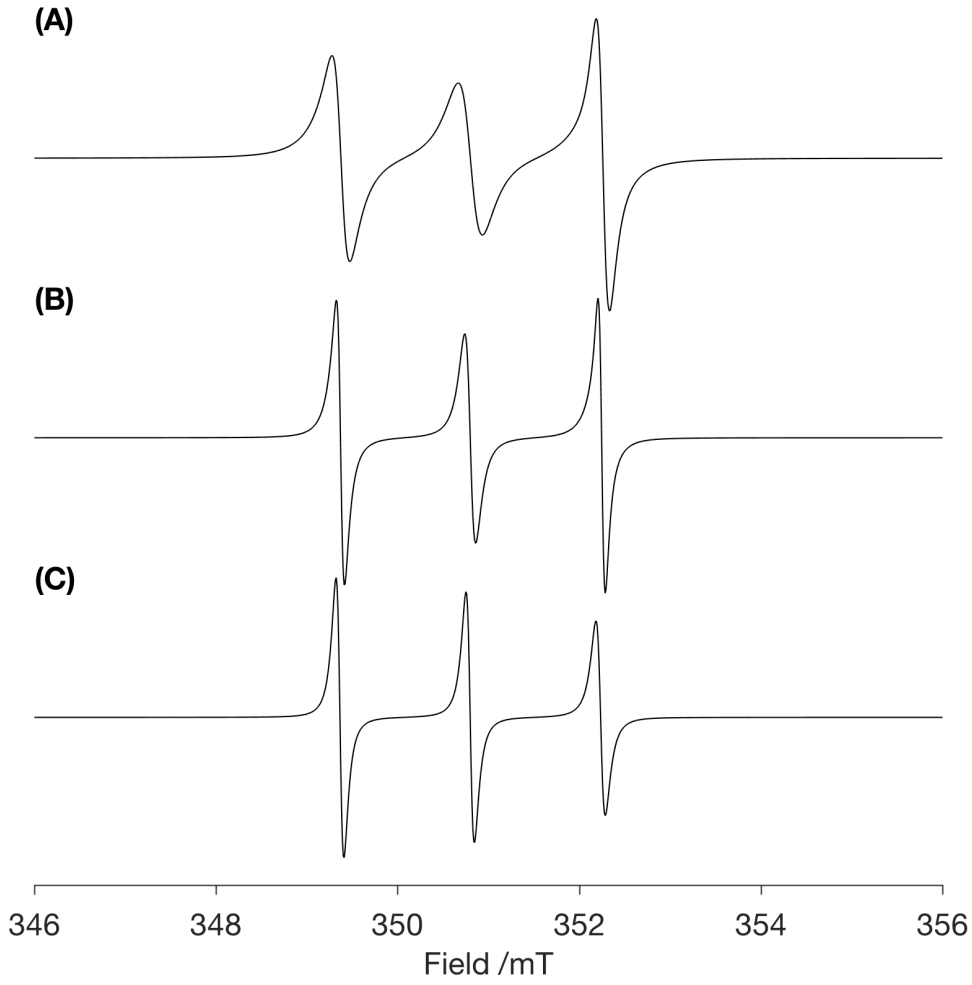

Figure 5.12 Simulation of the effect of the electron-electron dipolar interaction on the EPR spectra. With distances at 7.5 Å (A), 10 Å (B), 20 Å (C). [307] $g_{e1(xyz)}$; 2.0086, 2.0066, 2.0032, $A_{e1(x,y,z)}$; 6.23, 6.23, 35.7 mT, $g_{e2(xyz)}$; 2.0086, 2.0066, 2.0032, $A_{e2(x,y,z)}$; 6.23, 6.23, 35.7 mT, linewidth; 0.1 mT, τ_c; 0.01 ns.[106] Parameters from MTSSL bound peptide.[107]

This broadening of the EPR resonance for the double mutant in comparison to the single mutant is highlighted in Figure 5.13, where the two spectra are overlaid. It is necessary to note that there may also be variability in the spectra obtained from for the mutants depending on where the spin-label is in the chain, therefore a direct comparison of the line shapes of the two mutants should be taken with a sceptical view. Analysis of the

differences between the two spectra highlights that the central transitions seem to be quite similar but both the relative intensity and position of the two side peaks varies between mutants. It has previously been demonstrated that detailed analysis of variation in relative line heights and linewidths may be used to compute useful information regarding the interactions taking place and in the case of proteins containing multiple paramagnetic centres, distances can be determined.[306] Computational software (EasySpin[106]) was used to determine the values of the g-tensor, $g_{(x,y,z),}$ hyperfine interaction, $A_{(x,y,x),}$ and the rotational correlation time, τ_c for the mutants (see Figure 5.14).

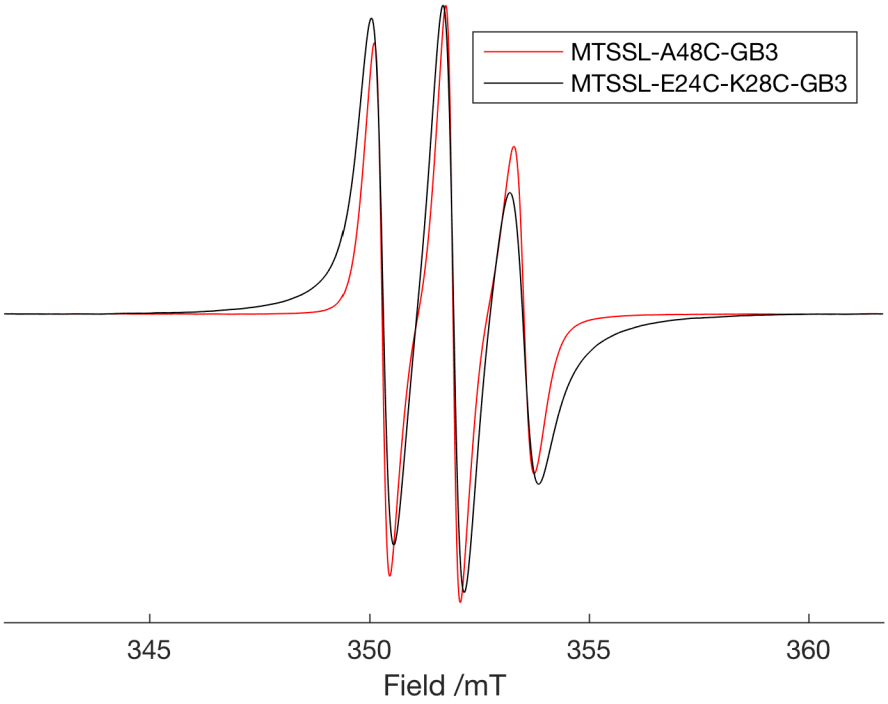

Figure 5.13 Comparing spectra of single and double mutant, 20 mg/mL MTSSL-A48C-GB3 (red), 20 mg/mL MTSSL-E24C-K28C-GB3 (black).

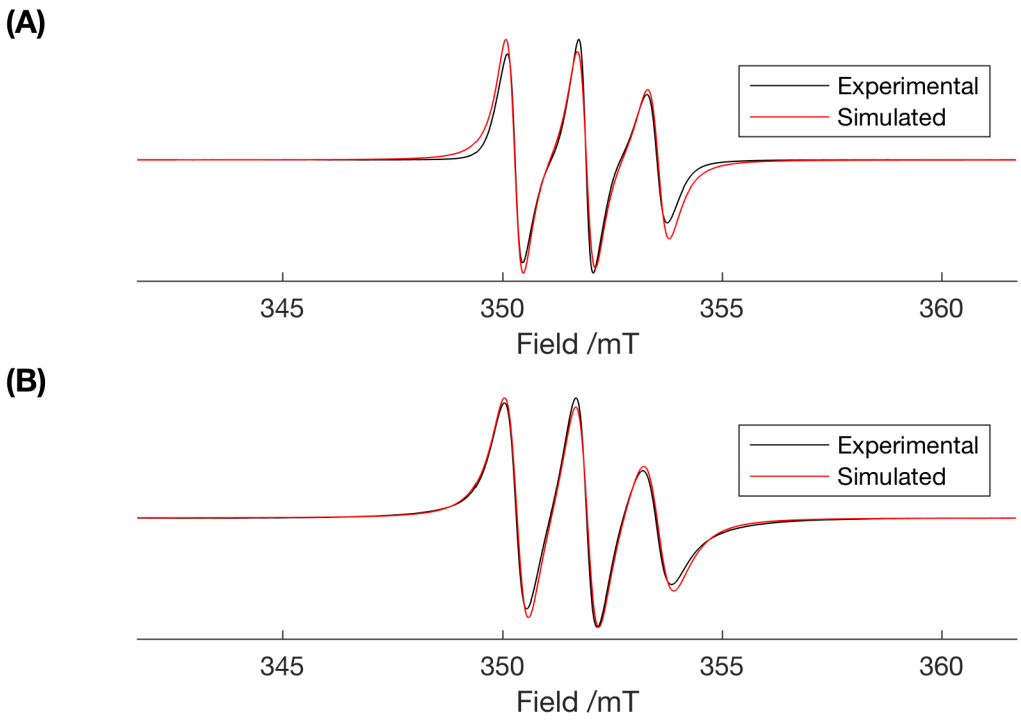

Figure 5.14 Fitting of spectra of single and double mutant, 20 mg/mL MTSSL-A48C-GB3 (A), 20 mg/mL MTSSL-A48C-GB3 $g_{(x,y,z)}$ 1.9810 ,2.0340, 2.0010, $A_{(x,y,x)}$ 17.2941, 14.4280, 105.9942 MHz, τ_c 0.31 ns. MTSSL-E24C-K28C-GB3 $g_{(x,y,z)}$ 1.9887, 2.0244, 2.0024, $A_{(x,y,x)}$ 17.2609, 13.9424, 104.4410 MHz, τ_c 0.81 ns (B).

5.3.4 NMR Characterisation at Ambient Temperature

Prior to DNP measurements, we characterised the mutants with and without spin-label to assess if the mutant proteins folded and crystallised correctly and to assess the effect of the free radicals on the relaxation behavior of the protein. Both 1D- and 2D-ssNMR experiments were utilised with ^{1}H $R_{1,}$ ^{15}N $R_{1,}$ ^{15}N $R_{1\rho}$ used to characterise the relaxation and level of quenching present.

5.3.4.1 1D-CP Spectra of Double Mutants

To characterise the mutant GB3 samples, 1D ^{1}H to ^{13}C and ^{1}H to ^{15}N spectra were recorded both with and without complete MTSSL labelling of the cysteine residues (Figure 5.15 and Figure 5.16). For the unlabelled mutant spectra, for the ^{1}H-^{13}C-CP spectrum, ^{13}C linewidths (from FWHM) of 0.5 ppm can be observed from the spectra, while in the ^{1}H-^{15}N-CP spectrum, ^{15}N linewidths of 1 ppm can be observed from the spectra. Within these spectra, it is clear to see well-resolved lines corresponding to individual resonances. From inspection of the profile of the spectra of the MTSSL spin-labelled mutants, it is clear that the linewidths are drastically broadened due to the presence of the spin-label, with the absence of clearly resolved lines. For the ^{1}H-^{13}C-CP spectrum of the MTSSL-E24C-K28C-GB3 sample (Figure 5.15, B) the linewidth of the C_{CO} envelope was 4.7 ppm with regions of the C_{α} envelope resolved up to 2.9 ppm. For the ^{1}H-^{15}N-CP spectrum of the MTSSL-E24C-K28C-GB3 sample (Figure 5.15, D) the linewidth of the backbone envelope was 11.8 ppm with the side chain region at 1.4 ppm. For the ^{1}H-^{13}C-CP spectrum of the MTSSL-D46C-A48C-GB3 sample (Figure 5.16, B) the linewidth of the C_{CO} envelope was 4.1 ppm with regions of the C_{α} envelope resolved up to 2.6 ppm. For the ^{1}H-^{15}N-CP spectrum of the MTSSL-D46C-A48C-GB3 sample (Figure 5.16, D) the linewidth of the backbone envelope was 12.7 ppm with the side chain region at 1.5 ppm. It is interesting to note the consistently broader linewidths in the MTSSL-E24C-K28C-GB3 sample in comparison to the MTSSL-D46C-A48C-GB3 sample. With the increased linewidths observed in the MTSSL labelled versions of the mutant crystals, this is likely attributed to the influence of the paramagnetic nitroxide radical influencing the T_2 relaxation of the protein. This increase in the homogeneous linewidth by T_2 relaxation is demonstrated in the following relaxation data. This drastically reduced T_2 also led to a reduced signal that could be acquired for each sample due to the quenching of the residues, making acquisition with many scans necessary. Fortunately, for the low-temperature DNP studies that will follow, it is likely that the electronic relaxation rate will be less at a lower temperature,

resulting in a less profound impact of quenching. This is a result of the electronic relaxation rate dependence of the T_2 relaxation, which is in turn dependent on temperature.

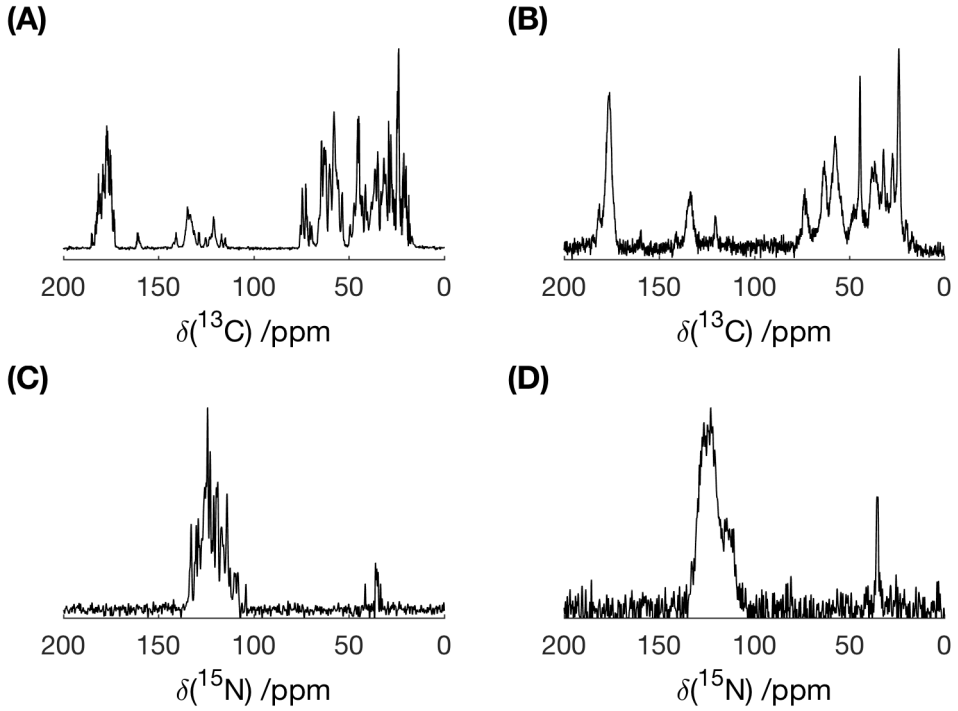

Figure 5.15 E24C-K28C-GB3 mutant 1D-spectra. 1D-^{1}H to ^{13}C CP spectrum of E24C-K28C-GB3 (A), 1D-^{1}H to ^{13}C CP spectrum of MTSSL-E24C-K28C-GB3 (B), 1D-^{1}H to ^{15}N CP spectrum of E24C-K28C-GB3 (C), 1D-^{1}H to ^{15}N CP spectrum of MTSSL-E24C-K28C-GB3 (D).

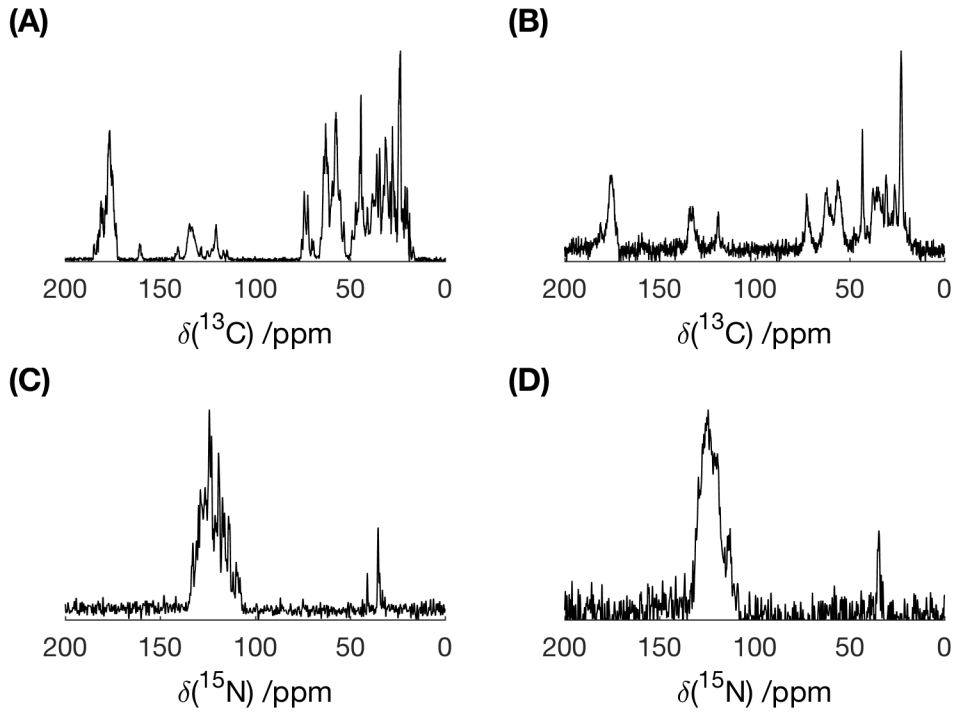

Figure 5.16 D46C-A48C-GB3 mutant 1D-spectra. 1D ^{1}H to ^{13}C CP spectrum of D46C-A48C-GB3 (A), 1D ^{1}H to ^{13}C CP spectrum of MTSSL-D46C-A48C-GB3 (B), 1D ^{1}H to ^{15}N CP spectrum of D46C-A48C-GB3 (C), 1D ^{1}H to ^{15}N CP spectrum of MTSSL-D46C-A48C-GB3 (D).

5.3.4.2 Relaxation Measurements of GB3 Samples at Ambient Temperatures

The ^{1}H R_1 value for the WT-GB3 sample was 1.58 s^{-1}. With the introduction of the cysteine mutations, the ^{1}H R_1 value was not significantly affected. The value for D46C-A48C-GB3 ^{1}H R_1 was 1.86 s^{-1} (Table 5.3). Comparing the ^{1}H R_1 between the WT and mutant proteins we see no significant variation in relaxation behaviour. This is as expected as both samples have no additional source of relaxation provided to the sample. With the covalent attachment of MTSSL bound to the sample, the ^{1}H R_1 is enhanced as would be expected, with a ^{1}H R_1 of MTSSL-D46C-A48C-GB3 of 6.45 s^{-1} (MTSSL-D46C-A48C-GB3, Table 5.3). Though MTSSL is characterised as a T_2 relaxation agent by its electronic relaxation rate, in close proximity to a nucleus a T_1 relaxation effect is exerted, as described by the Solomon–Bloembergen equations (see Chapter 4 for discussion of relaxation effects). The 1 in 5 MTSSL-A48C-GB3 ^{1}H R_1 is slightly lower than that of the double mutant, at 5.22 s^{-1}, as expected due to the reduction in radical density. Obtaining the data for the MTSSL-D46C-A48C-GB3 and 1 in 5 MTSSL-A48C-GB3 samples proved more difficult due to the lower intensity signal as a result of the quenching of the signal by

the spin-label. For the ^{15}N R_1 measurements the WT-GB3 and D46C-A48C-GB3 samples are within error of each other (see Table 5.3). For the MTSSL-D46C-A48C-GB3 the relaxation rate is enhanced in comparison to that of WT-GB3 (see Table 5.3). Comparing the ^{15}N $R_{1\rho}$ for the WT-GB3 and D46C-A48C-GB3 samples the two values are within error of each other. Comparing the two D46C-A48C-GB3 samples, the addition of the bound MTSSL relaxation agent has had the expected effect of enhancing the $R_{1\rho}$ relaxation rate. However, in the case of the 1 in 5 MTSSL-A48C-GB3 sample the relaxation rate has not significantly increased, potentially due to ^{15}N $R_{1\rho}$ not being as sensitive to relaxation enhancement than proton relaxation measurements. Comparing the ^{15}N $R_{1\rho}$ relaxation rate of that of the two MTSSL bound samples the results for the double mutant are as such due to the high concentration of relaxation agent. However, the diluted 1 in 5 single mutant did not demonstrate a significant increase in relaxation over the undoped samples. This could be due to the fact that the MTSSL-D46C-A48C-GB3 sample is fully labelled with two MTSSL molecules attached to each cysteine. In contrast, the A48C-GB3 sample has only 1 in 5 of the protein molecules with a spin-label attached to a single cysteine. Moreover, as mentioned above, while the ^{1}H R_1 value for the diluted single mutant showed an increase, neither of the ^{15}N relaxation measurements showed significant increase on doping (see Table 5.3).

Table 5.3 Values for ^{1}H R_1, ^{15}N R_1, ^{15}N $R_{1\rho}$ of various GB3 samples. Upper and lower 95% confidence limits are given in brackets.

Sample	^{1}H R_1 /s^{-1}	^{15}N R_1 /s^{-1}	^{15}N $R_{1\rho}$ at 20 kHz spin lock/ s^{-1}
WT-GB3	1.58 (1.51, 1.64)	0.053 (0.41, 0.065)	19.4 (18.3, 20.5)
D46C-A48C-GB3	1.86 (1.67, 2.04)	0.057 (0.039, 0.074)	23.6 (18.9, 28.4)
MTSSL-D46C-A48C-GB3	6.45 (4.36, 8.55)	0.11 (0.06, 0.16)	72.9 (57.3, 88.5)
A48C-GB3-1 in 5 MTSSL	5.22 (4.73, 5.70)	0.042 (0.025, 0.059)	24.4 (20.1, 28.8)

5.3.5 2D-^{15}N/^{13}C Correlation Spectra of GB3 Mutant Samples

To determine the effect of the mutagenesis of WT-GB3 on its crystal structure and corresponding peak positions in the nitrogen-carbon-correlation spectrum, 2D-NCA and 2D-NCO spectra were recorded for several mutant samples. The basis of the NCA and NCO experiments is the utilisation of double cross-polarisation (CP),[29, 308] in which polarisation generated on the high gyromagnetic ratio nuclei of the ^{1}H is subsequently transferred to the nearby ^{15}N nuclei via CP. From this point, a second CP step is employed to transfer the magnetisation from the ^{15}N nuclei to the nuclei of either $^{13}C_{\alpha}$ or $^{13}C_{CO}$, to perform an NCA or NCO experiment respectively. The magnetisation transfers correlate the protein backbone ^{15}N nuclei with either $C_{\alpha}^{(i)}$ for an NCA or $C_{CO}^{(i-1)}$ for an NCO. NCA and NCO in combination with ^{13}C/^{13}C-correlation experiments are often implemented in assigning and localising the connectivities present between amino acid residues. The experiment is instigated through an initial π-pulse on proton to create transverse magnetisation which is subsequently transferred to the ^{15}N and then transferred again to the ^{13}C nuclei. Depending on the evolution of ^{15}N in τ_1, NCA and NCO experiments have potential to be acquired as either 1D or 2D experiments. A meticulous approach towards the setting of the offset and Hartmann-Hahn condition used during the pulse sequence can dictate the direction of magnetisation transfer, i.e. whether that the magnetisation is transferred from ^{15}N to the C_{α} or the C_{CO}.

As can be observed in the NCA and NCO spectra of WT-GB3 in (Figure 5.17), there is a dispersion of peaks, indicating the protein is properly crystallised and well-folded, and the lack of doubling of peaks alludes to an absence of structural polymorphism present in the microcrystals. GB3 has 56 amino acid residues, and 55 resonances attributing to the correlation between the backbone ^{15}N with the backbone ^{13}C nuclei can be observed. The amino-terminus methionine residue, which is absent in the spectra, is unlikely to be observed in any protein system due to the formation of a cation on the amine, which rapidly exchanges its protons with the protons in the water solvating the protein.

The WT-GB3 2D-NCA/NCO spectra performed at room temperature and at 35 kHz can be seen in Figure 5.17, with a full assignment of each residue to aid in the analysis of the mutant GB3 spectra. From this spectrum, peak widths of ~0.5 ppm in the ^{15}N dimension and ~0.4 ppm in the ^{13}C dimension were observed. It is noteworthy that essentially every single resonance is site resolved, apart from T16 with T53 and E27 with K28 which are very closely positioned making separation of the peaks difficult.

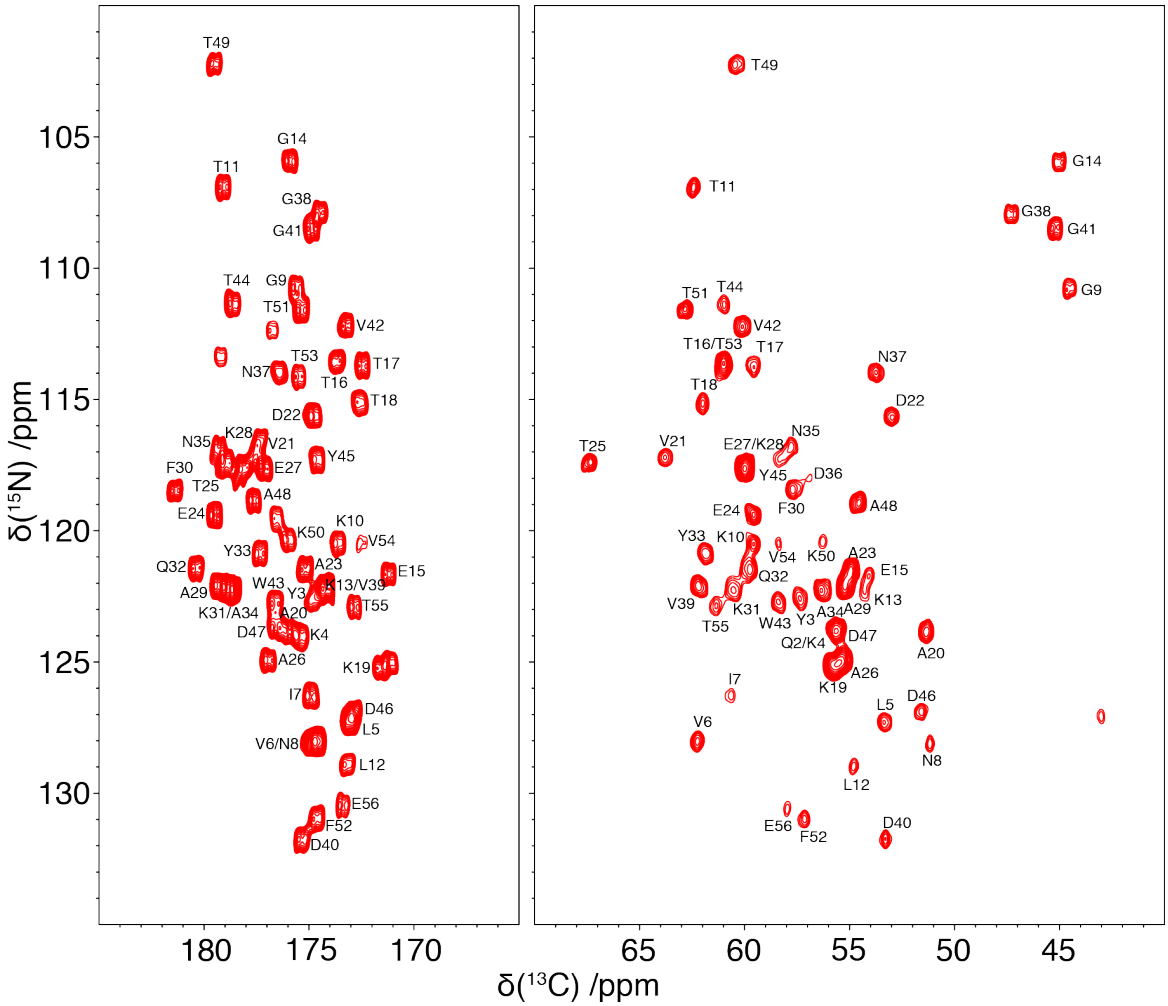

Figure 5.17 2D-NCO and 2D-NCA spectra of WT-GB3. Performed at 278 K, 35 kHz MAS, 14.1 T.

Through the comparison of the spectra of WT-GB3 against that of the A48C-GB3 mutant, one can observe that the peaks present for A48 have disappeared and new peaks for C48 are now present in the spectra. The A48^{15}N /D47$^{13}C_{CO}$ NCO correlation peak at 118.9 ppm, ~177.6 ppm and the A48^{15}N /A48$^{13}C_{\alpha}$ NCA correlation peak at 118.9 ppm, 54.4 ppm have been replaced with the C48^{15}N /D47$^{13}C_{CO}$ NCO correlation peak at 116.7 ppm, 177.5 ppm and the C48^{15}N /C48$^{13}C_{\alpha}$ NCA correlation peak at 116.7 ppm, 61.8 ppm. In addition, corresponding shifts in the surrounding peaks due to the change in the local magnetic field. Interestingly, it is the peaks closest along the backbone that experiences the greatest shift, not those in close proximity in terms of protein structure. The chemical shift of the succeeding amino acid, T49 is greatly perturbed. The WT resonance for the T49^{15}N /A48$^{13}C_{CO}$ NCO correlation peak is at 102.2 ppm, 179.6 ppm and the T49^{15}N /T49$^{13}C_{\alpha}$ NCA correlation peak is at 102.2 ppm, 60.6 ppm. However, the A48C mutant T49^{15}N

/C48$^{13}C_{CO}$ NCO correlation peak is at 104.6 ppm, 176.2 ppm and the T49^{15}N /T49$^{13}C_{\alpha}$ NCA correlation peak is at 104.6 ppm, 61.1 ppm (see Figure 5.18).

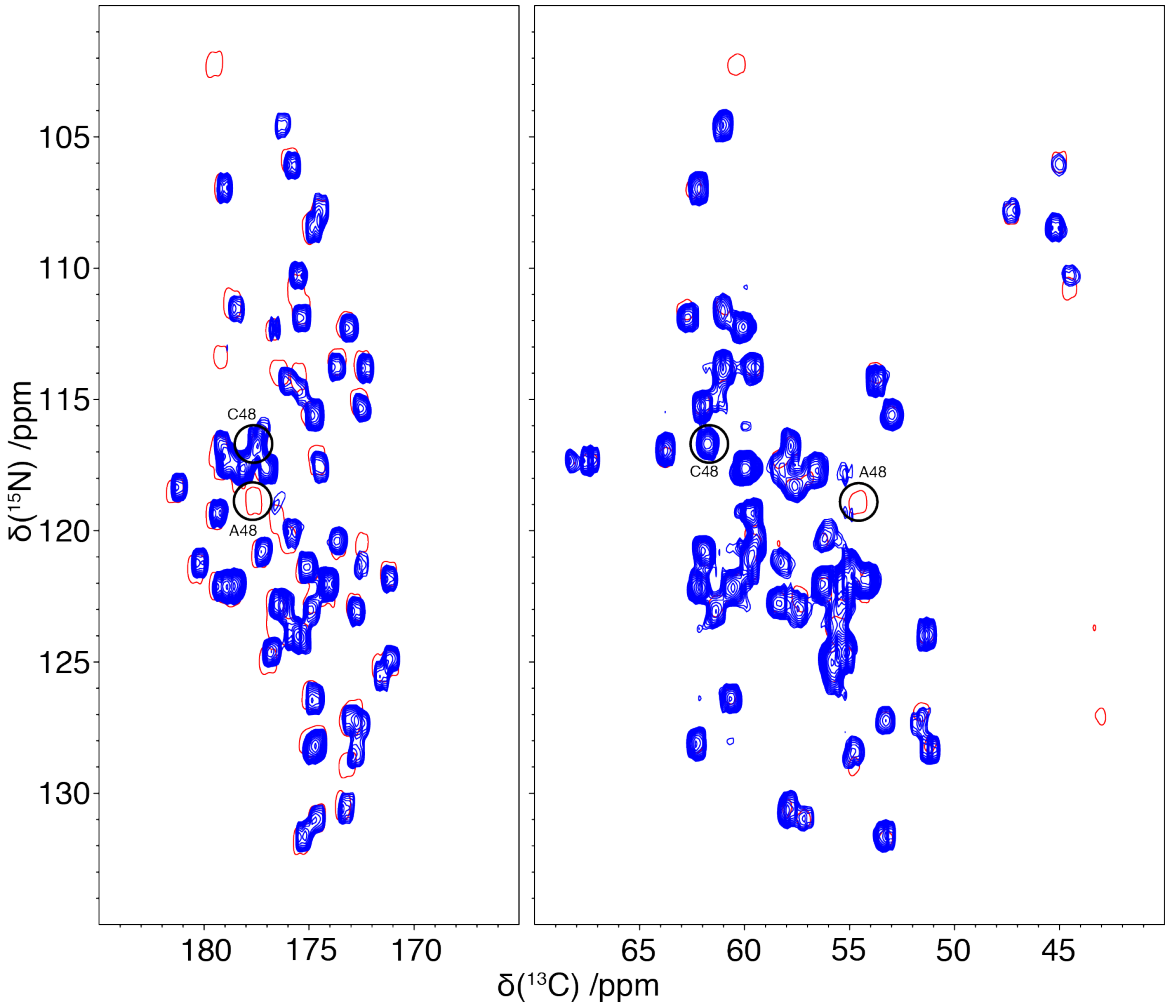

Figure 5.18 2D-NCO and 2D-NCA spectra of A48C-GB3 (blue) overlaid with an outline of the WT-GB3 spectra (red). Performed at 278 K, 35 kHz MAS, 14.1 T.

The 2D-NCA/NCO spectra for D46C-A48C-GB3 were also recorded. The presence of two new peaks in each spectrum is displayed. For the C48 mutation, the A48^{15}N /D47$^{13}C_{CO}$ NCO correlation peak at 118.9 ppm, 177.6 ppm and the A48^{15}N /A48$^{13}C_{\alpha}$ NCA correlation peak at 118.9 ppm, 54.4 ppm has been replaced with the C48^{15}N /D47$^{13}C_{CO}$ NCO correlation peak at 116.7 ppm, 177.5 ppm and the C48^{15}N /C48$^{13}C_{\alpha}$ NCA correlation peak at 116.7 ppm, 61.8 ppm. In the same way for the C46 mutation, the D46^{15}N /Y45$^{13}C_{CO}$ NCO correlation peak at 126.8 ppm, 172.7 ppm and the D46^{15}N /D46$^{13}C_{\alpha}$ NCA correlation peak at 126.8 ppm, 51.6 ppm has been replaced with the C46^{15}N/Y45$^{13}C_{CO}$ NCO correlation peak at 127.3 ppm, 174.6 ppm and the C46^{15}N /C46$^{13}C_{\alpha}$ NCA correlation peak at 127.3 ppm, 56.9 ppm (Figure 5.19).

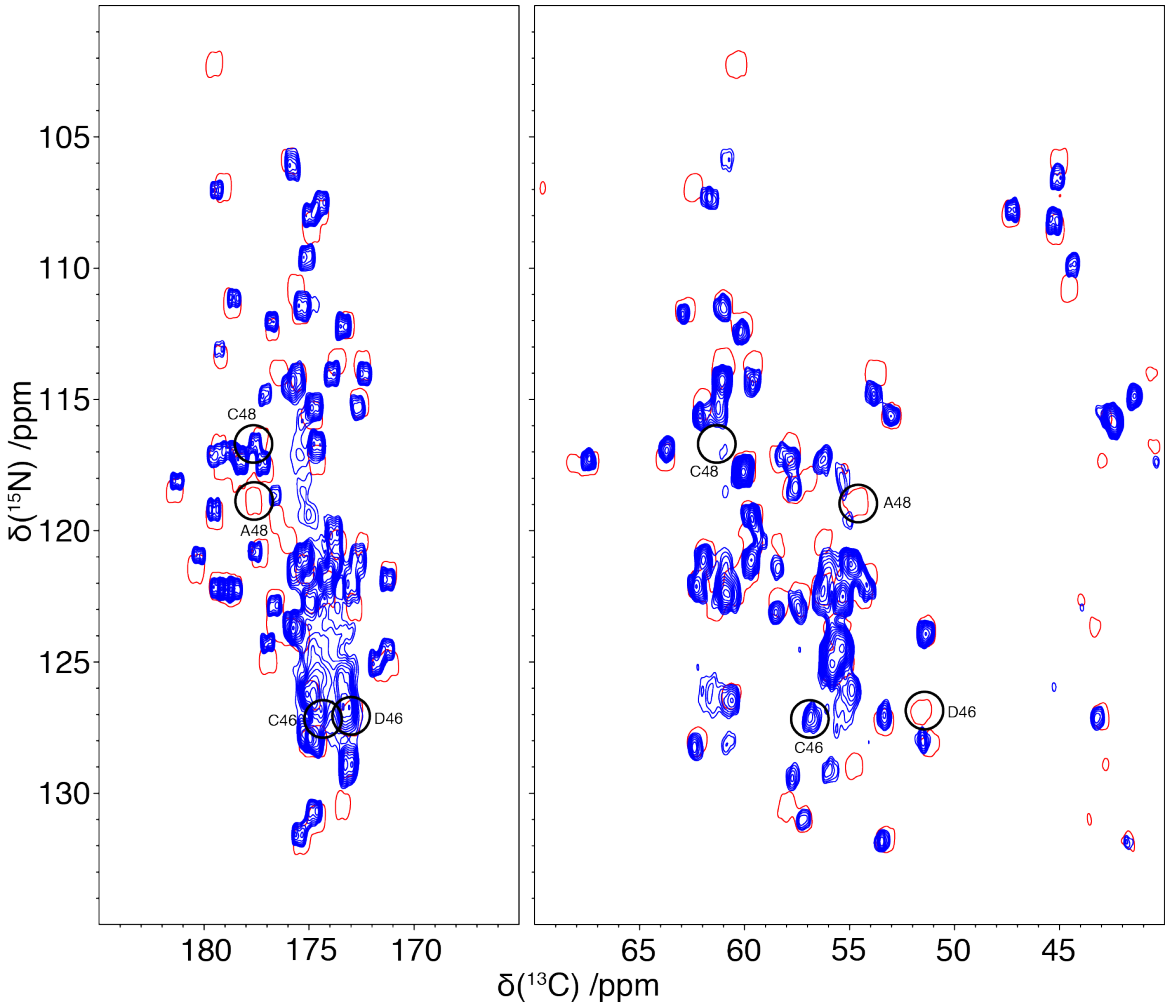

Figure 5.19 2D-NCO and 2D-NCA spectra D46C-A48C-GB3 (blue) overlaid with an outline of the WT-GB3 spectra (red). Performed at 278 K, 35 kHz MAS, 14.1 T.

The 2D-NCA/NCO spectra for E24C-K28C-GB3 were also recorded, which now displays the presence of two new peaks in each spectrum. For the C24 mutation, the E24^{15}N /A23$^{13}C_{CO}$ NCO correlation peak at 119.4 ppm, 179.5 ppm and the A48^{15}N /A48$^{13}C_{\alpha}$ NCA correlation peak at 119.4 ppm, 59.6 ppm has been replaced with the C28^{15}N /E27$^{13}C_{CO}$ NC_{CO} correlation peak at 117.0 ppm, 178.0 ppm and the C28^{15}N /C28$^{13}C_{\alpha}$ NCA correlation peak at 117.0 ppm, 55.8 ppm. In the same way for the C28 mutation, the K28^{15}N /E27$^{13}C_{CO}$ NCO correlation peak at 117.7 ppm, 178.0 ppm and the K28^{15}N /K28$^{13}C_{\alpha}$ NCA correlation peak at 117.7 ppm, 60.0 ppm has been replaced with the C28^{15}N /E27$^{13}C_{CO}$ NCO correlation peak at 117.2 ppm, 172.1 ppm and the C28^{15}N /C28$^{13}C_{\alpha}$ NCA correlation peak at 117.2 ppm, 62.0 ppm (Figure 5.20).

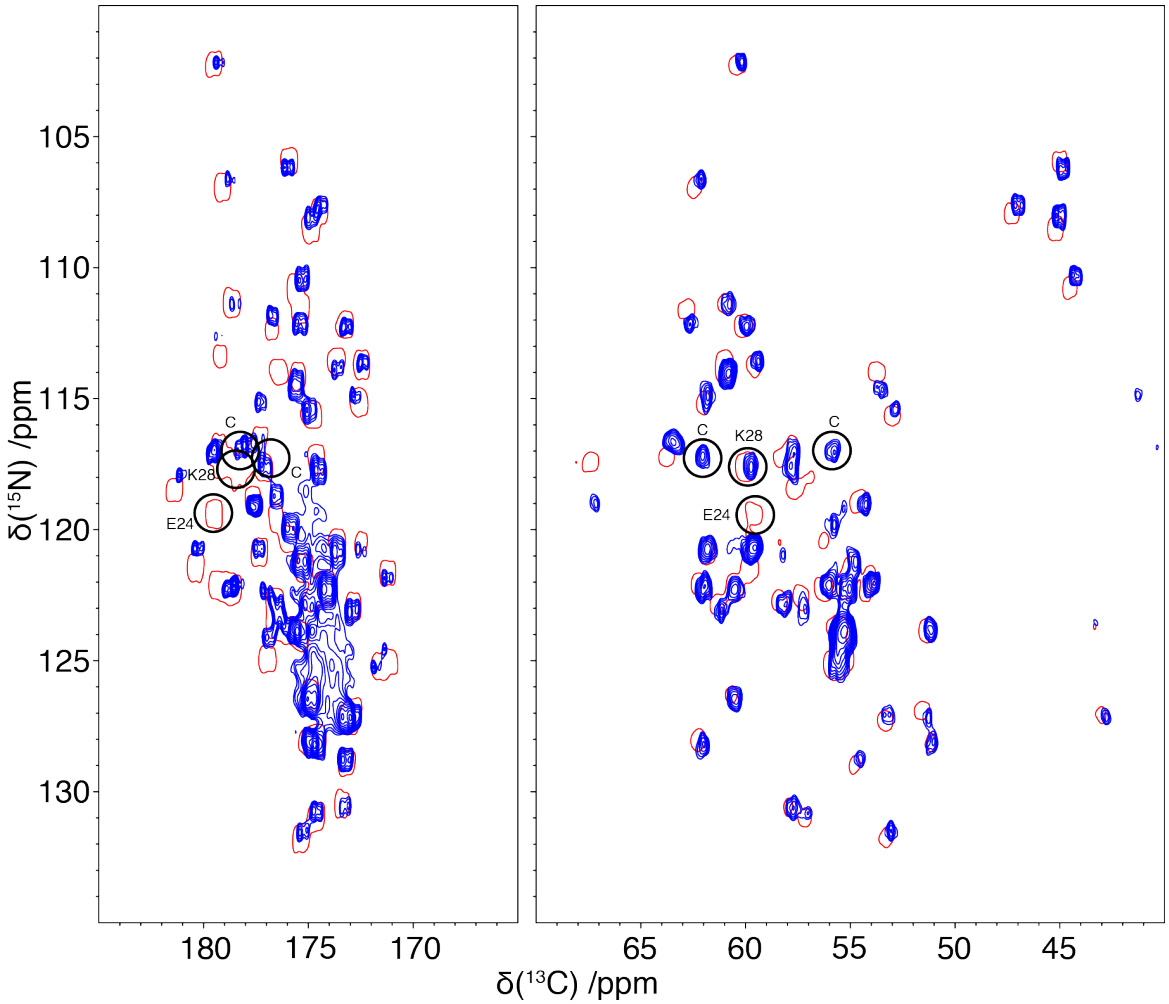

Figure 5.20 2D-NCO and 2D-NCA spectra of E24C-K28C -GB3 (blue) overlaid with an outline of the WT-GB3 spectra (red). Performed at 278 K, 35 kHz MAS, 14.1 T.

From the 2D-NCA/NCO spectra of the double mutants (see Figure 5.19 and Figure 5.20), unlike the WT-GB3 spectra, in addition to the expected peaks there was a broad peak region that could be seen in the NCO spectrum and in the NCA spectrum. This region doesn't seem to be located to a particular region of the protein, rather a background which may suggest the presence of a denatured component to the sample. Indeed, this broad envelope suggests that a portion of the sample may be non-crystalline, which could be due to an instability of the mutants leading to incomplete uniform crystallisation during the crystallisation process. It is also possible that any change in the sample occurred during the experiment under the heat exerted by the high powered rf-pulses. This is plausible because the mutation would likely lead to a protein that is inherently less heat stable.

To determine the effect on the spectra of adding in an MTSSL spin-label, the 2D-NCA/NCO spectra of 1 in 5 MTSSL labelled A48C-GB3 was acquired (see Figure 5.21). From this level of doping, as both components were ^{13}C,^{15}N enriched proteins, it is possible that the MTSSL-A48C-GB3 components were broadened. However, these corresponded to a small portion of the sample. A well-resolved spectrum could be observed of A48C-GB3, with a broadened region in the spectra also present at approximately 25 % the signal intensity and demonstrating line widths on the order of a 2.5 ppm. This region of broadening could not be attributed to broadening in a specific location on the protein.

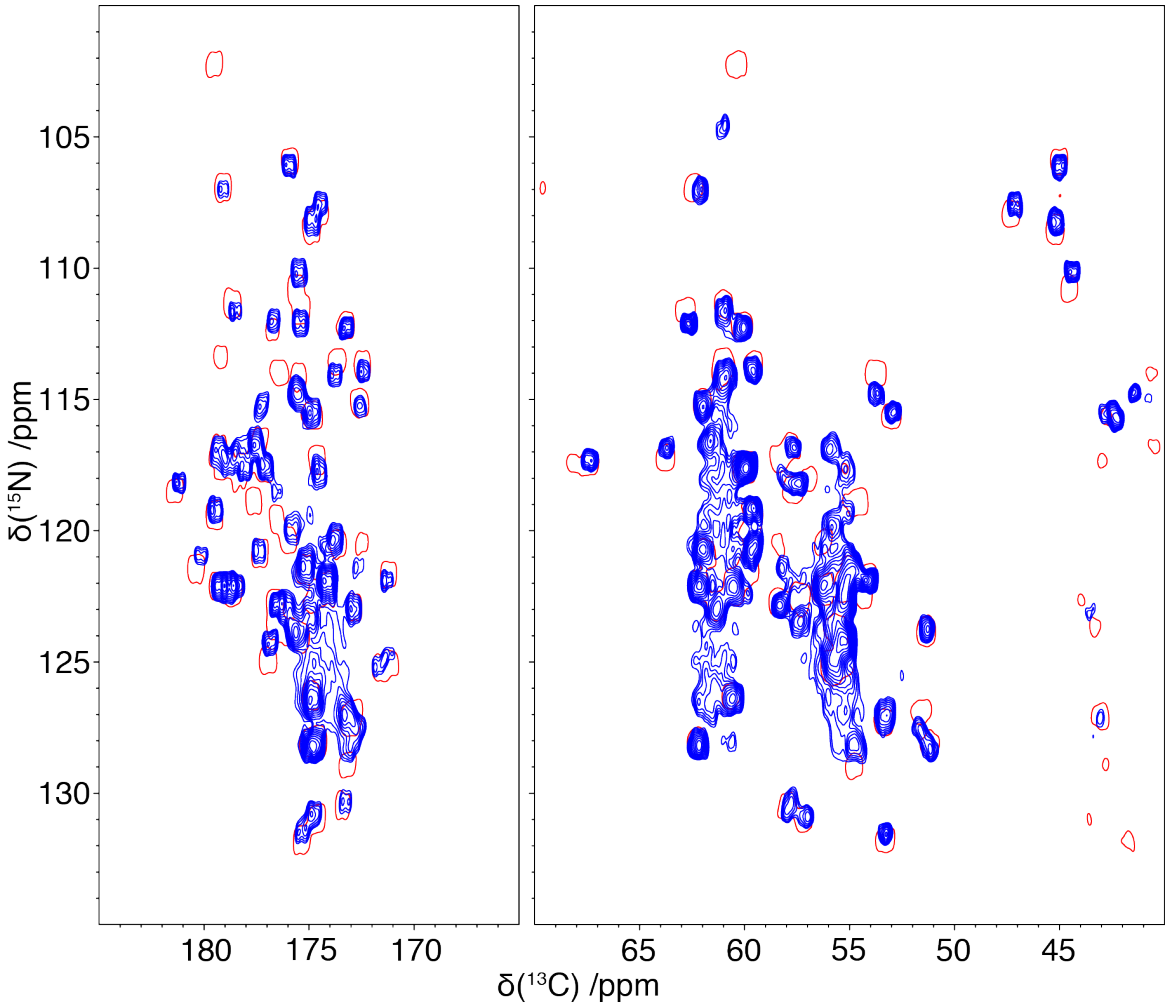

Figure 5.21 2D-NCO and 2D-NCA spectra of 1 in 5 MTSSL-A48C-GB3 (blue) overlaid with an outline of the WT-GB3 spectra (red). Performed at 278 K, 35 kHz MAS, 14.1 T. The sample was prepared with 1 in 5 labelling with MTSSL, with 1 in 5 protein molecules having two MTSSL derived nitroxide radicals covalently bound to the thiol groups of the present cysteine residues.

It was attempted to acquire fully MTSSL-labelled spectra of the double mutants at room temperature, but the high concentration of spin-labels led to high quenching, from the drastically enhanced T_2 relaxation resulting in homogeneously broadened lines. This was attempted for the MTSSL-E24C-K28C-GB3 mutant, but as both samples would likely have similar quenching effects at room temperature, it was deemed not worthwhile to continue with the other mutant (see Figure 5.22). For site-specific relaxation data, the samples with relaxation agents present in the samples did not possess sufficient resolution to warrant 2D relaxation characterisation.

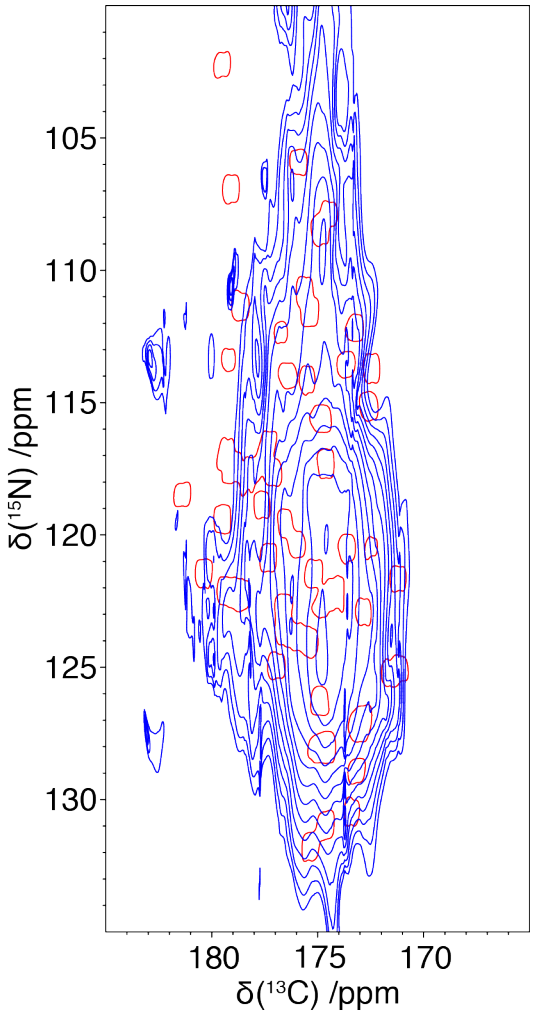

Figure 5.22 2D-NCO and 2D-NCA spectrum of MTSSL-E24C-K28C-GB3 (blue) overlaid with an outline of the WT-GB3 spectrum (red). Performed at 278 K, 35 kHz MAS, 14.1 T. Line broadening of 100 Hz applied in each dimension for the MTSSL-E24C-K28C-GB3 spectrum. The sample was prepared with complete labelling with MTSSL, with each protein molecule having two MTSSL derived nitroxide radicals covalently bound to the thiol groups of the present cysteine residues.

5.3.6 Analysis of CE-DNP Enhancements and $T_{DNP}(^1H)$

From the GB3 mutants previously purified and spin-labeled various microcrystalline and solution samples were prepared for the CE-DNP experiments that were to be conducted (see Table 5.4 for a list of samples studied).

Table 5.4 List of samples used for DNP studies.

12.5 mM AMUPol doped crystallised [U-^{13}C,^{15}N]WT GB3
12.5 mM AMUPol doped frozen solution [U-^{13}C,^{15}N]WT GB3, 30 mg/mL, 30 µL,
12.5 mM AMUPol doped crystallised [U-^{13}C,^{15}N]WT GB3, doped pre-crystallisation
Crystallised [U-^{13}C,^{15}N]MTSSL(1:5)-A48C- GB3
Crystallised [U-^{13}C,^{15}N]MTSSL-A48C- GB3
Frozen solution [U-^{13}C,^{15}N]MTSSL-A48C- GB3, 30 mg/mL, 30 µL,
Crystallised [U-^{13}C,^{15}N]MTSSL(1:5)-D46C-A48C- GB3
Crystallised [U-^{13}C,^{15}N]MTSSL- D46C-A48C- GB3
Frozen solution [U-^{13}C,^{15}N]MTSSL- D46C-A48C- GB3, 30 mg/mL, 30 µL,
Crystallised [U-^{13}C,^{15}N]MTSSL(1:5)-E24-K28-GB3
Crystallised [U-^{13}C,^{15}N]MTSSL)-E24-K28-GB3
Frozen solution [U-^{13}C,^{15}N]MTSSL-E24-K28-GB3, 30 mg/mL, 30 µL,

In preparation for the doping with AMUPol it was investigated whether the WT-GB3 protein would remain microcrystalline (15 mg sample taken) when transferred from the previous buffer where it was crystallised in (40:60 6.5 25mM bis-tris:hexylene glycol). This was achieved by first spinning down the pellet and pipetting 100 µL of 7:3 gylcerol-d_8/D_2O with 12.5mM AMUPol onto the supernatant and allowing the crystals to soak overnight. It was observed that the crystals were not dissolved in this change in the buffer. It was then investigated whether the crystals could be transferred to the DNP buffer and resuspended and left to allow to settle back to the bottom of the tube, and finally centrifuged. This proved successful in that there was no change in the size of the pellet so it could be assumed that the crystals in this batch had not been compromised using this method.

5.3.7 1D-CP CE-DNP Enhancement Experiments

5.3.7.1 Conventional DNP

As a point of reference, it was necessary to first investigate the enhancement that could be achieved with standard exogenous AMUPol doping of the microcrystalline sample, using 12.5 mM AMUPol doping to coincide with previous DNP studies of GB3.[263] For a direct comparison, 1D-^{1}H to ^{13}C CP and ^{1}H to ^{15}N CP experiments were performed. Both under the presence and in the absence of cw-MW irradiation to facilitate the CE, so that the enhancement achieved could be determined by measuring the difference in intensity for both sets of spectra (see Figure 5.23 (A) for the 1D-^{1}H to ^{15}N CP CE-DNP enhancement spectrum and Figure 5.23 (C) for the 1D-^{1}H to ^{13}C CP CE-DNP enhancement spectrum). Results of both enhancement values and T_{DNP}(^{1}H) are tabulated in Table 5.5.

For the WT-GB3 sample doped with 12.5 mM AMUPol, 1D-^{1}H to ^{13}C CP and ^{1}H to ^{15}N CP spectra demonstrated an enhancement of 32. The DNP enhancement proton longitudinal relaxation time (T_{DNP}(^{1}H)) was used to quantify the relaxation in the system with this level of sample doping as well as a means to determine the rate at which one can set the optimum recycle delay. The T_{DNP}(^{1}H) was 5.2 s.

Repeat experiments were conducted for the WT-GB3 sample which was soaked in the AMUPol infused DNP juice. Determining the enhancement from DNP by 1D-^{1}H to ^{13}C CP and ^{1}H to ^{15}N CP experiments both with and without cw-MW irradiation resulted in an enhancement of 36 from the 1D-^{1}H to ^{13}C CP and 40 from the 1D-^{1}H to ^{15}N CP

experiment. This change in enhancement could be due to the freeze-thaw cycle of cooling the sample down to 100 K and then allowing to return to room temperature. On warming the sample, oxygen gas trapped in the crystals could be released. Oxygen can inhibit the DNP enhancement[309] observed due to its paramagnetic properties as noted in a previous publication by Kubicki and Emsley.[310]

As little research has been performed on the optimum method for sample preparation of microcrystalline samples for DNP studies, the method of exogenous doping of the protein sample was investigated. The sample previously described was crystallised prior to doping with 12.5 mM AMUPol and then allowed to soak in the DNP juice before packing into a rotor for DNP experiments. As a potentially superior method to improve the homogeneity of which the AMUPol is dispersed within the sample, as an alternative to soaking the preformed crystals with AMUPol it was attempted to crystallise the GB3 sample under the presence of 12.5 mM AMUPol. This would actually result in a lower AMUPol concentration than the previous method if it is assumed that the AMUPol will be evenly spread through the sample, as the sample post crystallisation has a total volume of approximately 0.7 mL in comparison to the sample which has been recrystallised, spun down and soaked in the DNP juice. 1D-^{1}H to ^{13}C CP and ^{1}H to ^{15}N CP experiments both with and without cw-MW irradiation resulted in an enhancement of 9 being determined. Much lower than what was achieved for the soaking of the crystals in the DNP juice. Due to the limits of the study it could only be concluded that any effect of AMUPol diffusing into the crystals was not hindering the enhancement observed. It could, therefore, be determined that in the method of adding the AMUPol prior to crystallisation only served to dilute the radical.

To determine the merits of crystallisation on both the DNP enhancement and the spectral resolution at low-temperature under the presence of a DNP polarising agent and whether crystallisation is necessary, a sample of WT-GB3 as a frozen solution with 12.5 mM AMUPol doping was prepared. The signal enhancement was determined by use of 1D-^{1}H to ^{13}C CP and ^{1}H to ^{15}N CP experiments respectively. A massive enhancement of 120 was achieved in both instances, with a $T_{DNP}(^{1}H)$ determined as 2.8 s, giving an optimum recycle delay of 3.5 s, 2.5 s faster than that for the microcrystalline sample. To compare the absolute enhancement achieved one needs to take into account both the rate at which one can recycle as well as the DNP enhancement (evaluated in Table 5.7). If one can recycle 1.7 times faster with the frozen solution sample than the microcrystalline sample, this would further increase the benefit of a frozen solution over a microcrystalline sample.

However, one must also take into account the fact that in a frozen solution the amount of protein that one can fit in a rotor is significantly lower than that can be achieved with a microcrystalline sample. With approximately 1 mg of protein used in the frozen solution sample and 15 mg for the microcrystalline sample for a full 3.2 mm rotor. Therefore, it would still work out overall more beneficial to use a microcrystalline sample in terms of increased signal, and there is also the argument that there would be greater homogeneity in a microcrystalline sample in comparison to the frozen solution sample so one would expect narrower linewidths. This increase in linewidth was in general observed in the ^{1}H-$^{15}N/^{13}C$ CP DNP spectra for the envelopes of the nitrogen backbone, nitrogen side chain, C_{CO} and C_{α} region (see Table 5.6). However, if one is greatly limited in the amount of sample that can be produced, a strong argument for preparing the sample for CE-DNP as a frozen solution to maximise the signal per mg of protein can be made due to the greater signal enhancements achievable. See Figure 5.23 (B) for the 1D-^{1}H to ^{15}N CP CE-DNP enhancement spectrum and Figure 5.23 (D) for the 1D-^{1}H to ^{13}C CP CE-DNP enhancement spectrum.

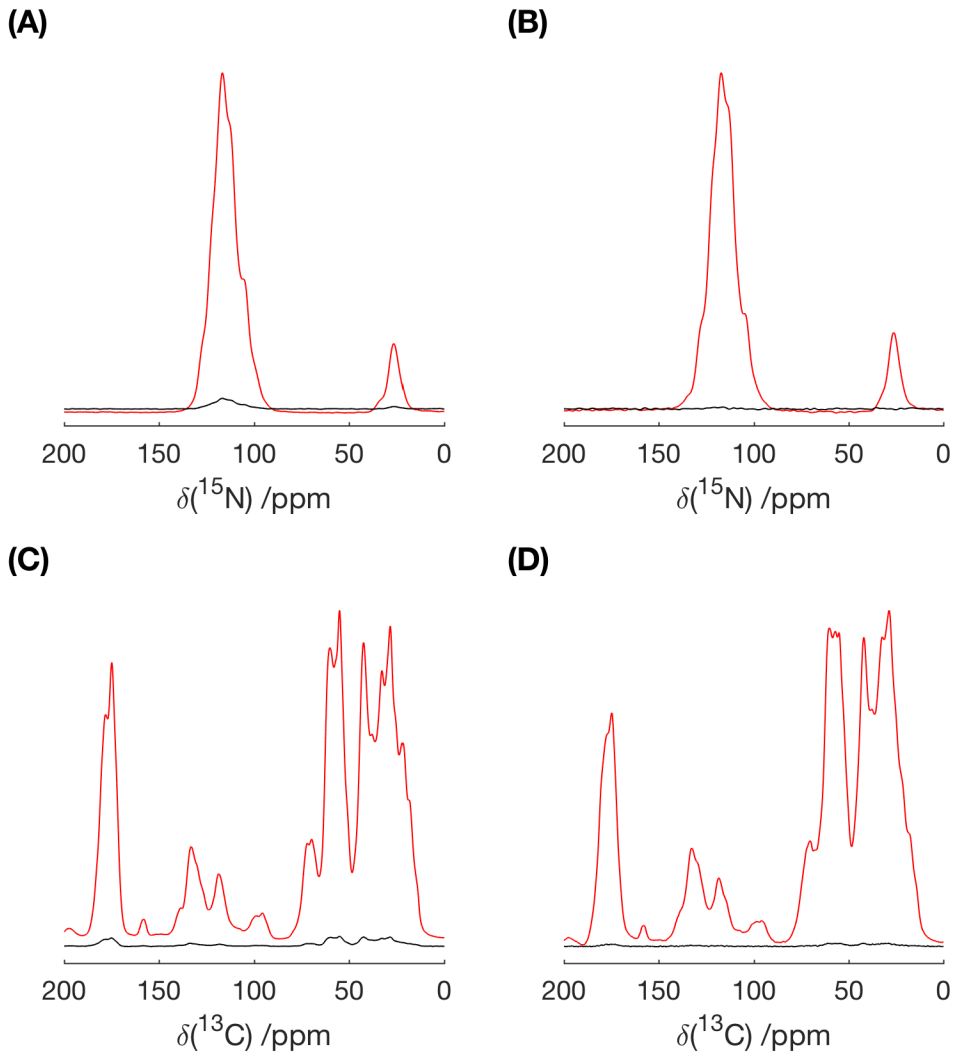

Figure 5.23 Enhancement of 12.5 mM AMUPol doped GB3 samples. 12.5 mM AMUPol doped microcrystalline GB3 1D-^{1}H to ^{15}N CP spectrum (A), 12.5 mM AMUPol doped frozen solution GB3 1D-^{1}H to ^{15}N CP spectrum (B), 12.5 mM AMUPol doped microcrystalline GB3 1D-^{1}H to ^{13}C CP spectrum (C), 12.5 mM AMUPol doped frozen solution GB3 1D-^{1}H to ^{13}C CP spectrum (D) MW on spectra shown in red, MW off spectra shown in black. The intensity in each spectrum has been scaled to the maximum of the MW on spectra.

5.3.7.2 DNP of Single Spin-Labelled Mutant

DNP enhancements were determined for the for the 1D-^{1}H to ^{15}N CP (see Figure 5.24 (A)) and 1D-^{1}H to ^{13}C CP CE-DNP (see Figure 5.24 (C)) spectra of microcrystalline, fully spin-labelled, MTSSL-A48C-GB3 sample. The 1D-^{1}H to ^{13}C CP experiment achieved an enhancement of 8 in comparison to no MW and an enhancement of 10 as determined from the ^{1}H to ^{15}N CP experiment. This discrepancy between the enhancements of the two

experiments is likely due to the reduced signal to noise observed for this sample, resulting in a less accurate measurement of the enhancement. The $T_{DNP}(^1H)$ of the fully MTSSL labelled A48C-GB3 sample was 1.2 s leading to an optimum recycle delay of 1.6 s. from the crystal structure of GB3 it can be observed that although there is only one MTSSL per protein molecule in this system, neighbouring labelled cysteine residues come in close enough proximity to participate in the CE (see Figure 5.6).

On repeating the enhancement determining experiment for the single mutant protein, MTSSL-A48C-GB3, with full spin-labeling, an increase in the enhancement was observed. The enhancement increased from the previously determined value of 10, to an enhancement of 14, determined via the ^1H to ^{15}N CP experiment. However, no change in the $T_{DNP}(^1H)$ was observed. This change in enhancement could be due to the freeze-thaw cycle of cooling the sample down to 100 K and then allowing the sample to return to room temperature. With the removal of trapped oxygen gas in the crystals improving the DNP enhancement,[309] as noted in a previous publication by Kubicki and Emsley.[310] Results of both enhancement values and $T_{DNP}(^1H)$ are tabulated in Table 5.5.

A 1 in 5 dilution of the MTSSL labelled A48C-GB3 sample with the non-spin-labelled variant was prepared as a microcrystalline sample, to evaluate the effect dilution has on the level of enhancement. It would be expected that the enhancement achieved for this sample would be greatly attenuated in comparison to the fully labelled microcrystalline sample. This is likely due to the probability of two spin-labels coming in close proximity for the CE to be satisfied. In addition, the efficiency of spin diffusion to transfer magnetisation throughout the system with the reduced concentration of radicals in the sample is lower. 1D-^1H to ^{13}C CP and ^1H to ^{15}N CP experiments were conducted and both indicated an enhancement of 4, confirming the expected reduction in enhancement achieved. The $T_{DNP}(^1H)$, in contrast to the relatively fast $T_{DNP}(^1H)$ is 1.2 s for the fully MTSSL labelled microcrystalline variant of this sample. The relaxation is faster than the AMUPol doped WT-GB3 sample. The $T_{DNP}(^1H)$ of the 1 in 5 diluted sample, when modelled as an exponential process, was 6.4 s, slightly greater than the $T_{DNP}(^1H)$ of the AMUPol doped sample which exhibited a $T_{DNP}(^1H)$ of 5.2 s, owing to the reduced amount of spin-label in the sample.

To determine the benefit of crystallisation to achieve inter-protein interactions to facilitate the CE a sample was prepared by concentrating the sample to ~30 mg/mL in pH 6.5 25

mM bis-tris and adding glycerol-d_8/D_2O to achieve 60/30/10 gylcerol-d_8/D_2O/H_2O ratio. This sample was then used as a frozen solution sample to measure the DNP enhancement. It would be expected that the enhancement achieved for this sample would, therefore, be much less in comparison to the microcrystalline sample due to the greater distances between samples and the lower likelihood that a spin pair would be frozen in proximity with the correct orientation to facilitate the CE. DNP enhancements were determined for the for the 1D-^{1}H to ^{15}N CP (see Figure 5.24 (B)) and 1D-^{1}H to ^{13}C CP CE-DNP (see Figure 5.24 (D)) spectra of the sample, an enhancement of 4 was observed, confirming the predicted reduction in enhancement. The T_{DNP}(^{1}H) was comparatively slower in contrast to the relatively fast T_{DNP}(^{1}H) of 1.2 s for the microcrystalline variant of this sample. The T_{DNP}(^{1}H) of the frozen solution sample, when modelled as a single exponential process, was 16 s. This was significantly longer than the T_{DNP}(^{1}H) of the AMUPol doped frozen solution WT-GB3 sample which exhibited a T_{DNP}(^{1}H) of 2.8 s. The relaxation was expected to be similar to the microcrystalline sample, as the distance between each spin-label and the protein molecule should be constant. However, the presence of glycerol in the sample would likely affect the relaxation rate. Glycerol would have a long longitudinal relaxation time in the sample as the sample is relatively dilute with regions of glycerol, not in contact with a spin-label. Due to spin diffusion, this slow rate of relaxation for the glycerol can average with that of the protein sample.

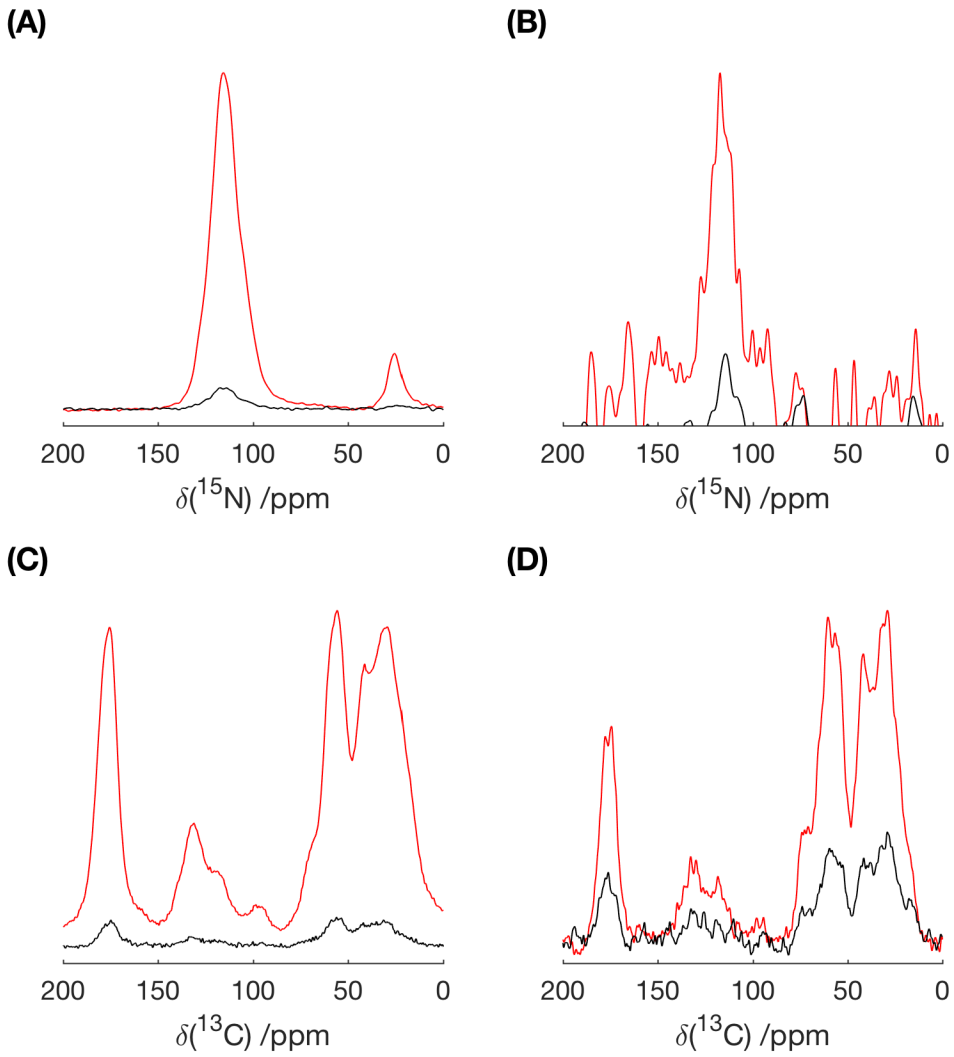

Figure 5.24 Enhancement of MTSSL-A48C-GB3 samples. Microcrystalline MTSSL-A48C-GB3 1D-^{1}H to ^{15}N CP spectrum (A), frozen solution MTSSL-A48C-GB3 1D-^{1}H to ^{15}N CP spectrum (B), microcrystalline MTSSL-A48C-GB3 1D-^{1}H to ^{13}C CP spectrum (C), frozen solution MTSSL-A48C-GB3 1D-^{1}H to ^{13}C CP spectrum (D) MW on spectra shown in red, MW off spectra shown in black. The intensity in each spectrum has been scaled to the maximum of the MW on spectra.

5.3.7.3 DNP of Double Spin-Labelled Mutant

The enhancements were then determined for a microcrystalline fully MTSSL labelled D46C-A48C-GB3 sample via 1D-^{1}H to ^{15}N CP (see Figure 5.25(A)) and 1D-^{1}H to ^{13}C CP CE-DNP (see Figure 5.25 (C)) spectra of the sample. It was expected that the enhancement of this sample would be much greater than that of the A48C mutant sample. Though only

an enhancement of 4 was achieved. This was potentially due to a problem with the sample that was packed into the rotor that led to poor crystal quality in this sample. It was noted that on preparing this sample the volume the crystalised protein occupied was much greater than expected so the crystal packing may not have been homogeneous and therefore led to an arrangement where the CE was not satisfied, thus the poor enhancement observed. The $T_{DNP}(^1H)$ was determined as previously and measured to be 0.2 s, given the short $T_{DNP}(^1H)$ it could also be that the concentration of radical was that high that the bulk of the resonances were in the quenched zone. Though it was noted that the buildup curve was not mono-exponential, possibly due to the two environments in the sample, that of the region close to the spin-label and that of the sample that is not close to the spin-label.

To determine the effect on dilution, which should naively have no effect on the observed enhancement as the pseudo-biradical is tethered to the sample, a 1 in 5 dilution of the MTSSL-D46C-A48C-GB3 sample was prepared and microcrystals prepared as previously described for other samples. The recorded enhancement was within error equivalent to that observed with the non-diluted sample, with an enhancement of 6.4 observed.

The enhancements were then determined for a frozen solution fully MTSSL labelled D46C-A48C-GB3 sample via 1D-^{1}H to ^{15}N CP (see Figure 5.25(B)) and 1D-^{1}H to ^{13}C CP CE-DNP and (see Figure 5.25 (D)) spectra of the sample. Both 1D-^{1}H to ^{13}C CP and ^{1}H to ^{15}N CP experiments were performed, with an enhancement of approximately 6 achieved. The $T_{DNP}(^1H)$ was measured as 2.0 s when modelled as a single exponential process. Comparing the 1D-^{1}H to ^{13}C CP CE-DNP spectrum of the sample in microcrystalline (see Figure 5.25 (C)) and frozen solution form (see Figure 5.25 (D)), it is noteworthy that the intensity of the carbonyl and C_β regions have been attenuated with respect to the C_α region. A comparison of the nitrogen backbone linewidths between the frozen solution and microcrystalline forms of the protein (see Table 5.6), indicate an increased linewidth of 45 %. The linewidths determined from the side chain could not be accurately determined considering the low signal to noise. The increased linewidth of the frozen solution form for the carbonyl envelope was less at only 6 % (see Table 5.6).

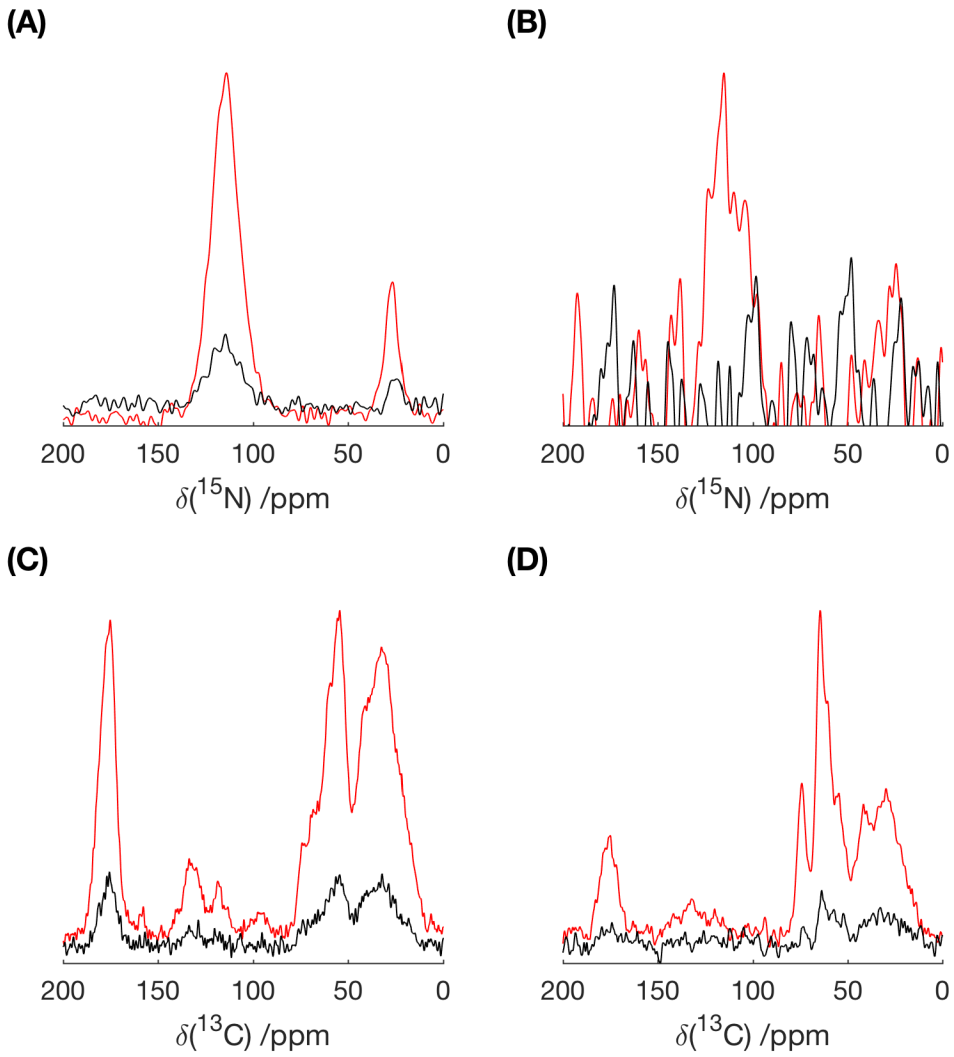

Figure 5.25 Enhancement of MTSSL-D46C-A48C-GB3 samples. Microcrystalline MTSSL-D46C-A48C-GB3 1D-^{1}H to ^{15}N CP spectrum (A), frozen solution MTSSL-D46C-A48C-GB3 1D-^{1}H to ^{15}N CP spectrum (B), microcrystalline MTSSL-D46C-A48C-GB3 1D-^{1}H to ^{13}C CP spectrum (C), frozen solution MTSSL-D46C-A48C-GB3 1D-^{1}H to ^{13}C CP spectrum (D) MW on spectra shown in red, MW off spectra shown in black. The intensity in each spectrum has been scaled to the maximum of the MW on spectra.

Through the use of 1D-^{1}H to ^{15}N CP CE-DNP (see Figure 5.26 (A)) and 1D-^{1}H to ^{13}C CP CE-DNP (see Figure 5.26 (C)) polarisation enhancement studies were then performed for another microcrystalline fully spin-labelled double mutant, MTSSL-E24C-K28C-GB3. An enhancement of 16 was achieved for both experiments. The enhancement achieved was not as high as that of doping a GB3 sample with AMUPol. At a factor of 2 less than that acquired for doping of WT-GB3 with 12.5 mM AMUPol. However, it was significantly

better than the fully spin-labelled single labelled mutant. MTSSL-A48C-GB3 relies on inter-protein interactions to achieve the CE in comparison to the intra-protein interactions present with two monoradicals tethered in close proximity to each other on the same protein. In addition to the enhancement of the CE-DNP, the sample also exhibited a much shorter $T_{DNP}(^1H)$ at 0.6 s than that of the AMUPol doped sample. This fast relaxation rate will contribute to the total sensitivity enhancement of the experiment as a whole (evaluated in Table 5.7). Unlike the D46C-A48C-GB3 sample, there were no abnormalities with the crystals observed.

Comparing the linewidths of the microcrystalline MTSSL-E24C-K28C-GB3 sample to the microcrystalline 12.5 mM AMUPol doped WT-GB3 sample (see Table 5.6), the nitrogen backbone envelope broadens by 34 %, the nitrogen side chain region by 17 %, the carbonyl region by only 1 %, the C_α region by 44 %, and the C_β by only 3 % in the case of the double spin-labelled mutant. It is evident from this that the MTSSL spin-label attached to the surface of the protein enacts a greater T_2 relaxation effect than the AMUPol dispersed within the solution. In part due to the close proximity of the relaxation agent to the location of the nuclei to be relaxed as dictated by the Solomon equations. However, the varying rates of their respective electronic relaxation rates will also play a part.

To compare the MTSSL-E24C-K28C-GB3 mutant microcrystalline sample to that of a frozen solution sample, a frozen solution sample was prepared in the same manner as for the MTSSL-A48C-GB3 mutant. Both 1D-^{1}H to ^{15}N CP CE-DNP (see Figure 5.26 (B)) and 1D-^{1}H to ^{13}C CP CE-DNP (see Figure 5.26 (D)) experiments were performed. Interestingly in contrast to the single mutant sample, which experienced a decrease in enhancement when comparing the microcrystalline form to a frozen solution and the doping of the WT sample with AMUPol. In this case, much greater enhancements were achieved under the conditions of a frozen solution. For the double spin-labelled sample, which relies on intra-protein connections for the achievement of the CE, the enhancement observed for the frozen solution was consistent with that observed for the microcrystalline sample, with an enhancement of 16 achieved. As with the single mutant spin-labelled MTSSL-A48C-GB3 sample, the value for the $T_{DNP}(^1H)$ measured was larger than that for the microcrystalline variant, at 1.2 s, likely due to the same reasons outlined for MTSSL-A48C-GB3 frozen solution sample. The results for MTSSL-E24C-K28C-GB3 mirror those seen for the MTSSL-E24C-K28C-GB3 sample, with the microcrystalline sample and frozen solution analogue exhibiting similar enhancement values, attributed to the enhancements being independent of the distance between residues.

Comparing the linewidths of the microcrystalline sample to that of the frozen solution sample, in general it was observed that the linewidths increased in the case of the frozen solution sample. The linewidth increased by 10 % for the nitrogen backbone envelope (see Table 5.6), though curiously the linewidth of the C_α region was 6 % less and the C_β region negligibly different. The nitrogen side chain region is broadened by 24 %, the carbonyl region by only 9 %.

Comparing the linewidths of the microcrystalline sample to that of the frozen solution sample, in general it was observed that the linewidths increased in the case of the frozen solution sample. The linewidth increased by 10 % for the nitrogen backbone envelope (see Table 5.6), though curiously the linewidth of the C_α region was 6 % less and the C_β region negligibly different. The nitrogen side chain region is broadened by 24 %, the carbonyl region by 9 %. Comparing the linewidths of the frozen solution MTSSL-E24C-K28C-GB3 sample to the frozen solution 12.5 mM AMUPol doped WT-GB3 sample (see Table 5.6), it was observed that the linewidths increased in the case of the double spin-labelled mutant. The nitrogen backbone envelope broadened by 46 %, the nitrogen side chain region by 37 %, the carbonyl region by only 3 %, the C_α region by 16 %, and the C_β by 9 %. It is clear that the covalently bound radical leads to a greater effect on the linewidth. This is predominately through T_2 enhancement effects. In contrast to the increase in width observed through the sample preparation as a frozen solution where increased linewidths are observed due to an increase in the conformational states present in the less organised matrix.

The enhancement of 16 achieved for the microcrystalline MTSSL-E24C-K28C-GB3 sample is greater, or on par with previous values quoted in the literature for experiments, research groups have performed to utilise covalently bound polarisation agents for CE-DNP[291-295, 297] (see section 5.1.4.5 for a review of the literature for spin-labelled DNP of proteins). As the progenitors of the concept, Vitzthum and Bodenhausen, in which they attached a biradical to the carboxy terminus of a decapeptide, achieved polarisation enhancements of 4-fold.[291] Following this work, Mally and Miller experimented with the prospect of endogenous radicals for DNP, by studying the naturally occurring radical system present in FMN, with the attached monoradical co-factor for exploitation of SE DNP, leading to them achieving enhancements of 15-fold.[292] From the McDermott group a study into the potential use of monoradical nitroxides covalently bound on the surface of a membrane protein via a pseudo-biradical for the CE was investigated. The results achieved

DNP enhancements up to 6-fold.[293] Smith and Long performed DNP enhancement experiments on peptides inside a lipid bilayer by using spin-labelled lipids, to achieve enhancements up to 8.9.[294] In a similar manner, Fernández-de-Alba and DePaeῬe used a biradical labelled lipid, with enhancements up to 8.1 achieved.[295] Voinov and Smirnov employed ToSMTSL, a variant of the biradical TOTAPOL, which could be covalently attached to the cysteine residues of a protein.[297] They used ToSMTSL to spin-label lipid reconstituted ASR and perform CE DNP. DNP enhancements ranging from 4 to 15-fold were achieved depending on sample preparation.[297] The microcrystalline MTSSL-E24C-K28C-GB3 sample was expected to function more efficiently for the CE in comparison to the microcrystalline MTSSL-D46C-A48C-GB3 mutant sample due to the greater motional restriction present in the alpha-helix, where the E24C and K28C mutations are present in contrast to the D46C and A48C mutations present in a connecting loop region.

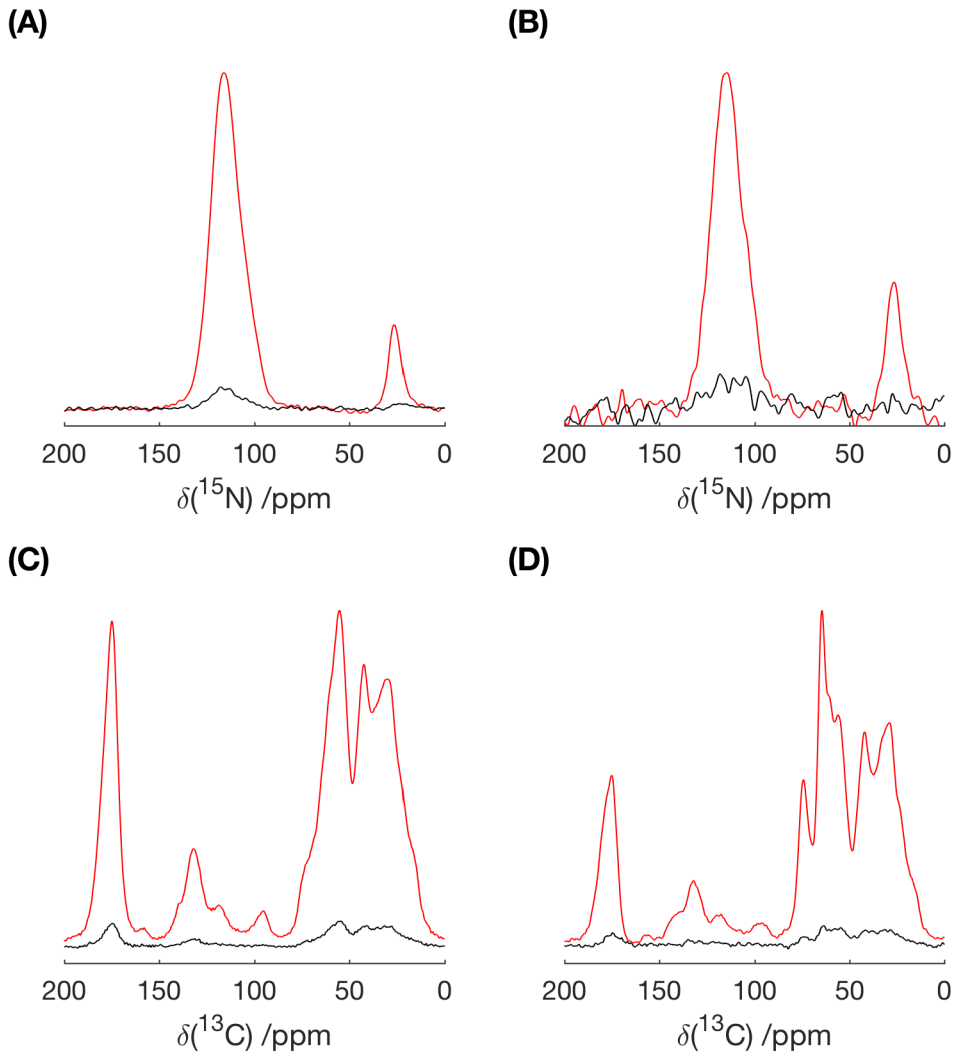

Figure 5.26 Enhancement of MTSSL-E24C-K28C-GB3 samples. Microcrystalline MTSSL-E24C-K28C-GB3 1D-^{1}H to ^{15}N CP spectrum (A), frozen solution MTSSL-E24C-K28C-GB3 1D-^{1}H to ^{15}N CP spectrum (B), microcrystalline MTSSL-E24C-K28C-GB3 1D-^{1}H to ^{13}C CP spectrum (C), frozen solution MTSSL-E24C-K28C-GB3 1D-^{1}H to ^{13}C CP spectrum (D) MW on spectra shown in red, MW off spectra shown in black. The intensity in each spectrum has been scaled to the maximum of the MW on spectra.

Table 5.5 Table of DNP enhancements (ε) and the DNP enhancement proton longitudinal relaxation time ($T_{DNP}(^1H)$) values obtained for GB3 samples. $T_{DNP}(^1H)$ determined from the C_{CO} envelope as this resonance does not overlap with that of gylcerol-d_8, therefore, more accurately representing that of the protein. 95 % confidence limits given in parentheses.

Sample	Enhancement /ε	$T_{DNP}(^1H)$ / s
12.5mM AMUPol doped microcrystalline WT-GB3	35.39	5.22 (4.92, 5.51)
12.5mM AMUPol doped frozen solution WT-GB3	115.72	2.75 (2.70, 2.80)
Microcrystalline WT-GB3, doping pre-crystallisation with 12.5mM AMUPol doped	8.99	9.30 (9.00, 9.60)
Microcrystalline MTSSL-A48C-GB3	8.34	1.23 (1.20, 1.26)
Microcrystalline MTSSL-A48C-GB3 1 in 5	3.96	6.87 (5.97, 7.77)
Frozen solution MTSSL-A48C-GB3	2.69	16.03 (14.36, 17.70)
Microcrystalline MTSSL-D46C-A48C-GB3	5.48	0.16 (0.14, 0.19)
Microcrystalline MTSSL-D46C-A48C-GB3 1 in 5	3.68	6.37(5.62, 7.13)
Frozen solution MTSSL-D46C-A48C-GB3	6.34	1.97 (0.95, 3.00)
Microcrystalline MTSSL-E24C-K28C-GB3	15.91	0.61 (0.53, 0.69)
Frozen solution MTSSL-E24C-K28C-GB3	12.84	1.16 (1.04, 1.27)

Table 5.6 Table of envelope widths from 1D-^{1}H to ^{15}N/^{13}C CP DNP spectra of GB3 samples. Widths taken as full width at half maximum (FWHM).

Sample	Width of ^{15}N backbone envelope /ppm	Width of ^{15}N side chain envelope /ppm	Width of C_{CO} envelope /ppm	Width of C_{α} envelope /ppm	Width of C_{β} envelope /ppm
Amupol doped Microcrystalline WT-GB3	13.8	6.4	9.2	10.9	24.9
Amupol doped Frozen solution WT-GB3	14	6.8	9.8	12.8	23.3
Microcrystalline MTSSL A48C-GB3	17.1	8.4	12.4	15.2	28.5
Frozen Solution MTSSL-A48C-GB3	13.4	N/A	9.9	15.2	23.7
Microcrystalline MTSSL-D46C-A48C-GB3	16.1	7.23	10.3	13.7	25.4
Frozen Solution MTSSL-D46C-A48C-GB3	23.3	N/A	10.9	8.9	25.8
Microcrystalline MTSSL-E24C-K28C-GB3	18.5	7.5	9.3	15.7	25.6

Frozen Solution MTSSL-E24C-K28C-GB3	20.4	9.3	10.1	14.8	25.5

5.3.8 Quantification of Absolute DNP Enhancements

The value of a DNP polarising agent is not solely represented by its DNP enhancement, but the total enhancement that can be achieved. Taking into account an enhancement per unit time in sensitivity due to the reduction in recycle delay, along with the negative effect of signal quenching from the spin-spin relaxation properties of the radical, one may determine the absolute DNP enhancement (Σ). Moreover, for one to be able to make a comparison with sensitivity enhancement of the sample measured under low-temperature conditions, one must also take into account the added enhancement achieved as a result of the properties of the Boltzmann distribution.

From the tabulation of the quenching factors, θ (see Table 5.7) it is evident that the MTSSL labelled mutants experienced a higher level of quenching in comparison to the AMUPol doped sample (indicated by lower values of θ for the MTSSL labelled mutants). Though θ is in favour of AMUPol doping over the use of covalently bound spin-labels, the $T_{DNP}(^1\mathrm{H})$ achieved supports the use of such labels by the faster relaxation rates enabling faster recycle delays to be achieved therefore enhancing the sensitivity per unit time. Comparing the absolute enhancements of each sample, the greatest enhancement achieved was that of 12.5 mM AMUPol doped frozen solution of WT-GB3 with $\Sigma = 174$ and $\Sigma^{\dagger} = 455$, clearly the most effective way to enhance the signal when the amount of sample that can be obtained is limited. Comparing the most effective spin-labelled GB3 mutant sample, microcrystalline MTSSL-E24C-K28C-GB3 with $\Sigma = 10.0$ and $\Sigma^{\dagger} = 29$ against the 12.5 mM AMUPol doped microcrystalline WT-GB3 sample with $\Sigma = 25$ and $\Sigma^{\dagger} = 76$, it is evident that the doping of the sample with AMUPol is a more effective means of polarisation enhancement. However, the difference is only a factor of 1.5, thus the two methods are reasonably comparable in terms of effectiveness and polarisation enhancement. For systems where doping with an exogenous radical is not an option,[296] it is clear that an endogenous radical can be sufficiently effective to achieve the enhancements required for analysis of biological samples.

Table 5.7 Tabulation of the calculated DNP enhancement values and absolute enhancements for the mutant samples. Where the mass of protein in rotor refers to the actual amount of protein put into the rotor not the entire mass of sample (protein plus DNP juice, buffer components etc.) The uncertainty of the last digit refers to the efficiency of packing the sample into the rotor. Integrated intensities were determined from the carbonyl peak of the ^{1}H-^{13}C-CP spectra. This was selected over the entire region as with the microwave off spectra the C_{α} region can be less intense due to the greater peak dispersion so more accurate integration values were attainable from the carbonyl region. In addition, this resonance does not overlap with that of gylcerol-d_8, therefore, more accurately representing that of the protein. All spectra were obtained with 8 scans. ε is the DNP enhancement factor (calculated as the quotient of integrated on spectrum to integrated off spectrum). θ is the quenching factor (calculated as integrated on spectrum divided by both ε and the integrated intensity of the WT-GB3 undoped spectrum). $T_1(^1\mathrm{H})$ or $T_{\mathrm{DNP}}(^1\mathrm{H})$ is the proton longitudinal relaxation time or the DNP enhancement proton longitudinal relaxation time respectively. κ is the quotient of $T_1(^1\mathrm{H})$ by $T_{DNP}(^1\mathrm{H})$. Σ is the absolute DNP enhancement calculated as ε multiplied by θ and the square root of κ and multiplied by the ratio of the protein mass in the rotor to account for sample amount differences. $\Sigma^{\dagger}$ is the absolute DNP enhancement, taking into account the added Boltzmann enhancement of low-temperature (but not accounting for the reduction in thermal noise at low-temperature). Saturation recovery experiment used to determine $T_1(^1\mathrm{H})$ or $T_{DNP}(^1\mathrm{H})$ values.

Sample	Mass of protein in rotor / mg	Integrated intensity off	Integrated intensity on	ε	θ	$T_1(^1\mathrm{H})$ Or $T_{DNP}(^1\mathrm{H})$ / s	κ	Σ	$\Sigma^{\dagger}$
Undoped microcrystalline WT-GB3	15.0(2)	-	1.11E+09	-	-	13.35 (12.65, 14.05)	-	-	-

12.5mM AMUPol doped microcrystalline WT-GB3	15.0(2)	4.98E+08	1.76E+10	35.39	15.91	5.22 (4.92, 5.51)	2.56	25.45	75.84
12.5mM AMUPol doped frozen solution WT-GB3	1.0(2)	5.04E+07	5.83E+09	115.72	5.26	2.75 (2.70, 2.80)	4.85	173.94	455.17
Microcrystalline WT-GB3, doping pre-crystallisation with 12.5mM AMUPol doped	15.0(2)	1.16E+09	1.04E+10	8.99	9.39	9.30 (9.00, 9.60)	1.44	11.25	33.53
Microcrystalline MTSSL-A48C-GB3	15.0(2)	1.53E+08	1.28E+09	8.34	1.15	1.23 (1.20, 1.26)	10.85	6.83	20.35
Microcrystalline MTSSL-A48C-GB3 1 in 5	15.0(2)	7.58E+07	3.00E+08	3.96	0.27	6.87 (5.97, 7.77)	1.94	0.38	1.13
Frozen solution MTSSL-A48C-GB3	1.0(2)	4.69E+07	1.26E+08	2.69	0.11	16.03 (14.36, 17.70)	0.83	1.56	4.66
Microcrystalline MTSSL-D46C-A48C-GB3	15.0(2)	8.68E+07	4.76E+08	5.48	0.42	0.16 (0.14, 0.19)	83.43	3.92	5.30

Microcrystalline MTSSL-D46C-A48C-GB3 1 in 5	15.0(2)	2.89E+08	1.06E+09	3.68	0.96	6.37(5.62, 7.13)	2.10	1.34	3.99
Frozen solution MTSSL-D46C-A48C-GB3	1.0(2)	1.37E+07	8.70E+07	6.34	0.08	1.97 (0.95, 3.00)	6.78	3.01	8.97
Microcrystalline MTSSL-E24C-K28C-GB3	15.0(2)	1.45E+08	2.31E+09	15.91	2.09	0.61 (0.53, 0.69)	21.89	9.77	29.11
Frozen solution MTSSL-E24C-K28C-GB3	1.0(2)	4.18E+07	5.36E+08	12.84	0.48	1.16 (1.04, 1.27)	11.51	24.62	73.37

5.3.9 Analysis of Linewidths from the 2D-Spectra Acquired Under DNP Conditions

To determine the effect of low-temperature and the incorporation of a high concentration of paramagnetic relaxation agents, 2D-correlation spectra were acquired of several of the GB3 samples. Both PDSD $^{13}C/^{13}C$-correlation experiments and $^{15}N/^{13}C$-correlation experiments were utilised to investigate the effects of line broadening and analyse the fine structure of the spectra.

5.3.9.1 $^{13}C/^{13}C$-Correlation Spectra

Comparing the resolution in the 2D-$^{13}C/^{13}C$-correlation experiment of microcrystalline GB3 doped with 12.5 mM AMUPol at 107 K to that of microcrystalline GB3 at ambient temperature it is clear that the resolution is greatly attenuated. Moreover, with typical ^{13}C linewidths of 0.4 ppm (60 Hz) at 14.1 T (150 MHz, ^{13}C frequency) and with fast enough MAS to remove homogenous components to the linewidth. To analyse the broadening effects observed, 2D-proton-driven spin-diffusion (PDSD) spectra were acquired under DNP conditions at 9.4 T (100 MHz, ^{13}C frequency), with 8 kHz MAS. This could be compared to ambient temperature 2D-dipolar assisted rotational resonance (DARR) spectra acquired at 14.1 T (150 MHz ^{13}C frequency), at 12.5 kHz MAS. It is worth noting that although the spinning frequency employed is not identical for each, both are within a similar range to remove homonuclear line broadening effects so should not devalue the comparison. The variation in the field will be taken into account by use of a line broadening factor, as linewidths at 14.1 T are 50 % narrower than the equivalent peak at 9.4 T.

Within the $^{13}C/^{13}C$-correlation spectra, information on the nature of the line broadening mechanism present can be alluded to. With inhomogeneous broadening originating from the presence of a distribution of molecular orientations, leading to a corresponding distribution of peaks spanning the diagonal of the spectra, and with the homogeneous line broadening components leading to a widening of the diagonal when measured along the anti-diagonal direction.[311]

For the 12.5 mM AMUPol doped microcrystalline WT-GB3 sample, the measured linewidths of the diagonal peaks were approximately 2 ppm and assumed to represent the homogeneous linewidth. As the diagonal peaks did not exhibit any obvious variation in the

linewidth, it could be concluded that the homogenous broadening imposed upon different regions of the protein was relatively linear. A critique of this postulate is that without site-specific relaxation measurements it is difficult to achieve a more rigorous analysis to justify the points raised.

If it is accepted that the homogeneous line broadening component of the peak widths is 2 ppm, from inspection of the off-diagonal peaks it can be deduced that the dominant effect exerted on the linewidths must be that of inhomogeneous broadening due to the range of conformers frozen in position, unable to interconvert at the low-temperatures employed.

The data indicate that the transverse relaxation enhancement exerted by the paramagnetic species present in the sample, which would be observed as an increased homogenous linewidth and hence a thickening of the diagonal envelope, is likely to not dominate the broadening. These highlighted observations are in line with previous results of DNP enhanced ssNMR experiments on biopolymers at low-temperature, where the inhomogeneous nature of broadening under this regime has been extensively analysed.[221]

In contrast to the homogeneous broadening, the inhomogeneous broadening was observed as having an equal effect throughout the protein. Indeed, this is logical to understand as one would not expect different regions of the protein to express the same level of conformational freedom, this is made apparent when considering residues on the surface of the protein in comparison to residues buried within the 3D-structure. Conveniently for GB3, there is only one tryptophan present in the entire protein (W43), and the unique chemical shift region of the aromatic residue allows for this peak to be separate from the bulk of the resonances, enabling one to determine the linewidth of an individual residue of the protein unambiguously. From the cross-peak of the C_β-C_γ resonance (38.51 ppm, 133.95 ppm, Figure 5.27) the measured linewidth is ~2 ppm. By checking the location of the tryptophan residue in the published crystal structure (PDB ID: 2LUM) it is clear that this residue resides deep within the centre of the β-sheets resulting in the residues indicated rigidity and thus lack of significant inhomogeneous broadening. This conformational restriction of residues buried within the centre of a protein has been noted before, specifically in the study of type-III secretion needles where the structural location imposes a large restriction on available conformational states.[186]

Comparing the low-temperature DNP spectrum to that of the homologous protein, GB1 it may seem that the resolution observed for GB3 at low-temperature is maintained to a

greater degree than that of GB1.[120] However, a direct comparison cannot be made as the GB1 spectra were recorded at 11.75 T and with MAS of 10 kHz. In addition, the method of sample preparation of the microcrystals may differ. It may be fruitful to further investigate the variation observed at both ambient temperature and low-temperature, considering that protein dynamics at ambient temperatures are indicative of the level of inhomogeneous broadening experienced at low-temperatures.[186] Moreover, relaxation data presented in Chapter 4 indicates that there is little difference in the dynamics of the two proteins. However, useful information on the relationship between protein dynamics and conformational trapping at low-temperatures may be elucidated through further investigations into homologous proteins.

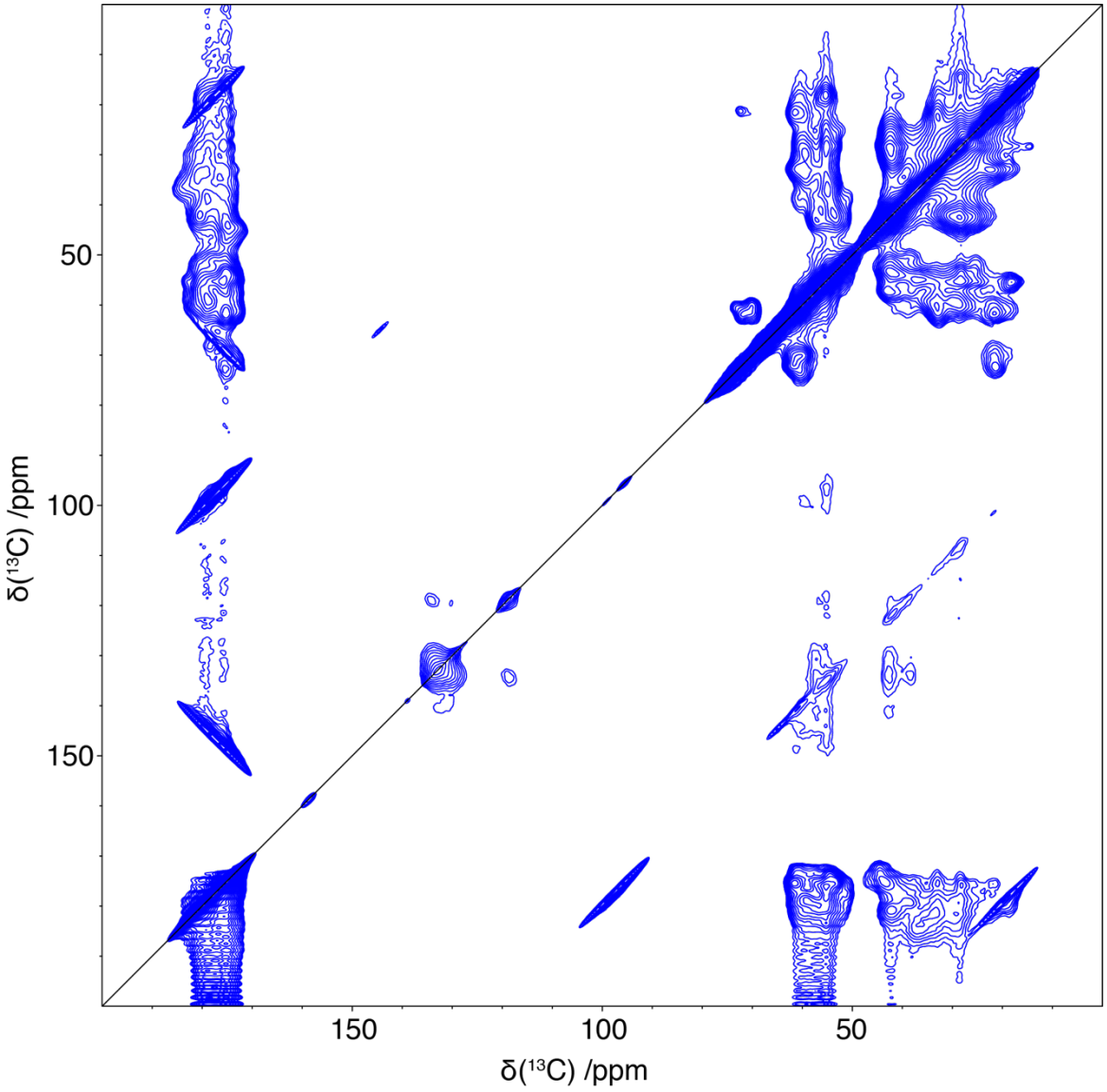

Figure 5.27 2D-PDSD spectrum of 12.5mM AMUPol doped WT-GB3 microcrystals. 20 Hz line broadening applied. Folded sideband present in all low-temperature 2D-PDSD spectra, visible at 180 ppm by 70 ppm and 175 ppm by 150 ppm.

Comparing the $^{13}C/^{13}C$-correlation spectrum of WT GB3 (278K, 12.5 kHz MAS and 600 MHz) obtained from a DARR experiment with 10 ms mixing against a $^{13}C/^{13}C$-correlation spectrum of WT-GB3 with 12.5 mM AMUPol doping (107 K, 8 kHz MAS and 400 MHz) obtained from a PDSD experiment with 10 ms mixing one can clearly see the significant increase in linewidths observed (see Figure 5.28). Where in the room-temperature spectrum, individual resonances can be identified with a width of around 0.5 ppm, for the low-temperature spectrum few individual resonances are observed. Rather the surrounding clusters are merged into an envelope.

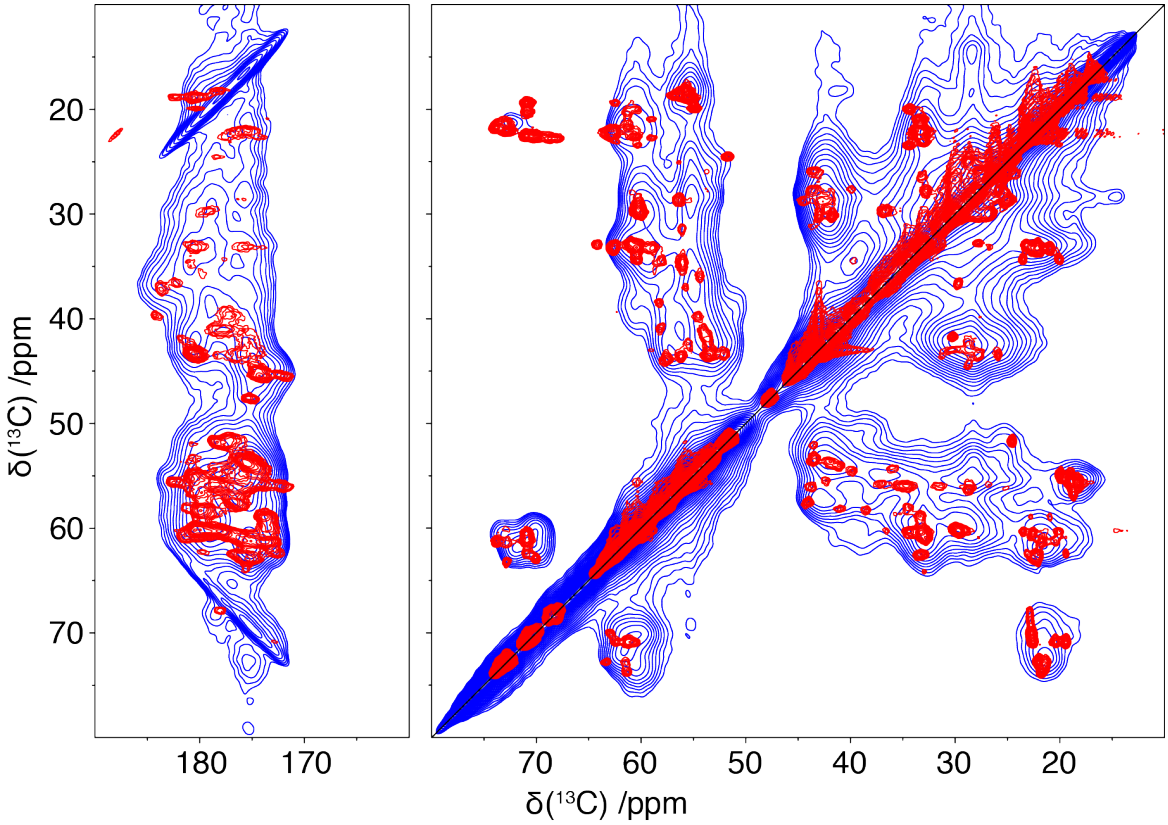

Figure 5.28 2D-PDSD spectrum of 12.5 mM AMUPol doped WT-GB3 microcrystals overlaid with 12.5 kHz DARR spectrum of WT-GB3 at ambient temperature. PDSD spectrum at 107 K with 10 ms mixing. Comparison to 12.5 kHz DARR at 278 K with 10 ms mixing. Both spectra displayed with 20 Hz line broadening in each dimension.

As a more direct comparison and to analyse the observed line broadening, the line broadening of the 12.5 kHz DARR spectrum was incrementally increased until a level that corresponded to the broadening observed in the low-temperature spectrum was reached. 150 Hz line broadening in each dimension afforded this result (see Figure 5.29 and Figure 5.30).

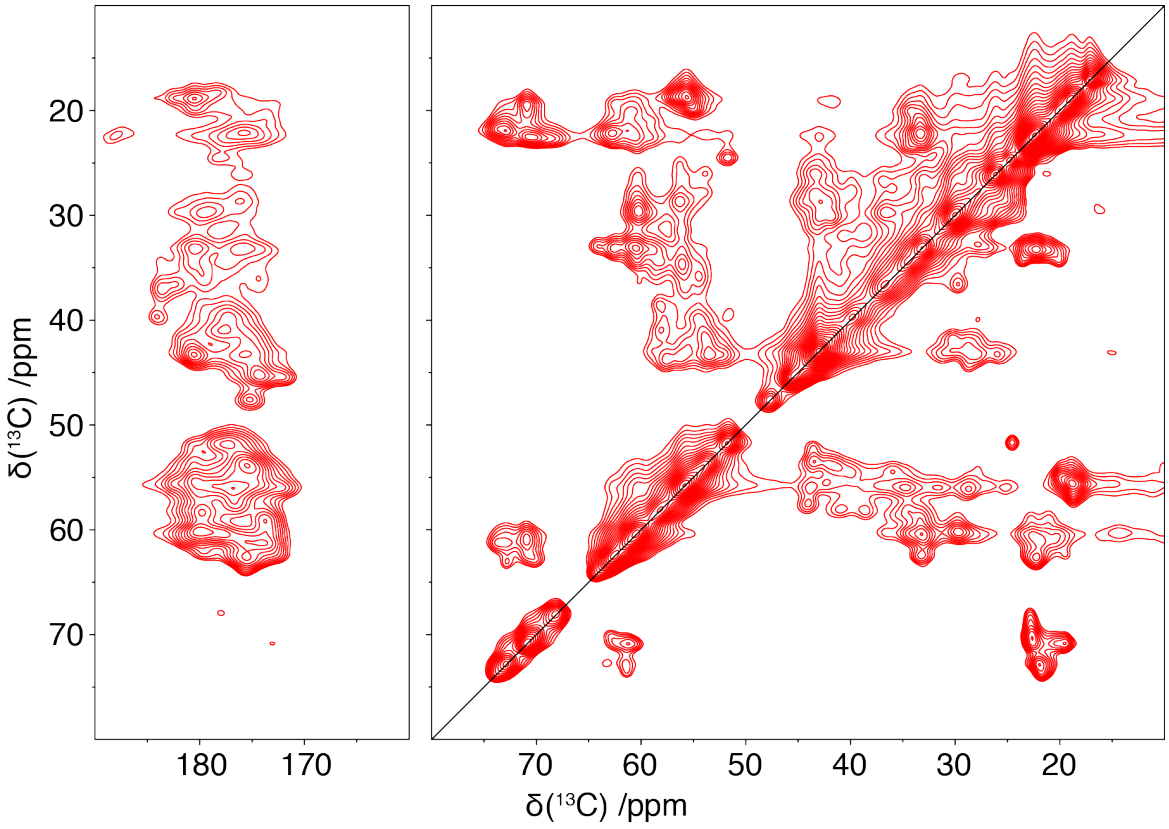

Figure 5.29 12.5 kHz DARR spectrum. At 278 K and a mixing time of 10 ms. Line broadening of 150 Hz to account for the difference in the field was applied for a comparison to the DNP enhanced PDSD spectrum.

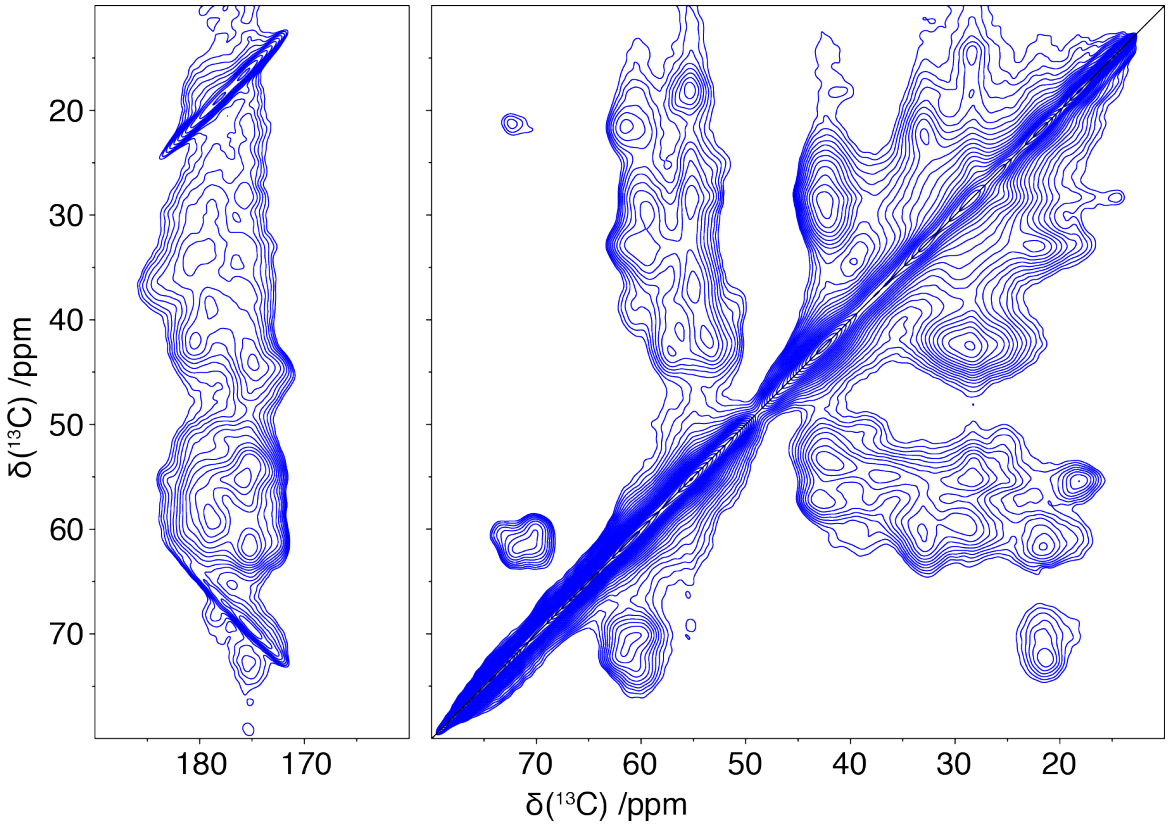

Figure 5.30 2D-PDSD spectrum of 12.5 mM AMUPol doped GB3 microcrystals at 107 K and a mixing time of 10 ms. 20 Hz line broadening. Folded sideband present in all low-temperature 2D-PDSD spectra, visible at 180 ppm by 70 ppm.

Comparing the 2D-^{13}C/^{13}C-correlation spectra of WT-GB3 under the DNP conditions in both a microcrystalline form and also a frozen solution shows a slight increase in line widths observed from the frozen solution. This is indicative of the greater variation in conformers present in the sample in a frozen solution in comparison to a microcrystalline sample where there is good short range and long-range uniformity in the sample (see Figure 5.31).

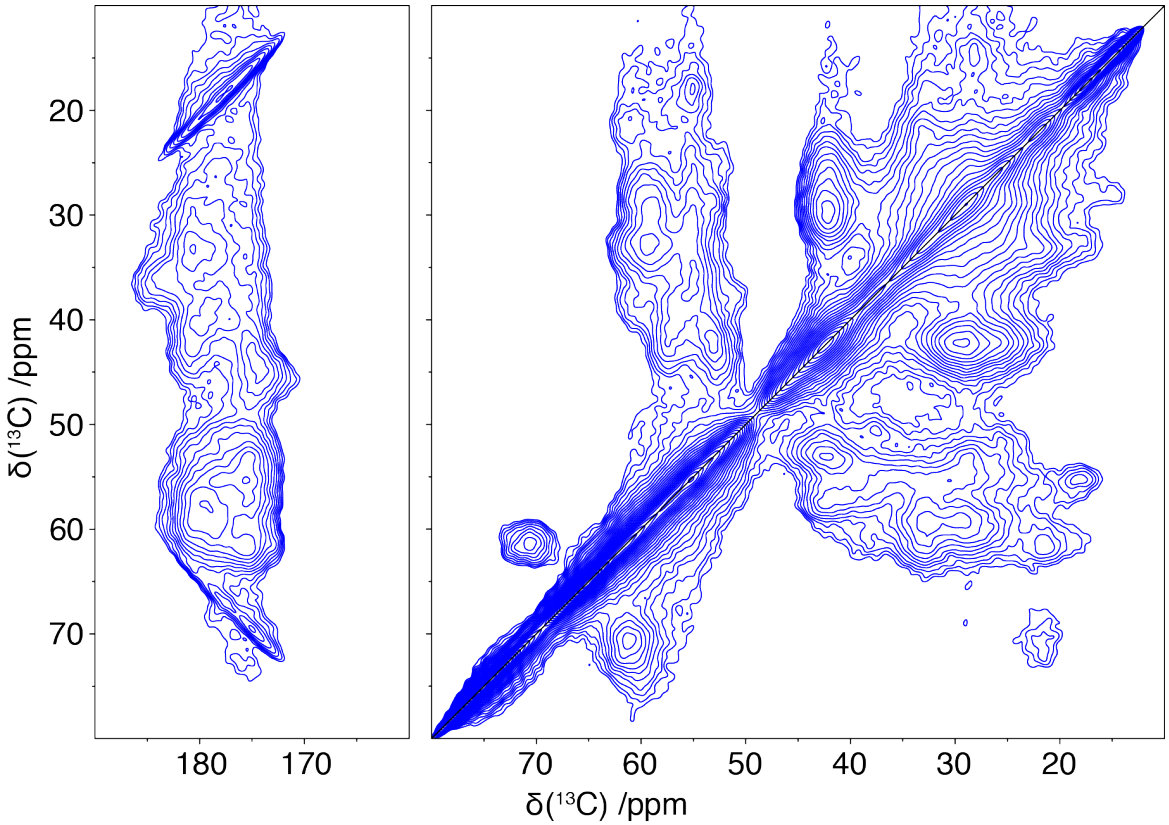

Figure 5.31 2D-PDSD spectrum of 12.5 mM AMUPol doped GB3 frozen solution at 107 K and a mixing time of 10 ms.

Investigating the effect of the AMUPol on the linewidths proved difficult in that without the AMUPol doping DNP enhancements could not be utilised in acquiring the spectra and therefore the signal is poor. However, it can be observed that there is no significant line broadening caused by the addition of AMUPol and that the major factor effecting the line broadening is that of the low-temperature freezing out the motions of the protein molecule. The freezing of motions leads to several conformers present in the sample at a given time. A comparison of the AMUPol doped WT-GB3 sample with the undoped WT-GB3 sample shows that there is little-observed increase in line widths of the spectrum on the addition of the AMUPol, suggesting that the broadening caused by the low-temperature is much greater than that the paramagnetic relaxation agent so any broadening caused is overshadowed. The 2D-PDSD spectrum of the undoped microcrystalline sample does seem to possess some fine structure, not present in the 12.5 mM AMUPol crystalline sample. Moreover, through investigation of the linewidths of these regions, there is on average between 0.5 ppm additional line broadening that can be attributed to the doping with AMUPol.

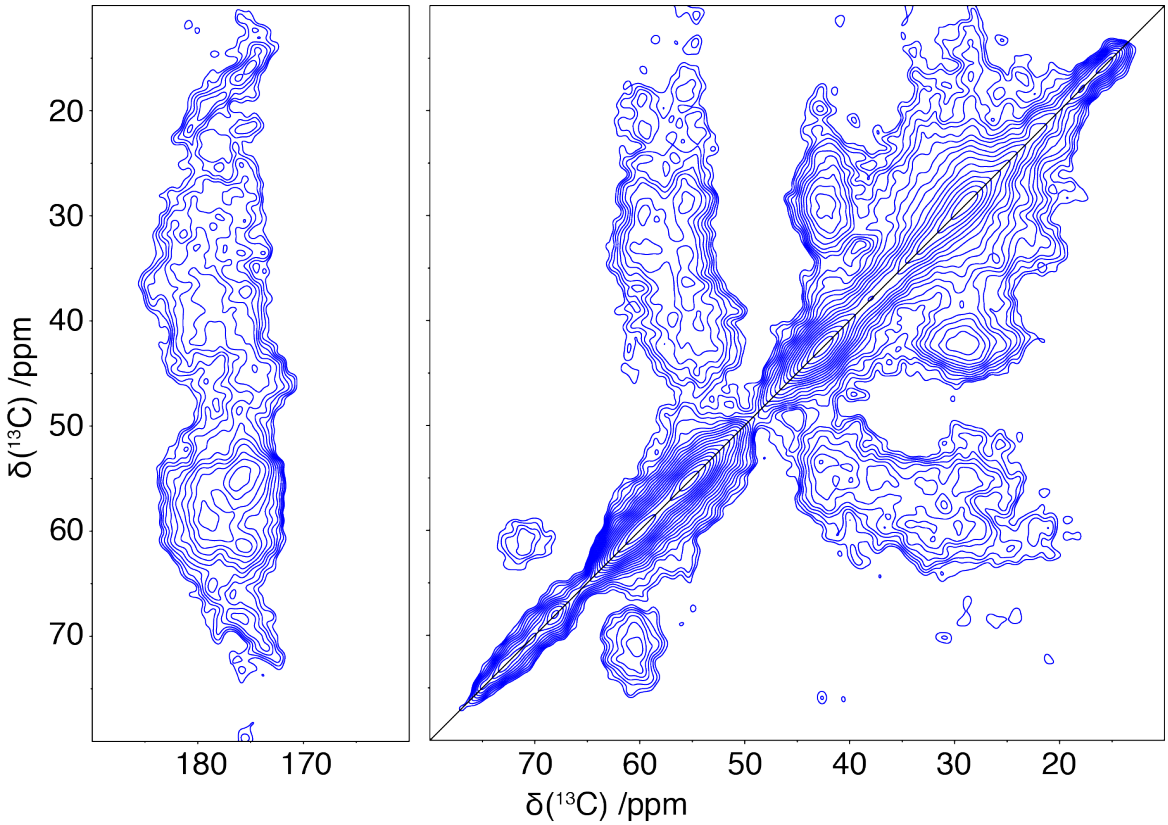

Figure 5.32 2D-PDSD spectrum of undoped GB3 microcrystals at 107 K and a mixing time of 10 ms.

Comparing the use 2D $^{13}C/^{13}C$-correlation spectrum of AMUPol doped WT-GB3 to MTSSL-labelled E24C-K28C-GB3 one can see that the MTSSL significantly broadened the lines, attributed to the doping of the sample covalently with the relaxation agent. The resolution observed is noticeably attenuated, with fine structure present in the spectra being obscured. Of note is the absence of threonine C_α/C_β cross-peak, characteristically present at ~60 ppm by ~70 ppm (see Figure 5.33).

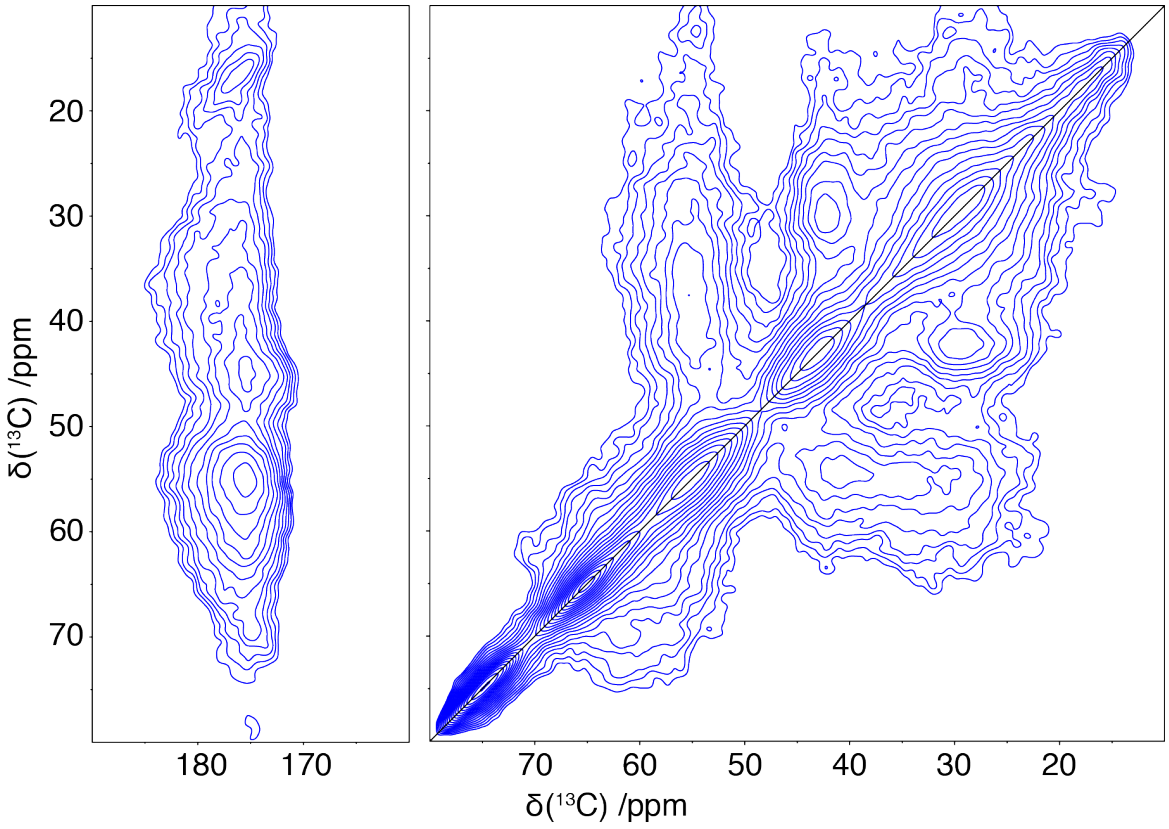

Figure 5.33 2D-PDSD spectrum of MTSSL labelled -E24C-K28C-GB3 microcrystals at 107 K and a mixing time of 10 ms.

5.3.9.2 $^{15}N/^{13}C$-Correlation Spectra

NCA spectra of several samples were also recorded. As with the $^{13}C/^{13}C$-correlation, one observes a broadening of the peaks in comparison to the room temperature spectra (see Figure 5.34). In general, the broadening of the low-temperature DNP spectra is so severe that no individual resonances or clusters of resonances can be picked out, save for the glycine region of the spectra at 45 ppm in the ^{13}C dimension and 110 ppm in the ^{15}N. In addition, a single resonance corresponding to the T25 residue, located on the periphery of the protein, with the side chain facing out of the surface of the protein at the carboxy end of the single α-helix present in the protein is present. The resonance is observed at 67 ppm in the ^{13}C dimension and 117 ppm in the ^{15}N. From this resonance, one can determine the line broadening of each individual resonance that is experienced under DNP conditions and make a comparison to the room temperature data. While the room-temperature data exhibits line widths of 0.8 ppm for the ^{15}N dimension and 1 ppm for the ^{13}C dimension, the DNP enhanced spectra exhibits line widths of 5.5 ppm for the ^{15}N dimension and 2.5 ppm for the ^{13}C dimension. Accordingly, this corresponds to a broadening of a factor of

approximately 7 for the ^{15}N dimension and 2.5 for the ^{13}C dimension. Interestingly the line widths of the ^{15}N were increased to a much greater extent. It is possibly the case that the ^{15}N CSA is affected to a greater extent than the ^{13}C CSA as the ^{15}N can interact with protons. In addition, there is a greater diversity of environments ^{15}N nuclei can adopt.[312-316] It is worth noting that the T49 resonance located at ~60 ppm in the ^{13}C dimension and ~102 ppm in the ^{15}N dimension, has disappeared in the low-temperature spectra. This residue is located on the connecting loop between β-sheets three and four. The reasoning behind this may be that due to the high range of conformations possible in the connecting loop. The resonance experiences an increased level of inhomogeneous broadening, indeed increasing the contour levels a broad resonance spreading through this region can be observed.

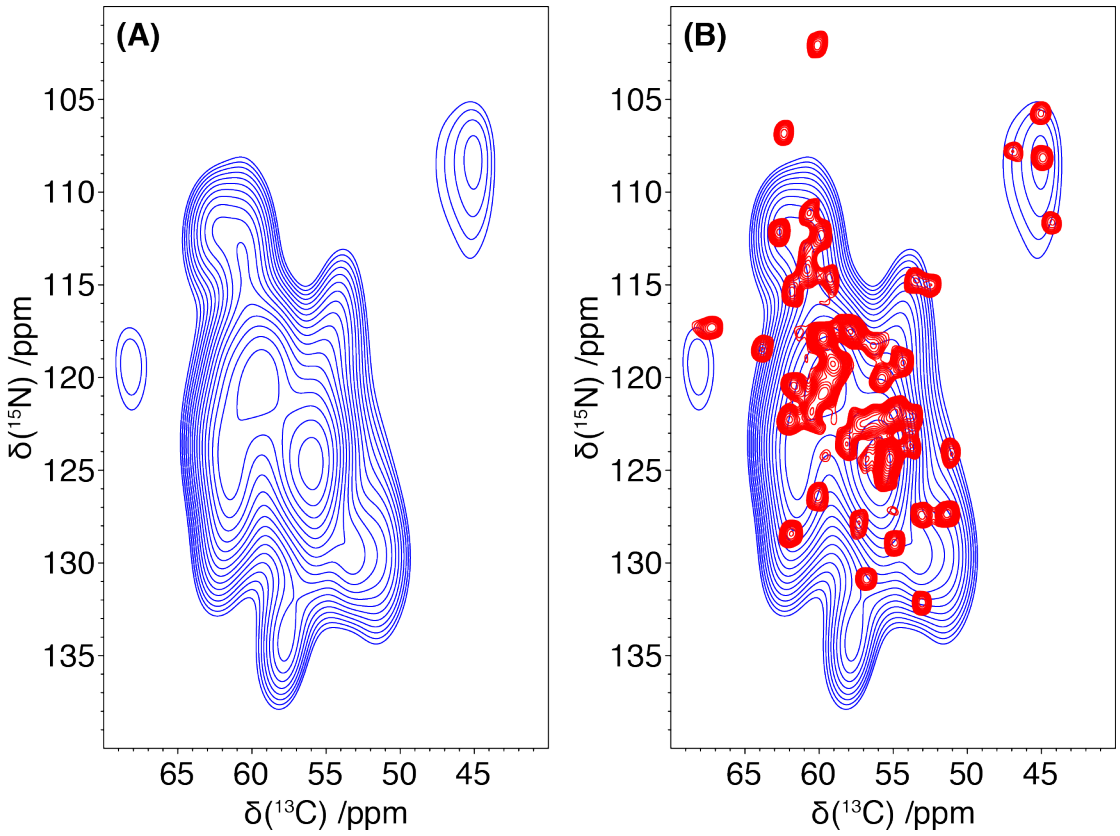

Figure 5.34 2D-NCA spectrum of 12.5 mM AMUPol doped microcrystalline WT-GB3 at 107 K(A). Spectrum overlaid with a 2D-NCA at 12.5 kHz MAS, 278 K of undoped microcrystalline WT-GB3 (B).

To determine the extent of line broadening experienced at low-temperature, the line broadening function applied to the room temperature spectrum was varied incrementally until the line widths were comparable to the low-temperature DNP spectrum (see Figure 5.35). The general shape of the protein envelope conforms to that of the low-temperature spectrum, indicating that the crystal structure has not changed under the low-temperature conditions where a glassy matrix has formed.

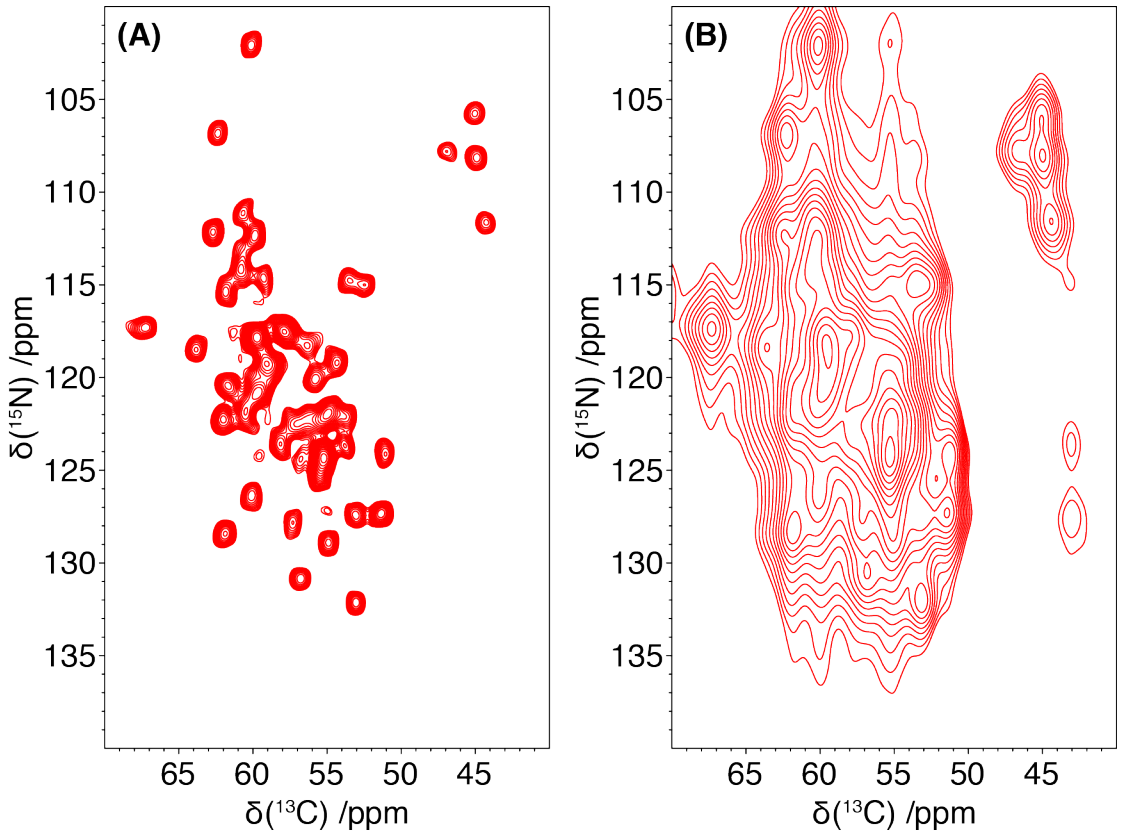

Figure 5.35 2D-NCA spectrum of undoped microcrystalline WT-GB3, at 12.5 kHz, 278 K, with 20 Hz line broadening (A) and with 150 Hz line broadening (B) for a direct comparison to the 2D-NCA spectrum acquired under the DNP conditions.

Comparing the low-temperature 2D-NCA spectrum of 12.5 mM AMUPol doped WT-GB3 in both microcrystalline and frozen solution form (see Figure 5.36) it can be determined that the improvement on resolution gained from the formation of crystals has only a small observable effect on resolution. Interestingly, the single resonance corresponding to the T25 residue, observed at 67 ppm in the ^{13}C dimension and 117 ppm in the ^{15}N, present in the microcrystalline spectrum, is not present in the frozen solution spectrum. This is potentially due to the formation of microcrystals reducing the conformational freedom of the residue leading to a sharper resonance, in comparison to the frozen solution spectrum where the resonance has been significantly broadened.

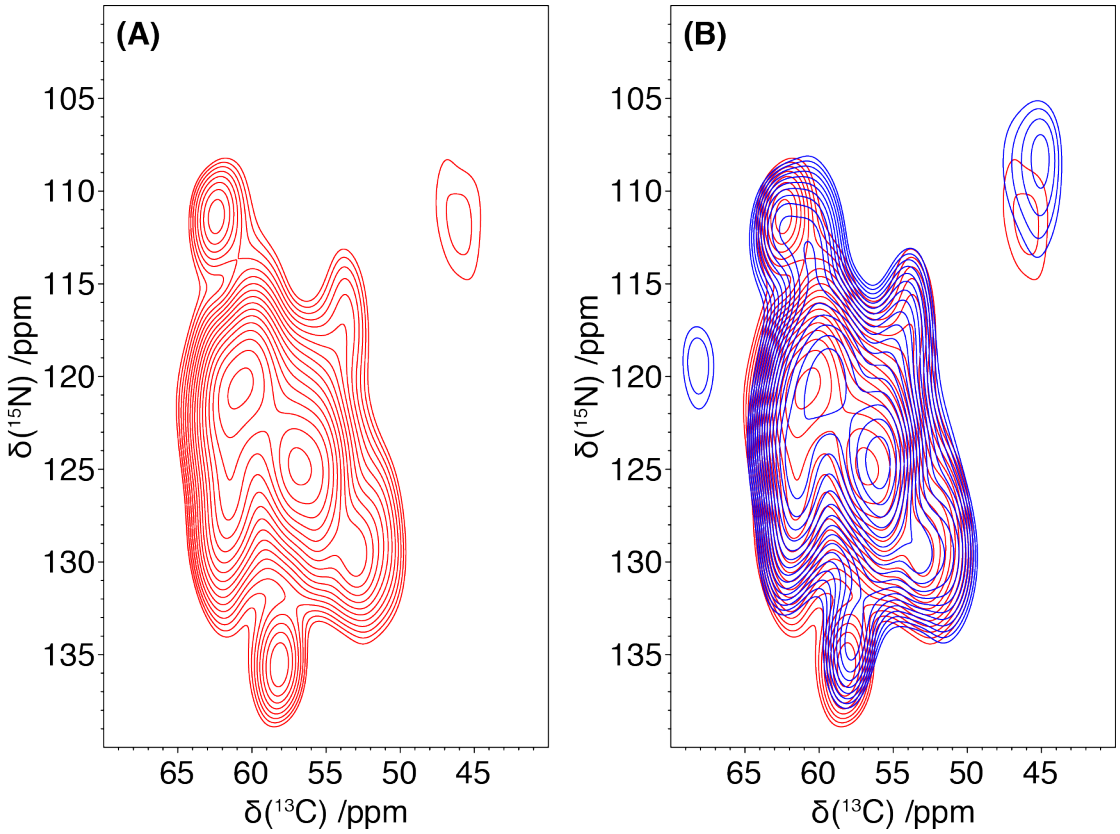

Figure 5.36 2D-NCA spectrum of 12.5mM AMUPol doped WT-GB3 frozen solution at 107 K. Acquired under DNP conditions (A) and the spectrum overlaid with the microcrystalline WT-GB3 spectrum acquired under DNP conditions.

The acquired 2D-NCA spectrum for the MTSSL labelled A48C-GB3 microcrystalline sample and MTSSL labelled E24C-K28C-GB3 sample demonstrates a greater broadening of the lines in comparison to the AMUPol doped WT-GB3 sample (see Figure 5.37). This is likely due to the close proximity of the polarising agent, that at close range, as described by the Solomon equations (see relaxation enhancement theory in Chapter 4) exerts a greater T_2 relaxation effect, leading to a greater homogeneous line broadening effect. Though in the context of low-temperature experiments where one typically does not use the experiments to ascertain an assignment of the spectra but rather to determine other useful information on the system this increased broadening may be acceptable. For circumstances where low-temperature experiments are to be required for assignment purposes, more specific labelling schemes are required to avoid ambiguity with residue assignment. Of interest from the spectra is the presence of the glycine region in the double spin-label sample, microcrystalline MTSSL-E24C-K28C-GB3 spectrum but not in the single spin-label sample, MTSSL-A48C-GB3. On inspection of the spectrum, increasing

the observed contours shows this region is still present, yet of approximately 50 % lower intensity than that in the double mutant.

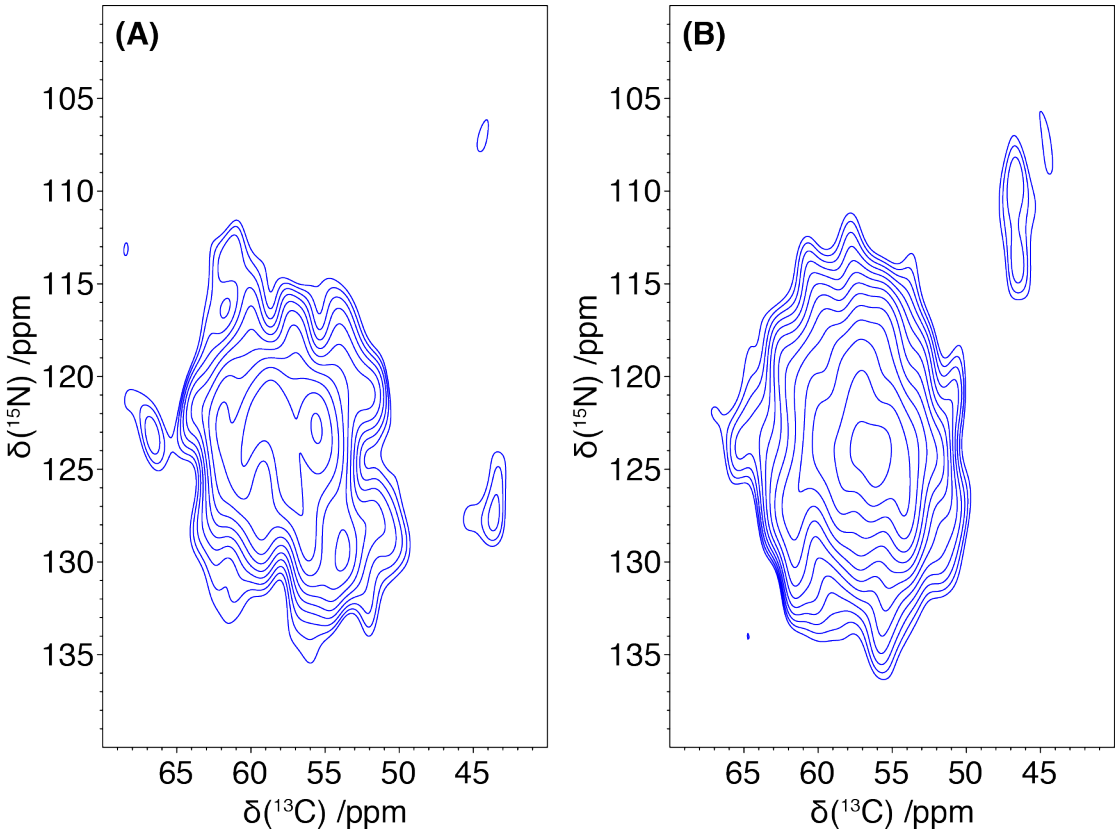

Figure 5.37 2D-NCA spectra of MTSSL labelled GB3 mutants. 2D-NCA spectrum of MTSSL-labelled microcrystalline A48C-GB3 at 107 K under DNP conditions (A) and NCA spectrum of microcrystalline MTSSL-labelled E24C-K28C-GB3 at 107 K under DNP conditions (B).

5.4 Conclusion

To summarise, we have successfully engineered GB3 cysteine mutants with two attached MTSSL spin-labels to act as a pseudo-biradical to elicit the CE. We have used a variety of techniques to validate the integrity of the system, including MS, CD, cw-EPR and moderate-speed room-temperature NMR measurements. We have examined the enhancement effects as a result of CE-DNP experiments and evaluated the resulting effects on the obtained spectra due to the incorporation of such polarisation agents. In conclusion, the employment of an intramolecular pseudo-biradical for the study of crystalline samples has been demonstrated, with the enhancement levels quantified both in terms of the DNP enhancement and absolute enhancements achieved. The use of such endogenous pseudo-biradicals have proven themselves to be a potential alternative to the use an exogenous biradical such as AMUPol and shows enhancement levels as good as those cited in the literature (see § 5.1.4.5). For situations where the employment of an exogenous biradical is not possible, on solubility grounds, it may be more suitable to use endogenous pseudo-biradicals which are widely available in comparison to covalently bound biradicals which are not currently available for general application and have not shown any considerable improvement on the aforementioned pseudo-biradicals.[297]

Chapter 6: Conclusions and Perspective

Solid-state nuclear magnetic resonance (ssNMR) is an invaluable tool for the study of biological systems. Throughout this project we have explored aspects of ssNMR with a focus on improving the sensitivity of the technique, be this through a physical improvement in signal to noise or an apparent improvement in sensitivity by enhancing the information content.

The model protein system, GB3, was successfully expressed, purified and crystallised. In addition, site-directed mutagenesis was performed to create cysteine mutants for the attachment of spin-labels to the protein surface. The purification of GB3 and its mutants was confirmed with mass spectroscopy (MS) and the purity of the samples determined through SDS-PAGE. MS was also used to confirm spin-labelling of cysteine mutants.

One of the major time-consuming steps in biomolecular ssNMR is resonance assignment. The second order dipolar recoupling scheme, the mixed rotational and rotary resonance (MIRROR) sequence[1] was employed to facilitate protein backbone assignment under moderate spinning speeds. This was achieved through the band selective nature of MIRROR, enabling the bidirectional transfer of magnetisation from the C_{CO} site to the adjacent C_α, and to the C_α of the next amino acid. When incorporated into to a 3D-NCOCA experiment this doubles the information content providing correlations from $C_{CO}^{(i-1)}$ to both $C_\alpha^{(i-1)}$ and $C_\alpha^{(i)}$. The presence of these two correlations permits the sequential assignment of the protein backbone without the need for conducting multiple 3D experiments. In addition, as the $n = 0$ MIRROR condition is inherently low frequency; being determined entirely by the separation of the C_{CO} and C_α envelopes. This allows the recoupling scheme to be performed under low rf-amplitudes enabling the construction of 'low-power' experiments facilitating further reductions in the data acquisition time. The scheme was applied under both low-power and high-power proton decoupling and CP schemes, with little reduction in decoupling ability under lower-power decoupling schemes and minimal reduction in CP transfers. The magnetisation transfers from the $C_{CO}^{(i-1)}$ to both $C_\alpha^{(i-1)}$ and $C_\alpha^{(i)}$ was investigated both experimentally and through numeric spin simulations. The experimental investigations determined that the magnetisation was transferred at a similar rate to each site, independent of the longer distance to the $C_\alpha^{(i)}$ site. The simulations determined which protons were necessary to facilitate magnetisation transfer to the

individual C_α sites. In conclusion, the MIRROR recoupling scheme was shown to be helpful in enhancing the information content of NMR spectra and by extension the reduction in time taken to conduct the experiment. The technique for backbone assignment could likely be applied to other, more complex proteins, where sufficient spectral resolution can be achieved to enable sequential assignment from a uniformly labelled $^{15}N,^{13}C$ sample.

In terms of future work, for the use of a 3D-NCOCA exploiting the MIRROR recoupling, it would be informative to apply the technique to a membrane protein for backbone assignment. Investigations into the effect of sample deuteration on the technique would also prove insightful. Moreover, through combining the technique with paramagnetic assisted condensed data collection (PACC)[317], further enhancements in sensitivity per unit time could be realised.

We have investigated the use of relaxation agents to assist in the measurement of both room-temperature and cryogenic NMR experiments. The room-temperature relaxation properties and dynamics of GB3 was explored. Site-specific R_1 and $R_{1\rho}$ measurements of microcrystalline [U-$^{13}C,^{15}N$]GB3 were used to understand the relaxation of residues in the protein and gain understanding into how this relates to the dynamics of the protein. A comparison was made to compare WT-GB3 to a cysteine mutant of the protein, A48C-GB3. In addition, the relaxation of GB3 was compared to the homologous protein GB1, which has had its site-specific relaxation properties rigorously analysed.[219] Low-temperature NMR measurements of microcrystalline [U-$^{13}C,^{15}N$]GB3 were used to investigate the effect temperature has on the ^1H longitudinal relaxation, ^1H T_1. It was observed that at temperatures above the glass transition point of the matrix, reduction in temperature led to a minimal change in the relaxation rate. As the temperature was further reduced, the molecular motions were frozen, leading to a rapid decrease in the ^1H T_1 relaxation time. In addition, the effect on the resolution as a function of temperature was explored. Through these measurements, it was evident that at low-temperature spectral resolution is severely compromised, caused by a freezing out of motions. This results in an inhomogeneous broadening of the lines which cannot be removed through MAS. However, it is also apparent that the degree of dynamics present relates to the level of broadening experienced,[186] with rigid, core amino acid residues exhibiting narrow peak widths. Of note the lone tryptophan (W43) with a line width of ~2 ppm determined from the AMUPol doped WT-GB3 sample. This resonance is buried deep within the centre of the protein structure and thus exhibits significant motional restriction. As a result, the inhomogeneous

line broadening of this resonance is lower than that present in more mobile regions of the protein.

MAS-ssNMR saturation recovery and spin echo experiments were performed on microcrystalline [U-^{15}N]GB3 to obtain the ^{1}H T_1 and ^{15}N transverse relaxation constants, ^{15}N T_2, respectively. The ^{1}H T_1 values were determined in a site-specific manner in an attempt to ascertain if and where relaxation agents locate themselves in the samples. It could be concluded that at 10 kHz MAS speed and with a dopant concentration of 1 mM there was no significant difference between the values for ^{1}H T_1 constants for individual nitrogen backbone resonances in each sample. Repeating the experiments at higher spinning speeds to reduce spin diffusion may provide information on if and where the relaxation agents locate themselves in the sample. An investigation into the relaxivity of dopant agents was carried out through varying the concentration of dopant in microcrystalline [U-^{15}N]GB3 samples. The proton longitudinal relaxivity, ^{1}H r_1, at 295 K was determined to be 16.1±1.3 $s^{-1}mM^{-1}$ for Gd-DTPA and 0.93±0.01 $s^{-1}mM^{-1}$ for Ho-DTPA. With the aim of enhancing the sensitivity of ssNMR, measurements at low-temperature represent an attractive means of enhancement. With the exploitation of the Boltzmann distribution and reduction in thermal noise the primary means of signal enhancement. A means of reducing the massive ^{1}H T_1 at low-temperature would greatly assist in low-temperature measurements. However, the spectral resolution of proteins at low-temperature, due to inhomogeneous broadening remains a problem. This could be potentially alleviated through careful choice of the cryo-protectant agent to allow some degree of motion at reduced temperatures.[318] It may also be fruitful for investigation into a means of preparation of protein samples with reduced conformers to alleviate the inhomogeneous broadening.

Further low-temperature relaxation studies are required to fully understand the mechanisms of relaxation enhancements at low-temperature. Particularly, it would be interesting to perform relaxation measurements on both Gd^{3+} and Ho^{3+} doped GB3 samples at low-temperature and measure the relaxation rate as a function of temperature. In addition, observing the spectral resolution at low-temperature would also prove useful for determining the utility of the relaxation agents.

We have designed a pseudo-biradical attached to a protein and used protein engineering to create optimal geometry for the cross effect (CE). The correct formation of this has been

checked by mass spectroscopy (MS), circular dichroism (CD), continuous wave electron paramagnetic resonance (cw-EPR) and moderate-speed room-temperature ssNMR measurements.

We have examined the enhancement effects as a result of CE-DNP experiments and evaluated the resulting effects on the obtained spectra due to the incorporation of such polarisation agents. In addition to the enhancements owed to the CE, the absolute enhancements of the samples were quantified. Such absolute enhancements extend to account for the impact on the relaxation rate and signal quenching of the polarising agent. The MTSSL labelled mutants experienced a higher level of quenching in comparison to the AMUPol doped sample (indicated by lower values of θ for the MTSSL labelled mutants). Though θ is in favour of AMUPol doping over the use of covalently bound spin-labels, the $T_{DNP}(^1\mathrm{H})$ achieved supports the use of such labels by the faster relaxation rates enabling faster recycle delays to be achieved. Comparing the absolute enhancements of each sample, the greatest enhancement achieved was that of 12.5 mM AMUPol doped frozen solution of WT-GB3 with $\Sigma = 174$ and $\Sigma^{\dagger} = 455$. Therefore, when the amount of sample that can be obtained is limited this would be the sample preparation of choice. Comparing the most effective spin-labelled GB3 mutant sample, microcrystalline MTSSL-E24C-K28C-GB3 with $\Sigma = 10.0$ and $\Sigma^{\dagger} = 29$ against the 12.5 mM AMUPol doped microcrystalline WT-GB3 sample with $\Sigma = 25$ and $\Sigma^{\dagger} = 76$, it is evident that the doping of the sample with AMUPol is a more effective means of polarisation enhancement. However, the difference is only a factor of 1.5, thus the two methods are reasonably comparable in terms of effectiveness and polarisation enhancement. In terms of the broadening effects of the radical on the spectra, it was clear that the use of the pseudo-biradicals led to a significant broadening in comparison to the amount experienced with AMUPol doping. As far as we are aware, this is the first demonstration of an intramolecular pseudo-biradical for the enhancement of protein ssNMR spectra through the CE. We can conclude from our study that, the employment of endogenous pseudo-biradicals pose a potential alternative to the use an exogenous biradical, such as AMUPol. Moreover, they show enhancement levels as good as those cited in the literature.[291-295, 297] For situations where the employment of an exogenous biradical is not possible, it may be more suitable to use pseudo-biradicals. Pseudo-biradicals are widely available in comparison to covalently bound biradicals which are not currently available for general application and have not shown any considerable improvement on the aforementioned pseudo-biradicals.[297]

For the CE-DNP experiments, it may be worthwhile to explore the employment of lanthanide radicals as polarisation agents,[282-283] particularly Gd^{3+} and Ho^{3+}, as they are shown to have limited adverse effects on the spectral resolution. Moreover, the electronic relaxation rate of Ho^{3+} aligns favourably as a strong longitudinal relaxation agent at low-temperature.[174] The design of covalently bound lanthanide radicals has previously been demonstrated in the literature,[319] though their application to the CE has yet to be explored. Currently, cryogenic NMR experiments are conducted at relatively low MAS speeds due to complications with probe design for high speeds at cryogenic temperatures. Advancements in spinning speeds for cryogenic NMR will undoubtedly improve the utility of the technique through improvements in resolution as a result of improved averaging of anisotropic interactions.

To summarise, several means of sensitivity enhancements for ssNMR of biological samples have been explored. In a field where the main limitation of the technique is the inherent low sensitivity, pathways to alleviating this limitation are of paramount importance. Through the design of a 3D experiment to enhance the information content at moderate spinning speeds, investigations into relaxation agents for low-temperature ssNMR and novel methods for DNP of biomolecules, we have strived towards contributing towards sensitivity enhancements for ssNMR.

Chapter 7: Appendices

Appendix A A Novel Approach to Protein Assignment in ssNMR

7.1 MIRROR Simulations

7.1.1 Example Script

The following function and script to call it were used to compute spin dynamics simulations with Spinach.

```
% Simulation of MIRROR/DARR recouping. Function called with 1H rf field and mas frequency
% as input values. Relatively simple geometry employed. Can be used with
% proton_recoupling_expt to generate a plot of matching conditions.
% i.kuprov@soton.ac.uk
% aanevzor@ncsu.edu
function [C4z,C5z,C6z,timestep,nsteps]=proton_recoupling_modified(h1field,masfreq)
% System specification
sys.magnet=14.1;
sys.isotopes={'13C','13C','13C','1H','1H','1H'};
% Interactions
inter.zeeman.scalar={  50.0000  170.000  50.0000 0.3413 0.3413 0.3413 };
inter.coordinates={
                [ 0.00000000    0.00000000    0.000000]
                [ 1.32000000    0.75000000    0.000000]
                [ 3.75000000    0.57000000    0.000000]
                [ 0.00000000    -1.0000000    0.000000]
                [ 2.42000000    -1.0000000    0.000000]
                [ 3.75000000    1.57000000    0.000000]
};
  % Cai-1 CO Cai 1H(cai-1), 1H(N), 1H(cai)
inter.temperature=298;
% Basis set
bas.formalism='sphten-liouv';
bas.approximation='IK-1';
bas.connectivity='full_tensors';
bas.level=1; bas.space_level=3;
% Spinach housekeeping
spin_system=create(sys,inter);
spin_system=basis(spin_system,bas);
% MAS parameters
parameters.rate=masfreq;
parameters.axis=[1 1 1];
parameters.max_rank=3;
parameters.grid='Repulsion_ab_100_oct';
%Set up initial density operator (I_2z)
parameters.rho0=state(spin_system, {'Lz'},{2});
%Set up detect operator (I_3z)
parameters.coil=state(spin_system, {'Lz'},{1});
```

```
parameters.decouple={};
parameters.sweep=5e4;
parameters.npoints=40960;
parameters.offset=15000;
parameters.spins={'13C'};
parameters.decouple={};
parameters.axis_units='ppm';
parameters.invert_axis=1;
parameters.zerofill=8192;
parameters.rf_power=h1field;
parameters.verbose=1;
% Run the simulation and collect data for spin 6
C6z=singlerot(spin_system,@mirror,parameters,'nmr');
% Repeat with spin 5 to look at loss of magnetization
parameters.rho0=state(spin_system,{'Lz'},{2});
parameters.coil=state(spin_system,{'Lz'},{2});
C5z=singlerot(spin_system,@mirror,parameters,'nmr');
% Repeat with spin 4 to look at loss of magnetization
parameters.rho0=state(spin_system,{'Lz'},{2});
parameters.coil=state(spin_system,{'Lz'},{3});
C4z=singlerot(spin_system,@mirror,parameters,'nmr');
timestep=1/parameters.sweep;
nsteps=parameters.npoints+1;
end
clear
output=zeros(40960,200);
%for n=1:200
n=1;
[C4z,C5z,C6z,timestep,nsteps]=proton_recoupling_modified(18500,35000);
C4zoutput(:,n)=real(C4z);
C5zoutput(:,n)=real(C5z);
C6zoutput(:,n)=real(C6z);
hold on
%rffield=[1:1:200];
% rffield=rffield*250;
timebase=[0:1:40959];
timebase=timebase*0.0000025;
% figure(1)
% subplot(2,1,1)
% mesh(rffield,timebase,C2zoutput)
% subplot(2,1,2)
% mesh(rffield,timebase,C3zoutput)
figure(1)
subplot(3,1,1)
plot(timebase,real(C4z));
title('Magnetisation build up on Cai')
subplot(3,1,2)
plot(timebase,real(C5z));
title('Magnetisation decay on CO')
subplot(3,1,3)
plot(timebase,real(C6z));
title('Magnetisation build up on Cai-1')
savefig('Magnetisation_Build_Up.fig')
save variables.mat C5z C6z C4z timebase C4zoutput C5zoutput C6zoutput n nsteps output timestep
```

7.1.2 Parameter Convergence for Spin Simulation

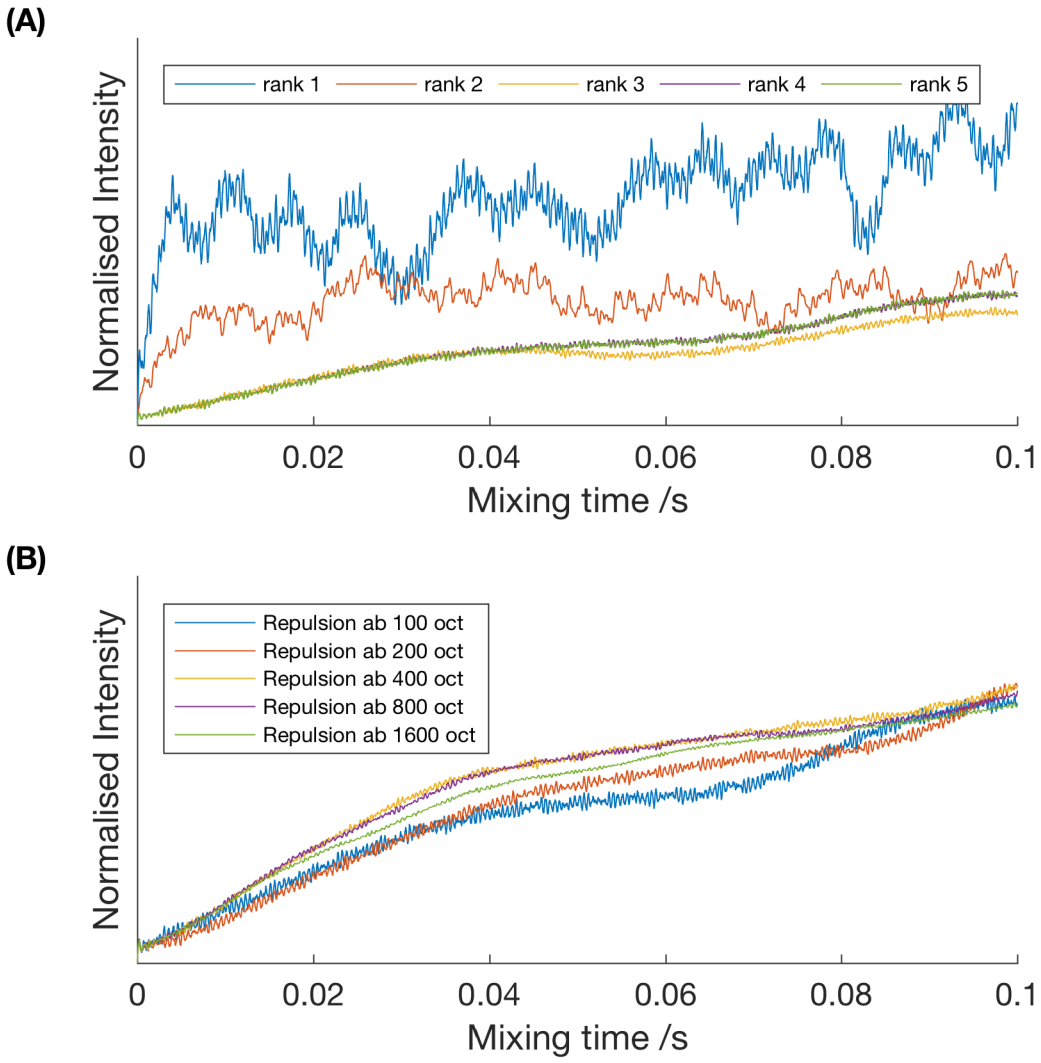

Figure 7.1 Convergence of parametersOf Spinach simulation.[35] Convergence of rank (A). Rank 4 and 5 overlays therefore rank converged at 4. Convergence of repulsion grid (B). Repulsion grid converged at ab 400 oct.

7.2 Rates of Backbone Transfers and Ratio Between the Final Peak Intensities

Table 7.1 Rates of backbone transfers and ratio between the final peak intensities. Analysis of rate of transfer from the $C_{CO}^{(i-1)}$ to the $C_{\alpha}^{(i)}$ and $C_{\alpha}^{(i-1)}$ resonances and ratio of the two intensities for assigned resonances in GB3. *Denotes regions with spectral overlap resulting in anomalous ratios.

Residue	NCA /sec	NcoCA /sec	$I_{NCA/NcoCA}$
2GlnC_α*	0.035	0.043	1.53
3TyrC_α	0.040	0.069	0.68
4LysC_α*	0.040	0.039	0.68
5LeuC_α	0.037	0.041	0.38
6ValC_α*	0.030	0.048	0.77
7IleC_α	0.041	0.038	0.39
8AsnC_α	0.014	0.043	0.74
9GlyC_α	0.019	0.035	0.44
10LysC_α*	0.043	0.042	0.69
11ThrC_α	0.031	0.037	0.34
12LeuC_α	0.026	0.038	0.34
13LysC_α*	0.031	0.033	1.03
14GlyC_α	0.025	0.036	0.45
15GluC_α	0.026	0.033	0.80
16ThrC_α*	0.041	0.040	1.03
17ThrC_α*	0.025	0.036	0.52
18ThrC_α	0.049	0.040	0.33
19LysC_α*	0.028	0.038	1.12
20AlaC_α*	0.027	0.033	0.79
21ValC_α	0.014	0.038	0.16
22AspC_α	0.035	0.054	0.46

23AlaC_α	0.037	0.041	0.60
24GluC_α	0.028	0.047	0.38
25ThrC_α*	0.027	0.039	0.95
26AlaC_α*	0.045	0.033	0.48
27GluC_α*	0.045	0.046	0.98
28LysC_α*	0.045	0.043	1.20
29AlaC_α*	0.037	0.046	0.81
30PheC_α*	0.036	0.038	0.31
31LysC_α*	0.040	0.051	1.22
32GlnC_α*	0.042	0.055	1.10
33TyrC_α	0.042	0.063	0.36
34AlaC_α	0.032	0.036	1.06
35AsnC_α	0.033	0.064	0.75
36AspC_α	0.026	0.051	0.42
37AsnC_α*	0.024	0.033	0.58
38GlyC_α	0.018	0.055	0.64
39ValC_α*	0.059	0.037	1.25
40AspC_α	0.023	0.036	0.67
41GlyC_α	0.031	0.048	0.27
42ValC_α	0.040	0.031	0.50
43TrpC_α	0.035	0.040	0.56
44ThrC_α	0.019	0.047	0.79

45TyrC_α	0.045	0.043	0.91
46AspC_α	0.059	0.048	0.32
47AspC_α*	0.038	0.035	1.30
48AlaC_α*	0.025	0.050	0.81
49ThrC_α	0.038	0.033	0.40
50LysC_α	0.023	0.053	0.47
51ThrC_α	0.034	0.053	0.48
52PheC_α	0.013	0.037	0.86
53ThrC_α*	0.041	0.054	2.61
54ValC_α	0.025	0.042	0.75
55ThrC_α	0.023	0.036	0.56
56GluC_α	0.016	0.043	0.53

7.3 Comparison of High and Low-Power Data Collection Schemes

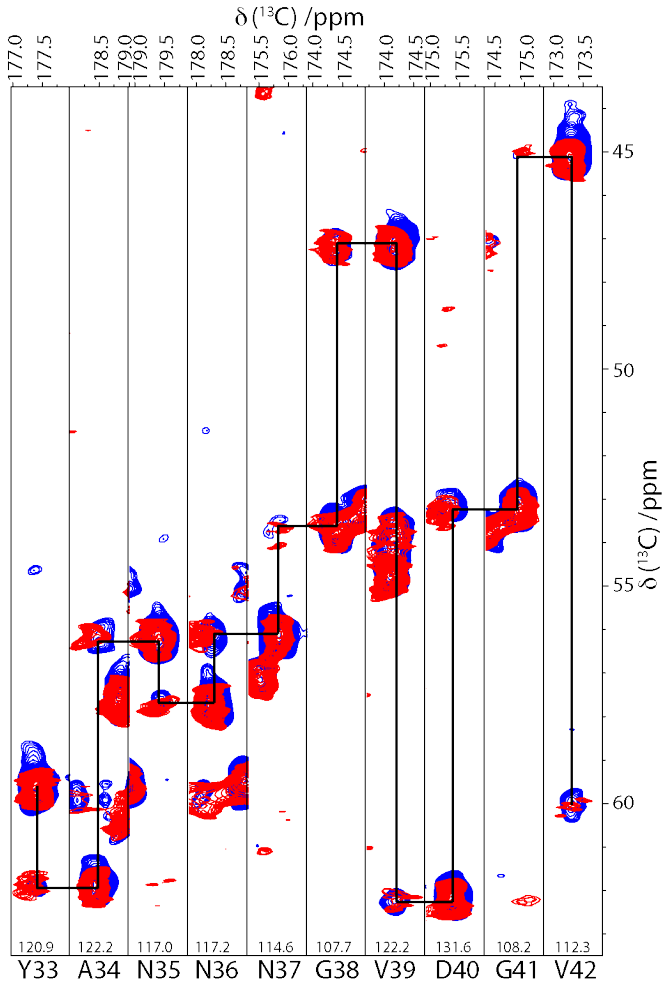

Figure 7.2 Comparison of high-power and low-power data collection schemes. Overlay of a high-power 3D-NCOCA MIRROR experiment (red), with that of a low-power 3D-NCOCA MIRROR experiment (blue). The chemical shift for the ^{15}N plane is given at the bottom of each slice. 3D-NCOCA sequential assignment example.

Appendix B Dynamic Nuclear Polarisation of Spin-Labelled Proteins

7.3.1 EPR Simulations Scripts

The following script (or variation depending on spectra simulated) written in MATLAB using EasySpin[106] computational software was used to compute EPR parameters of each mutant.

```
% fit EPR spectra for g, A, correlation time ==============================
% outputs best fit parameters and spectra in 'fitvalue.mat' ==============
clear
% load in all the experimental data and put it in a structured array 'expt'
[expt(1).B,expt(1).spec,expt(1).param] = eprload('GB3_A48C_20mgml_3517cf_200sw_5s_180scan.DSC');
% define Exp, Sys and Vary parameters=====================================
g = [1.96543,2.05286,1.99635];
A = mt2mhz([6.16,5.15,37.8]/10); % G -> MHz
Sys = struct('g',g,'Nucs','14N','A',A);
Sys.logtcorr = -9.5;
Vary.g = [0.1 0.1 0.1];
Vary.logtcorr = 2;
Vary.A = [1 1 5];   % in MHz
FitOpt.Method = 'simplex int';  % use Nelder-Mead and single integral
FitOpt.Scaling = 'minmax';  % scale for min and max intensity
FitOpt.PrintLevel = 0;  % suppress progress output
% loop fitting function over number of spectra ============================
for i = 1:1:numel(expt)
   Exp.mwFreq = expt(i).param.MWFQ / 10^9;
   Exp.Range = [expt(i).B(1)/10 expt(i).B(end)/10];  % sim range matches expt
   % baseline correction ------------------------------------------------
   trend = linspace(expt(i).spec(1),expt(i).spec(end),numel(expt(i).spec));
   expt(i).spec = expt(i).spec - trend';
   % run simulation -----------------------------------------------------
   spec = expt(i).spec;
   [bestfit(i).param,bestfit(i).spec] = esfit_fun(i,spec,Sys,Vary,Exp);
   % plot out sim and expt data -----------------------------------------
   figure(i)
   hold on
   plot(expt(i).B/10,expt(i).spec,'color','k')
   npoints = numel(bestfit(i).spec);
   simx = linspace(Exp.Range(1),Exp.Range(2),npoints);
   plot(simx,bestfit(i).spec,'color','r')
   residual = expt(i).spec' - bestfit(i).spec;
   plot(simx,residual,'b')
   legend('experimental','simulated','residual')
end
fitvalues = bestfit;
save fitvalues.mat fitvalues;
shg
```

7.3.2 Room-Temperature Relaxation Experiments Fittings

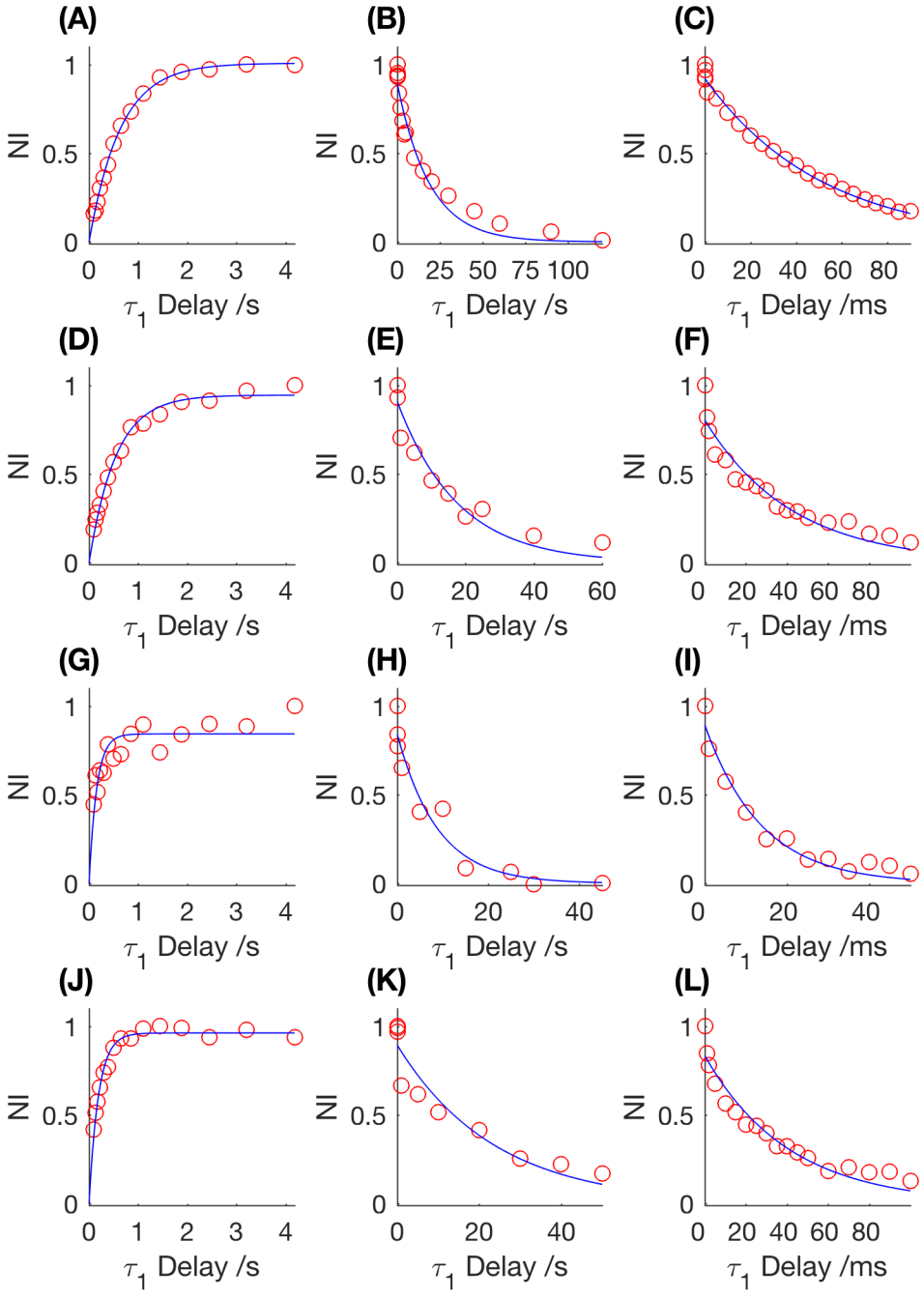

Figure 7.3 Room temperature mutant GB3 relaxation measurements. ^{1}H R_1 fitting for WT-GB3 (A), ^{15}N R_1 fitting for WT-GB3 (B), ^{15}N $R_{1\rho}$ fitting for WT-GB3 (C), ^{1}H R_1 fitting for D46C-A48C-GB3 (D), ^{15}N R_1 fitting for D46C-A48C-GB3 (E), ^{15}N $R_{1\rho}$ fitting for D46C-A48C-GB3 (F), ^{1}H R_1 fitting for MTSSL-D46C-A48C-GB3 (G), ^{15}N R_1 fitting for MTSSL-D46C-A48C-GB3 (H), ^{15}N $R_{1\rho}$ fitting for MTSSL-D46C-A48C-GB3 (I), ^{1}H R_1 fitting for 1 in 5 MTSSL-A48C-GB3 (J), ^{15}N R_1 fitting for 1 in 5 MTSSL-A48C-GB3 (K), ^{15}N $R_{1\rho}$ fitting for 1 in 5 MTSSL-A48C-GB3 (L).

7.3.3 Low-Temperature Relaxation Fittings

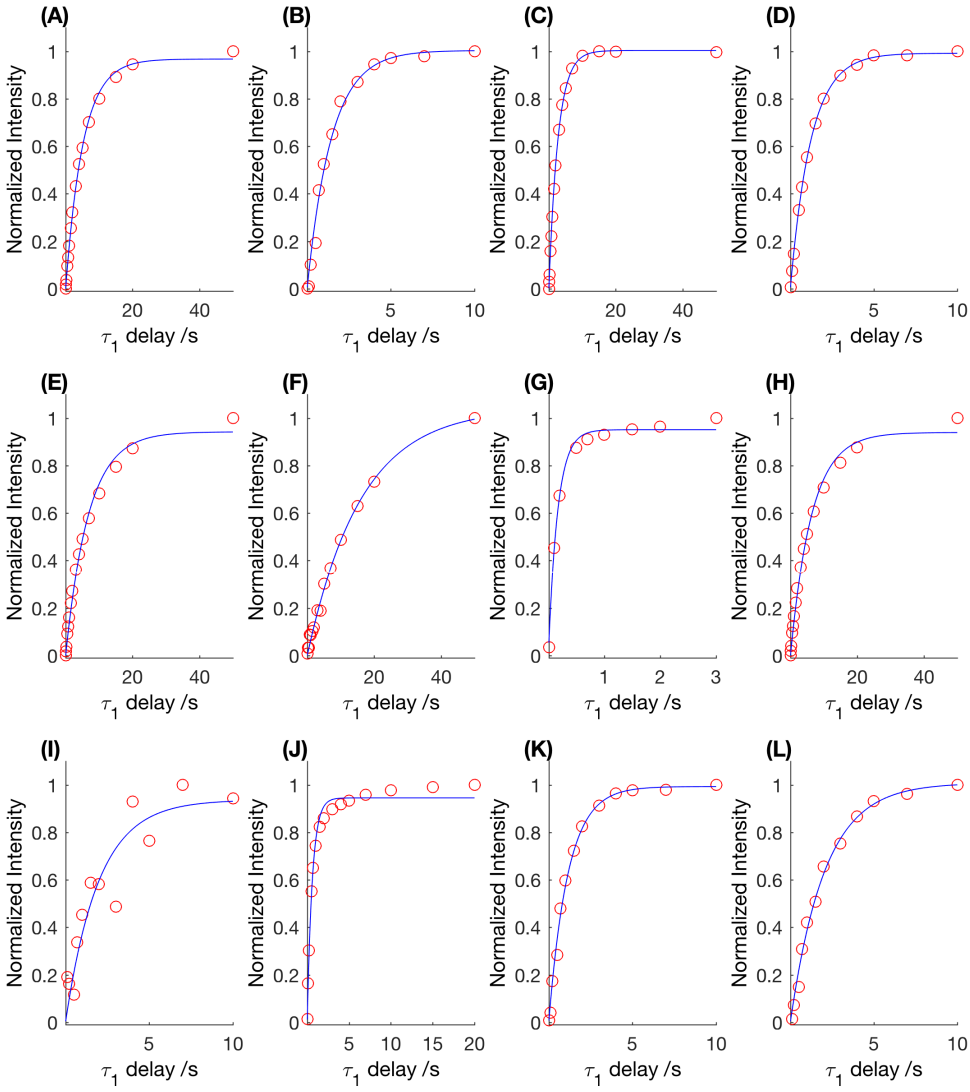

Figure 7.4 Fittings of T_{DNP}(^{1}H) for GB3 samples.12.5 mM doped microcrystalline WT-GB3 (A), 12.5 mM doped pre-crystallisation, microcrystalline WT-GB3 (B), 12.5 mM doped frozen solution WT-GB3 (C), microcrystalline MTSSL-A48C-GB3 (D), 1 in 5 diluted spin-label microcrystalline MTSSL-A48C-GB3 (E), frozen solution MTSSL-A48C-GB3 (F), microcrystalline MTSSL-D46C-A48C-GB3 (G), 1 in 5 diluted spin-label microcrystalline MTSSL-D46C-A48C-GB3 (H), frozen solution MTSSL-D46C-A48C-GB3 (I), microcrystalline MTSSL-E24C-K28C-GB3 (J), frozen solution MTSSL-E24C-K28C-GB3 (K), undoped microcrystalline WT-GB3 (L). Data acquired at 107 K, 8 kHz MAS, 400 MHz B_0 field on ^{1}H.

7.3.4 2D-PDSD Spectrum of GB3 Samples at 107 K

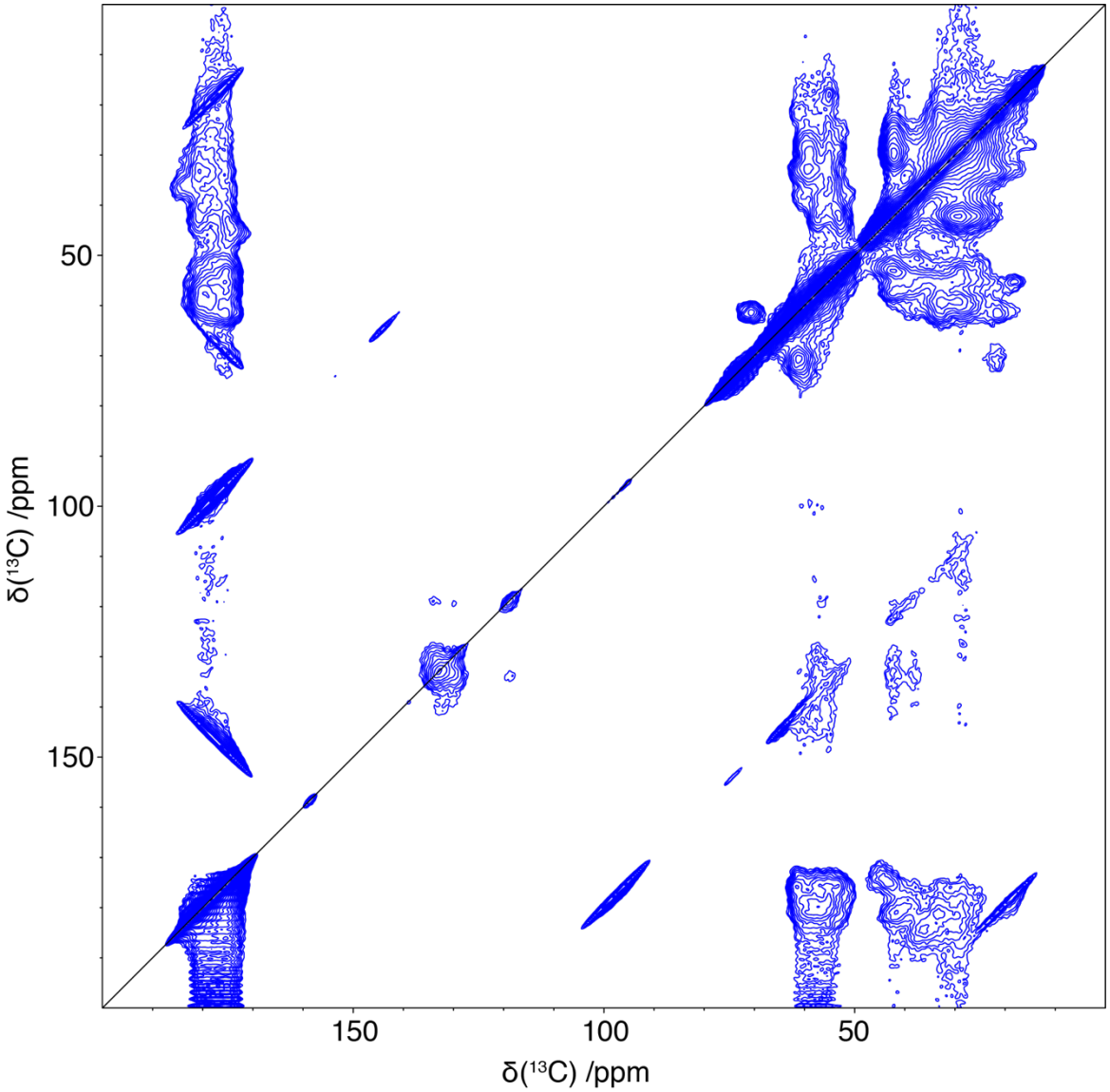

Figure 7.5 2D-PDSD spectrum of 12.5mM AMUPol doped WT-GB3 frozen solution. A mixing time of 10 ms was used. 20 Hz line broadening was applied.

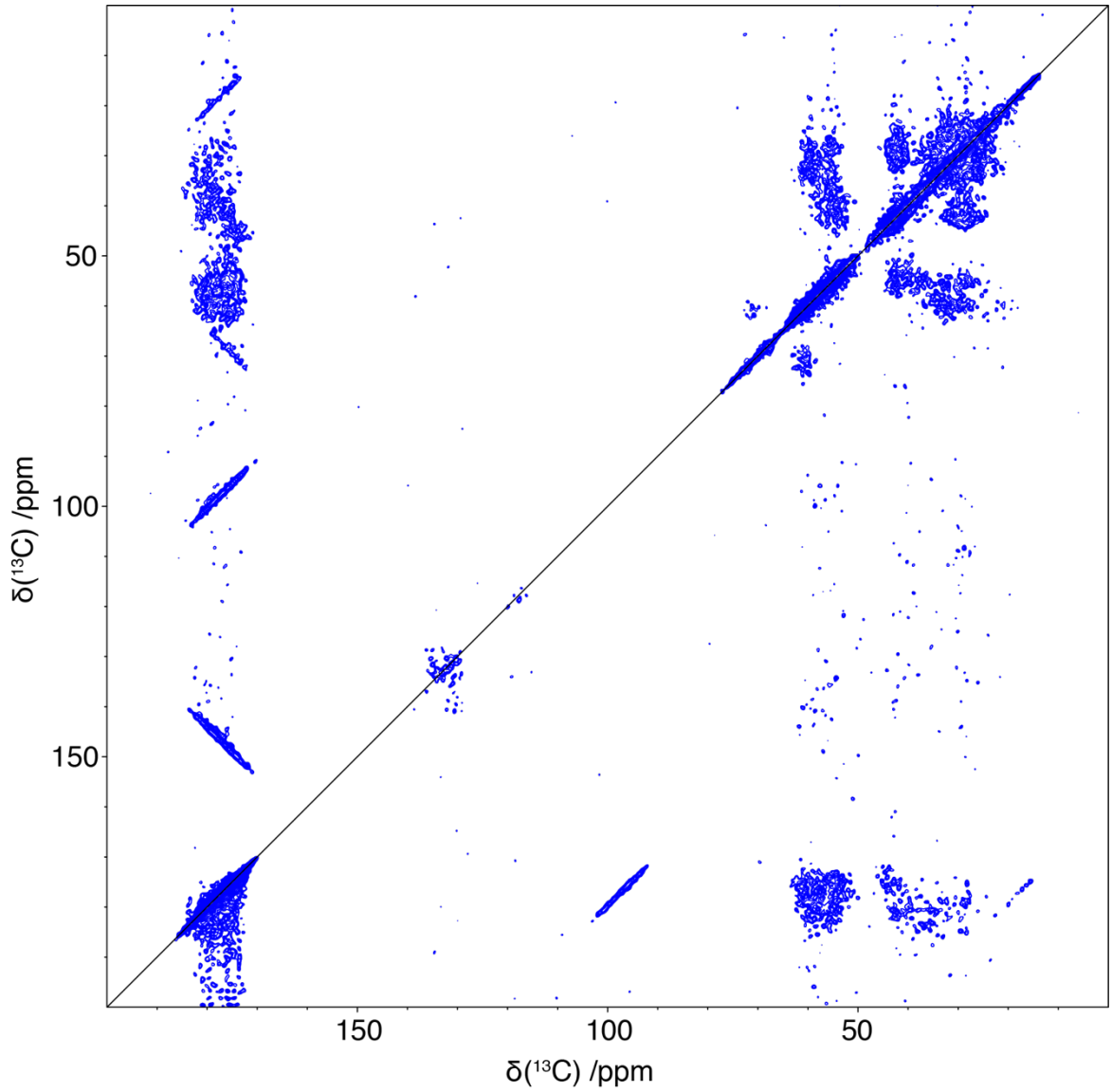

Figure 7.6 2D-PDSD spectrum of Undoped WT-GB3 microcrystals. A mixing time of 10 ms was used. 20 Hz line broadening was applied.

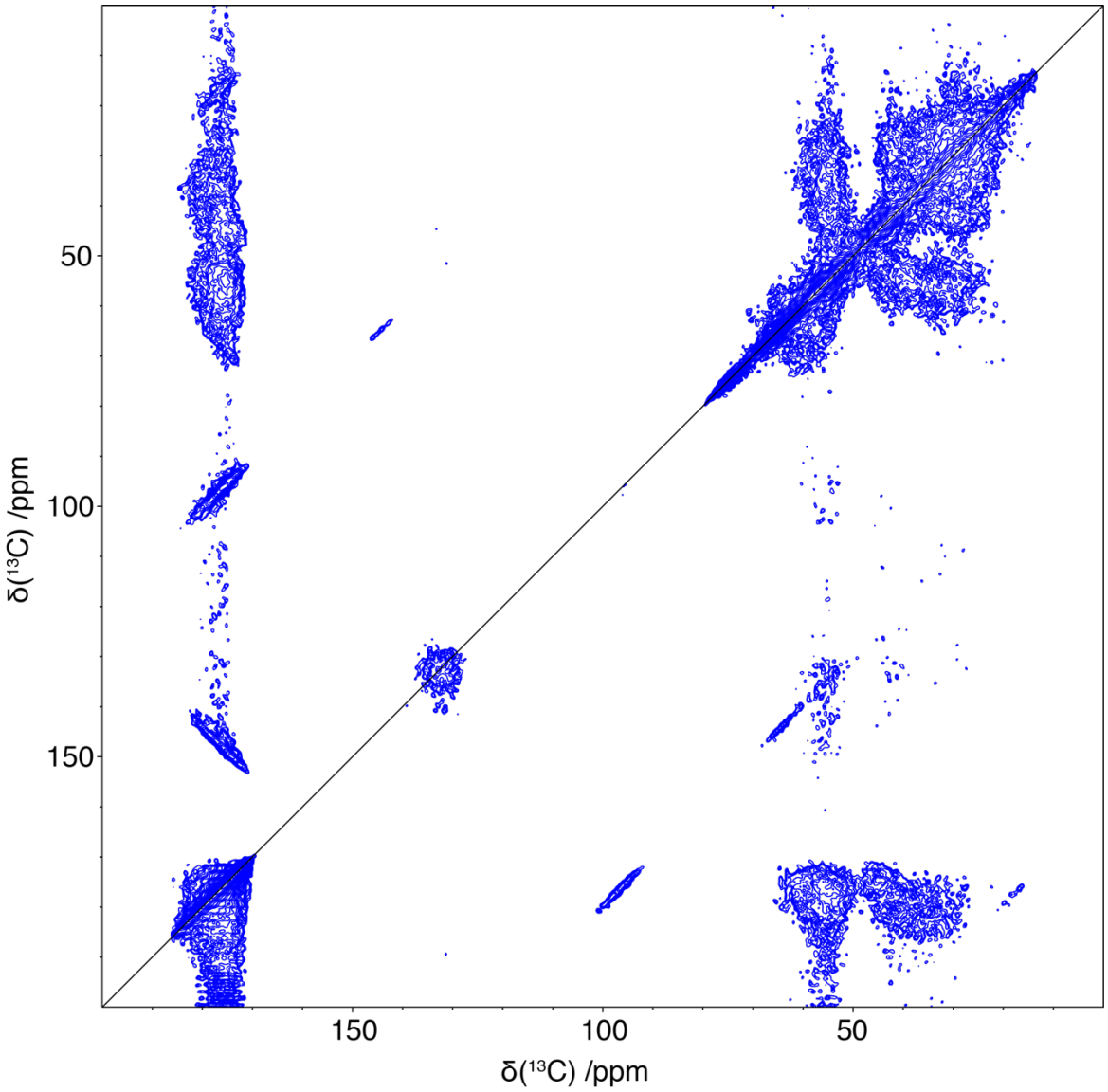

Figure 7.7 2D-PDSD spectrum of MTSSL-E24C-K28C-GB3 microcrystals. A mixing time of 10 ms was used. 20 Hz line broadening was applied.

List of References

1. Scholz, I.; Huber, M.; Manolikas, T.; Meier, B. H.; Ernst, M., MIRROR recoupling and its application to spin diffusion under fast magic-angle spinning. *Chem Phys Lett* **2008,** *460*, 278.
2. Bloch, F.; Rabi, I. I., Atoms in Variable Magnetic Fields. *Rev Mod Phys* **1945,** *17*, 237.
3. Purcell, E. M.; Torrey, H. C.; Pound, R. V., Resonance Absorption by Nuclear Magnetic Moments in a Solid. *Phys Rev* **1946,** *69*, 37.
4. Wang, S.; Ladizhansky, V., Recent advances in magic angle spinning solid state NMR of membrane proteins. *Prog Nucl Magn Reson Spectrosc* **2014,** *82*, 1.
5. Park, S. H.; Das, B. B.; Casagrande, F.; Tian, Y.; Nothnagel, H. J.; Chu, M.; Kiefer, H.; Maier, K.; De Angelis, A. A.; Marassi, F. M.; Opella, S. J., Structure of the chemokine receptor CXCR1 in phospholipid bilayers. *Nature* **2012,** *491*, 779.
6. Andreas, L. B.; Reese, M.; Eddy, M. T.; Gelev, V.; Ni, Q. Z.; Miller, E. A.; Emsley, L.; Pintacuda, G.; Chou, J. J.; Griffin, R. G., Structure and Mechanism of the Influenza A M218–60 Dimer of Dimers. *J Am Chem Soc* **2015,** *137*, 14877.
7. Comellas, G.; Rienstra, C. M., Protein Structure Determination by Magic-Angle Spinning Solid-State NMR, and Insights into the Formation, Structure, and Stability of Amyloid Fibrils. *Annu Rev Biophys* **2013,** *42*, 515.
8. Lu, J.-X.; Qiang, W.; Yau, W.-M.; Schwieters, Charles D.; Meredith, Stephen C.; Tycko, R., Molecular Structure of β-Amyloid Fibrils in Alzheimer's Disease Brain Tissue. *Cell* **2013,** *154*, 1257.
9. Schütz, A. K.; Vagt, T.; Huber, M.; Ovchinnikova, O. Y.; Cadalbert, R.; Wall, J.; Güntert, P.; Böckmann, A.; Glockshuber, R.; Meier, B. H., Atomic-Resolution Three-Dimensional Structure of Amyloid β Fibrils Bearing the Osaka Mutation. *Angew Chem Int Ed* **2015,** *54*, 331.
10. Castellani, F.; van Rossum, B.-J.; Diehl, A.; Rehbein, K.; Oschkinat, H., Determination of Solid-State NMR Structures of Proteins by Means of Three-Dimensional 15N−13C−13C Dipolar Correlation Spectroscopy and Chemical Shift Analysis. *Biochemistry* **2003,** *42*, 11476.
11. Ernst, M.; Detken, A.; Böckmann, A.; Meier, B. H., NMR Spectra of a Microcrystalline Protein at 30 kHz MAS. *J Am Chem Soc* **2003,** *125*, 15807.

12. Franks, W. T.; Wylie, B. J.; Stellfox, S. A.; Rienstra, C. M., Backbone Conformational Constraints in a Microcrystalline U-15N-Labeled Protein by 3D Dipolar-Shift Solid-State NMR Spectroscopy. *J Am Chem Soc* **2006,** *128*, 3154.
13. Jolly, M. M.; Jarvis, J. A.; Carravetta, M.; Levitt, M. H.; Williamson, P. T. F., Bidirectional band-selective magnetization transfer along the protein backbone doubles the information content of solid-state NMR correlation experiments. *J Biomol NMR* **2017,** *69*, 197.
14. Levitt, M. H., *Spin Dynamics: Basics of Nuclear Magnetic Resonance*. Wiley: 2008.
15. Keeler, J., *Understanding NMR Spectroscopy*. Wiley: 2011.
16. Abragam, A., *The Principles of Nuclear Magnetism*. Clarendon Press: 1961.
17. Ernst, R. R.; Bodenhausen, G.; Wokaun, A., *Principles of Nuclear Magnetic Resonance in One and Two Dimensions*. Clarendon Press: 1987.
18. Haeberlen, U., *High Resolution NMR in Solids Selective Averaging: Supplement 1 Advances in Magnetic Resonance*. Elsevier Science: 2012.
19. Duer, M. J., *Introduction to Solid-State NMR Spectroscopy*. Wiley: 2005.
20. Mehring, M., *Principles of high-resolution NMR in solids*. Springer-Verlag: 1983.
21. Slichter, C. P., *Principles of Magnetic Resonance*. Springer Berlin Heidelberg: 1996.
22. Levine, I. N., *Quantum chemistry*. Allyn and Bacon: 1983.
23. Varshalovich, D. A.; Moskalev, A. N.; Khersonskiĭ, V. K., *Quantum Theory of Angular Momentum: Irreducible Tensors, Spherical Harmonics, Vector Coupling Coefficients, 3nj Symbols*. World Scientific Pub.: 1988.
24. Maricq, M. M.; Waugh, J. S., NMR in rotating solids. *J Chem Phys* **1979,** *70*, 3300.
25. Lowe, I. J., Free Induction Decays of Rotating Solids. *Phys Rev Lett* **1959,** *2*, 285.
26. Rose, M. E., *Elementary Theory of Angular Momentum*. Dover: 1995.
27. Hartmann, S. R.; Hahn, E. L., Nuclear Double Resonance in the Rotating Frame. *Phys Rev* **1962,** *128*, 2042.
28. Pines, A.; Gibby, M. G.; Waugh, J. S., Proton-enhanced NMR of dilute spins in solids. *J Chem Phys* **1973,** *59*, 569.
29. Baldus, M.; Petkova, A. T.; Herzfeld, J.; Griffin, R. G., Cross polarization in the tilted frame: assignment and spectral simplification in heteronuclear spin systems. *Mol Phys* **1998,** *95*, 1197.

30. Baldus, M.; Geurts, D. G.; Hediger, S.; Meier, B. H., Efficient N-15-C-13 polarization transfer by adiabatic-passage Hartmann-Hahn cross polarization. *J Magn Reson, Ser A* **1996,** *118*, 140.
31. Hediger, S.; Meier, B. H.; Kurur, N. D.; Bodenhausen, G.; Ernst, R. R., NMR cross polarization by adiabatic passage through the Hartmann—Hahn condition (APHH). *Chem Phys Lett* **1994,** *223*, 283.
32. Zhang, S. M.; Meier, B. H.; Ernst, R. R., Mismatch-Compensated Cross Polarization. W-MOIST, an Improved Pulse Scheme. *J Magn Reson, Ser A* **1994,** *108*, 30.
33. Metz, G.; Ziliox, M.; Smith, S. O., Towards quantitative CP-MAS NMR. *Solid State Nucl Magn Reson* **1996,** *7*, 155.
34. Metz, G.; Wu, X. L.; Smith, S. O., Ramped-Amplitude Cross Polarization in Magic-Angle-Spinning NMR. *J Magn Reson, Ser A* **1994,** *110*, 219.
35. Hogben, H. J.; Krzystyniak, M.; Charnock, G. T. P.; Hore, P. J.; Kuprov, I., Spinach – A software library for simulation of spin dynamics in large spin systems. *J Magn Reson* **2011,** *208*, 179.
36. Lesage, A.; Bardet, M.; Emsley, L., Through-Bond Carbon−Carbon Connectivities in Disordered Solids by NMR. *J Am Chem Soc* **1999,** *121*, 10987.
37. Ernst, M., Heteronuclear spin decoupling in solid-state NMR under magic-angle sample spinning. *J Magn Reson* **2003,** *162*, 1.
38. Haeberlen, U.; Waugh, J. S., Coherent Averaging Effects in Magnetic Resonance. *Phys Rev* **1968,** *175*, 453.
39. Shaka, A. J.; Keeler, J.; Frenkiel, T.; Freeman, R., An improved sequence for broadband decoupling: WALTZ-16. *J Magn Reson* **1983,** *52*, 335.
40. Yu, Y.; Fung, B. M., An Efficient Broadband Decoupling Sequence for Liquid Crystals. *J Magn Reson* **1998,** *130*, 317.
41. Bennett, A. E.; Rienstra, C. M.; Auger, M.; Lakshmi, K. V.; Griffin, R. G., Heteronuclear decoupling in rotating solids. *J Chem Phys* **1995,** *103*, 6951.
42. Weingarth, M.; Bodenhausen, G.; Tekely, P., Low-power decoupling at high spinning frequencies in high static fields. *J Magn Reson* **2009,** *199*, 238.
43. Takegoshi, K.; Mizokami, J.; Terao, T., 1H decoupling with third averaging in solid NMR. *Chem Phys Lett* **2001,** *341*, 540.

44. Detken, A.; Hardy, E. H.; Ernst, M.; Meier, B. H., Simple and efficient decoupling in magic-angle spinning solid-state NMR: the XiX scheme. *Chem Phys Lett* **2002,** *356*, 298.

45. Gan, Z.; Ernst, R. R., Frequency- and phase-modulated heteronuclear decoupling in rotating solids. *Solid State Nucl Magn Reson* **1997,** *8*, 153.

46. Fung, B. M.; Khitrin, A. K.; Ermolaev, K., An Improved Broadband Decoupling Sequence for Liquid Crystals and Solids. *J Magn Reson* **2000,** *142*, 97.

47. Bräuniger, T.; Wormald, P.; Hodgkinson, P., Improved Proton Decoupling in NMR Spectroscopy of Crystalline Solids Using the SPINAL-64 Sequence. *Monatsh Chem* **2002,** *133*, 1549.

48. Thakur, R. S.; Kurur, N. D.; Madhu, P. K., Swept-frequency two-pulse phase modulation for heteronuclear dipolar decoupling in solid-state NMR. *Chem Phys Lett* **2006,** *426*, 459.

49. Vinther, J. M.; Nielsen, A. B.; Bjerring, M.; Eck, E. R. H. v.; Kentgens, A. P. M.; Khaneja, N.; Nielsen, N. C., Refocused continuous-wave decoupling: A new approach to heteronuclear dipolar decoupling in solid-state NMR spectroscopy. *J Chem Phys* **2012,** *137*, 214202.

50. Lee, M.; Goldburg, W. I., Nuclear-Magnetic-Resonance Line Narrowing by a Rotating rf Field. *Phys Rev* **1965,** *140*, A1261.

51. Burum, D. P.; Linder, M.; Ernst, R. R., Low-power multipulse line narrowing in solid-state NMR. *J Magn Reson* **1981,** *44*, 173.

52. Rhim, W. K.; Elleman, D. D.; Vaughan, R. W., Analysis of multiple pulse NMR in solids. *J Chem Phys* **1973,** *59*, 3740.

53. Oas, T. G.; Griffin, R. G.; Levitt, M. H., Rotary resonance recoupling of dipolar interactions in solid-state nuclear magnetic resonance spectroscopy. *J Chem Phys* **1988,** *89*, 692.

54. Levitt, M. H.; Oas, T. G.; Griffin, R. G., Rotary Resonance Recoupling in Heteronuclear Spin Pair Systems. *Isr J Chem* **1988,** *28*, 271.

55. Nielsen, N. C.; Bildso/e, H.; Jakobsen, H. J.; Levitt, M. H., Double-quantum homonuclear rotary resonance: Efficient dipolar recovery in magic-angle spinning nuclear magnetic resonance. *J Chem Phys* **1994,** *101*, 1805.

56. Ernst, M.; Samoson, A.; Meier, B. H., Low-power decoupling in fast magic-angle spinning NMR. *Chem Phys Lett* **2001,** *348*, 293.

57. Ernst, M.; Samoson, A.; Meier, B. H., Low-power XiX decoupling in MAS NMR experiments. *J Magn Reson* **2003,** *163*, 332.

58. Kotecha, M.; Wickramasinghe, N. P.; Ishii, Y., Efficient low-power heteronuclear decoupling in 13C high-resolution solid-state NMR under fast magic angle spinning. *Magn Reson Chem* **2007,** *45*, S221.
59. De Paëpe, G.; Lesage, A.; Steuernagel, S.; Emsley, L., Transverse Dephasing Optimised NMR Spectroscopy in Solids: Natural-Abundance 13C Correlation Spectra. *ChemPhysChem* **2004,** *5*, 869.
60. De Paëpe , G.; Lesage, A.; Emsley, L., The performance of phase modulated heteronuclear dipolar decoupling schemes in fast magic-angle-spinning nuclear magnetic resonance experiments. *J Chem Phys* **2003,** *119*, 4833.
61. De Paëpe, G.; Giraud, N.; Lesage, A.; Hodgkinson, P.; Böckmann, A.; Emsley, L., Transverse Dephasing Optimized Solid-State NMR Spectroscopy. *J Am Chem Soc* **2003,** *125*, 13938.
62. De Paëpe , G., Dipolar Recoupling in Magic Angle Spinning Solid-State Nuclear Magnetic Resonance. *Annu Rev Phys Chem* **2012,** *63*, 661.
63. Levitt, M. H., *Spin Dynamics: Basics of Nuclear Magnetic Resonance*. Wiley: 2013.
64. Linser, R.; Fink, U.; Reif, B., Proton-detected scalar coupling based assignment strategies in MAS solid-state NMR spectroscopy applied to perdeuterated proteins. *J Magn Reson* **2008,** *193*, 89.
65. Chen, L.; Kaiser, J. M.; Polenova, T.; Yang, J.; Rienstra, C. M.; Mueller, L. J., Backbone assignments in solid-state proteins using J-based 3D Heteronuclear correlation spectroscopy. *J Am Chem Soc* **2007,** *129*, 10650.
66. Bloembergen, N.; Purcell, E. M.; Pound, R. V., Relaxation Effects in Nuclear Magnetic Resonance Absorption. *Phys Rev* **1948,** *73*, 679.
67. Bloembergen, N., On the interaction of nuclear spins in a crystalline lattice. *Physica* **1949,** *15*, 386.
68. Meier, B. H.; Earl, W. L., Excitation of multiple quantum transitions under magic angle spinning conditions: Adamantane. *J Chem Phys* **1986,** *85*, 4905.
69. Baum, J.; Munowitz, M.; Garroway, A. N.; Pines, A., Multiple-quantum dynamics in solid state NMR. *J Chem Phys* **1985,** *83*, 2015.
70. Slichter, C. P., *Principles of Magnetic Resonance*. Springer Berlin Heidelberg: 2013.

71. Suter, D.; Ernst, R. R., Spin diffusion in resolved solid-state NMR spectra. *Phys Rev B* **1985,** *32*, 5608.
72. Jeener, J.; Meier, B. H.; Bachmann, P.; Ernst, R. R., Investigation of exchange processes by two-dimensional NMR spectroscopy. *J Chem Phys* **1979,** *71*, 4546.
73. Szeverenyi, N. M.; Sullivan, M. J.; Maciel, G. E., Observation of spin exchange by two-dimensional fourier transform 13C cross polarization-magic-angle spinning. *J Magn Reson* **1982,** *47*, 462.
74. Castellani, F.; van Rossum, B.; Diehl, A.; Schubert, M.; Rehbein, K.; Oschkinat, H., Structure of a protein determined by solid-state magic-angle-spinning NMR spectroscopy. *Nature* **2002,** *420*, 98.
75. Takegoshi, K.; Nakamura, S.; Terao, T., 13C–1H dipolar-assisted rotational resonance in magic-angle spinning NMR. *Chem Phys Lett* **2001,** *344*, 631.
76. Takegoshi, K.; Nakamura, S.; Terao, T., C-13-H-1 dipolar-driven C-13-C-13 recoupling without C-13 rf irradiation in nuclear magnetic resonance of rotating solids. *J Chem Phys* **2003,** *118*, 2325.
77. Takegoshi, K.; Nakamura, S.; Terao, T., 13C–1H dipolar-assisted rotational resonance in magic-angle spinning NMR. *Chem Phys Lett* **2001,** *344*, 631.
78. Bloembergen, N., On the interaction of nuclear spins in a crystalline lattice. *Physica* **1949,** *15*, 386.
79. Raleigh, D. P.; Levitt, M. H.; Griffin, R. G., Rotational resonance in solid state NMR. *Chem Phys Lett* **1988,** *146*, 71.
80. Creuzet, F.; McDermott, A.; Gebhard, R.; van der Hoef, K.; Spijker-Assink, M.; Herzfeld, J.; Lugtenburg, J.; Levitt, M.; Griffin, R., Determination of membrane protein structure by rotational resonance NMR: bacteriorhodopsin. *Science* **1991,** *251*, 783.
81. Bayro, M. J.; Huber, M.; Ramachandran, R.; Davenport, T. C.; Meier, B. H.; Ernst, M.; Griffin, R. G., Dipolar truncation in magic-angle spinning NMR recoupling experiments. *J Chem Phys* **2009,** *130*, 114506.
82. Gullion, T.; Schaefer, J., Rotational-echo double-resonance NMR. *J Magn Reson* **1989,** *81*, 196.
83. Gullion, T., Introduction to rotational-echo, double-resonance NMR. *Concepts Magn Reson* **1998,** *10*, 277.
84. Hing, A. W.; Vega, S.; Schaefer, J., Measurement of Heteronuclear Dipolar Coupling by Transferred-Echo Double-Resonance NMR. *J Magn Reson, Ser A* **1993,** *103*, 151.

85. Hing, A. W.; Vega, S.; Schaefer, J., Transferred-echo double-resonance NMR. *J Magn Reson* **1992,** *96*, 205.

86. Kiihne, S.; Mehta, M. A.; Stringer, J. A.; Gregory, D. M.; Shiels, J. C.; Drobny, G. P., Distance Measurements by Dipolar Recoupling Two-Dimensional Solid-State NMR. *J Phys Chem A* **1998,** *102*, 2274.

87. Hohwy, M.; Rienstra, C. M.; Jaroniec, C. P.; Griffin, R. G., Fivefold symmetric homonuclear dipolar recoupling in rotating solids: Application to double quantum spectroscopy. *J Chem Phys* **1999,** *110*, 7983.

88. De Paëpe, G.; Lewandowski, J. R.; Loquet, A.; Böckmann, A.; Griffin, R. G., Proton assisted recoupling and protein structure determination. *J Chem Phys* **2008,** *129*, 245101.

89. Paëpe, G. D.; Lewandowski, J. R.; Griffin, R. G., Spin dynamics in the modulation frame: Application to homonuclear recoupling in magic angle spinning solid-state NMR. *J Chem Phys* **2008,** *128*, 124503.

90. Brinkmann, A.; Edén, M.; Levitt, M. H., Synchronous helical pulse sequences in magic-angle spinning nuclear magnetic resonance: Double quantum recoupling of multiple-spin systems. *J Chem Phys* **2000,** *112*, 8539.

91. Verel, R.; Ernst, M.; Meier, B. H., Adiabatic Dipolar Recoupling in Solid-State NMR: The DREAM Scheme. *J Magn Reson* **2001,** *150*, 81.

92. Verel, R.; Baldus, M.; Ernst, M.; Meier, B. H., A homonuclear spin-pair filter for solid-state NMR based on adiabatic-passage techniques. *Chem Phys Lett* **1998,** *287*, 421.

93. Hohwy, M.; Jakobsen, H. J.; Edén, M.; Levitt, M. H.; Nielsen, N. C., Broadband dipolar recoupling in the nuclear magnetic resonance of rotating solids: A compensated C7 pulse sequence. *J Chem Phys* **1998,** *108*, 2686.

94. Hou, G.; Yan, S.; Sun, S.; Han, Y.; Byeon, I.-J. L.; Ahn, J.; Concel, J.; Samoson, A.; Gronenborn, A. M.; Polenova, T., Spin Diffusion Driven by R-Symmetry Sequences: Applications to Homonuclear Correlation Spectroscopy in MAS NMR of Biological and Organic Solids. *J Am Chem Soc* **2011,** *133*, 3943.

95. Hou, G.; Yan, S.; Trébosc, J.; Amoureux, J.-P.; Polenova, T., Broadband homonuclear correlation spectroscopy driven by combined R2nv sequences under fast magic angle spinning for NMR structural analysis of organic and biological solids. *J Magn Reson* **2013,** *232*, 18.

96. Weingarth, M.; Demco, D. E.; Bodenhausen, G.; Tekely, P., Improved magnetization transfer in solid-state NMR with fast magic angle spinning. *Chem Phys Lett* **2009,** *469*, 342.

97. Hu, B.; Lafon, O.; Trébosc, J.; Chen, Q.; Amoureux, J.-P., Broad-band homo-nuclear correlations assisted by 1H irradiation for bio-molecules in very high magnetic field at fast and ultra-fast MAS frequencies. *J Magn Reson* **2011,** *212*, 320.

98. Overhauser, A. W., Polarization of Nuclei in Metals. *Phys Rev* **1953,** *92*, 411.

99. Abragam, A.; Bleaney, B., *Electron paramagnetic resonance of transition ions*. Clarendon P.: 1970.

100. Hagen, W. R., EPR spectroscopy as a probe of metal centres in biological systems. *Dalton Trans* **2006**, 4415.

101. Abdelkader, E. H.; Feintuch, A.; Yao, X.; Adams, L. A.; Aurelio, L.; Graham, B.; Goldfarb, D.; Otting, G., Protein conformation by EPR spectroscopy using gadolinium tags clicked to genetically encoded p-azido-l-phenylalanine. *Chem Commun* **2015,** *51*, 15898.

102. Yagi, H.; Banerjee, D.; Graham, B.; Huber, T.; Goldfarb, D.; Otting, G., Gadolinium Tagging for High-Precision Measurements of 6 nm Distances in Protein Assemblies by EPR. *J Am Chem Soc* **2011,** *133*, 10418.

103. Martorana, A.; Bellapadrona, G.; Feintuch, A.; Di Gregorio, E.; Aime, S.; Goldfarb, D., Probing Protein Conformation in Cells by EPR Distance Measurements using Gd3+ Spin Labeling. *J Am Chem Soc* **2014,** *136*, 13458.

104. Páli, T.; Kóta, Z., Studying Lipid–Protein Interactions with Electron Paramagnetic Resonance Spectroscopy of Spin-Labeled Lipids. In *Lipid-Protein Interactions: Methods and Protocols*, Kleinschmidt, J. H., Ed. Humana Press: Totowa, NJ, 2013; pp 297.

105. Milov, A. D.; Ponomarev, A. B.; Tsvetkov, Y. D., Electron-electron double resonance in electron spin echo: Model biradical systems and the sensitized photolysis of decalin. *Chem Phys Lett* **1984,** *110*, 67.

106. Stoll, S.; Schweiger, A., EasySpin, a comprehensive software package for spectral simulation and analysis in EPR. *J Magn Reson* **2006,** *178*, 42.

107. Bennati, M.; Gerfen, G. J.; Martinez, G. V.; Griffin, R. G.; Singel, D. J.; Millhauser, G. L., Nitroxide Side-Chain Dynamics in a Spin-Labeled Helix-Forming Peptide Revealed by High-Frequency (139.5-GHz) EPR Spectroscopy. *J Magn Reson* **1999,** *139*, 281.

108. Owenius, R.; Engström, M.; Lindgren, M.; Huber, M., Influence of Solvent Polarity and Hydrogen Bonding on the EPR Parameters of a Nitroxide Spin Label Studied by 9-GHz and 95-GHz EPR Spectroscopy and DFT Calculations. *J Phys Chem A* **2001,** *105*, 10967.

109. Lauffer, R. B., Paramagnetic metal complexes as water proton relaxation agents for NMR imaging: theory and design. *Chem Rev* **1987,** *87*, 901.

110. McDermott, A. E., Structural and dynamic studies of proteins by solid-state NMR spectroscopy: rapid movement forward. *Curr Opin Struct Biol* **2004,** *14*, 554.

111. Zech, S. G.; Wand, A. J.; McDermott, A. E., Protein Structure Determination by High-Resolution Solid-State NMR Spectroscopy: Application to Microcrystalline Ubiquitin. *J Am Chem Soc* **2005,** *127*, 8618.

112. Franks, W. T.; Zhou, D. H.; Wylie, B. J.; Money, B. G.; Graesser, D. T.; Frericks, H. L.; Sahota, G.; Rienstra, C. M., Magic-Angle Spinning Solid-State NMR Spectroscopy of the β1 Immunoglobulin Binding Domain of Protein G (GB1): 15N and 13C Chemical Shift Assignments and Conformational Analysis. *J Am Chem Soc* **2005,** *127*, 12291.

113. Nadaud, P. S.; Helmus, J. J.; Jaroniec, C. P., 13C and 15N chemical shift assignments and secondary structure of the B3 immunoglobulin-binding domain of streptococcal protein G by magic-angle spinning solid-state NMR spectroscopy. *Biomol NMR Assigm* **2007,** *1*, 117.

114. Derrick, J. P.; Wigley, D. B., The Third IgG-Binding Domain from Streptococcal Protein G: An Analysis by X-ray Crystallography of the Structure Alone and in a Complex with Fab. *J Mol Biol* **1994,** *243*, 906.

115. Ulmer, T. S.; Ramirez, B. E.; Delaglio, F.; Bax, A., Evaluation of Backbone Proton Positions and Dynamics in a Small Protein by Liquid Crystal NMR Spectroscopy. *J Am Chem Soc* **2003,** *125*, 9179.

116. Vögeli, B.; Kazemi, S.; Güntert, P.; Riek, R., Spatial elucidation of motion in proteins by ensemble-based structure calculation using exact NOEs. *Nat Struct Mol Biol* **2012,** *19*, 1053.

117. Frericks Schmidt, H. L.; Sperling, L. J.; Gao, Y. G.; Wylie, B. J.; Boettcher, J. M.; Wilson, S. R.; Rienstra, C. M., Crystal Polymorphism of Protein GB1 Examined by Solid-State NMR Spectroscopy and X-ray Diffraction. *J Phys Chem B* **2007,** *111*, 14362.

118. Wylie, B. J.; Sperling, L. J.; Nieuwkoop, A. J.; Franks, W. T.; Oldfield, E.; Rienstra, C. M., Ultrahigh resolution protein structures using NMR chemical shift tensors. *Proc Natl Acad Sci* **2011,** *108*, 16974.

119. Hall, J. B.; Fushman, D., Characterization of the overall and local dynamics of a protein with intermediate rotational anisotropy: Differentiating between conformational exchange and anisotropic diffusion in the B3 domain of protein G. *J Biomol NMR* **2003,** *27*, 261.

120. Lewandowski, J. R.; Halse, M. E.; Blackledge, M.; Emsley, L., Direct observation of hierarchical protein dynamics. *Science* **2015,** *348*, 578.

121. Yao, L.; Grishaev, A.; Cornilescu, G.; Bax, A., Site-Specific Backbone Amide 15N Chemical Shift Anisotropy Tensors in a Small Protein from Liquid Crystal and Cross-Correlated Relaxation Measurements. *J Am Chem Soc* **2010,** *132*, 4295.

122. Yao, L.; Vögeli, B.; Ying, J.; Bax, A., NMR Determination of Amide N−H Equilibrium Bond Length from Concerted Dipolar Coupling Measurements. *J Am Chem Soc* **2008,** *130*, 16518.

123. Martin, R. W.; Zilm, K. W., Preparation of protein nanocrystals and their characterization by solid state NMR. *J Magn Reson* **2003,** *165*, 162.

124. Andreas, L. B.; Jaudzems, K.; Stanek, J.; Lalli, D.; Bertarello, A.; Le Marchand, T.; Paepe, D. C. D.; Kotelovica, S.; Akopjana, I.; Knott, B.; Wegner, S.; Engelke, F.; Lesage, A.; Emsley, L.; Tars, K.; Herrmann, T.; Pintacuda, G., Structure of fully protonated proteins by proton-detected magic-angle spinning NMR. *Proc Natl Acad Sci USA* **2016,** *113*, 9187.

125. Marchetti, A.; Jehle, S.; Felletti, M.; Knight, M. J.; Wang, Y.; Xu, Z. Q.; Park, A. Y.; Otting, G.; Lesage, A.; Emsley, L.; Dixon, N. E.; Pintacuda, G., Backbone Assignment of Fully Protonated Solid Proteins by 1H Detection and Ultrafast Magic-Angle-Spinning NMR Spectroscopy. *Angew Chem Int Ed* **2012,** *51*, 10756.

126. Barbet-Massin, E.; Pell, A. J.; Retel, J. S.; Andreas, L. B.; Jaudzems, K.; Franks, W. T.; Nieuwkoop, A. J.; Hiller, M.; Higman, V.; Guerry, P.; Bertarello, A.; Knight, M. J.; Felletti, M.; Le Marchand, T.; Kotelovica, S.; Akopjana, I.; Tars, K.; Stoppini, M.; Bellotti, V.; Bolognesi, M.; Ricagno, S.; Chou, J. J.; Griffin, R. G.; Oschkinat, H.; Lesage, A.; Emsley, L.; Herrmann, T.; Pintacuda, G., Rapid Proton-Detected NMR Assignment for Proteins with Fast Magic Angle Spinning. *J Am Chem Soc* **2014,** *136*, 12489.

127. Wang, S. L.; Parthasarathy, S.; Xiao, Y. L.; Nishiyama, Y.; Long, F.; Matsuda, I.; Endo, Y.; Nemoto, T.; Yamauchi, K.; Asakura, T.; Takeda, M.; Terauchi, T.;

Kainosho, M.; Ishii, Y., Nano-mole scale sequential signal assignment by H-1-detected protein solid-state NMR. *Chem Commun* **2015,** *51*, 15055.

128. Agarwal, V.; Penzel, S.; Szekely, K.; Cadalbert, R.; Testori, E.; Oss, A.; Past, J.; Samoson, A.; Ernst, M.; Bockmann, A.; Meier, B. H., De Novo 3D Structure Determination from Sub-milligram Protein Samples by Solid-State 100 kHz MAS NMR Spectroscopy. *Angew Chem Int Ed* **2014,** *53*, 12253.
129. Theint, T.; Nadaud, P. S.; Surewicz, K.; Surewicz, W. K.; Jaroniec, C. P., 13C and 15N chemical shift assignments of mammalian Y145Stop prion protein amyloid fibrils. *Biomol NMR Assigm* **2017,** *11*, 75.
130. Ravotti, F.; Wälti, M. A.; Güntert, P.; Riek, R.; Böckmann, A.; Meier, B. H., Solid-state NMR sequential assignment of an Amyloid-β(1–42) fibril polymorph. *Biomol NMR Assigm* **2016,** *10*, 269.
131. Wiegand, T.; Gardiennet, C.; Ravotti, F.; Bazin, A.; Kunert, B.; Lacabanne, D.; Cadalbert, R.; Guntert, P.; Terradot, L.; Bockmann, A.; Meier, B. H., Solid-state NMR sequential assignments of the N-terminal domain of HpDnaB helicase. *Biomol NMR Assigm* **2016,** *10*, 13.
132. Schnell, I., Merging concepts from liquid-state and solid-state NMR spectroscopy for the investigation of supra- and biomolecular systems. *Curr Anal Chem* **2005,** *1*, 3.
133. Su, Y. C.; Sarell, C. J.; Eddy, M. T.; Debelouchina, G. T.; Andreas, L. B.; Pashley, C. L.; Radford, S. E.; Griffin, R. G., Secondary Structure in the Core of Amyloid Fibrils Formed from Human beta(2)m and its Truncated Variant Delta N6. *J Am Chem Soc* **2014,** *136*, 6313.
134. Pauli, J.; Baldus, M.; van Rossum, B.; de Groot, H.; Oschkinat, H., Backbone and side-chain C-13 and N-15 signal assignments of the alpha-spectrin SH3 domain by magic angle spinning solid-state NMR at 17.6 tesla. *Chembiochem* **2001,** *2*, 272.
135. Sperling, L. J.; Berthold, D. A.; Sasser, T. L.; Jeisy-Scott, V.; Rienstra, C. M., Assignment Strategies for Large Proteins by Magic-Angle Spinning NMR: The 21-kDa Disulfide-Bond-Forming Enzyme DsbA. *J Mol Biol* **2010,** *399*, 268.
136. Schuetz, A.; Wasmer, C.; Habenstein, B.; Verel, R.; Greenwald, J.; Riek, R.; Bockmann, A.; Meier, B. H., Protocols for the Sequential Solid-State NMR Spectroscopic Assignment of a Uniformly Labeled 25 kDa Protein: HET-s(1-227). *Chembiochem* **2010,** *11*, 1543.

137. Higman, V. A.; Flinders, J.; Hiller, M.; Jehle, S.; Markovic, S.; Fiedler, S.; van Rossum, B. J.; Oschkinat, H., Assigning large proteins in the solid state: a MAS NMR resonance assignment strategy using selectively and extensively C-13-labelled proteins. *J Biomol NMR* **2009,** *44*, 245.

138. Mithu, V. S.; Bakthavatsalam, S.; Madhu, P. K., C-13-C-13 Homonuclear Recoupling in Solid-State Nuclear Magnetic Resonance at a Moderately High Magic-Angle-Spinning Frequency. *PLoS One* **2013,** *8*.

139. Bax, A.; Ikura, M., An efficient 3D NMR technique for correlating the proton and 15 N backbone amide resonances with the α-carbon of the preceding residue in uniformly 15 N/13 C enriched proteins. *J Biomol NMR* **1991,** *1*, 99.

140. Grzesiek, S.; Bax, A., An efficient experiment for sequential backbone assignment of medium-sized isotopically enriched proteins. *J Magn Reson* **1992,** *99*, 201.

141. Daviso, E.; Eddy, M. T.; Andreas, L. B.; Griffin, R. G.; Herzfeld, J., Efficient resonance assignment of proteins in MAS NMR by simultaneous intra- and inter-residue 3D correlation spectroscopy. *J Biomol NMR* **2013,** *55*, 257.

142. Bayro, M. J.; Huber, M.; Ramachandran, R.; Davenport, T. C.; Meier, B. H.; Ernst, M.; Griffin, R. G., Dipolar truncation in magic-angle spinning NMR recoupling experiments. *J Chem Phys* **2009,** *130*.

143. Shi, C. W.; Fasshuber, H. K.; Chevelkov, V.; Xiang, S. Q.; Habenstein, B.; Vasa, S. K.; Becker, S.; Lange, A., BSH-CP based 3D solid-state NMR experiments for protein resonance assignment. *J Biomol NMR* **2014,** *59*, 15.

144. Chevelkov, V.; Giller, K.; Becker, S.; Lange, A., Efficient CO-CA transfer in highly deuterated proteins by band-selective homonuclear cross-polarization. *J Magn Reson* **2013,** *230*, 205.

145. Chevelkov, V.; Shi, C.; Fasshuber, H. K.; Becker, S.; Lange, A., Efficient band-selective homonuclear CO–CA cross-polarization in protonated proteins. *J Biomol NMR* **2013,** *56*, 303.

146. Takegoshi, K.; Nomura, K.; Terao, T., Rotational Resonance in the Tilted Rotating-Frame. *Chem Phys Lett* **1995,** *232*, 424.

147. Detken, A.; Hardy, E. H.; Ernst, M.; Kainosho, M.; Kawakami, T.; Aimoto, S.; Meier, B. H., Methods for sequential resonance assignment in solid, uniformly C-13, N-15 labelled peptides: Quantification and application to antamanide. *J Biomol NMR* **2001,** *20*, 203.

148. Weingarth, M.; Demco, D. E.; Bodenhausen, G.; Tekely, P., Improved magnetization transfer in solid-state NMR with fast magic angle spinning. *Chem Phys Lett* **2009,** *469*, 342.

149. Hu, B. W.; Lafon, O.; Trebosc, J.; Chen, Q.; Amoureux, J. P., Broad-band homo-nuclear correlations assisted by H-1 irradiation for bio-molecules in very high magnetic field at fast and ultra-fast MAS frequencies. *J Magn Reson* **2011,** *212*, 320.

150. Lewandowski, J. R.; De Paepe, G.; Eddy, M. T.; Struppe, J.; Maas, W.; Griffin, R. G., Proton Assisted Recoupling at High Spinning Frequencies. *J Phys Chem B* **2009,** *113*, 9062.

151. Chevelkov, V.; Shi, C.; Fasshuber, H. K.; Becker, S.; Lange, A., Efficient band-selective homonuclear CO-CA cross-polarization in protonated proteins. *J Biomol NMR* **2013,** *56*, 303.

152. Detken, A.; Ernst, M.; Meier, B. H., Towards biomolecular structure determination by high-resolution solid-state NMR: Assignment of solid peptides. *Chimia* **2001,** *55*, 844.

153. Cukkemane, A.; Nand, D.; Gradmann, S.; Weingarth, M.; Kaupp, U. B.; Baldus, M., Solid-state NMR [13C, 15N] resonance assignments of the nucleotide-binding domain of a bacterial cyclic nucleotide-gated channel. *Biomol NMR Assigm* **2012,** *6*, 225.

154. Schuetz, A.; Wasmer, C.; Habenstein, B.; Verel, R.; Greenwald, J.; Riek, R.; Böckmann, A.; Meier, B. H., Protocols for the sequential solid-state NMR spectroscopic assignment of a uniformly labeled 25 kDa protein: HET-s(1-227). *ChemBioChem* **2010,** *11*, 1543.

155. Wasmer, C.; Zimmer, A.; Sabate, R.; Soragni, A.; Saupe, S. J.; Ritter, C.; Meier, B. H., Structural Similarity between the Prion Domain of HET-s and a Homologue Can Explain Amyloid Cross-Seeding in Spite of Limited Sequence Identity. *J Mol Biol* **2010,** *402*, 311.

156. Kotecha, M.; Wickramasinghe, N. P.; Ishii, Y., Efficient low-power heteronuclear decoupling in C-13 high-resolution solid-state NMR under fast magic angle spinning. *Magn Reson Chem* **2007,** *45*, S221.

157. Morcombe, C. R.; Zilm, K. W., Chemical shift referencing in MAS solid state NMR. *J Magn Reson* **2003,** *162*, 479.

158. Delaglio, F.; Grzesiek, S.; Vuister, G. W.; Zhu, G.; Pfeifer, J.; Bax, A., NMRPipe: A multidimensional spectral processing system based on UNIX pipes. *J Biomol NMR* **1995,** *6*, 277.

159. Vranken, W. F.; Boucher, W.; Stevens, T. J.; Fogh, R. H.; Pajon, A.; Llinas, P.; Ulrich, E. L.; Markley, J. L.; Ionides, J.; Laue, E. D., The CCPN data model for NMR spectroscopy: Development of a software pipeline. *Proteins* **2005,** *59*, 687.

160. Stevens, T. J.; Fogh, R. H.; Boucher, W.; Higman, V. A.; Eisenmenger, F.; Bardiaux, B.; van Rossum, B. J.; Oschkinat, H.; Laue, E. D., A software framework for analysing solid-state MAS NMR data. *J Biomol NMR* **2011,** *51*, 437.

161. Ulrich, E. L.; Akutsu, H.; Doreleijers, J. F.; Harano, Y.; Ioannidis, Y. E.; Lin, J.; Livny, M.; Mading, S.; Maziuk, D.; Miller, Z.; Nakatani, E.; Schulte, C. F.; Tolmie, D. E.; Wenger, R. K.; Yao, H. Y.; Markley, J. L., BioMagResBank. *Nucleic Acids Res* **2008,** *36*, D402.

162. Chevelkov, V.; Shi, C.; Fasshuber, H. K.; Becker, S.; Lange, A., Efficient band-selective homonuclear CO-CA cross-polarization in protonated proteins. *Journal of Biomolecular NMR* **2013,** *56*, 303.

163. Wittmann, J. J.; Hendriks, L.; Meier, B. H.; Ernst, M., Controlling spin diffusion by tailored rf-irradiation schemes. *Chem Phys Lett* **2014,** *608*, 60.

164. Kay, L. E.; Ikura, M.; Tschudin, R.; Bax, A., Three-dimensional triple-resonance NMR spectroscopy of isotopically enriched proteins. *J Magn Reson* **1990,** *89*, 496.

165. Farmer, B. T.; Venters, R. A.; Spicer, L. D.; Wittekind, M. G.; Müller, L., A refocused and optimized HNCA: Increased sensitivity and resolution in large macromolecules. *J Biomol NMR* **1992,** *2*, 195.

166. Grzesiek, S.; Bax, A., Improved 3D triple-resonance NMR techniques applied to a 31 kDa protein. *J Magn Reson* **1992,** *96*, 432.

167. Vijayan, V.; Demers, J. P.; Biernat, J.; Mandelkow, E.; Becker, S.; Lange, A., Low-Power Solid-State NMR Experiments for Resonance Assignment under Fast Magic-Angle Spinning. *ChemPhysChem* **2009,** *10*, 2205.

168. Wickramasinghe, N. P.; Shaibat, M. A.; Jones, C. R.; Casabianca, L. B.; Dios, A. C. d.; Harwood, J. S.; Ishii, Y., Progress in C13 and H1 solid-state nuclear magnetic resonance for paramagnetic systems under very fast magic angle spinning. *J Chem Phys* **2008,** *128*, 052210.

169. Ishii, Y.; Yesinowski, J. P.; Tycko, R., Sensitivity enhancement in solid-state C-13 NMR of synthetic polymers and biopolymers by H-1 NMR detection with high-speed magic angle spinning. *J Am Chem Soc* **2001,** *123*, 2921.

170. Meier, B. H., Cross polarization under fast magic angle spinning: thermodynamical considerations. *Chem Phys Lett* **1992,** *188*, 201.

171. Laage, S.; Sachleben, J. R.; Steuernagel, S.; Pierattelli, R.; Pintacuda, G.; Emsley, L., Fast acquisition of multi-dimensional spectra in solid-state NMR enabled by ultra-fast MAS. *J Magn Reson* **2009,** *196*, 133.

172. Demers, J. P.; Vijayan, V.; Becker, S.; Lange, A., Tailored low-power cross-polarization under fast magic-angle spinning. *J Magn Reson* **2010,** *205*, 216.

173. Tycko, R., NMR at Low and Ultra low Temperatures. *Acc Chem Res* **2013,** *46*, 1923.

174. Peat, D. T.; Horsewill, A. J.; Kockenberger, W.; Linde, A. J. P.; Gadian, D. G.; Owers-Bradley, J. R., Achievement of high nuclear spin polarization using lanthanides as low-temperature NMR relaxation agents. *Phys Chem Chem Phys* **2013,** *15*, 7586.

175. Adams, R. W.; Aguilar, J. A.; Atkinson, K. D.; Cowley, M. J.; Elliott, P. I. P.; Duckett, S. B.; Green, G. G. R.; Khazal, I. G.; Lopez-Serrano, J.; Williamson, D. C., Reversible Interactions with para-Hydrogen Enhance NMR Sensitivity by Polarization Transfer. *Science* **2009,** *323*, 1708.

176. Ardenkjaer-Larsen, J. H.; Jóhannesson, H.; Petersson, J. S.; Wolber, J., Hyperpolarized Molecules in Solution. In *In vivo NMR Imaging: Methods and Protocols*, Schröder, L.; Faber, C., Eds. Humana Press: Totowa, NJ, 2011; pp 205.

177. Bowers, C. R.; Weitekamp, D. P., Transformation of Symmetrization Order to Nuclear-Spin Magnetization by Chemical Reaction and Nuclear Magnetic Resonance. *Phys Rev Lett* **1986,** *57*, 2645.

178. Roberts, L. D.; Dabbs, J. W. T., Nuclear Orientation. *Annu Rev Nucl Part Sci* **1961,** *11*, 175.

179. Thurber, K. R.; Tycko, R., Biomolecular solid state NMR with magic-angle spinning at 25 K. *J Magn Reson* **2008,** *195*, 179.

180. Solomon, I., Relaxation Processes in a System of Two Spins. *Phys Rev* **1955,** *99*, 559.

181. Otting, G., Protein NMR Using Paramagnetic Ions. *Annu Rev Biophys* **2010,** *39*, 387.

182. Alsaadi, B. M.; Rossotti, F. J. C.; Williams, R. J. P., Electron relaxation rates of lanthanide aquo-cations. *J Chem Soc, Dalton Trans* **1980**, 2147.

183. Blum, H.; Cusanovich, M. A.; Sweeney, W. V.; Ohnishi, T., Magnetic interactions between dysprosium complexes and two soluble iron-sulfur proteins. *J Biol Chem* **1981,** *256*, 2199.

184. Cavanagh, J.; Fairbrother, W. J.; Palmer, A. G.; Skelton, N. J.; Rance, M., *Protein NMR Spectroscopy: Principles and Practice*. Elsevier Science: 2010.

185. Idiyatullin, D.; Nesmelova, I.; Daragan, V. A.; Mayo, K. H., Comparison of (13)C(α)H and (15)NH backbone dynamics in protein GB1. *Protein Science : A Publication of the Protein Society* **2003,** *12*, 914.

186. Fricke, P.; Mance, D.; Chevelkov, V.; Giller, K.; Becker, S.; Baldus, M.; Lange, A., High resolution observed in 800 MHz DNP spectra of extremely rigid type III secretion needles. *J Biomol NMR* **2016,** *65*, 121.

187. Mayzel, M.; Rosenlöw, J.; Isaksson, L.; Orekhov, V. Y., Time-resolved multidimensional NMR with non-uniform sampling. *J Biomol NMR* **2014,** *58*, 129.

188. Schanda, P.; Brutscher, B., Very Fast Two-Dimensional NMR Spectroscopy for Real-Time Investigation of Dynamic Events in Proteins on the Time Scale of Seconds. *J Am Chem Soc* **2005,** *127*, 8014.

189. Mulleti, S.; Singh, A.; Brahmkhatri, V. P.; Chandra, K.; Raza, T.; Mukherjee, S. P.; Seelamantula, C. S.; Atreya, H. S., Super-Resolved Nuclear Magnetic Resonance Spectroscopy. *Sci Rep* **2017,** *7*, 9651.

190. Lewandowski, J. R., Advances in Solid-State Relaxation Methodology for Probing Site-Specific Protein Dynamics. *Acc Chem Res* **2013,** *46*, 2018.

191. Spiess, H. W., Deuteron NMR — a new tool for studying chain mobility and orientation in polymers. In *Characterization of Polymers in the Solid State I: Part A: NMR and Other Spectroscopic Methods Part B: Mechanical Methods*, Kaush, H. H.; Zachman, H. G., Eds. Springer Berlin Heidelberg: Berlin, Heidelberg, 1985; pp 23.

192. Siemer, A. B.; Huang, K.-Y.; McDermott, A. E., Protein–ice interaction of an antifreeze protein observed with solid-state NMR. *Proc Natl Acad Sci* **2010,** *107*, 17580.

193. Ngai, K.; Capaccioli, S.; Shinyashiki, N., The protein "glass" transition and the role of the solvent. *J Phys Chem B* **2008,** *112*, 3826.

194. Bajaj, V. S.; van der Wel, P. C.; Griffin, R. G., Observation of a low-temperature, dynamically driven structural transition in a polypeptide by solid-state NMR spectroscopy. *J Am Chem Soc* **2008,** *131*, 118.

195. Vugmeyster, L.; Ostrovsky, D.; Ford, J. J.; Lipton, A. S., Freezing of dynamics of a methyl group in a protein hydrophobic core at cryogenic temperatures by deuteron NMR spectroscopy. *J Am Chem Soc* **2010,** *132*, 4038.
196. Duer, M. J., *Solid State NMR Spectroscopy: Principles and Applications*. Wiley: 2001.
197. Torchia, D.; Szabo, A., Spin-lattice relaxation in solids. *J Magn Reson* **1982,** *49*, 107.
198. Redfield, A. G., On the theory of relaxation processes. *IBM J Res Dev* **1957,** *1*, 19.
199. Argyres, P.; Kelley, P., Theory of spin resonance and relaxation. *Phys Rev* **1964,** *134*, A98.
200. Bloch, F., Nuclear Induction. *Phys Rev* **1946,** *70*, 460.
201. Baud, M. F.; Hubbard, P. S., Nonexponential Spin-Lattice Relaxation of Protons in Solid C H 3 CN and Solid Solutions of C H 3 CN in C D 3 CN. *Phys Rev* **1968,** *170*, 384.
202. Woessner, D., Spin Relaxation Processes in a Two-Proton System Undergoing Anisotropic Reorientation. *J Chem Phys* **1962,** *36*, 1.
203. Wangsness, R. K.; Bloch, F., The dynamical theory of nuclear induction. *Phys Rev* **1953,** *89*, 728.
204. Bloembergen, N.; Purcell, E. M.; Pound, R. V., Relaxation effects in nuclear magnetic resonance absorption. *Phys Rev* **1948,** *73*, 679.
205. Khutsishvili, G., Spin diffusion. *Soviet Physics Uspekhi* **1966,** *8*, 743.
206. Cheung, T. T. P., Spin diffusion in NMR in solids. *Phys Rev B* **1981,** *23*, 1404.
207. Clough, S.; Gray, K., Spin Diffusion and Nuclear Magnetic Resonance in Rotating Solids. *Proceedings of the Physical Society* **1962,** *80*, 1382.
208. Mehring, M., *Principles of High Resolution NMR in Solids*. Springer Berlin Heidelberg: 2012.
209. Schanda, P.; Ernst, M., Studying Dynamics by Magic-Angle Spinning Solid-State NMR Spectroscopy: Principles and Applications to Biomolecules. *Prog Nucl Magn Reson Spectrosc* **2016,** *96*, 1.
210. Peng, J. W.; Thanabal, V.; Wagner, G., 2D heteronuclear NMR measurements of spin-lattice relaxation times in the rotating frame of X nuclei in heteronuclear HX spin systems. *J Magn Reson* **1991,** *94*, 82.

211. Lipari, G.; Szabo, A., Model-free approach to the interpretation of nuclear magnetic resonance relaxation in macromolecules. 1. Theory and range of validity. *J Am Chem Soc* **1982,** *104*, 4546.

212. Wittebort, R.; Szabo, A., Theory of NMR relaxation in macromolecules: restricted diffusion and jump models for multiple internal rotations in amino acid side chains. *J Chem Phys* **1978,** *69*, 1722.

213. Jaroniec, C. P., Solid-state nuclear magnetic resonance structural studies of proteins using paramagnetic probes. *Solid State Nucl Magn Reson* **2012,** *43-44*, 1.

214. Bloembergen, N., Proton Relaxation Times in Paramagnetic Solutions. *J Chem Phys* **1957,** *27*, 572.

215. Bloembergen, N.; Morgan, L. O., Proton Relaxation Times in Paramagnetic Solutions. Effects of Electron Spin Relaxation. *J Chem Phys* **1961,** *34*, 842.

216. Atsarkin, V. A.; Demidov, V. V.; Vasneva, G. A.; Odintsov, B. M.; Belford, R. L.; Radüchel, B.; Clarkson, R. B., Direct Measurement of Fast Electron Spin−Lattice Relaxation: Method and Application to Nitroxide Radical Solutions and Gd3+ Contrast Agents. *J Phys Chem A* **2001,** *105*, 9323.

217. Owenius, R.; Terry, G. E.; Williams, M. J.; Eaton, S. S.; Eaton, G. R., Frequency Dependence of Electron Spin Relaxation of Nitroxyl Radicals in Fluid Solution. *J Phys Chem B* **2004,** *108*, 9475.

218. van Beek, J. D., matNMR: A flexible toolbox for processing, analyzing and visualizing magnetic resonance data in Matlab®. *J Magn Reson* **2007,** *187*, 19.

219. Lamley, J. M.; Lougher, M. J.; Sass, H. J.; Rogowski, M.; Grzesiek, S.; Lewandowski, J. R., Unraveling the complexity of protein backbone dynamics with combined (13)C and (15)N solid-state NMR relaxation measurements. *Phys Chem Chem Phys* **2015,** *17*, 21997.

220. Ringe, D.; Petsko, G. A., The 'glass transition' in protein dynamics: what it is, why it occurs, and how to exploit it. *Biophys Chem* **2003,** *105*, 667.

221. Linden, A. H.; Franks, W. T.; Akbey, Ü.; Lange, S.; van Rossum, B.-J.; Oschkinat, H., Cryogenic temperature effects and resolution upon slow cooling of protein preparations in solid state NMR. *J Biomol NMR* **2011,** *51*, 283.

222. Luyet, B.; Rasmussen, D., Study by differential thermal analysis of the temperatures of instability of rapidly cooled solutions of glycerol, ethylene glycol, sucrose and glucose. *Biodynamica* **1967,** *10*, 167.

223. Gao, C.; Zhou, G.-Y.; Xu, Y.; Hua, T.-C., Glass transition and enthalpy relaxation of ethylene glycol and its aqueous solution. *Thermochim Acta* **2005,** *435*, 38.

224. Angell, C. A., Formation of Glasses from Liquids and Biopolymers. *Science* **1995,** *267*, 1924.

225. Shimon, D.; Hovav, Y.; Feintuch, A.; Goldfarb, D.; Vega, S., Dynamic nuclear polarization in the solid state: a transition between the cross effect and the solid effect. *Phys Chem Chem Phys* **2012,** *14*, 5729.

226. Abragam, A.; Goldman, M., Principles of dynamic nuclear polarisation. *Rep Prog Phys* **1978,** *41*, 395.

227. Joo, C.-G.; Casey, A.; Turner, C. J.; Griffin, R. G., In Situ Temperature-Jump Dynamic Nuclear Polarization: Enhanced Sensitivity in Two Dimensional 13C−13C Correlation Spectroscopy in Solution. *J Am Chem Soc* **2008,** *131*, 12.

228. Ardenkjaer-Larsen, J. H.; Fridlund, B.; Gram, A.; Hansson, G.; Hansson, L.; Lerche, M. H.; Servin, R.; Thaning, M.; Golman, K., Increase in signal-to-noise ratio of > 10,000 times in liquid-state NMR. *Proc Natl Acad Sci USA* **2003,** *100*, 10158.

229. Sze, K. H.; Wu, Q.; Tse, H. S.; Zhu, G., Dynamic Nuclear Polarization: New Methodology and Applications. In *NMR of Proteins and Small Biomolecules*, Zhu, G., Ed. Springer Berlin Heidelberg: Berlin, Heidelberg, 2012; pp 215.

230. Becerra, L. R.; Gerfen, G. J.; Temkin, R. J.; Singel, D. J.; Griffin, R. G., Dynamic nuclear polarization with a cyclotron resonance maser at 5 T. *Phys Rev Lett* **1993,** *71*, 3561.

231. Maly, T.; Debelouchina, G. T.; Bajaj, V. S.; Hu, K.-N.; Joo, C.-G.; Mak-Jurkauskas, M. L.; Sirigiri, J. R.; van der Wel, P. C. A.; Herzfeld, J.; Temkin, R. J.; Griffin, R. G., Dynamic nuclear polarization at high magnetic fields. *J Chem Phys* **2008,** *128*.

232. Ni, Q. Z.; Daviso, E.; Can, T. V.; Markhasin, E.; Jawla, S. K.; Swager, T. M.; Temkin, R. J.; Herzfeld, J.; Griffin, R. G., High Frequency Dynamic Nuclear Polarization. *Acc Chem Res* **2013,** *46*, 1933.

233. Mentink-Vigier, F.; Akbey, Ü.; Oschkinat, H.; Vega, S.; Feintuch, A., Theoretical aspects of Magic Angle Spinning - Dynamic Nuclear Polarization. *J Magn Reson* **2015,** *258*, 102.

234. Carver, T. R.; Slichter, C. P., Polarization of Nuclear Spins in Metals. *Phys Rev* **1953,** *92*, 212.

235. Can, T. V.; Caporini, M. A.; Mentink-Vigier, F.; Corzilius, B.; Walish, J. J.; Rosay, M.; Maas, W. E.; Baldus, M.; Vega, S.; Swager, T. M.; Griffin, R. G., Overhauser effects in insulating solids. *J Chem Phys* **2014,** *141*, 064202.

236. Jeffries, C. D., Polarization of Nuclei by Resonance Saturation in Paramagnetic Crystals. *Phys Rev* **1957,** *106*, 164.

237. Hwang, C. F.; Hill, D. A., New Effect in Dynamic Polarization. *Phys Rev Lett* **1967,** *18*, 110.

238. Hwang, C. F.; Hill, D. A., Phenomenological Model for the New Effect in Dynamic Polarization. *Phys Rev Lett* **1967,** *19*, 1011.

239. Abragam, A.; Borghini, M., Chapter VIII Dynamic Polarization of Nuclear Targets. In *Progress in Low Temperature Physics*, Gorter, C. J., Ed. Elsevier: 1964; Vol. 4, pp 384.

240. Hovav, Y.; Feintuch, A.; Vega, S., Dynamic nuclear polarization assisted spin diffusion for the solid effect case. *J Chem Phys* **2011,** *134*.

241. Hovav, Y.; Feintuch, A.; Vega, S., Theoretical aspects of dynamic nuclear polarization in the solid state - The cross effect. *J Magn Reson* **2012,** *214*, 29.

242. Hovav, Y.; Feintuch, A.; Vega, S., Theoretical aspects of dynamic nuclear polarization in the solid state - spin temperature and thermal mixing. *Phys Chem Chem Phys* **2013,** *15*, 188.

243. Loening, N. M.; Rosay, M.; Weis, V.; Griffin, R. G., Solution-State Dynamic Nuclear Polarization at High Magnetic Field. *J Am Chem Soc* **2002,** *124*, 8808.

244. Höfer, P.; Parigi, G.; Luchinat, C.; Carl, P.; Guthausen, G.; Reese, M.; Carlomagno, T.; Griesinger, C.; Bennati, M., Field Dependent Dynamic Nuclear Polarization with Radicals in Aqueous Solution. *J Am Chem Soc* **2008,** *130*, 3254.

245. Corzilius, B.; Smith, A. A.; Barnes, A. B.; Luchinat, C.; Bertini, I.; Griffin, R. G., High-Field Dynamic Nuclear Polarization with High-Spin Transition Metal Ions. *J Am Chem Soc* **2011,** *133*, 5648.

246. Corzilius, B.; Smith, A. A.; Griffin, R. G., Solid effect in magic angle spinning dynamic nuclear polarization. *J Chem Phys* **2012,** *137*, 054201.

247. Wenckebach, W. T.; Swanenburg, T. J. B.; Poulis, N. J., Thermodynamics of spin systems in paramagnetic crystals. *Phys Rep* **1974,** *14c*, 181.

248. Wenckeback, W. T.; van den Heuvel, G. M.; Hoogstraate, H.; Swanenburg, T. J. B.; Poulis, N. J., Experimental Proof of the Strong Coupling Between the Electron Spin-Spin Reservoir and a Nuclear Spin System in Dilute Paramagnetic Crystals. *Phys Rev Lett* **1969,** *22*, 581.

249. Kobayashi, T.; Lafon, O.; Thankamony, A. S. L.; Slowing, I. I.; Kandel, K.; Carnevale, D.; Vitzthum, V.; Vezin, H.; Amoureux, J.-P.; Bodenhausen, G.; Pruski, M., Analysis of sensitivity enhancement by dynamic nuclear polarization in solid-state NMR: a case study of functionalized mesoporous materials. *Phys Chem Chem Phys* **2013,** *15*, 5553.

250. Thurber, K. R.; Yau, W.-M.; Tycko, R., Low-temperature dynamic nuclear polarization at 9.4 T with a 30 mW microwave source. *J Magn Reson* **2010,** *204*, 303.

251. Rossini, A. J.; Zagdoun, A.; Lelli, M.; Canivet, J.; Aguado, S.; Ouari, O.; Tordo, P.; Rosay, M.; Maas, W. E.; Coperet, C.; Farrusseng, D.; Emsley, L.; Lesage, A., Dynamic Nuclear Polarization Enhanced Solid-State NMR Spectroscopy of Functionalized Metal-Organic Frameworks. *Angew Chem Int Ed* **2012,** *51*, 123.

252. Rossini, A. J.; Zagdoun, A.; Lelli, M.; Gajan, D.; Rascon, F.; Rosay, M.; Maas, W. E.; Coperet, C.; Lesage, A.; Emsley, L., One hundred fold overall sensitivity enhancements for Silicon-29 NMR spectroscopy of surfaces by dynamic nuclear polarization with CPMG acquisition. *Chem Sci* **2012,** *3*, 108.

253. Jacso, T.; Franks, W. T.; Rose, H.; Fink, U.; Broecker, J.; Keller, S.; Oschkinat, H.; Reif, B., Characterization of Membrane Proteins in Isolated Native Cellular Membranes by Dynamic Nuclear Polarization Solid-State NMR Spectroscopy without Purification and Reconstitution. *Angew Chem Int Ed* **2012,** *51*, 432.

254. Thurber, K. R.; Yau, W.-M.; Tycko, R., Low-temperature dynamic nuclear polarization at 9.4T with a 30mW microwave source. *J Magn Reson* **2010,** *204*, 303.

255. Barnes, A. B.; Corzilius, B.; Mak-Jurkauskas, M. L.; Andreas, L. B.; Bajaj, V. S.; Matsuki, Y.; Belenky, M. L.; Lugtenburg, J.; Sirigiri, J. R.; Temkin, R. J.; Herzfeld, J.; Griffin, R. G., Resolution and polarization distribution in cryogenic DNP/MAS experiments. *Phys Chem Chem Phys* **2010,** *12*, 5861.

256. Maly, T.; Debelouchina, G. T.; Bajaj, V. S.; Hu, K.-N.; Joo, C.-G.; Mak–Jurkauskas, M. L.; Sirigiri, J. R.; Wel, P. C. A. v. d.; Herzfeld, J.; Temkin, R. J.; Griffin, R. G., Dynamic nuclear polarization at high magnetic fields. *J Chem Phys* **2008,** *128*, 052211.

257. Hu, K.-N.; Song, C.; Yu, H.-h.; Swager, T. M.; Griffin, R. G., High-frequency dynamic nuclear polarization using biradicals: A multifrequency EPR lineshape analysis. *J Chem Phys* **2008,** *128*, 052302.

258. Rosay, M.; Tometich, L.; Pawsey, S.; Bader, R.; Schauwecker, R.; Blank, M.; Borchard, P. M.; Cauffman, S. R.; Felch, K. L.; Weber, R. T.; Temkin, R. J.; Griffin, R. G.; Maas, W. E., Solid-state dynamic nuclear polarization at 263 GHz: spectrometer design and experimental results. *Phys Chem Chem Phys* **2010,** *12*, 5850.

259. Lumata, L.; Merritt, M. E.; Kovacs, Z., Influence of deuteration in the glassing matrix on (13)C dynamic nuclear polarization(). *Phys Chem Chem Phys* **2013,** *15*, 7032.

260. Wickramasinghe, N. P.; Parthasarathy, S.; Jones, C. R.; Bhardwaj, C.; Long, F.; Kotecha, M.; Mehboob, S.; Fung, L. W. M.; Past, J.; Samoson, A.; Ishii, Y., Nanomole-scale protein solid-state NMR by breaking intrinsic H-1 T-1 boundaries. *Nat Methods* **2009,** *6*, 215.

261. Takahashi, H.; Lee, D.; Dubois, L.; Bardet, M.; Hediger, S.; De Paepe, G., Rapid Natural-Abundance 2D C-13-C-13 Correlation Spectroscopy Using Dynamic Nuclear Polarization Enhanced Solid-State NMR and Matrix-Free Sample Preparation. *Angew Chem Int Ed* **2012,** *51*, 11766.

262. Lee, D.; Hediger, S.; De Paëpe, G., Is solid-state NMR enhanced by dynamic nuclear polarization? *Solid State Nucl Magn Reson* **2015,** *66-67*, 6.

263. Jarvis, J. A.; Haies, I.; Lelli, M.; Rossini, A. J.; Kuprov, I.; Carravetta, M.; Williamson, P. T. F., Measurement of 14N quadrupole couplings in biomolecular solids using indirect-detection 14N solid-state NMR with DNP. *Chem Commun* **2017**.

264. Ardenkjær-Larsen, J. H.; Laursen, I.; Leunbach, I.; Ehnholm, G.; Wistrand, L. G.; Petersson, J. S.; Golman, K., EPR and DNP Properties of Certain Novel Single Electron Contrast Agents Intended for Oximetric Imaging. *J Magn Reson* **1998,** *133*, 1.

265. Lumata, L.; Ratnakar, S. J.; Jindal, A.; Merritt, M.; Comment, A.; Malloy, C.; Sherry, A. D.; Kovacs, Z., BDPA: An Efficient Polarizing Agent for Fast Dissolution Dynamic Nuclear Polarization NMR Spectroscopy. *Chemistry* **2011,** *17*, 10825.

266. Hu, K.-N.; Yu, H.-h.; Swager, T. M.; Griffin, R. G., Dynamic Nuclear Polarization with Biradicals. *J Am Chem Soc* **2004,** *126*, 10844.

267. Song, C.; Hu, K.-N.; Joo, C.-G.; Swager, T. M.; Griffin, R. G., TOTAPOL: A Biradical Polarizing Agent for Dynamic Nuclear Polarization Experiments in Aqueous Media. *J Am Chem Soc* **2006,** *128*, 11385.

268. Matsuki, Y.; Maly, T.; Ouari, O.; Karoui, H.; Le Moigne, F.; Rizzato, E.; Lyubenova, S.; Herzfeld, J.; Prisner, T.; Tordo, P., Dynamic nuclear polarization with a rigid biradical. *Angew Chem* **2009,** *121*, 5096.

269. Sauvée, C.; Casano, G.; Abel, S.; Rockenbauer, A.; Akhmetzyanov, D.; Karoui, H.; Siri, D.; Aussenac, F.; Maas, W.; Weber, R. T.; Prisner, T.; Rosay, M.; Tordo, P.; Ouari, O., Tailoring of Polarizing Agents in the bTurea Series for Cross-Effect Dynamic Nuclear Polarization in Aqueous Media. *Chemistry* **2016,** *22*, 5598.

270. Jeschke, G., Conformational dynamics and distribution of nitroxide spin labels. *Prog Nucl Magn Reson Spectrosc* **2013,** *72*, 42.

271. Doll, A.; Bordignon, E.; Joseph, B.; Tschaggelar, R.; Jeschke, G., Liquid state DNP for water accessibility measurements on spin-labeled membrane proteins at physiological temperatures. *J Magn Reson* **2012,** *222*, 34.

272. Crabb, D.; Meyer, W., Solid polarized targets for nuclear and particle physics experiments. *Annu Rev Nucl Part Sci* **1997,** *47*, 67.

273. Hu, K.-N., Polarizing agents and mechanisms for high-field dynamic nuclear polarization of frozen dielectric solids. *Solid State Nucl Magn Reson* **2011,** *40*, 31.

274. Pylaeva, S.; Ivanov, K. L.; Baldus, M.; Sebastiani, D.; Elgabarty, H., Molecular Mechanism of Overhauser Dynamic Nuclear Polarization in Insulating Solids. *J Phys Chem Lett* **2017,** *8*, 2137.

275. Haze, O.; Corzilius, B.; Smith, A. A.; Griffin, R. G.; Swager, T. M., Water-Soluble Narrow-Line Radicals for Dynamic Nuclear Polarization. *J Am Chem Soc* **2012,** *134*, 14287.

276. Lelli, M.; Chaudhari, S. R.; Gajan, D.; Casano, G.; Rossini, A. J.; Ouari, O.; Tordo, P.; Lesage, A.; Emsley, L., Solid-State Dynamic Nuclear Polarization at 9.4 and 18.8 T from 100 K to Room Temperature. *J Am Chem Soc* **2015,** *137*, 14558.

277. Koelsch, C. F., Syntheses with Triarylvinylmagnesium Bromides. α,γ-Bisdiphenylene-β-phenylallyl, a Stable Free Radical. *J Am Chem Soc* **1957,** *79*, 4439.

278. Ardenkjær-Larsen, J. H.; Fridlund, B.; Gram, A.; Hansson, G.; Hansson, L.; Lerche, M. H.; Servin, R.; Thaning, M.; Golman, K., Increase in signal-to-noise ratio of > 10,000 times in liquid-state NMR. *Proc Natl Acad Sci* **2003,** *100*, 10158.

279. Reddy, T. J.; Iwama, T.; Halpern, H. J.; Rawal, V. H., General Synthesis of Persistent Trityl Radicals for EPR Imaging of Biological Systems. *J Org Chem* **2002,** *67*, 4635.

280. Barnes, A. B.; Paëpe, G. D.; van der Wel, P. C. A.; Hu, K. N.; Joo, C. G.; Bajaj, V. S.; Mak-Jurkauskas, M. L.; Sirigiri, J. R.; Herzfeld, J.; Temkin, R. J.; Griffin, R. G., High-Field Dynamic Nuclear Polarization for Solid and Solution Biological NMR. *Appl Magn Reson* **2008,** *34*, 237.

281. Lumata, L.; Merritt, M. E.; Malloy, C. R.; Sherry, A. D.; Kovacs, Z., Impact of Gd3+ on DNP of [1-13C]Pyruvate Doped with Trityl OX063, BDPA, or 4-Oxo-TEMPO. *J Phys Chem A* **2012,** *116*, 5129.

282. Gordon, J.; Fain, S. B.; Rowland, I. J., Effect of Lanthanide Ions on Dynamic Nuclear Polarization Enhancement and Liquid State T(1) Relaxation. *Magn Reson Med* **2012,** *68*, 1949.

283. Benmelouka, M.; Van Tol, J.; Borel, A.; Port, M.; Helm, L.; Brunel, L. C.; Merbach, A. E., A High-Frequency EPR Study of Frozen Solutions of GdIII Complexes: Straightforward Determination of the Zero-Field Splitting Parameters and Simulation of the NMRD Profiles. *J Am Chem Soc* **2006,** *128*, 7807.

284. Farrar, C. T.; Hall, D. A.; Gerfen, G. J.; Inati, S. J.; Griffin, R. G., Mechanism of dynamic nuclear polarization in high magnetic fields. *J Chem Phys* **2001,** *114*, 4922.

285. Hu, K. N.; Bajaj, V. S.; Rosay, M.; Griffin, R. G., High-frequency dynamic nuclear polarization using mixtures of TEMPO and trityl radicals. *J Chem Phys* **2007,** *126*.

286. Bajaj, V. S.; Farrar, C. T.; Hornstein, M. K.; Mastovsky, I.; Vieregg, J.; Bryant, J.; Elena, B.; Kreischer, K. E.; Temkin, R. J.; Griffin, R. G., Dynamic nuclear polarization at 9T using a novel 250 GHz gyrotron microwave source. *J Magn Reson* **2003,** *160*, 85.

287. Hall, D. A.; Maus, D. C.; Gerfen, G. J.; Inati, S. J.; Becerra, L. R.; Dahlquist, F. W.; Griffin, R. G., Polarization-Enhanced NMR Spectroscopy of Biomolecules in Frozen Solution. *Science* **1997,** *276*, 930.

288. Marvin, D.; Hale, R.; Nave, C.; Citterich, M. H., Molecular models and structural comparisons of native and mutant class I filamentous bacteriophages: Ff (fd, f1, M13), If1 and IKe. *J Mol Biol* **1994,** *235*, 260.

289. Rosay, M.; Zeri, A.-C.; Astrof, N. S.; Opella, S. J.; Herzfeld, J.; Griffin, R. G., Sensitivity-Enhanced NMR of Biological Solids: Dynamic Nuclear Polarization of Y21M fd Bacteriophage and Purple Membrane. *J Am Chem Soc* **2001,** *123*, 1010.

290. Can, T. V.; Ni, Q. Z.; Griffin, R. G., Mechanisms of dynamic nuclear polarization in insulating solids. *J Magn Reson* **2015,** *253*, 23.

291. Vitzthum, V.; Borcard, F.; Jannin, S.; Morin, M.; Mieville, P.; Caporini, M. A.; Sienkiewicz, A.; Gerber-Lemaire, S.; Bodenhausen, G., Fractional Spin-Labeling of Polymers for Enhancing NMR Sensitivity by Solvent-Free Dynamic Nuclear Polarization. *ChemPhysChem* **2011,** *12*, 2929.

292. Maly, T.; Cui, D. T.; Griffin, R. G.; Miller, A. F., H-1 Dynamic Nuclear Polarization Based on an Endogenous Radical. *J Phys Chem B* **2012,** *116*, 7055.

293. Wylie, B. J.; Dzikovski, B. G.; Pawsey, S.; Caporini, M.; Rosay, M.; Freed, J. H.; McDermott, A. E., Dynamic nuclear polarization of membrane proteins: covalently bound spin-labels at protein-protein interfaces. *J Biomol NMR* **2015,** *61*, 361.

294. Smith, A. N.; Caporini, M. A.; Fanucci, G. E.; Long, J. R., A Method for Dynamic Nuclear Polarization Enhancement of Membrane Proteins. *Angew Chem Int Ed* **2015,** *54*, 1542.

295. Fernandez-de-Alba, C.; Takahashi, H.; Richard, A.; Chenavier, Y.; Dubois, L.; Maurel, V.; Lee, D.; Hediger, S.; De Paepe, G., Matrix-Free DNP-Enhanced NMR Spectroscopy of Liposomes Using a Lipid-Anchored Biradical. *Chem-Eur J* **2015,** *21*, 4512.

296. Takahashi, H.; Ayala, I.; Bardet, M.; De Paepe, G.; Simorre, J. P.; Hediger, S., Solid-State NMR on Bacterial Cells: Selective Cell Wall Signal Enhancement and Resolution Improvement using Dynamic Nuclear Polarization. *J Am Chem Soc* **2013,** *135*, 5105.

297. Voinov, M. A.; Good, D. B.; Ward, M. E.; Milikisiyants, S.; Marek, A.; Caporini, M. A.; Rosay, M.; Munro, R. A.; Ljumovic, M.; Brown, L. S.; Ladizhansky, V.; Smirnov, A. I., Cysteine-Specific Labeling of Proteins with a Nitroxide Biradical for Dynamic Nuclear Polarization NMR. *J Phys Chem B* **2015,** *119*, 10180.

298. Gajan, D.; Schwarzwalder, M.; Conley, M. P.; Gruning, W. R.; Rossini, A. J.; Zagdoun, A.; Lelli, M.; Yulikov, M.; Jeschke, G.; Sauvee, C.; Ouari, O.; Tordo, P.; Veyre, L.; Lesage, A.; Thieuleux, C.; Emsley, L.; Coperet, C., Solid-Phase Polarization Matrixes for Dynamic Nuclear Polarization from Homogeneously Distributed Radicals in Mesostructured Hybrid Silica Materials. *J Am Chem Soc* **2013,** *135*, 15459.

299. Klauda, J. B.; Venable, R. M.; Freites, J. A.; O'Connor, J. W.; Tobias, D. J.; Mondragon-Ramirez, C.; Vorobyov, I.; MacKerell, A. D.; Pastor, R. W., Update of the CHARMM All-Atom Additive Force Field for Lipids: Validation on Six Lipid Types. *J Phys Chem B* **2010,** *114*, 7830.

300. Lee, J.; Cheng, X.; Swails, J. M.; Yeom, M. S.; Eastman, P. K.; Lemkul, J. A.; Wei, S.; Buckner, J.; Jeong, J. C.; Qi, Y. F.; Jo, S.; Pande, V. S.; Case, D. A.; Brooks, C. L.; MacKerell, A. D.; Klauda, J. B.; Im, W., CHARMM-GUI Input Generator for NAMD, GROMACS, AMBER, OpenMM, and CHARMM/OpenMM Simulations Using the CHARMM36 Additive Force Field. *J Chem Theory Comput* **2016,** *12*, 405.

301. Jo, S.; Kim, T.; Iyer, V. G.; Im, W., CHARMM-GUI: A web-based graphical user interface for CHARMM. *J Comput Chem* **2008,** *29*, 1859.

302. Brooks, B. R.; Bruccoleri, R. E.; Olafson, B. D.; States, D. J.; Swaminathan, S.; Karplus, M., CHARMM: A program for macromolecular energy, minimization, and dynamics calculations. *J Comput Chem* **1983,** *4*, 187.

303. Pettersen, E. F.; Goddard, T. D.; Huang, C. C.; Couch, G. S.; Greenblatt, D. M.; Meng, E. C.; Ferrin, T. E., UCSF Chimera—A visualization system for exploratory research and analysis. *J Comput Chem* **2004,** *25*, 1605.

304. Berliner, L. J.; Grunwald, J.; Hankovszky, H. O.; Hideg, K., A novel reversible thiol-specific spin label: Papain active site labeling and inhibition. *Anal Biochem* **1982,** *119*, 450.

305. Miles, A. J.; Wallace, B. A., Synchrotron radiation circular dichroism spectroscopy of proteins and applications in structural and functional genomics. *Chem Soc Rev* **2006,** *35*, 39.

306. Persson, M.; Harbridge, J. R.; Hammarstrom, P.; Mitri, R.; Martensson, L. G.; Carlsson, U.; Eaton, G. R.; Eaton, S. S., Comparison of electron paramagnetic resonance methods to determine distances between spin labels on human carbonic anhydrase II. *Biophys J* **2001,** *80*, 2886.

307. Blank, A., A new approach to distance measurements between two spin labels in the > 10 nm range. *Phys Chem Chem Phys* **2017,** *19*, 5222.

308. Baldus, M.; Geurts, D. G.; Hediger, S.; Meier, B. H., Efficient15N–13C Polarization Transfer by Adiabatic-Passage Hartmann–Hahn Cross Polarization. *J Magn Reson, Ser A* **1996,** *118*, 140.

309. Le, D.; Ziarelli, F.; Phan, T. N. T.; Mollica, G.; Thureau, P.; Aussenac, F.; Ouari, O.; Gigmes, D.; Tordo, P.; Viel, S., Up to 100% Improvement in Dynamic Nuclear Polarization Solid-State NMR Sensitivity Enhancement of Polymers by Removing Oxygen. *Macromol Rapid Commun* **2015,** *36*, 1416.

310. Kubicki, D. J.; Rossini, A. J.; Purea, A.; Zagdoun, A.; Ouari, O.; Tordo, P.; Engelke, F.; Lesage, A.; Emsley, L., Amplifying Dynamic Nuclear Polarization of

Frozen Solutions by Incorporating Dielectric Particles. *J Am Chem Soc* **2014,** *136*, 15711.

311. Taylor, G. F.; Wood, S. P.; Mörs, K.; Glaubitz, C.; Werner, J. M.; Williamson, P. T. F., Morphological Differences between β(2)-Microglobulin in Fibrils and Inclusion Bodies. *ChemBioChem* **2011,** *12*, 556.
312. Saitô, H.; Ando, I.; Ramamoorthy, A., Chemical shift tensor – The heart of NMR: Insights into biological aspects of proteins. *Prog Nucl Magn Reson Spectrosc* **2010,** *57*, 181.
313. Harbison, G. S.; Herzfeld, J., Solid-State Nitrogen- 15 Nuclear Magnetic Resonance Study of the Schiff Base in Bacteriorhodopsin. *Biochemistry* **1983,** *22*, 1.
314. Harbison, G. S.; Jelinski, L. W.; Stark, R. E.; Torchia, D. A.; Herzfeld, J.; Griffin, R. G., 15N chemical shift and 15N-13C dipolar tensors for the peptide bond in [1-13C]glycyl[15N]glycine hydrochloride monohydrate. *J Magn Reson* **1984,** *60*, 79.
315. De Groot, H. J. M.; Harbison, G. S.; Herzfeld, J.; Griffin, R. G., Nuclear magnetic resonance study of the Schiff base in bacteriorhodopsin: counterion effects on the nitrogen-15 shift anisotropy. *Biochemistry* **1989,** *28*, 3346.
316. Poon, A.; Birn, J.; Ramamoorthy, A., How Does an Amide-15N Chemical Shift Tensor Vary in Peptides? *J Phys Chem B* **2004,** *108*, 16577.
317. Parthasarathy, S.; Nishiyama, Y.; Ishii, Y., Sensitivity and Resolution Enhanced Solid-State NMR for Paramagnetic Systems and Biomolecules under Very Fast Magic Angle Spinning. *Acc Chem Res* **2013,** *46*, 2127.
318. Siemer, A. B.; Huang, K.-Y.; McDermott, A. E., Protein linewidth and solvent dynamics in frozen solution NMR. *PLoS One* **2012,** *7*, e47242.
319. Otting, G., Prospects for lanthanides in structural biology by NMR. *J Biomol NMR* **2008,** *42*, 1.